

Integrated Daylighting and Artificial Lighting Control based on High Dynamic Range Vision Sensors

THÈSE N° 8277 (2017)

PRÉSENTÉE LE 15 DÉCEMBRE 2017

À LA FACULTÉ DE L'ENVIRONNEMENT NATUREL, ARCHITECTURAL ET CONSTRUIT
LABORATOIRE D'ÉNERGIE SOLAIRE ET PHYSIQUE DU BÂTIMENT
PROGRAMME DOCTORAL EN ENERGIE

ÉCOLE POLYTECHNIQUE FÉDÉRALE DE LAUSANNE

POUR L'OBTENTION DU GRADE DE DOCTEUR ÈS SCIENCES

PAR

Ali MOTAMED

acceptée sur proposition du jury:

Dr J. Van Herle, président du jury
Prof. J.-L. Scartezzini, directeur de thèse
Dr R. Ferrini, rapporteur
Dr B. Bueno, rapporteur
Prof. M. Andersen, rapporteuse



ÉCOLE POLYTECHNIQUE
FÉDÉRALE DE LAUSANNE

Suisse
2017

In the memory of my beloved mother...

Acknowledgements

I am extremely thankful to the many people who have provided me with support, guidance and assistance and made the completion of this PhD thesis possible:

Prof. Jean-Louis Scartezzini for his scientific rigor, constant support and the independence he allowed me to benefit from, which encouraged me to strengthen my critical thinking ability,

Prof. Jan Van Herle, Prof. Marilyn Andersen, Dr. Rolando Ferrini, Dr. Bruno Bueno for accepting to be members of the jury of my doctoral exam and for their constructive remarks and feedbacks which helped to improve the quality of my work,

Laurent Deschamps, IT administrator of the LESO solar experimental building, and the whole IT team, for their tremendous continuous supervision, improvements and maintenance of my experiment testbeds, and Paul Becquelin for preparing the online subjective questionnaires,

Commission for Innovation and Technology (CTI) of the Swiss Confederation through the Swiss Competence Center for Energy Research on Future Energy Efficient Buildings and Districts (SCCER FEEB&D), who funded this work and provided information exchange events to foster collaborations and innovations beyond the scope of my project,

Zeno Karl Schindler (ZKS) Foundation for financing my exchange programs in Singapore and Germany through their doctoral grant,

Yujie Wu and Marta Benedetti, for their enjoyable friendship during these years of sharing the same office room, for their patience during the implementation and debugging of my shading control system,

Dr. Apiparn Borisuit, my predecessor at LESO-PB whose excellent work and assistance from abroad paved my way to building on her work seamlessly,

Pierre Loesch for his assistance in the modification of the testbed and the design of new fixtures for the most recent version of the High Dynamic Range vision sensor, for his conscientiousness and efficiency,

Our industrial partners Regent Lighting and Griesser SA for their in-kind contribution to the upgrade of my testbed in the LESO experimental building on the first and third floor and their technical support,

Edo Franzi, Pascal Nussbaum, Sigolène Bechetoille, who helped us in utilizing the previous version of the HDR vision sensor (IcyCAM) as well as in acquiring and developing its new generation, Vision-In-Package (VIP),

Dr. Andreas Schueler, for his great professionalism in scientific collaboration as well as hands-on support in arranging the monochromator and vignetting effect evaluation testbed,

Dr. Adam Rysanek and Prof. Arno Schlueter, at Singapore ETH center, for hosting me at their institute during an exchange program and for the friendly environment they provided,

Dr. Tilmann Kuhn, Dr. Bruno Bueno, Angelina Katsifaraki and Marouane Boudhaim who hosted me at Fraunhofer Institute for Solar Energy (ISE) for 9 months of fruitful collaboration and scientific guidance and for granting me facilitating means to smoothly manage my experiments from Lausanne,

Dr. Jan Wienold, for his scientific support, which helped me to better apprehend the concept of discomfort glare sensation and for the welcoming atmosphere during our calibration and validation project,

Peter Hansen, for joyful teamwork on the validation process of VIP and for kindly letting me use shading laboratory equipment,

Maíra Dias, visiting scholar from University of Campinas, Brazil, whose sensing device Oculux enabled me to deepen my understanding of the issues of positioning the vision sensor in an indoor environment,

Thanks to Suzanne L'Eplattenier and Marlène Muff, each of whom I have at some point or another pestered with completely unreasonable requests,

Special thanks to Barbara Smith, with whom I had interesting discussions about variety of subjects. Her meticulous and attentive revision of the drafts of this thesis manuscript made it more eloquent and free of mistakes,

All the good people at LESO-PB, my fellow PhD candidates and post-doc colleagues, Pietro Florio, Olivia Bouvard, Dan Assouline, Nahid Mohajeri, Dasun Perera, Dasaraden Mauree, Silvia Coccolo, Anna Krammer and Jing Gong, who all contributed to a warm and friendly atmosphere,

My greatest appreciation to all my amazing Persian friends inside and outside of EPFL for the memories that we share and the joyful time that we spent together, Hanif, Payam, Hossein, Mahmoud, Sina, Sohrab, Zohreh, Babak, Ramin, Sareh, Bahareh, Maryam, Elmira, Baharak, Mohammad and Amir,

The family of Amini (Nasrin, Khosro, Pouria, Parisa, Amin, Lara, Mansour, Mohsen and Reza) with whom I experienced amazing unforgettable moments and have enjoyed discovering Switzerland and Europe,

Finally, I would like to thank my beloved wife, Parya, who has accompanied me with patience throughout this research with invaluable attention and encouragement. Parya, I apologize for all the evenings you had to spend alone. And of course thanks to my family, my mother, M.D. Afsaneh Motamedi, who unfortunately did not have the chance to be present at this day, my father, Ali Asghar and my lovely sister Niloufar, for encouragement to embark on this journey and for their unwavering support.

Lausanne, 4th December 2017

Abstract

One fifth of the electricity consumption of Swiss buildings is due to electric lighting. Integrated control of sun shading and artificial lighting can mitigate this demand while maintaining user comfort. However, the drawback of existing building control approaches is that they do not consider one of the main aspects of human-centric lighting: visual comfort.

The goal of this doctoral thesis is to develop an integrated energy efficient sun shading and electric lighting control system that incorporates widely accepted visual comfort criteria and privileges daylighting over electric lighting.

The first part is dedicated to High Dynamic Range (HDR) vision sensor calibration, programming, validation and preliminary testing. A sensor originally developed by the Centre Suisse d'Electronique et de Microtechnique (CSEM) was photometrically, spectrally and geometrically calibrated and validated with respect to reliable illuminance and multi-point luminance meters. This HDR vision sensor was then equipped with an embedded image processing routine in order to assess 'on the fly' discomfort glare indices. It has been demonstrated that the developed device, is able to serve as an enhanced visual comfort feedback sensor in building automation systems. On the other hand, it can be employed to characterize highly glazed facades and workspaces regarding visual comfort and glare risks, as demonstrated in a project in Singapore.

Three monitoring campaigns are reported in the second part of this thesis.

Firstly, 30 human subjects occupied two identical office rooms of the LESO solar experimental building for 15 afternoons to compare the performance of a fuzzy logic control system incorporating two HDR vision sensors with respect to a 'best-practice' controller. Subjective self-reported visual comfort surveys, paper- and computer-based visual tests and monitoring of the electric lighting consumption were carried out simultaneously in both offices. It was shown that the electricity demand of the office with the advanced controller is 32% lower than that of the reference room, while the subjects' visual performance remained comparable.

Secondly, an eight-month data monitoring campaign was carried out in the same building in order to study the ability of a novel control approach to maintain optimal visual and thermal comfort conditions while reducing the energy performance gap of a room as well as its electric lighting demand. The experimental results showed that the advanced controller mitigated the performance gap during the heating season by 72% with regard to standard occupant behavior and by 19% with respect to a best-practice automated system. This system reduced backup heating demand leading to lower CO₂ gas emissions. At the same time, visual comfort constraints regarding Daylight Glare Probability (DGP) and workplane horizontal illuminance were respected during work hours.

Finally, a self-commissioning integrated controller for Venetian blinds enhanced with a learning module was developed and validated for 22 days in a daylighting testbed at the Fraunhofer Institute for Solar Energy (ISE) in Freiburg, Germany. It has been shown that the visual comfort constraints are respected for 96% of the work hours and that the controller can successfully limit the number of shading movements.

The market potential for HDR vision sensors and integrated control platforms has been studied and possible commercialization tracks have been identified.

Keywords: building automation, fuzzy logic based controller, HDR vision sensor, human-centric approach, self-commissioning smart buildings, visual comfort, performance gap, photometric calibration, solar energy.

Resumé

Un cinquième de la consommation électrique des bâtiments Suisses est due à l'éclairage artificiel. Ainsi, le contrôle intégré des protections solaires et de l'éclairage artificiel peut atténuer cette demande tout en préservant le confort de l'utilisateur. Cependant, l'inconvénient des approches actuelles de contrôle des bâtiments réside dans l'absence d'un aspect essentiel de l'éclairage centré sur l'humain : le confort visuel.

L'objectif de cette thèse de doctorat est de développer un système de contrôle de stores et d'éclairage, intégré et à faible consommation, qui utilise des critères de confort visuel reconnus, et privilégie la lumière naturelle à l'éclairage artificiel.

La première partie de la thèse est consacrée à la calibration, programmation, validation et test préliminaire d'un capteur visuel High Dynamic Range (HDR). Un capteur, développé par le Centre Suisse D'Electronique et de Microtechnique (CSEM), a été utilisé, calibré d'un point de vue photométrique, spectral et géométrique, et validé sur la base de mesures d'éclairement et de luminance multipoint. Ce capteur HDR a été équipé d'un microprocesseur permettant un traitement de l'image, afin d'obtenir des indices d'éblouissement d'inconfort à la volée. Il a été démontré que cet appareil peut offrir un retour d'information au sein d'un système de contrôle, mais aussi fournir des indications quant au confort visuel et risque d'éblouissement dans le cas de facades et d'espaces de travail vitrés.

Dans la deuxième partie, une première expérience rassemblant 30 sujets dans deux bureaux identiques (de référence et avancé) prit place au sein du bâtiment expérimental du LESO durant 15 après-midis, afin de tester un système de contrôle à logique floue utilisant deux capteurs visuel HDR par rapport à un contrôleur référence dans l'état de l'art. Les sujets ont été soumis à des questionnaires et à des tests visuels, à la fois papier et assistés par ordinateur. La consommation liée à l'éclairage a été par ailleurs mesurée pendant ces tests. Les résultats démontrèrent que le contrôleur avancé diminue la consommation, en préservant un confort visuel comparable à celui offert par le contrôleur de référence.

Une deuxième expérience de huit mois a été conduite dans le même bâtiment afin de tester une nouvelle approche de contrôle visant à conserver des confort visuel et thermiques optimaux tout en réduisant l'écart de performance énergétique et la consommation liée à l'éclairage au sein d'un bureau. Les résultats ont montré que le contrôleur avancé a, pendant la saison de chauffage, atténué l'écart de performance par rapport un utilisateur standard de 72% et un contrôleur de référence de 19%. De plus, les contraintes visuelles relatives au Daylight Glare Probability (DGP) et à l'éclairement sur le plan de travail horizontal furent respectées pendant la présence de l'occupant.

Enfin, un régulateur de stores vénitiens adapté aux caractéristiques du bureau et doté d'un module d'apprentissage a été développé et validé pour 22 jours au sein d'un banc d'essai de lumière naturelle de l'Institut pour L'Energie Solaire de Fraunhofer (ISE), à Fribourg, en Allemagne. Il a été démontré que les contraintes de confort visuel sont respectées pendant les heures de travail et que le contrôleur parvient à limiter les mouvements des stores.

Le potentiel commercial des capteurs de vision HDR et des plates-formes de contrôle intégrées a été étudié et des voies de commercialisation possibles ont été identifiées.

Mots-clés : approche centrée sur l'humain, automatisation du bâtiment, capteur de vision HDR, contrôleur à la base de logique floue, bâtiment intelligents, confort visuel, l'écart de performance, calibrage photométrique, énergie solaire.

چکیده

یک پنجم از انرژی مصرفی در ساختمان‌های سوئیس مربوط به روشنایی می‌باشد. کنترل یکپارچه سامانه آفتابگیر و روشنایی الکتریکی میتواند در کاهش مصرف انرژی و حفظ راحتی ساکنین موثر باشد. اما در حال حاضر، در سامانه خودکار موجود، یکی از جنبه‌های اصلی راحتی ساکنین در نظر گرفته نشده است: راحتی بصری.

هدف این رساله دکترا، طراحی و ساخت سامانه خودکار یکپارچه برای کنترل سامانه آفتابگیر و روشنایی در جهت کاهش مصرف انرژی است، ضمن اینکه راحتی بصری حفظ شود. این کار از طریق مزیت بخشی بر نور خورشید به نور الکتریکی محقق میشود.

قسمت اول این رساله به کالیبره کردن، برنامه نویسی، ارزیابی و تست‌های اولیه مربوط به حسگر بصری با دامنه دینامیک بالا تخصیص داده شده است. این حسگر توسط مرکز میکروتکنیک و الکترونیک سوئیس (CSEM) تولید شده و در آزمایشگاه دانشگاه از لحاظ فوتومتریک، طیفی، هندسی کالیبره شده است و نسبت به لوکسمتر و لومینانس متر مرجع ارزیابی گردیده است. این حسگر در مرحله بعد مجهز به سامانه پردازش تصویر شده است که میتواند به صورت لحظه‌ای راحتی بصری را ارزیابی و ارسال نماید. همگونه که در پروژه سنگاپور نشان داده شده است، این دستگاه نوین مخصوصاً برای ارزیابی راحتی بصری در ساختمان‌های هوشمند با پنجره‌های بزرگ کاربرد دارد.

در قسمت دوم این رساله، سه آزمایش مجزا انجام شده است:

در آزمایش اول، از ۳۰ نفر در طول ۱۵ بعد از ظهر در دو دفتر یکسان، در ساختمان آزمایشگاه LESO، استفاده کردیم. این افراد دو سامانه خودکار را مورد ارزیابی قرار دادند: (۱) بهترین سامانه کنترل موجود در بازار، (۲) سامانه کنترلی پیشرفته مبتنی بر منطق فازی که دو حسگر با دامنه دینامیک بالا را در خود جا داده است (موضوع رساله). آنها از طریق ثبت در فرم‌های مخصوص نظرات خود را اعلام میکردند. ضمن اینکه همزمان، میزان انرژی مصرف شده در دو دفتر اندازه گیری شده است. این آزمایش نشان داد که مصرف انرژی در دفتر پیشرفته نسبت به دفتر دوم ۳۲٪ کاهش داشته است و اینکه دو دفتر از لحاظ راحتی بصری یکسان ارزیابی شده اند.

در قسمت دوم آزمایش، طی ۸ ماه یک سامانه کنترلی جدیدی را آزمایش کردیم که شرایط بهینه برای راحتی گرمایی و بصری را فراهم میکرد و مصرف انرژی گرمایشی را کاهش میداد. نتایج آزمایش نشان داد که سامانه پیشرفته قادر به کاهش شکاف عملکرد انرجتیکی ساختمان به اندازه ۷۲٪ نسبت به یک فرد معمولی ساکن در ساختمان، و به اندازه ۱۹٪ نسبت به سامانه بروز موجود در بازار بوده است.

در قسمت نهایی، با استفاده از سامانه هوشمند (هوش مصنوعی) ضمن حفظ قابلیت‌های ذکر شده، روند نصب و راه اندازی سامانه اتوماسیون به صورت خودکار در آمد. این سامانه برای ۲۲ روز در موسسه انرژی خورشیدی Fraunhofer در آلمان مورد آزمایش قرار گرفت و نشان داد که در ۹۶٪ طول آزمایش، الزامات راحتی بصری برآورد شده است. این قابلیت هوشمند، روند نصب و راه اندازی را برای مصرف کننده اقتصادی خواهد کرد.

مطالعات اولیه بازار برای صنعتی کردن این سامانه اتوماسیون از طریق شرکای صنعتی پروژه انجام شده است و نقشه راه برای مراحل آینده ترسیم گردیده است.

کلید واژگان: اتوماسیون ساختمان، سامانه خودکار مبتنی بر منطق فازی، حسگر بصری با دامنه دینامیک بالا، رویکرد انسان محور، ساختمان هوشمند، راحتی بصری، شکاف عملکرد انرجتیکی ساختمان، کالیبراسیون فوتومتریک، انرژی خورشیدی.

Nomenclature

Photometric/radiometric quantities

E_d	[lx]	direct vertical illuminance at the eye as a result of all glare sources
E_{desk}	[lx]	horizontal illuminance at the work plane
E_i	[lx]	indirect illuminance at the eye level
E_V	[lx]	vertical illuminance captured by HDR vision sensor (VIP)
$GS_{normalized}(\theta)$	[-]	normalized grayscale value of a pixel w. r. t. the grayscale value of the pixel at image center
M_{lum}	[cd. m ⁻²]	luminance map
$m_{lum}(x, y)$	[cd. m ⁻²]	luminance of the pixel located at the coordinates (x, y) on the luminance map
$M_{greyscale}$	[-]	grayscale map, raw output from HDR vision sensor (VIP or IcyCAM)
$m_{greyscale}(x, y)$	[-]	grayscale value of the pixel located at the coordinates (x, y)
M_{glare_pixel}	[-]	glaring pixel map: categorizing pixels in glare source and background images
$m_{glare_pixel}(x, y)$	[binary]	value of glaring pixel map at coordinates (x, y)
M_{glare_pixel}	[-]	glare source map, designating glare source index to each pixel of an image
$\sum L_s$	[cd. m ⁻²]	sum of the luminance of all glare sources
$\sum \omega_s$	[sr]	solid angle subtended by all the glare sources
$\sum (L \cdot \omega)_s$	[cd. m ⁻² . sr ⁻¹]	luminance of all the glare sources, pixel-wise weighted by solid angle
$\Psi_{lum}(GS)$	[cd. m ⁻²]	conversion function derived by photometric calibration
L_{VIP}	[cd. m ⁻²]	luminance measured by a reference sensor corresponding to a pixel of image captured by VIP
$L_{average}$	[cd. m ⁻²]	average luminance of a luminance map
R_{VIP}	[W. m ⁻² . sr ⁻¹]	radiance measured by a reference sensor corresponding to a pixel of image captured by VIP
$S_{raw}(\lambda)$	[-]	uncorrected spectral sensitivity of VIP
$S(\lambda)$	[-]	corrected spectral sensitivity of VIP
T_{glare}	[cd. m ⁻²]	threshold for glare pixel identification
$V_{VIP}(d_p)$		vignetting correction factor as a function of distance [pixel] from image center

Discomfort glare quantities

DGI	[-]	Daylight Glare Index
DGP	[-]	Daylight Glare Probability
DGP_{ref}	[%]	threshold value between visual comfort and discomfort zone based on DGP
CGI	[-]	CIE Glare Index
UGR	[-]	CIE's Unified Glare Rating System

Polar and solid angles and pixel coordinates

α_h	[°]	horizontal angle of light connecting observer's view point to an object, measured with respect to the line of sight
α_v	[°]	vertical angle of light connecting observer's view point to an object measured with respect to the line of sight
α_{VIP}	[°]	angular distance from the optical center of the image captured by VIP
σ	[°]	angle between line of sight and line from observer's point of view to an object
d_p	[pixel]	distances from center of an image captured by VIP
H_{image}	[pixel]	height of an image captured by an HDR vision sensor

H	[<i>pixel</i>]	vertical distance between glare source and view direction
D	[<i>m</i>]	distance of the observer's point of view to plane of source in view direction
$\omega(x, y)$	[<i>sr</i>]	solid angle of pixel at coordinates (x, y)
ω_s	[<i>sr</i>]	solid angle subtended by the source <i>s</i>
Ω_s	[<i>sr</i>]	solid angle subtended by the source, modified by the position of the source
τ	[$^\circ$]	angle from vertical of plane containing source and line of sight
W_{image}	[<i>pixel</i>]	width of an image captured by an HDR vision sensor
X_L, X_r, Y_t, Y_b	[<i>pixel</i>]	distances from center of the image captured by an HDR vision sensor
Y		horizontal distance between glare source and the view direction

Energy Quantities

$\overline{FU}(i)$	[%]	monthly averaged solar gain utilization factor for scenario <i>i</i>
FU_i	[%]	solar heat gain utilization factor for scenario <i>i</i>
g	[–]	solar energy transmittance of a double glazing
GVS	[$W \cdot m^{-2}$]	global vertical irradiance on the facade of a building
$P_{el,norm}$	[<i>kWh</i>]	electric lighting energy consumption, normalized to the occupancy rate
Q_N	[<i>kWh</i>]	net heat demand of a building to compensate for thermal losses
Q_F	[<i>kWh</i>]	thermal losses through the facade of a building
Q_c	[<i>kWh</i>]	backup heating needs
Q_{SU}	[<i>kWh</i>]	useful solar gain through the facade of a building
Q_o	[<i>kWh</i>]	metabolic heat gain from the occupant(s) of a building
Q_v	[<i>kWh</i>]	heat exchange of an office room with its neighboring offices
Q_e	[<i>kWh</i>]	heat exchange with the outdoor through the air change
Q_L	[<i>kWh</i>]	heat gain from the lighting system and other electric appliances (i.e. computers)
Q_p	[<i>kWh</i>]	potential solar gain through the windows of a building
S_t	[m^2]	maximum equivalent capture surface of window for solar gain

Automation symbols

A	[m^2]	surface area of the window pane of one office room
$Act_{v,t}$	[–]	the decision regarding the relative priority of visual and thermal comfort
α_c	[–]	electric lighting dimming level ratio between after and after applying dimming command <i>c</i>
α_{ref}	[$^\circ$]	reference sun azimuth, used for determining the time of experiments
α_{req}	[–]	required combination of dimming ratios α_c to change the lighting level from $\gamma_{current}$ to $\gamma_{required}$
$\hat{\alpha}_{sw}$	[$^\circ$]	relative sun azimuth with respect to the workstation orientation
$\hat{\alpha}_f$	[$^\circ$]	relative sun azimuth of the sun with respect to the facade orientation
act_f	[–]	final decision of the command filtering system
b	[–]	relative electric lighting power consumption while the lighting is in the minimum dimming level status
β_{cut}	[$^\circ$]	critical slat angle of the venetian blinds obtained by “cut-off” method
β_{cARSA}	[$^\circ$]	critical slat angle of the venetian blind obtained by “anti-reflection slat angle” method
B_t	[<i>greyscale</i>]	background map in presence detection algorithm at current time step <i>t</i>
C_p	[$KJ \cdot K^{-1} \cdot Kg^{-1}$]	Specific thermal capacity of the indoor air at 25° and 1atm for constant pressure
DQ	[–]	geometry-based controller's decision quality (overaction, underaction or acceptable)
δ_s	[$^\circ$]	angular deviation of the edge of a slat of a venetian blind w.r.t. to its middle point due to its curvature
$\sigma_{p,t}$	[<i>greyscale</i>]	covariance value of pixel <i>p</i> and time <i>t</i> of background image

$d_{G_{p,t}}$	[greyscale]	distance between the value of pixel p captured at time step t and the same pixel from the background map from previous step (B_{t-1})
$\epsilon_{relative}$	[-]	relative error to quantify the accuracy of VIP luminance and illuminance readings
η	[%]	monthly occupancy rate of an office room
G_{fit}	[%]	indicator of goodness of fit between test and reference data
GS	[-]	gray-scale values for pixels of images captured by an HDR vision sensor
h_{sun}	[°]	sun height measured from the horizontal plane at the observation location
\bar{Y}	[-]	monthly average shading opening fraction
Y_{light}	[-]	status of electric lighting system
Y_{down}	[-]	opening fraction of the roller shading of normal window
Y_{top}	[-]	opening fraction of the roller shading of anidolic window
$Y_{down_{current}}$	[-]	current opening fraction of the roller shading of normal window
$Y_{top_{current}}$	[-]	current opening fraction of the roller shading of anidolic window
$Y_{resired}$	[-]	desired electric lighting dimming level
$Y_t(obj)$	[-]	status (presence, absence) of the object obj at current time step t
$Y_{presence}$	[binary]	occupancy status in an office room
I_t	[greyscale]	raw image, grayscale map captured by vision sensor at time step t
$\mu_{p,t}$	[greyscale]	average value of pixel p and time step t of background image
ME_t	[binary]	moving edge matrix in presence detection algorithm
MM_t	[-]	moving mask matrix at time step t in presence detection algorithm
μ_β	[-]	memory parameter of the learning module for the venetian blind's slat angle
μ_p	[-]	memory parameter of the learning module for the venetian blind's position
O_{sh}	[cm]	height of the lowest slat of the venetian blind measured from the floor of the office
$Y_{shading}$	[-]	roller shading opening fraction
P_s	[-]	Guth's position index for source s
$P_{Guth}(\tau, \sigma)$	[-]	Guth's position index for a pixel located at coordinate (τ, σ)
$P(Y_{presence})$	[-]	probability of the office occupancy
$PMM_{p,t}$	[binary]	primary motion mask for pixel p at time step t
$\pi_t(obj)$	[%]	presence probability of object obj at time step t
r_{blob}	[pixel]	searching radius for forming blobs from the moving edges
ρ	[Kg.m ⁻³]	density of the air
$\rho_{respect}$	[-]	Visual comfort constraints respect ratio
$\rho_{increase}$	[-]	multiplier to increase the probability upon confirming the presence of a tracked object in presence detection algorithm
$\rho_{decrease}$	[-]	multiplier to decrease the probability upon confirming the presence of a tracked object in presence detection algorithm
\mathcal{R}	[-]	reliability of the outcome of the Fuzzy Inference System (FIS)
RGBE	[-]	image format by Gregory Ward, 4 values: red, green blue and exponential
RMSE	[%]	Root Mean Square Error between predicted/modeled and measured data
SEM	[-]	Standard Error of Mean for 95% confidence interval
S_x	[-]	Geometry-based control action x
T	[h]	total duration of the measurement campaign
T_\perp	[-]	light transmittance of window glazing
T_{in}, T_{out}	[°]	indoor and outdoor air temperature
$T_{arrival}$	[s]	time interval between the time of arrival of an office occupant and the time of being detected as a presence object
$T_{remember}$	[s]	time interval between the time of departure of an office occupant and the time of being classified as an absent object
τ_{hot}	[°C]	upper threshold for prioritizing thermal comfort controller
τ_{cold}	[°C]	lower threshold for prioritizing thermal comfort controller
$\tau_{distance}$	[pixel]	threshold for detecting the edges based on the distance between the new readings and the background image

τ_{edge}	[<i>pixel</i>]	threshold for detecting moving edges based on consecutive image subtraction
$\tau_{presence}$	[–]	threshold above which an object is labeled as <i>present</i> in presence detection algorithm
$\tau_{absence}$	[–]	threshold below which an object is labeled as <i>absent</i> in presence detection algorithm
U	[$W.m^{-2}.k^{-1}$]	thermal transmittance of the entire window (glazing and frame)
V	[m^3]	volume of the air in an office room
y_0	[–]	value of fuzzy inference output

Contents

Acknowledgements.....	iii
Abstract.....	v
Resumé.....	vii
Nomenclature	xi
1. Introduction.....	1
1.1. Buildings	1
1.2. Building Stakeholders	1
1.3. Problem Statement	5
1.4. Structure of Thesis.....	6
2. Literature Review	9
2.1. Visual Comfort	9
2.1.1. Daylight Glare Index (DGI)	9
2.1.2. CIE Glare Index (CGI)	10
2.1.3. Unified Glare Rating (UGR)	10
2.1.4. Daylight Glare Probability (DGP).....	10
2.1.5. Unified Glare Probability (UGP)	11
2.1.6. Critical Analysis	11
2.2. Indoor Lighting Sensing Technologies	12
2.2.1. Predecessors of HDR Vision Sensor	12
2.2.2. HDR Imaging Techniques	13
2.2.3. HDR Vision Sensor for Monitoring Purposes	13
2.2.4. HDR Vision Sensor for Control Purposes.....	14
2.3. Building Management Systems	15
2.3.1. Statement of Control Issue	15
2.3.2. Conventional Controllers	17
2.3.3. Agent-based Smart Control Systems	17
2.3.4. Model Predictive Control (MPC)	18
2.3.5. Fuzzy Logic Controllers.....	18
2.3.6. Critical Analysis	19
2.4. Normative Efforts	19
2.4.1. Indoor Lighting	19

2.4.2.	Energy in Buildings.....	20
2.5.	Anteriority Search.....	20
3.	Cyber-Physical Testbeds.....	25
3.1.	LESO Solar Experimental Building.....	25
3.1.1.	Presence Detection Algorithm.....	27
3.1.2.	Electric Lighting.....	39
3.1.3.	Control Platform.....	39
3.1.4.	HDR Vision Sensor Calibration Test Room.....	42
3.2.	Daylighting Test Environment in Singapore.....	42
3.2.1.	Singapore-Berkeley Daylight Testbed.....	42
3.2.2.	3for2 Building.....	44
3.3.	Daylight Testbed in Fraunhofer ISE.....	46
3.3.1.	Rotating Testbed.....	46
3.3.2.	Sensors of Daylight Testbed.....	48
3.3.3.	Actuators of Daylight Testbed.....	48
4.	HDR Vision Sensor.....	51
4.1.	Introduction.....	51
4.2.	Sensor Calibration.....	52
4.2.1.	Purpose of the Calibration.....	53
4.2.2.	Preliminary Testing.....	54
4.2.3.	Spectral Calibration.....	57
4.2.4.	Photometric Calibration.....	63
4.2.5.	Geometrical Calibration.....	65
4.3.	Calibration Checking.....	69
4.3.1.	Photometric Sensors.....	69
4.3.2.	Illumination Conditions.....	70
4.3.3.	Experimental Results.....	71
4.4.	Implementation of DGP Rating in the Embedded System.....	74
4.4.1.	Illuminance and Average Luminance.....	75
4.4.2.	Glare Pixel Map.....	78
4.4.3.	Glare Source Map.....	79
4.4.4.	Analyzing the Glare Sources for Features Extraction.....	80
4.4.5.	Evaluating the Glare Source Indices.....	81
4.5.	Robustness and Accuracy Tests.....	82
4.6.	Uniformity and Accuracy Verification.....	83
4.6.1.	Introduction and Goal.....	83
4.6.2.	Experimental Setup.....	84
4.6.3.	Experiment Procedure.....	84

4.6.4.	Experimental Results	86
4.7.	HDR Vision Sensor as Characterization Device	88
4.7.1.	Introduction	88
4.7.2.	Experimental Results	89
4.7.3.	Discussion and Conclusion	92
4.8.	Optimal Location for HDR Vision Sensor	93
4.8.1.	Foreword.....	93
4.8.2.	Methodology.....	94
4.8.3.	Experimental Results	96
4.8.4.	Discussion and Conclusion	100
5.	In-situ Monitoring in LESO building.....	101
5.1.	Fuzzy Logic	101
5.1.1.	Fuzzy Sets.....	101
5.1.2.	Fuzzy Inference System.....	102
5.1.3.	Fuzzy Logic Control	103
5.2.	Short-term Experimentation	104
5.2.1.	Reference and Advanced Controllers	104
5.2.2.	Design of Experiment.....	106
5.2.3.	Experimental Results	109
5.2.4.	Discussion	112
5.2.5.	Limitations	114
5.2.6.	Conclusion and Outlook.....	114
5.3.	Long-term Experimentation	115
5.3.1.	Objectives of Control Platform	115
5.3.2.	Experiment Protocol	115
5.3.3.	Advanced Controller	115
5.3.4.	‘Best Practice’ Controller	119
5.3.5.	Design of Experiment.....	120
5.3.6.	Experimental Results and Post Occupancy Evaluation	121
5.3.7.	Discussion	137
5.3.8.	Limitations	138
5.3.9.	Conclusion.....	138
6.	Self-Commissioning Venetian Blinds Controller	141
6.1.	Motivation	141
6.2.	Control Approach	142
6.2.1.	Main principles	142
6.2.2.	Geometry-Based Rules.....	145
6.2.3.	Closed-loop Shading Actuation	147

6.2.4.	Learning Process	148
6.3.	Testbed Preparation	150
6.4.	Experimental Results	150
6.4.1.	Underactions during Learning Phase	151
6.4.2.	Example of Overaction	152
6.4.3.	Successful Action during Operation Phase	153
6.4.4.	Overall Analysis of the Experiment	154
6.5.	Discussion	157
6.6.	Conclusion	158
6.7.	Future Outlook	159
7.	Conclusion	161
7.1.	Achievements	161
7.1.1.	HDR Vision Sensor	161
7.1.2.	Advanced Control System	162
7.2.	Solution Limitations	163
7.3.	Technology Transfer	163
7.3.1.	Human Centric Lighting Control System	164
7.3.2.	Enhanced Sensor Commercialization	165
7.4.	Future Outlook	167
	Bibliography	169
A.	Appendix A	181
A.1.	Overview of the FLC	181
A.2.	FLC Membership Functions	181
B.	Appendix B	183
B.1.	The LESO Solar Experimental Building	183
B.1.1.	Shading Position	183
B.1.2.	Data Acquisition Fault Detection	183
B.1.3.	Data Logging File Structure	183
B.1.4.	Location of the sensors	184
B.2.	Daylight Testbed at Fraunhofer Institute for Solar Energy (ISE)	184
B.2.1.	Data Logging File Structure	184
B.2.2.	Controller Implementation	186
C.	Appendix C	187
D.	Appendix D	189
D.1.	Foreword	189
D.2.	Background	189
D.3.	Experiment	189
D.4.	Adaptation to Control Platform	190

E.	Appendix E.....	193
E.1.	Equidistant vs Orthographic Projection.....	193
E.2.	Curve Fitting to Simplify the Solid Angle Calculation Process	194
E.3.	Comparison of the Solid Angle Subtended by Pixel in IcyCAM and VIP	194
E.4.	VIP Saturated as Exposed to Sun at Sun Set.....	194
E.5.	Spectral Composition of the Light Sources Used for Spectral Calibration of VIP	195
E.5.1.	Transferring the Data over Telemetry Channel.....	195
F.	Appendix F.....	197
G.	Appendix G	199

Chapter 1

Introduction

1.1. Buildings

As man became biped, during the Old Stone Age 2.5 million years ago, he started looking for some comfort and protection in caves and began to build crude shelters. A building as a shelter represents a physical division of the human habitat, i.e. a place of comfort and security, at times where the outside may be severe and harmful. Ever since, housing conditions have been one of the main concerns of humans, and who thrived to improve the indoor comfort by discovering new tools.

Buildings, as a principal element of urban ecosystems, engage stakeholders from different sectors of society during their life cycle: policy makers, architects, engineers, building constructors/manager, and of course, building occupants. Each agent influences this cycle for a period of time and advocates its own priorities (Section 1.2), which in most of the cases are in contradiction with the ones of the other agents. The building user, however, is the last to join this cycle. At this time, it is too late to intervene with building settings in a systematic way if the building does not fulfill its main purpose: to provide a comfortable and safe environment to its occupants.

Ergo, it is indispensable to adopt a “human centric” approach from the beginning of a building’s life cycle, i.e. starting with the needs and concerns of people for whom the building is designed for, and ending with novel solutions that suit their needs. Only in this way may we finally reach the optimal solution (e.g. the Pareto front of a multi-objective function), satisfying the occupant and fulfilling the priorities of all stakeholders.

In this doctoral thesis, a human-centric approach is chosen in order to empower the building automation scheme with smart control systems integrating novel visual comfort sensors. This chapter takes the reader step by step through the thought process of the writer in understanding the problem and in grasping the motivation behind this research activity.

1.2. Building Stakeholders

From the policymakers’ point of view, it is important to reduce the carbon footprint of buildings and consequently reduce their energy consumption as well as national dependency on imported energy carriers. The Swiss Federal Council announced in 2011 its decision to withdraw from nuclear energy on a step-by-step basis. Thereafter, the Swiss parliament adopted a resolution to mandate the Swiss Federal Office of Energy (SFOE) to elaborate the new Energy Strategy 2050 for the country. The outlined strategy urges for energy efficiency in different domains of activities, including the building sector. Their decision is partially based on the facts that buildings account for more than one third of the whole primary energy demand in the Western World and are also responsible for more than 30% of CO₂ emissions [1], [2]; more on this topic will be discussed in Section 2.4.2. Electric lighting can represent up to one third of the electricity needs in office buildings [3], [4]. This figure might not be generalizable to the entire building sector.

However, there is a consensus among building energy actors, including scientists, engineers and lighting designers, that developing energy efficient lighting systems is noticeably important [5].

Policymakers incentivize building constructors to design buildings as energy efficient as possible. However, as the occupant enters a building for the sake of maintaining his visual and thermal conditions in a comfort zone, s/he interacts with the Heating, Ventilation and Air Conditioning (HVAC) system, electric lighting and shading systems. Offering a comfortable environment usually lessens the energy performance of the building in comparison with the predictions of designers. This discrepancy between real and predicted energy performance of the building is called the “performance gap”. A recent study on 26 recently retrofitted post-war buildings in Geneva shows that the main causes of the performance gap are related to the quality of execution, operation and user behavior (both occupant and energy operator) [6]. Occupants typically have an even greater impact on passive buildings because of the active role that they may take in optimizing their own comfort [7]. All subjects observed in a study by Reinhart et al. [8] in 10 daylit offices for 10 months used their blinds to avoid direct sunlight being consistently above $50 \text{ W} \cdot \text{m}^{-2}$, and incoming solar gains above $450 \text{ W} \cdot \text{m}^{-2}$. One of the indicators of the performance gap of the building is a factor named Utilization Factor of the solar gain (FU) suggested by Scartezzini et al. [9]. FU indicates the portion of potential solar gain that is effectively collected through the facade and used by the building. The higher this portion is, the more energy efficient the building is. This factor will be detailed in Section 5.3.6.3.

The notion of human comfort varies considerably from person to person. Gender [10], age [11], [12] and ethnic background [13], [14] are among the factors that may influence an occupant’s visual and thermal comfort zone. In other words, in spite of ample literature of recent years on the concept of thermal [15], [16] and visual [17] comfort, there are several evidences of considerable interpersonal differences [18], [19].

The following question may be raised regarding the manual control of shading and electric lighting: if occupants are the best managers of their own lighting and shading systems, then why not let them themselves control these systems in their built environment? Lindelöf once answered this question in an unfavorable way: we humans are hedonistically lazy. In another words, we do not mind small levels of discomfort, in the pursuit of net pleasure (pleasure minus pain), especially if the alternative is to continuously adjust a shading device [20]. O’Brien et al. [21] stated that occupants are not illogical and irrational but rather that they attempt to restore their comfort in the easiest possible way. Several studies have demonstrated, however, that building occupants are usually poor in making appropriate usage of daylight by controlling the blinds at their disposal [22]. Three office rooms monitored in central London were found with occupants leaving on average 40% of the building’s glazed area occluded by their venetian blinds, without any obvious correlation with the available sunlight. Nonetheless, the building users very likely reject automated shading devices and electric lighting, if visual comfort and performance is not maintained in the working space and if amendments of shading positions and/or lighting levels are too numerous.

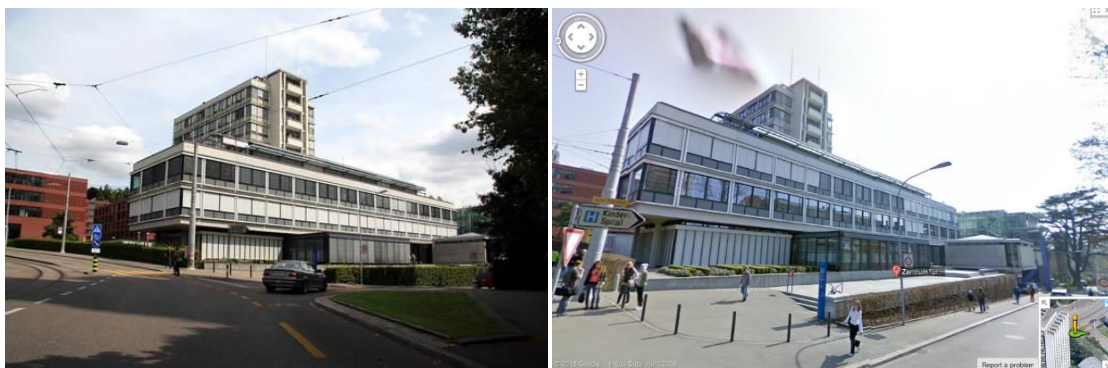


Figure 1.1 — Example of fully deployed roller blinds on the shaded facade, demonstration of deficiency of manual control (adopted from a presentation by Kostro, Dentristry university of Zurich [23]).

Moreover, Paule et al. [24] showed that manual controllers of sun shading systems are very few and poorly used in office rooms: less than 1.7 movement blinds/week regardless of the orientation or season were observed on an administrative building of the EPFL Science park. Another reason to believe that the occupants are basically lazy in using

shading devices is based on a study by Suter et al. [25] that monitored the use of venetian blinds in eight office rooms over 30 weeks, assessing the condition of the blinds every 15 minutes. He found that the use of shading devices depends on how accessible the controls and their actuation system are (manual or motorized). This finding was recently confirmed by Sadeghi et al. [26], who conducted a field study in four south facing offices with 147 office occupants over 40 days with four shading and dimmable lighting control interfaces. The tendency to use daylight in office rooms with easy-to-access control is relatively higher than in offices with low level of accessibility. This fact, accordingly, leads to lower use of electric lighting and potentially electric energy savings. From our own daily experience, we know that only a few people adjust their blinds regularly and that we may often adjust it only when a certain level of discomfort is experienced.

On the other hand, in contemporary architecture, building designers prefer large window to wall ratios. The trend of covering buildings with a large area of glazing, imposes further demands and constraints on the regulation of daylight [27]. The “Gherkin” tower in London is an example of high-tech sustainable architecture with a glazed envelope, that addresses the necessity of measures to guarantee indoor human comfort (Figure 1.2).



Figure 1.2 – The Gherkin (Swiss Re) Tower in 30 St. Mary Axe London designed by Norman Foster [28].

At the first glance, to address occupant needs, one should design passive buildings in a way that they are visually and thermally comfortable and privilege the use of daylight. Researchers are studying this field and several innovative facade designs were proposed and implemented over past years. Anidolic Daylighting Systems (ADS) [29], [30], as shown in Figure 1.3 (b), are an example of successful passive design which collects the daylight from the sky vault and redirects it toward the ceiling and the deeper part of the building. Moreover, a seasonal dependent microstructure [31] installed on the glazing improves the daylight provision during winter and reduces discomfort glare and excessive solar gain during summer. However, the occupant’s global comfort is not guaranteed during all the time: a solar protection is required in any case (Figure 1.3 (a)).

An appropriate Building Management System (BMS) could in principle cope with this issue. Nonetheless, in the current state of practice, BMS do not really consider occupants and their needs at all. In a state-of-practice, an illuminance sensor is installed on the rooftop of a building and as the readings exceed a certain threshold, the blinds are deployed; they are subsequently retracted late in the evening [32]. In a less rudimentary approach, a brightness sensor is installed on the ceiling of an office room to roughly estimate the workspace lighting environment at a not well-chosen location of the room, and based on default control strategies, shading or electric lighting, or both, are commanded. More on this topic is presented in Section 2.3.

Many studies show that taking these physical variables as control inputs is not sufficient. For example, a study by Reinhart [8] showed that using only vertical illuminance as input for automated venetian blind control systems leads to 88% of control actions being overridden by occupants. Similarly, having studied the reaction of occupants of 40 offices

over 5 months, Meerbeek et al. in 2014 [32] found that most of the offices that have an automated control mode of external venetian blinds, were led by an external illuminance sensor that was switched off. In other words, these studies show that the existing BMSs are not acceptable by the building occupants and that they are rejected after their installation. On the other hand, they are not reliable enough from the perspective of the building services engineers as they do not accurately measure the light flux perceived from the occupant's view point, ergo do not make reliable actions.



Figure 1.3 — (a) LESO solar experimental building in Lausanne, Switzerland, on a summer day. Almost all the ADS are covered by external roller blinds to avoid visual and thermal discomfort [33]; (b) Anidolic Daylighting System (ADS) installed on the upper section of a facade [31].

For those occupants who do not have the chance to turn off an automated system, lack of occupant consideration in building control would, in extreme cases, lead to, the appearance of the “Sick Building Syndrome (SBS)” [34]. McIntyre et al. [35] identified six building features significantly related to SBS, two of which directly associated with energy efficient control strategies: (i) application of energy conservation measures and (ii) lack of control opportunity to establish a comfortable environment. In those cases, the occupants report their dissatisfaction to the building manager and often times the automated system is switched off, which leads to missed opportunities in enhancing energy performance as well as in benefiting from positive neurobiological effects of daylight on occupants. The impacts of exposure to light, as the most powerful cue (Zeitgeber) for internal clock entrainment, on human's alertness, sleep quality, mood and performance are called Non-Image Forming (NIF) effects [36]–[39].

To address these issues, numerous research groups study on “human centric” approach in building simulation, design and automation. Among them, one may name Lawrence Berkeley National Laboratory [40]–[45]; Ray Herrick Laboratories at Purdue University [26], [46]–[52]; iHomeLab in Lucerne University of Applied Sciences and Arts [53]; The Human-IST (Human-Centered Interaction Science and Technology) Institute of the University of Fribourg [54], [55]; The Interdisciplinary Laboratory of Performance-Integrated Design (LIPID) at Swiss Federal Institute of Technology in Lausanne (EPFL) [56]–[60]; Singapore Berkeley Alliance for Building Efficiency and Sustainability in the Tropics [61]–[64]; Human Building Interaction Laboratory (HBI) in Carleton University [65], [66]; Innovation in Integrated Informatics (iLa) in University of Southern California [67]–[73]; Fraunhofer Institute for Solar Energy (ISE) [74].

This fact stresses out the necessity of a personalized device for evaluating the visual comfort, i.e. discomfort glare in the indoor environment. Many researchers over the past sixty years have contributed to advancing the theory of visual comfort based on subjective assessments in electric- or daylit environments. Throughout these experiments, scientific-grade calibrated sensors [17] (Figure 1.4 (a)) as well as digital Single Lens Reflex (dSLR) photography, as shown in Figure 1.4 (b) [26] are used to produce calibrated luminance maps, a manual procedure being also used to assess discomfort glare indices. Clearly, these bulky technologies with manual image analysis may not go beyond the laboratory setup.

In order to transform this idea to a marketable form, the proposed solution should be economically viable and easy to commission. Many model-based shading control strategies have been proposed over the past few years [46], [52], [65], [75]. These approaches are quite successful in preparing a comfortable environment (Section 2.3). Nonetheless, since these models are costly to build and complicated to tune and commission, they are not really interesting for industrial implementation. A continuous visual comfort assessment in an operational environment imposes several constraints:

- the sensor should not require too much modification of the environment so as not to impede the occupant from performing their normal tasks.
- It should not be intrusive and endanger the privacy of the occupants.
- It should be self-commissioning and require low maintenance.

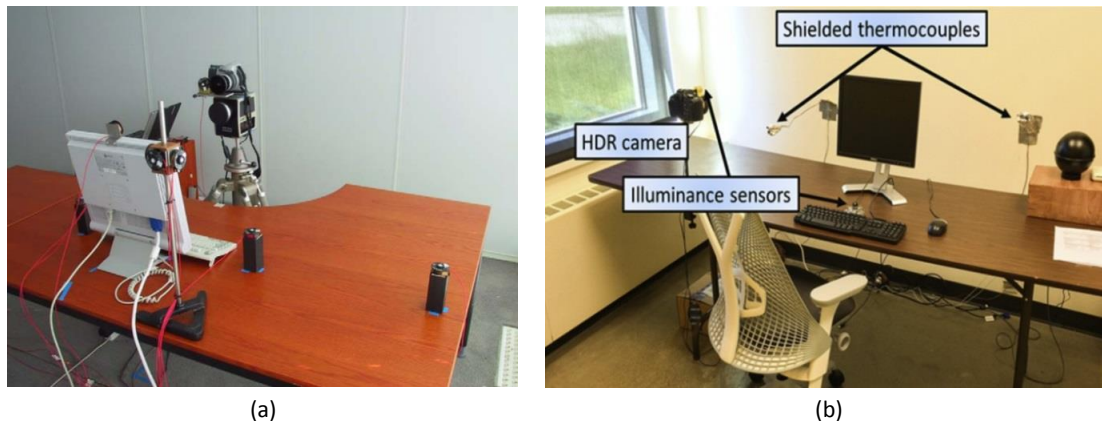


Figure 1.4 – (a) CCD camera at eye position in Danish Building Research Institute, testbed for developing Daylight Glare Probability (DGP) in 2006 [17]; (b) Canon T2i equipped with fisheye lens Sigma 4.5 to capture the luminance distribution in 2016 [26].

1.3. Problem Statement

Bearing these arguments in mind, the research questions the author addresses by this doctoral thesis are as follows:

- How can the notion of visual comfort be introduced into a Building Management System (BMS)?
- What is the impact magnitude of such a novel system on electric lighting demand and user acceptance in a single occupied office room?
- Is it possible to improve the energy performance of a building, to reduce its CO_2 emission and to mitigate a possible performance gap without jeopardizing the occupant's visual and thermal comfort?
- Is it possible to facilitate the commissioning of the enhanced BMS without compromising its performance?

The ultimate goal of this PhD thesis is to develop an integrated energy efficient shading and electric lighting control system that can incorporate visual comfort criteria, that privileges daylight to electric lighting and that is easy to install.

Aiming to this goal throughout this doctorate, the author kept an eye on the practical implementation aspects of this novel technology and chosen solutions that facilitate their transfer in a marketable form, provided that they satisfy the required specifications.

The positive biological impact of light on occupants' mood, health and performance in the shading and electric lighting control strategy were also addressed in this doctoral thesis. For this reason, the author was involved in the supervision of a master student, and later directly collaborated with her during her doctoral research. However, these research activities go beyond the scope of this research work and the reader may refer to [76]–[78] for further details regarding this subject.

1.4. Structure of Thesis

The content of each thesis chapter is summarized as follows:

Chapter 2: Literature review

This chapter consists of 5 sections. In each section, the state-of-the-art of a specific subject of this interdisciplinary thesis is covered. First of all, the theory of visual comfort is elaborated. Numerous discomfort glare indices have been suggested by laboratory and in-situ experiments. The most frequently used ones are presented and after a critical analysis, one of them, the Daylight Glare Probability (DGP), is chosen as a tool for the rest of the thesis. In the next section, the indoor sensing technologies and their properties are studied. One of these technologies is chosen as the reference scenario for this thesis. Similar approaches integrating High Dynamic Range (HDR) vision sensors are critically reviewed. In the next section, the control problem is clearly defined and existing BMS solutions are categorized and described. Following this study, a conclusion is reached that the rule-based control system enhanced with a learning system suits the best the requirements of this thesis. In Section 2.4, the normative efforts in the field of indoor lighting and building energy demand and carbon footprint are studied. This chapter is completed with a critical review on the filled and granted patents in the field of human centric lighting.

Chapter 3: Cyber-physical testbeds

Three cyber-physical testbeds are used in the course of this thesis: i) the LESO solar experimental building on the EPFL campus, Lausanne, Switzerland; ii) SinBerBEST daylighting testbed and 3for2 innovative building in Singapore; and iii) rotating daylight testbed in Fraunhofer Institute for Solar Energy (ISE). This chapter consists of three sections and each section is dedicated to one of the testbeds.

Chapter 4: HDR vision sensor

The focus of this chapter is on the characterization, calibration, programming and validation of the HDR vision sensor. The history of the HDR vision sensor in the course of this project is explained in Section 4.1. In the following section, the latest version of the sensor, named VIP, is characterized and calibrated. The calibration result is validated in a joint project with Laboratory of Integrated Performance in Design (LIPID) and elaborated in Section 4.3. The author implemented the DGP index evaluation on the embedded processor of the two generations of the HDR vision sensor. The detail of this development is presented in Section 4.4. Robustness and accuracy of the embedded software is demonstrated in Sections 4.5 & 4.6. In Section 4.7, the use of an HDR vision sensor as a building facade characterization device is demonstrated. Finally in Section 4.8, the author assesses how realistic it is to consider the readings from a stationary HDR vision sensor, installed in the vicinity of an office occupant, as an indicator of the actual exposure of the occupant to daylight.

Chapter 5 Experiments in the LESO solar experimental building

This chapter is dedicated to the approach, results and discussions of a short-term and a long-term experiment in the LESO solar experimental building. The control platform developed in previous steps (Section 3.1.3) and the HDR vision sensor prepared in Chapter 4 are put into practice and the design of experiments and the results are presented in this chapter. In the first section, a review on the theory of fuzzy logic is presented. The second section, the description of short-term experiments performed during 15 afternoons in October and November 2015 is presented. This section also includes a discussion of indoor lighting conditions in comparison with similar past studies. Section 5.3 details the long-term experiment in the same offices carried out from August 2016 till March 2017. A comprehensive discussion about the influence of the different shading control strategies on the performance gap is also presented in this section.

Chapter 6: Self-commissioning venetian blind control system

Ease of commissioning procedures for a venetian blind control system in a new environment is the subject of a series of experiments presented in this chapter. A rule-based control system enhanced by a learning system is the core idea of this chapter. These experiments are conducted in the daylight testbed at Fraunhofer ISE. The most important

performance criteria, such as learning system convergence rate, visual comfort constraints satisfaction and number of shading movements are evaluated and presented at the end of this chapter.

Chapter 2

Literature Review

This literature review is partially included in two publications by the author and his colleagues [79], [80]. In this chapter, firstly a review on the important visual comfort assessment approaches and theory is presented. Section 2.2 describes the implementation of the stated theory in the laboratory and relevant environment through HDR vision sensors. In the third section, the main scientific publications on lighting and shading control strategies are presented. In the fourth section, the normative efforts for integrating the scientific findings in the building regulation sector are detailed. Finally, this chapter is concluded by a review on the most relevant patents granted on Building Management Systems (BMS).

2.1. Visual Comfort

Almost no area related to human welfare can as of today be called exact science. Medical sciences are very likely the most rational area, which emerged from empirical roots, however, depends profoundly on statistics and probabilities. Understanding the underlying principles of vision, one of the most complicated senses of the human being, is therefore regarded as difficult and heavily interrelated to other non-physical factors. Ergo, they are still far from being completely revealed: accordingly, there is no universally accepted notion of visual comfort.

One of the first easily available studies on visual comfort dates back to 1937 [81]. This book was meant to provide guidelines for maximizing the industrial output from factory workers during post WWI. The effect of light on the workers' productivity was also part of the investigation.

Technology provides a real opportunity to understand the relation between monitored lighting conditions and user response. The most important aspect of this response addressed in the literature is glare, which should be absolutely avoided. Development of several indices offers deeper insight into the impact of luminance distribution in the view field on glare. The most used metrics are detailed and explained in Sections 2.1.1 to 2.1.5. On the other hand, the publications that deal with visual comfort from a general point of view use "Vertical Eye Illuminance" as an approximation of glare indices.

In the following sections, the definitions of five discomfort glare indices are presented and a short history of each index is reviewed. There are several common variables in their definitions: L_{s_i} is the luminance of the i th glare source [$cd \cdot m^{-2}$], ω_{s_i} is the solid angle of the i th glare source [sr], P_i is the Guth position index for i th source based on Figure 10 of Wienold et al. [17], Ω_{s_i} is the solid angle subtended by the i th glare source, modified by its position [sr] and L_b is the background luminance [$cd \cdot m^{-2}$].

2.1.1. Daylight Glare Index (DGI)

This index is the updated version of an index called British Glare Index (*BGI*) which was originally developed in 1950 for small sources with solid angle inferior to $0.027 [sr]$ [82]. In order to have a metric to predict the glare from large sources

such as window, the *BGI* was adapted. The study was conducted at Cornell University (USA) and the Building Research Establishment (BRE). Fluorescent lamps behind an opal-diffusing screen were used to develop this index, expressed by Eq. (2-1) [17]:

$$DGI = 10 \log_{10} \left(0.48 \cdot \sum_{i=1}^n \frac{L_{s_i}^{1.6} \cdot \Omega_{s_i}^{0.8}}{L_b + 0.07 \omega_{s_i}^{0.5} \cdot L_{s_i}} \right) \quad (2-1)$$

The *DGI* generally overestimates discomfort under daylight conditions since there is higher tolerance of mild discomfort glare from daylight than from similar artificial light [83], [84]. Despite its shortcomings in a daylight environment, the index is still widely used in discomfort glare research.

2.1.2. CIE Glare Index (CGI)

In 1979 the international situation of glare assessment theory was unsatisfactory and the methods adopted in different countries gave discrepant predictions [85]. Thus, the International Commission on Illumination (usually abbreviated CIE for its French name, Commission internationale de l'éclairage) adopted the equation (2-2) proposed by Einhorn [86] to bridge differences by a unified glare assessment method.

$$CGI = 8 \cdot \log_{10} \left(2 \cdot \frac{[1 + E_d/500]}{E_d + E_i} \cdot \sum_{i=1}^n \frac{L_{s_i}^2 \cdot \omega_{s_i}}{P_i^2} \right) \quad (2-2)$$

where E_d is the direct vertical illuminance due to all glare sources [lx], E_i is the indirect illuminance ($E_i = \pi L_b$) [lx] both observed from the observer's point of view. The latter parameter is explained in detail in Section 4.4.4.1. There was no subjective assessment carried out for the development of the *CGI*.

2.1.3. Unified Glare Rating (UGR)

In order to combine the advantage of *CGI* to evaluate the glare sensation for electric lighting systems with limited size, to take into account the Guth's position index, and to overcome the difficulties in calculating direct illuminance required under *CGI* metric, the CIE developed the *UGR* index as presented in Eq. (2-3).

$$UGR = 8 \cdot \log_{10} \left(\frac{0.25}{L_b} \cdot \sum_{i=1}^n \frac{L_{s_i}^2 \cdot \omega_{s_i}}{P_i^2} \right) \quad (2-3)$$

The *UGR* index is a simplification of *CGI* for computational ease, while with the existing technologies these approach is no longer necessary. On the other hand, the visual adaptation to direct light is not considered *UGR*.

2.1.4. Daylight Glare Probability (DGP)

In 2006, Wienold et al. [17] benefited from the advantages offered by the development of CCD cameras for creating HDR images of a scene and to improve the understanding of the relation between monitored lighting conditions and the user response. His efforts led to the introduction of a new glare index called Daylight Glare Probability, which is a function of the vertical eye illuminance, as well as of glare source luminance, its solid angles and its position index.

$$DGP = 5.87 \cdot 10^{-5} \cdot E_v + 9.18 \cdot 10^{-2} \log_{10} \left(1 + \sum_{i=1}^n \frac{L_{s_i}^2 \cdot \omega_{s_i}}{E_v^{1.87} \cdot P_i^2} \right) + 0.16 \quad (2-4)$$

where E_v is the vertical eye illuminance [lx]. Jakubiec [87] found that *DGP* most likely perform well in a variety of daylighting conditions and space types. Furthermore, a long-term simulation and survey study has shown that 53.7% to 70.1% of the occupant's visual comfort perception can be resolved by analyzing *DGP*. There are three departures of *DGP* relative to other metrics presented so far:

- i) glare sources are detected by comparing the regions of high luminance with averages luminance of the whole hemisphere in the field of view. This allows for detecting label specular reflections as glare sources.
- ii) Vertical illuminance is introduced as the first half of the index. This means that an excessively bright scene can lead to comfort glare without considerable visual contrast.

iii) The DGP's value scale is more intuitive in comparison to other indices, signifying the percentage of people who would experience discomfort glare in given lighting condition.

However, some publications claim that *DGP* is not effective in predicting contrast-based discomfort glare due to the strong linear dependence on vertical illuminance [88]. Another recent study by Konstantzos [89] has also proposed some corrections to the equation parameters, when the sun is in the view field of the occupant.

Table 2.1 present the threshold for interpreting the values of *DGI*, *UGR* and *DGP*. The glare sensations "imperceptible" & "perceptible" are considered as visual comfort zone. Thus, if the DGP is lower than 0.35, the lighting condition is considered as comfortable.

<i>Glare Sensation</i>	<i>DGI</i>	<i>UGR</i>	<i>DGP</i>
<i>Imperceptible</i>	<18	<13	<0.30
<i>Perceptible</i>	18-24	13-22	0.30-0.35
<i>Disturbing</i>	24-31	22-28	0.35-0.45
<i>Intolerable</i>	>31	>28	>0.45

Table 2.1 –DGI, UGR and DGP and their respective threshold for interpreting their values.

2.1.5. Unified Glare Probability (UGP)

In the most recent and well-known study regarding five green buildings in Australia, Hirning et al. [88], [90], [91], conducted 493 surveys paired with HDR images. The study was carried out in open plan offices, showing that the participants are more sensitive to discomfort glare than existing indices would predict. Thus a new index, Unified Glare Probability (*UGP*), based on a linear transformation of *UGR*, was suggested for Australia and more specifically open plan green buildings:

$$UGP = 0.26 \cdot \log_{10} \left(\frac{0.25}{L_b} \sum_{i=1}^n \frac{L_{s_i}^2 \cdot \omega_{s_i}}{P_i^2} \right) \quad (2-5)$$

The concept of green buildings is explained in Section 2.4.2.

2.1.6. Critical Analysis

Yun et al. [92] in a 2014 study recommended the vertical eye illuminance (E_v) in place of the DGI or DGP due to the difficulty of their calculation in a real scene. This confirms that there is a need in the daylighting research community for affordable reliable easy-to-implement HDR imaging equipment. Konis [93] in the same year performed a two-week study of fourteen participants in the core zone of a side-lit office building in San Francisco. The sky conditions during this experiment were clear: it revealed that the indicators based on luminance contrast and window luminance were more relevant to estimate the subjective evaluations of discomfort glare than vertical or horizontal illuminance. Another study by Reinhart and Voss [8] shows that using only vertical illuminance as a control input for a venetian blind control strategy leads to low user acceptance. For their studies, 88% of the decisions by the automatic system are overridden by the occupants.

The domain of visual comfort assessment is an evolving field and requires very likely more time to reach maturity by characterizing a universally accepted notion. In-situ studies also show that maintaining acceptable visual comfort conditions for the majority of people is challenging, as the perception of glare and sufficient illuminance varies considerably amongst individuals [94]. The author has encountered many other publications that confirm or invalidate the findings of this literature review. They differ greatly in the experiment protocol, the number and ethnic background of the subjects, lighting conditions and subjective/objective assessment methodology. In the course of this thesis, glare indices are regarded merely as tools, rather than a concept that must be validated or improved. Even though these tools might not be accurate for some individuals on some occasions, they are utilized for this thesis for the sake of a proof-of-concept, with the hope that they will be improved in the near future by the research community.

Nevertheless, among the studied metrics, the *DGP* index is the most relevant one to the experiments in this thesis. First of all, all the experiments, except for the one in Singapore (Section 4.7), are carried out in daylit spaces, thus the DGI

and *CGI* may not perform optimally. The same argument is valid for *UGR* since it is the simplified version of the *CGI*. Secondly, the test-beds are single occupied. Thus, the experiment conditions of development of the *UGP* index is not valid.

Bearing the stated limitations in mind, the conclusions drawn by the present experiments can be generalized to other conditions provided that a suitable glare index is chosen. For example, for the open-plan offices, the *UGP* index can be applied and for moments when the sun disk is in the field of view, the suggested modification by Konstantzos [89] to *DGP* coefficients can be taken into account.

2.2. Indoor Lighting Sensing Technologies

2.2.1. Predecessors of HDR Vision Sensor

There are several types of sensors that are used in the BMS. Most devices are used for occupancy sensing such as Passive Infrared Occupancy (PIR) (Figure 2.1 (b)), ultrasonic occupancy, microwave, and passive acoustic sensors: they can only roughly tell if a space is occupied, but cannot provide information about the number and identification of occupants, or their location in a space [95]. In spite of these shortcomings, several authors have tried to explore the potentials of integration of such sensors in energy saving strategies [96]–[100]. As an alternative for these technologies, Wen et al. [101] utilized a MEMS-based ‘Smart Dust motes’, wireless platform which can be placed directly on the workplace to improve the environment sensing (Figure 2.1 (a)). This sensor can be configured with a variety of onboard sensors such as illuminance meters and humidity meters and consist of a wireless communication unit. In other cases, in order to overcome the shortcomings of occupancy detectors, some researchers suggested to use a network of occupancy sensors and carried-out a more extensive analysis of sensor data [100], [102].

These solutions are cost-effective; however, they may not provide the BMS with precise information on the lighting condition perceived from the occupant point of view. In other words, adaption of daylighting systems in building design and control is impeded by the technical difficulties of estimating and maintaining the workplace illuminance in a given range within office buildings. Very similar issues have prevented designers and researchers from long-term cross-examinations of novel luminance-based metrics developed by means of data monitored in field settings in order to verify the generalizability of these metrics. As an alternative they tried to measure alternative photometric quantities (such as vertical irradiance on the external facade [47]) for visual comfort appraisal. It is understood that this type of data provides us only with an approximation of lighting conditions into buildings.

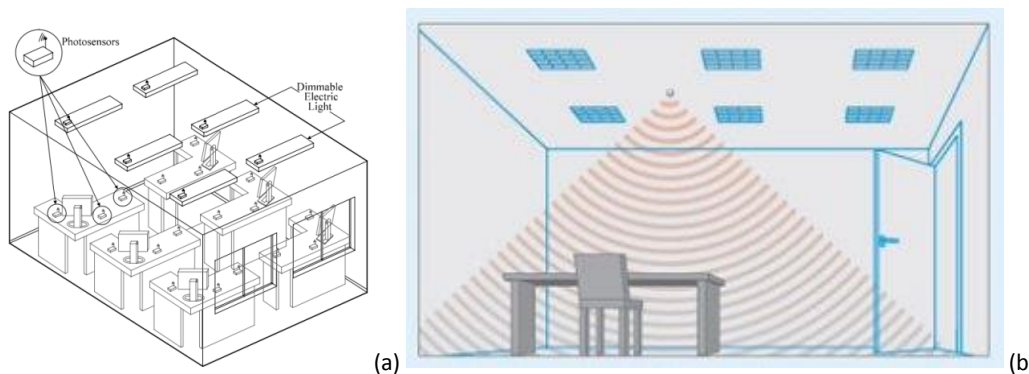


Figure 2.1 – Two examples of sensors used in building control; (a) Smart Dust motes placed on the workplace [101]; (b) Passive Infrared sensor [96].

The best practice for daylight-linked electric lighting and shading control within non-residential buildings, if existing at all, relies on the measurements of ceiling mounted rudimentary luminance meters. This approach guarantees neither achievement of the occupant’s visual comfort and performance nor optimal energy management of electric lighting and shading.

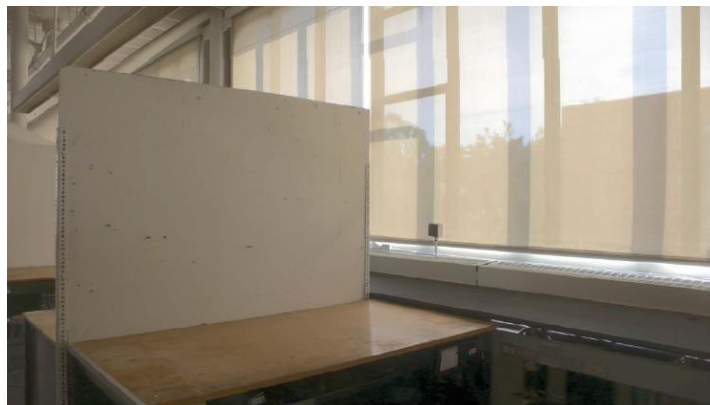
2.2.2. HDR Imaging Techniques

HDR imaging techniques [103], [104] have been used pervasively as a *monitoring tool* for lighting design and engineering (Section 2.2.3), but not as a *sensing technology* for control purposes (Section 2.2.4).

An approximate evaluation of visual comfort can be performed by installing a vision sensor as close as possible to the occupant seated at a workstation: in this case one can capture the task in the view field from the occupant's point of view. The sensor should measure the photometric properties of the incident light flux in a similar way that human eyes perceive it. In other words, this sensor should enable imaging of the view field with an adequately large dynamic range. The dynamic range of the human vision system is about 140 dB, ranging from $10e-6$ to $10e8 \text{ cd.m}^{-2}$ [105]. This requirement gave rise to a technique for capturing High Dynamic Range (HDR) images by merging several Low Dynamic Range (LDR) pictures of a static scene (Figure 2.2 (a)) using Charge Coupled Device (CCD) cameras. Each picture is taken with a certain exposure value (by varying shutter speed for instance), in an attempt to capture the full dynamic range from direct sunlight to deep shadow. The advantage of the HDR imaging technique is to provide a complete record of the size, position and luminance of the glare sources from the viewpoint of the subject. Moreover, the detection of glare sources with considerable difference in average luminance may benefit from a greater accuracy, as shown in Figure 2.2 (b).



(a)



(b)

Figure 2.2 – Classical method for HDR vision systems (a) Low Dynamic Range (LDR) images captured by varying exposure value in order to capture brightest to dimmest lights. (b) High Dynamic Range image generated by the LDR ones merging (e.g. by means of Photosphere software) [106].

Of the available file formats one is of particular interest: the Radiance RGBE (.hdr) codec was created in 1989 as part of the Radiance lighting simulations and rendering software. Since this format is not used as the principal tool in this thesis, the reader is invited to learn more on this topic in [107], [91].

2.2.3. HDR Vision Sensor for Monitoring Purposes

In laboratory conditions, the use of calibrated dSLR charge-coupled device (CCD) cameras together with an HDR image processing software is the predominant experimental method for luminance mapping and glare risk assessment. Some recent examples are as follows: Bellia et al. in 2009 [108] tested a conventional HDR camera (Canon EOS 20D) for

monitoring purposes and rapid evaluation of glare indices (e.g. DGI). Konstantzos et al. [109] utilized more recently a calibrated Canon 550D camera, equipped with a Sigma 4.5mm fisheye lens for luminance mapping in order to validate the use of DGP for glare risks assessment, when the sun is in the field of view of building occupants even through low openness fabric of sun shading system. Xiong et al. in 2016 [50] used the same camera for evaluating the performance of three model predictive control strategies in preventing discomfort glare. Another researcher from the same team, Sadeghi et al. [26] recently used a calibrated dSLR camera (Canon T2i), among several other illuminance meters, in order to obtain the luminance map from the occupant's point of view during a 60-day long monitoring campaign in four identical south-facing offices (Figure 1.4 (b)). Hirning et al. used a Nikon Coolix 8400 for evaluating lighting conditions alongside tailored-made post-occupancy evaluation surveys performed in open plan green buildings (Figure 2.3 (a)) [88], [90]. In another study, Fan et al. [110] installed an HDR camera on several workstations in order to set up a methodology facilitating the long-term monitoring of visual comfort in a contemporary working environment. This method was later applied during a field-based study in an academic building comprising a five-perimeter zone for workstations ([108], [111]). Having collected nearly 4800 subjective glare risk assessments paired with HDR images over a year, the authors observed that several basic variables derived from HDR images, such as the vertical illuminance measured at the eyes level (pupilar illuminance), reveal higher correlation with the subjective responses than the existing glare indices, such as DGI and UGR. For more examples, the reader may refer to [13], [87], [92], [93], [104], [112]–[115].

One notes that all the state-of-the-art image processing protocols are carried out through a tedious manual procedure. This procedure is clearly not suitable for building automation application and is one of the barriers in diffusing the knowledge in the domain of visual comfort to the building automation world.

Moreover, in all of these approaches, the imaging systems are vertically mounted as close as possible to a seated office occupant. In Section 4.8 of this thesis, a series of experiments are carried out to find the location and orientation of the stationary HDR vision sensor. Some of the ideas for the locations, i.e. on a tripod, desk lamp or back wall, are inspired by the reviewed studies.

It can be concluded that an opportunity to automatically assess the glare indices would foster the routine implementation of visual comfort parameters in BMS.

2.2.4. HDR Vision Sensor for Control Purposes

Several pioneer researchers has recently suggested HDR vision sensors for building automation purposes.

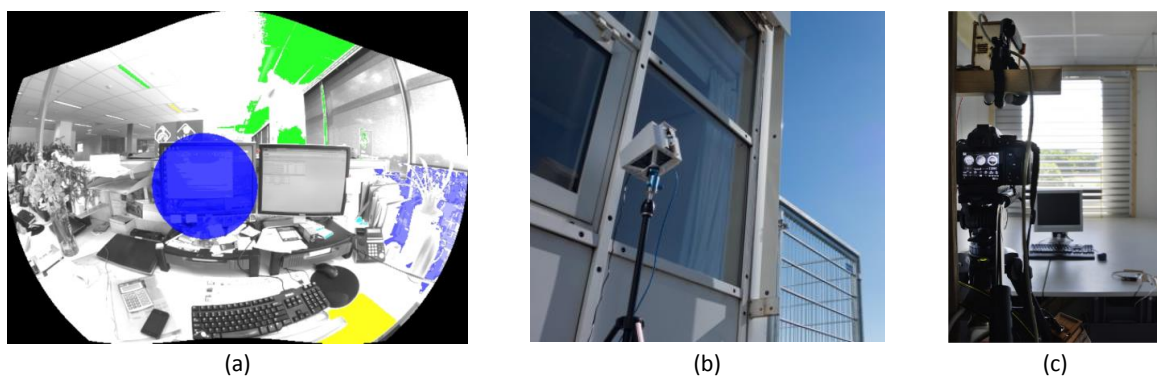


Figure 2.3 – (a) Example of application of digital camera for luminance mapping and glare assessment in open plan offices[91] (b) sensor and its embedded FPGA chip positioned in front of the building facade [27];(c) position of the high-resolution camera, the controller system and the illuminance sensors in the office room [116].

For example, Wu et al. [27] used an HDR vision sensor position on the facade of a testbed on the EPFL campus in order to measure the luminance map of the sky and ground dome. This map is further used as input for an on-board RADIANCE model to evaluate the indoor illumination criteria, such as horizontal illuminance and DGP. The results will be further employed for adjusting the shading position and electric lighting power.

Iwata et al. [117] has used a self-developed glare metric, called Predicted Glare Sensation Vote (PGSV) to control the slat angles and shading positions of venetian blinds. The metric is not measured directly but calculated based on semi-analytical models. Their approach has led to a greater slat angle than that in a cut-off-angle strategy and leads to 30% energy consumption reduction and 46–50% of view satisfaction (percentage of time occupants are satisfied with outside views).

The closest work the author found to the approach suggested in this thesis is a recent study made by Goovaert et al. [116]. This study was published one month before the completion of this doctoral thesis. They have proposed to use a low resolution (5 megapixels) calibrated camera equipped with a fisheye lens as a photometric sensor for luminance mapping: HDR images are formed by merging several LDR images. In the last step, the *evalglare* software is used to calculate the DGP index. Evalglare [118] is a radiance-based tool for HDR images processing and glare indices evaluation. The DGP index is used as a metric for activating the shading system in a single occupied and in an open plan office. Three control scenarios, inspired from the state-of-the-art, are implemented for one of the case studies: a single occupied daylight office room equipped with a venetian blind. The scenarios are vaguely explained in the article and are listed as follows:

Scenario 1: If value of the DGP index exceeds a predefined threshold, the venetian blind is completely closed. Based on the evaluation of the DGP index, the shading slats are tilted by 10° increments until DGP reaches below the threshold.

Scenario 2: This scenario is similar to scenario 1 but updates the threshold for the DGP index by taking into account the occupant's feedback.

Scenario 3: The cut-off angle strategy (explained in details in 6.2.2) is applied as soon as the vertical irradiance on the facade reaches $150 [W \cdot m^{-2}]$. Then, if the DGP index is higher than a predefined threshold, they apply Scenario 1.

Finally, by means of a survey, they evaluated the occupants' feedback regarding the indoor lighting environment.

The following concerns can be raised regarding this study:

- The approach for designing the control system is not reproducible based on the details provided in the article and represent a rudimentary control approach.
- A photometric calibration of a high-resolution dSLR camera in regards to a point luminance meter is elaborated; however there is no evidence in the article or in the catalog of the image sensor (OV5647) proving that the spectral sensitivity of the sensor is close enough to the photopic curve $V(\lambda)$. Moreover, the sensor that they have used features the traditional HDR imaging technique whose shortcomings are addressed in Section 2.2.2.
- All of the three control approaches lead to unnecessary blind movements, since for finding the optimum shading slat angle, numerous consecutive closed-loop actuations need to be made.
- In the second scenario, the method by which the occupant's feedbacks are considered for changing the DGP index comfort threshold is neither justified or clear. Consequently, it prevents the reader from grasping the influence of updating the comfort zone boundaries on the performance of the shading control strategies.
- The subjective assessment is not performed and reported systematically; the acceptability of the control strategy by the users cannot be deduced from the outcome of the subjective survey.

2.3. Building Management Systems

2.3.1. Statement of Control Issue

As stated in Section 1.2, the comfort zone for indoor environment is a multivariable problem that does not have necessarily a unique and identical solution for all occupants. For example, taking a thermal comfort model suggested by Fanger [15], one knows that at best possible conditions, one may still predict that 5% of the target population are dissatisfied (optimal Predicted Percentage of Dissatisfied (PPD)). Thus, any notion of mathematical discomfort model is, at best case, limited to 95% of the population.

Bearing this point in mind, the goal of a smart BMS regarding occupants' comfort and energy performance should be as follows:

- Acceptable comfort level: Maintain the comfort physical variables (temperature, air quality and illuminance) in an acceptable range for optimally 95% of the population and possibly adjust to each individual by learning from their interactions;
- Energy efficiency: Combine the comfort zone management with an energy efficient approach.

Aiming toward the stated requirements, following actuators should be optimally regulated:

- Sun shading; control the incoming solar heat gain and daylight flux, as well as mitigate glare sensation by occupants;
- Artificial electric lighting; offer the minimal required workspace lighting conditions by compensating the lack of daylight for a particular task;
- HVAC systems; provide the required indoor fresh air by regulating air flows as well as backup heating/cooling needs [119].

From the control system point of view, the optimal solution is the one that can successfully minimize a *cost function* that incorporates a limited notion of human discomfort and energy demand as well as other factors such as number of actuations per day.

Since air quality control is not part of this thesis, only two aspects of human comfort, e.g. *visual* comfort and *thermal* comfort, were considered in this review.

One of the earliest Daylight-Linked Control (DLC) systems was proposed by Rubinstein et al. in 1989 [120]. They elaborated three different control algorithms for maintaining constant total light level on a desk surface through photoelectrical lighting system. Ever since, researchers and practitioners have proposed a great amount of control systems. Despite benefits, their use is limited. Bellia et al. [121] recently presented an interesting review underlying the main obstacles to the DLC applications in three categories:

- i) lack of knowledge about specific sensors such as photosensor and their calibration;
- ii) lack of calculation tools to justify the interventions from the economic point of view and finally;
- iii) people's interpretation on *control* systems that might limit their freedom in their environment.

Extensive research was carried out in recent years to address these three issues. Firstly, Doulos et al. [122] suggested a multi-criteria decision making tools to facilitate the commissioning procedure of ceiling-mounted photosensors and to estimate their optimal positioning and view field. The proposed methodology is verified through simulations as well as an experimental setup. Moreover, the same authors targeted a second obstacle, i.e. the lack of calculations tool, in 2008 by quantifying the energy saving potential of DLC systems and consequently estimating the payback period. Eighteen commercial electronic dimming ballasts (EDB) were tested; their transfer functions of emitted light flux versus power input were extracted. These pieces of critical information were applied in a series of simulations for closed-loop and integral reset scenarios. Finally, Sadeghi et al. [26] performed extensive experiments to extend the current knowledge of human-building interactions to advanced shading and lighting systems. They monitored physical variables, actuation and operation states of BMS as well as subjective variables, such as occupant comfort and perception. Xiong et al. [50], through simulated and experimental setup, successfully demonstrated the application of model predictive control (MPC) algorithms. This approach is based on the ability to anticipate the future events, such as human comfort or building energy demand, and take appropriate actions for shading and lighting system in the current time accordingly. Their approach however did not cover thermal comfort aspects. They utilize a fast reliable semi-analytical lighting-glare model to determine the interior lighting conditions, lighting energy demand and the Daylight Glare Probability, for predetermined shading positions based on the sensors readings on each building facade. Their approach aimed at minimizing the lighting energy demand while satisfying glare constraints that resulted in reduced shading operations.

Misjudgment at the design stage of how building occupants should interact with the shading system can lead to operational problems and high rejection rate. Considering human building interaction in the indoor environment control has a considerable impact on the occupant's satisfaction and gives him the feeling that he manages his environment [119]. Several normative documents acknowledge the difficulty of quantifying the visual discomfort for a large population. The IESNA Lighting handbook [123], for instance, reports the correlations between many glare indices and found that all give reasonable predictions of the average discomfort of a group of people, but only poor predictions for an individual's response. The importance of this issue for the research community is clear [1].

Genetic Algorithms (GA) have shown to be very efficient optimization methods for user adaptation tasks with regard to other methods. Taking user wishes into account, as implemented by Guillemin et al. [124] in a three-level architecture, resulted in a system that reduced the users' rejection by 25%. User adaptation was performed in this case by means of GAs that optimize the parameters of a fuzzy logic controller. However, this work did not include recent developments regarding visual comfort theory.

Having analyzed 121 studies, Shaikh et al. [1] categorize the various building control schemes for indoor environment in four sections which are depicted in Figure 2.4.

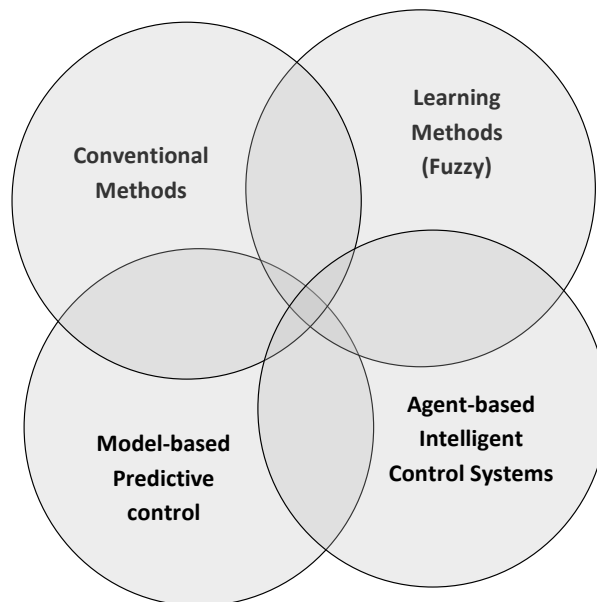


Figure 2.4 – Rough classification of the different approaches to control systems for indoor building environment [119].

Among the suggested controllers, both learning methods and conventional methods were considered in this project.

2.3.2. Conventional Controllers

Many standard control schemes, such as an on/off switching controller, P, PI and PID controllers have been extensively used in building engineering [1]. However due to a lack of any direct a priori knowledge of the system to be controlled and their constant parameters, they usually provide a poor performance for noisy environments; gains selection is another issue. These control strategies do not consider comfort issues but were only designed for energy savings purposes. In spite of these disadvantages, implementing HDR imaging sensors to monitor the lighting conditions of an office from the occupant's point of view, can simplify the whole control issue and make traditional controllers a favorable first approach. This is basically the approach implemented in a recent study by Goovaert et al. [116].

2.3.3. Agent-based Smart Control Systems

In order to develop Human Centric approaches, control engineers have come up with an interesting solution based on the "divide-and-conquer" approach. They break the problem into many simple sub-problems (structuring). The

resolution of sub-problems is integrated to modify the current global system state over agent–agent coordination. The multi-agent controller system (MAST) is designed and then implemented on a more general framework based on controller–agents which are guided by a coordinator–agent [125]. Each MAST control system is composed of two systems: (i) a low-level feedback system responsible for indoor conditions control within specific building zones and (ii) a high-level supervision system responsible for an intelligent coordination and planning.

2.3.4. Model Predictive Control (MPC)

MPC runs at each time step an optimization algorithm over a finite horizon to find the optimum solution to a cost function, provided that the solution respects the constraints. The finite horizon in the future can range from hours to weeks. The cost function can include any type of energy consumption as well as some criteria such as the number of shading and lighting actuation per day. Constraints can be defined based on the visual or thermal comfort zone. Evaluating the cost and constraint functions for future steps requires system models or *predictive* models. The system model can be built either on physical analytical knowledge of the system or on regression models based on collected field data. Disturbances such as solar gains and human presence may be integrated in the predictive models.

This approach is mostly advantageous for building heating systems due to their slow dynamic. Integrating building thermal model leads to efficient disturbance rejection [1]. One of the first successful implementations of MPC in a building was performed by Nygard Ferguson at EPFL in the 90s [126]. She achieved 27% energy savings for a floor heating system during a heating season compared to a conventional control approach and improved thermal comfort conditions. Another study by Lee et al. [127] showed that predictive control algorithms may significantly increase the energy efficiency of systems with non-linear solar-optical properties, such as automated venetian blinds. Moreover, this method is able to take into account the energy price variation and can easily be included in the optimization problem formulation.

Oldewurtel et al. [128], [129] showed through large-scale simulation studies that a Stochastic Model Predictive Control (SMPC) strategy for building climate control and weather prediction outperforms current control practice (e.g. a Rule Based Control (RBC) strategy). This approach has proven to satisfy comfort constraints during a three-month period in fully occupied and instrumented typical Swiss office buildings [130]. Other examples of successful practical implementation of MPC can be found in the literature [131]–[134]. Another advantage of this approach is that it does not require potentially intrusive sensors in the built environment.

2.3.5. Fuzzy Logic Controllers

The ability to act according to a symbolic language as well as fuzzy rules is the basic characteristic of this advanced control strategy. Human beings, on the other hand, perceive it in a better way due to the linguistic and fuzzy approach. Fuzzy controllers have been widely implemented in BMS [119].

In principle fuzzy control is conceptually simple and designed to be intuitive to a human [135]. It is a process of mapping from a given set of inputs to a set of outputs. In the first step, the inputs are fuzzified: they are taken to determine the *magnitude* to which they belong to each appropriate “linguistic variable”. For example, to what extent the horizontal illuminance [L_x] at the workplane can be associated with the notion of a “Dark” environment (fuzzy variable). In the next step, these variables are inserted in a collection of logical rules (AND, OR, NOT) to map the fuzzified input variables to fuzzified output variables. For example,

$$1. \text{ If (workplane illuminance is "Dark") or (sun height is "Night") then (shading position is "Open")} \quad (2-6)$$

The output of all the rules are combined or *aggregated* in order to evaluate the fuzzy value of the outputs. In the final stage, the fuzzy variables (such as “shading position” in Eq. (2-6)) are *defuzzified*, or translated back to single crisp values. A more detailed description will be provided in Section 5.1.

Application of fuzzy controllers for visual comfort based on linguistic terms was initiated by Dounis et al. [136] in 1993. Later, he presented [119] a fuzzy controller for thermal and visual comfort purposes in a building. The controller does not use any analytical formula or equations: high-level control variables such as thermal and visual comfort are

concerned. Equations are used to drive the actuators. Many recent fuzzy controllers are implemented and evaluated in a simulation environment [137], [138]. On the other hand, some strategies [139] outline the process of developing and tuning a fuzzy controller in order to control external roller blinds of a testbed in order to match the thermal and visual comfort conditions in a room by managing the energy flow through the window.

To the author's best knowledge, no studies were dedicated since then to the implementation of fuzzy control in a full-scale experiment involving the integration of HDR vision sensors for visual comfort energy efficiency.

2.3.6. Critical Analysis

In this section, a critical analysis of the presented methods is performed and the decision for the control strategy in this thesis is justified.

As stated in Section 2.3.2, the use of conventional controllers may not lead to satisfactory results in a noisy environment and prior knowledge about the system is required. The MAST system is not relevant at the current scale of the project since the experiments are carried out in a single zone and single occupied offices. A supervisory control approach may be needed in a more complicated environment, such as open-plan offices. The drawback of the MPC approach is the necessity to first model the buildings [119] as well as the need to use stochastic models of driving variables, such as the weather and occupants behavior. Moreover, the convergence of the optimization problem is not guaranteed all the time. Finally, this approach is computationally expensive since at each time step an optimization problem needs to be solved.

The Fuzzy Logic Controller (FLC) is the suitable option for this doctoral thesis since it does not require any model or prior knowledge about the principles of the room lighting model. It is more time-efficient to prototype, adjust and improve the controller with respect to the other control approaches, especially in the LESO solar experimental building with its complex double-fenestration design. The only drawback of the FLC system is the necessity to tune the parameters of the fuzzy rules prior to installation (Appendix A). This drawback is addressed by introducing a model-free learning system to enhance the rules and attenuate or accentuate their outputs (Chapter 6).

2.4. Normative Efforts

In this section, the most important norms concerning indoor lighting, visual comfort and energy performance of buildings are discussed.

2.4.1. Indoor Lighting

The CIE guide on interior lighting [140] concludes that "the experience has shown that an illuminance for general lighting of the order of 1000 lx is least likely to give rise to complaints, providing careful attention is paid to the avoidance of glare and to an appropriate balance of luminance of relevant surfaces in the room". It also provides a chart with recommended illuminance ranges for three different representative tasks.

The Lighting of Indoor Work Place report from CIE [141] recommends for office rooms, conference rooms and CAD workstations a mean illuminance of 500 lx on the work plane, a maximum Unified Glare Rating (UGR) of 19, and a minimum Color Rendering Index (CRI) of 80. Moreover, it suggests that the daylight factor should not fall below 1% on the work plane, 3 m away from a side window and 1 m from the walls.

More recently, the Indoor Lighting Standard SFS-EN 12464-1 [142] provided recommendations for an appropriate visual performance for paper reading/writing in office rooms: the horizontal illuminance on the workplane should in this case be comprised between 300 lx and 500 lx depending on the task and activity and distributed in a homogenous way on the work plane i.e. $U_o = 0.4$. U_o stands for illuminance uniformity and is evaluated as the ratio of minimum illuminance to average illuminance on a surface. Discomfort glare sensations due to luminaires and/or windows should be avoided, implying a Unified Glare Rating (UGR) < 19.

In the latest draft of the European Standard on Daylight of Buildings [143] submitted for public enquiry in 2016, DGP is proposed as a metric for evaluating glare in the built environment. Based on this draft, the fraction of the time through

a year that the DGP exceeds a certain threshold is suggested as a metric to assess the lighting environment in buildings, according to the following expression:

$$f_{DGP,exceed} = \frac{\text{glare exceedance time}}{\text{reference usage time}} = \frac{t_{glare}}{t_{ref}} \quad (2-7)$$

where t_{glare} is the amount of time throughout the year when DGP exceeds the threshold DGP_t and t_{ref} is the working hours, e.g. 8 AM to 6 PM on Monday to Friday through the year. DGP_t is chosen based on Table 2.2. The maximum exceeding time in the year is 5%.

Values of threshold DGP_t for different levels of glare protection			
	Minimum	Medium	High
Recommendation for DGP_t	0.45	0.40	0.35

Table 2.2 – Recommended values of the threshold for DGP as a function of different levels of glare protection [143].

In recent years, several standards concerning the biological effect of light on occupants in an indoor environment were developed. DIN SPEC 67600:2013 [144] and the WELL building standard [145] are the most relevant ones for healthy indoor lighting. However, as they are out of the scope of this thesis, they will not be further explored.

2.4.2. Energy in Buildings

The US benchmark for “design, construction and operation of high performance green buildings”, designed by the Leadership in Energy and Environmental Design (LEED) Green Building Rating System, is a system of credits for buildings aiming at meeting certain sustainable development targets. In its second version, an intensive use of daylight and a sound view to the outside are considered. For example, in order to obtain credit 8.1 among several requirements, computer simulations should demonstrate that at least 75% of all regulatory occupied areas benefit from about 250 lx under clear sky condition at noon on the equinox, 75 cm above the floor (work plane height). Moreover, more than three quarters of all the occupied area must benefit from a glazing factor of 2% at least. The glazing factor is defined as $\frac{\text{Window area}}{\text{Floor area}} \times \text{Window geometry factor} \times \frac{\text{Actual } T_{vis}}{\text{Minimum } T_{vis}} \times \text{Window height factor}$. The reader is referred to the purchasable LEED reference guide for more details regarding this rating system [146].

On the other hand, as stated in Section 1.2, the Swiss Federal Council announced in 2011 its decision to withdraw from nuclear energy on a step-by-step basis. Thereafter, the Swiss parliament adopted the resolution to mandate the Swiss Federal Office of Energy (SFOE) to elaborate the new Energy Strategy 2050 for the country. The strategy urges for energy efficiency in different domains of activities in Switzerland, including the building sector. This decision is partially based on the facts that buildings account for more than one third of total primary energy demand in the Western World; they are also responsible for more than 30% of the CO₂ emissions [1], [2].

Finally, on June 7th 2017, the Swiss parliament endorsed the international historic Paris climate accord (COP21). By this endorsement, Switzerland commits to reducing the CO₂ emissions by 50% by 2030 compared to the 1990 level [147]. The building sector being responsible for 40% of the Swiss CO₂ emissions, this is the reason why a joint effort of the Confederation and the Cantons will be made in this field [148].

2.5. Anteriority Search

Technology transfer to industry is one of the final goals of any project in applied sciences. Thus it is crucial that methods and/or solutions can be protected by registering the intellectual property: conflicts of interests should be spotted and possible infringing of existing patents should be avoided.

An assisted patent search at the Swiss Federal Institute of Intellectual Property was carried out in April 2016 by introducing the main keywords of our novel control approach. This study was supported by the Technology Transfer Office (TTO) responsible for managing the intellectual property of EPFL institutes. In total 38 relevant patents were identified in this preliminary search. The considerable number of associated patents granted in recent years, filled

mostly by European and North American companies, shows the increasing attention of the industry to this approach. In this section, the most relevant patents are more closely analyzed:

Hassan et al. from Objectvideo Inc. patented [149] in 2008 a concept that paves the way (Figure 2.5 (a)) to a video-based daylighting control. It comprises receiving video image information from a scene (Figure 2.5 (b)) in order to estimate the lighting conditions, i. e. brightness (or radiance) evaluated for the whole or a specific region of interest, and to regulate the light flux delivered to the scene according to these estimations. The advantage of their method is to use only one imaging device to evaluate the illuminance at different areas of interests. In our approach, a ceiling-mounted HDR vision sensor does the same tasks (Appendix G) in a more accurate way. Visual comfort is moreover not an issue in their approach.

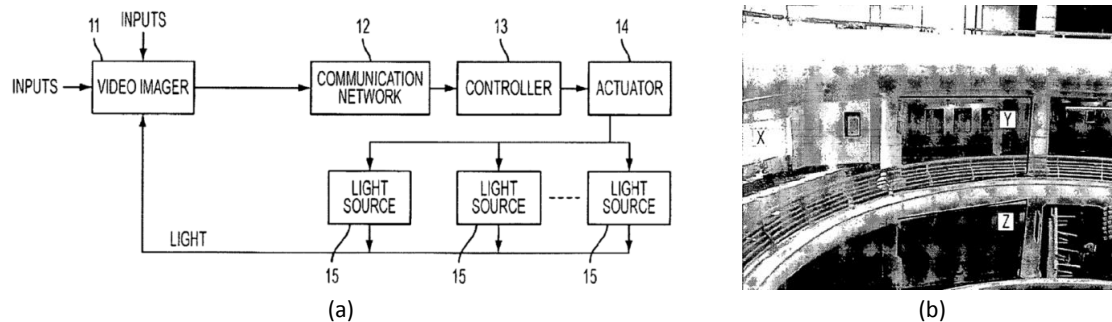


Figure 2.5 – (a) Exemplary embodiment of the video based photo-sensor for lighting control; (b) image captured in indoor environment showing different areas of interest in scene [149].

Another interesting approach was suggested by Bernd in 2010 [150] as a system to control the sun shading systems by means of image recognition. The basic idea is to reduce the direct light transmission through the shading by using several controllable shading elements (#4 in Figure 2.6): detection of a typical pattern (#7) caused by a direct light transmission and control of the shading elements are used to reduce their number. An imaging device (#6) is used to capture an image and detect the presence of a given pattern (e.g. bright/dark stripes) on the picture. In case the stated pattern exists, the controller commands the blinds so as to eliminate the pattern.

The aim of this approach is to avoid the presence of direct sunlight on specific areas. The approach envisaged in this doctoral thesis differs significantly from theirs by the following: (i) it does not assess glare risks from the occupant's point of view; (ii) it eliminates a specific pattern observed without leading necessarily to a comfortable lighting environment and (iii) the resulting work plane illuminance is not necessarily sufficient.

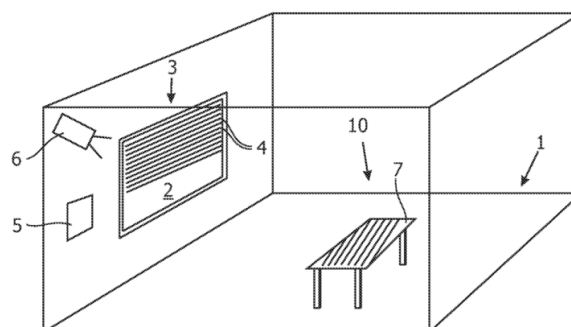


Figure 2.6 – Three-dimensional view of a first embodiment of a system for controlling a shading device according to the invention [150].

A system that can practically implement automated zone-based control of electric lighting, blinds and temperature set-points in an integrated way was suggested in 2013 [151]. It basically aims at an optimal visually and thermally comfortable environment by taking into account different types of use, orientation, location in each zone. The

integrated electric lighting and shading controller (Figure 2.7) is characterized by important differences compared to the approach of this thesis: (i) the sensing infrastructure, essential to comfort regulators, is basically a ceiling mounted single-pixel photosensor; (ii) the controller does not take into account the sun profile and (iii) the visual comfort rules consider only the horizontal illuminance as visual comfort indicator (e.g. no glare index).

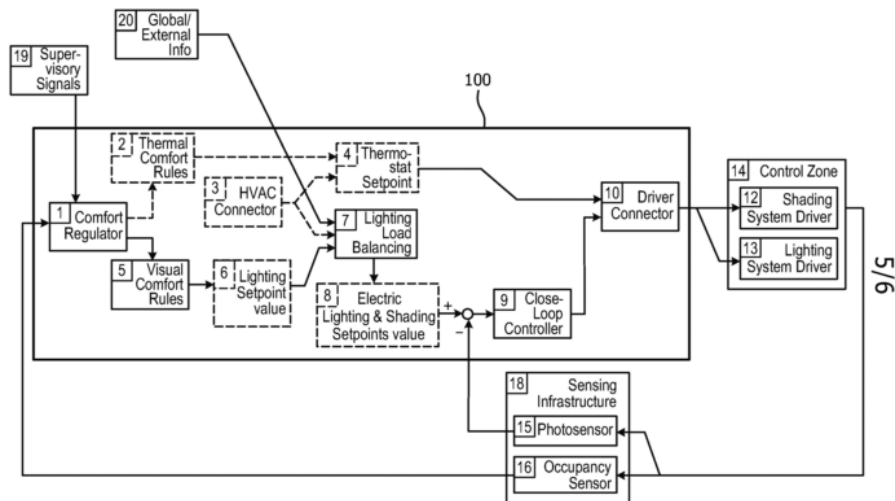


Figure 2.7 – Schematic block diagram of an integrated controller using the electric lighting control feature and shading control feature [151].

David [152] patented in 2013 a system for controlling the optical transmission of several electrochromic windows (e.g. with an electro-controllable optical transmission (V_k in Figure 2.8(a)), comprising a spatial brightness sensor method able to map the luminance of sample surface X as well as the luminance of a window. By the way of a transfer function, a software controls the optical transmission of the window in order to provide a certain brightness on surface X . Clearly in this method, the visual comfort of the occupant is not directly taken into account.

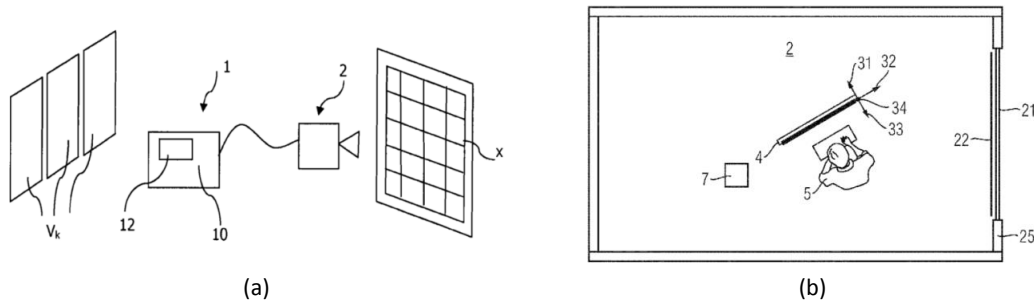


Figure 2.8 – Functional diagram of the control system proposed by Saint-Gobain Glass France [152]; (b) layout of a system to control the shading system by a transfer function [153].

In 2015 Delu et al. [154] registered a utility model that drives an LED-based artificial lamp by Pulse Width Modulation (PWM) signals by taking the visual comfort criterion derived from readings of a single pixel illuminance sensor. This approach is different from the one suggested in this thesis principally in the following ways: (i) the visual comfort criterion does not encompass contrast in the field of view; and (ii) it is not applicable in real office rooms as no integrated daylight management strategy is used.

The Fraunhofer Society for the Advancement of Applied Research patented [153] a device and method in 2016 managing the incident light flux on a specific task area. They proposed to establish a transfer function, through measurements of at least one sensor installed at the workstation (either of 31, 32, 33, 34 in Figure 2.8(b)), to map the luminance distribution on the work plane as well as the characteristics of a light source, such as the sun or artificial lighting. Having

created this model, they may use it to generate a control signal for at least one light source; electric light, sun shading or electrochromic glazing.

Lundy et al. [155] patented a software in 2016 to monitor and control a motorized shading system as shown in Figure 2.9 (a). Their emphasis is placed on interaction with the occupants in order to provide them the information required to decide on the acceptance or rejection of the shading position recommendations issued by the control system. For example, as shown in Figure 2.9 (b), they recommend to the occupants to lower the brightness threshold and to consider this decision for future control actions regarding the windows. The control approach of this patent is close to one suggested in this thesis: their shading control, for instance, is based on a work plane protection algorithm [109] and the venetian slat angles are set to a critical cut-off-angle [156]. However, there are fundamental differences between the two approaches: (i) their notion of visual comfort relies on the ceiling mounted illuminance meter, (ii) the impact of window actions on the thermal comfort is neglected and (iii) even though their approach prioritizes the occupant’s wishes, they do not suggest any personalized vision sensor.

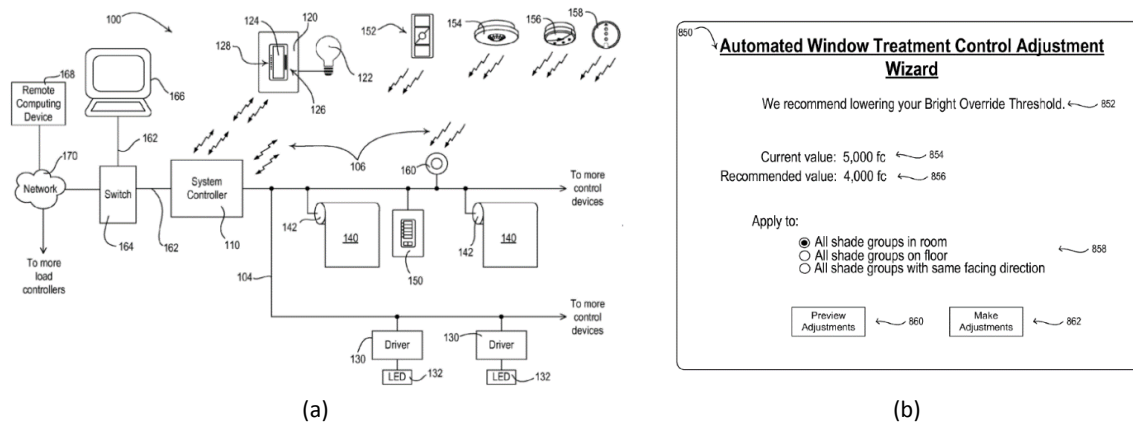


Figure 2.9 – (a) Simplified block diagram of an example load control system; (b) the user interface to recommend the occupant to adjust the thresholds for lighting system [155].

This anteriority search revealed that the proposed approach in this doctoral thesis, as detailed in Sections 5.2.1 and 5.3.3, differentiates itself from the state-of-practice.

Chapter 3

Cyber-Physical Testbeds

Almost all of the studies in this doctoral thesis are carried out experimentally in three cyber-physical testbeds: i) the LESO solar experimental building (so called *LESO building* in this text) on EPFL campus; ii) CREATE tower, SinBerBEST daylighting testbed and 3for2 innovative building in Singapore; and iii) daylight testbed at Fraunhofer Institute for Solar Energy (ISE). A clear description of the testbeds guarantees the reproducibility of the results by other researchers. This chapter consists of three sections and each section is dedicated to one testbed.

3.1. LESO Solar Experimental Building

Two identical south-facing office rooms of the LESO building, illustrated in Figure 3.1 and located on the EPFL campus (lat. $46^{\circ}32'$, long. $6^{\circ}35'$, altitude 410 meters a.s.l., yearly mean south vertical radiation $3159 [MJ.m^{-2}]$), were used as the setup for in-situ experimentations. The building is a passive solar building with a heavy thermal mass ($\bar{M} = 1040 [kg.m^{-2}]$) and its thermal insulation level is high ($\bar{U} = 0.55 [W.m^{-2}.K^{-1}]$). It is a middle size administrative building, whose main axis has east-west orientation and its main wooden facade is facing south exactly. The building is divided into three thermally insulated floors and each floor is sub-divided into three thermally independent rooms. The building features no active cooling or ventilation system and it is naturally ventilated by stack effect [157]. Occupancy of the LESO building is typical of an office building, with an average of 15 people occupying the overall laboratory from 8 AM to 6 PM. More detailed information on the building can be found in publications by Scartezzini et al. [9] and Altherr et al. [30] and the PhD thesis of Zarkadis [158].

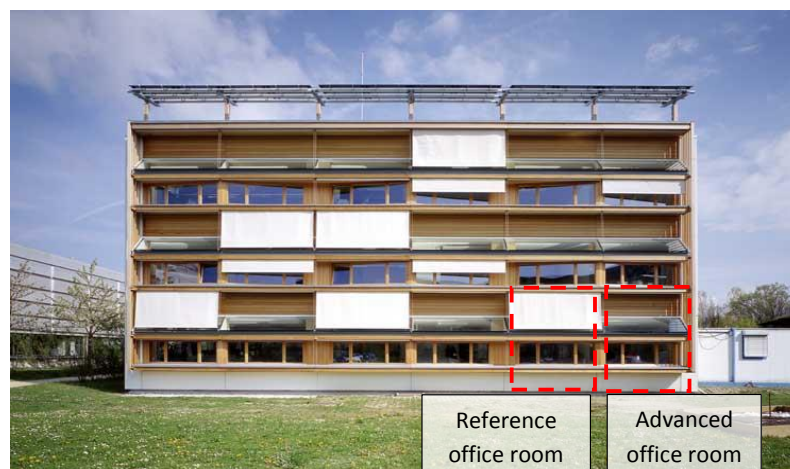


Figure 3.1 – LESO solar experimental building [159]. Two offices on the ground floor are used for the experiments presented in Chapter 5.

Both advanced and reference offices were equipped with a conventional window on the lower part of the Southern facade and an Anidolic Daylighting System (ADS) on the upper part (Figure 3.2, right). This system collects both the direct and diffuse daylight fluxes issued from the sun and the sky vault through a zenithal collector, composed of a non-imaging optical component (anidolic element) located behind a double insulated glazing [30], [160]. The floor area of each room is identical and equal to $15.7 \text{ [m}^2\text{]}$ (e.g. 4.75 [m] (depth) \cdot 3.3 [m] (facade)) and their height is 2.8 [m] . The layout of the sensors and actuators in the reference and advanced office rooms is shown in Figure 3.2 & Figure 3.3 respectively.

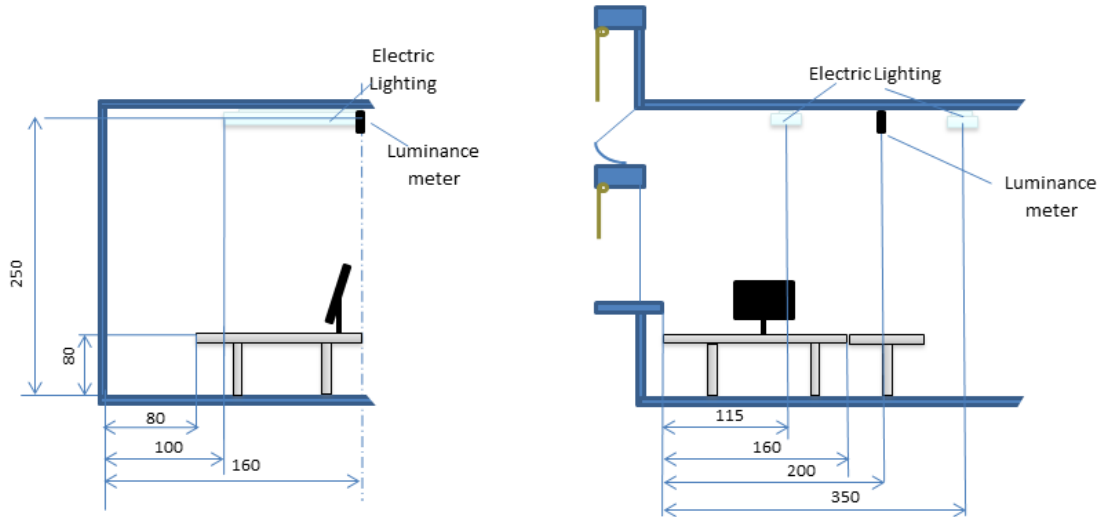


Figure 3.2 – Schematic representation of reference office room setup in LESO building.

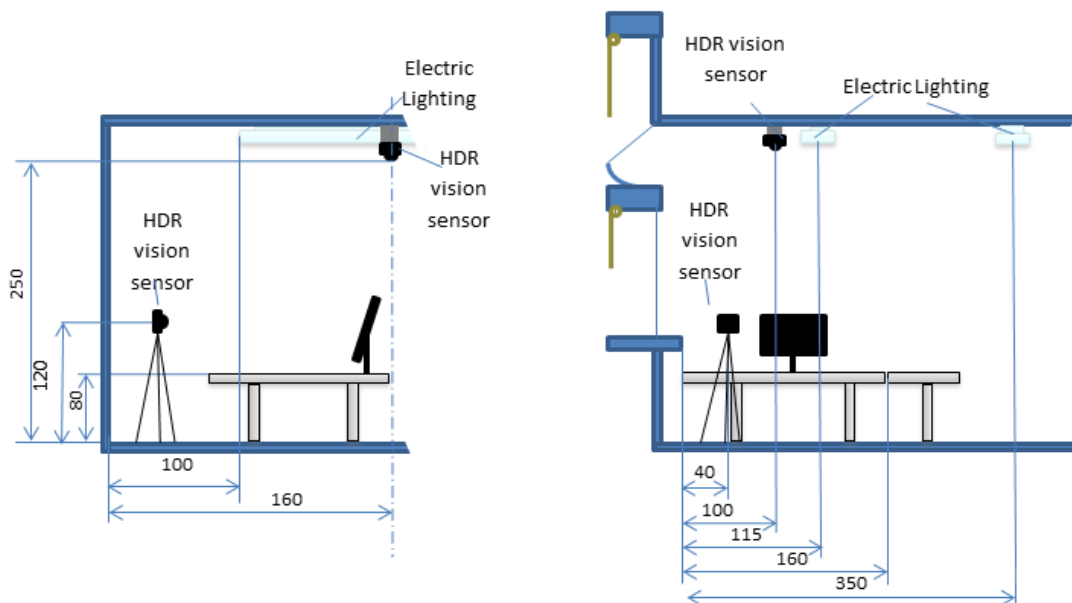


Figure 3.3 – Schematic representation of advanced office room setup in LESO building.

One west-facing workstation per office was used to perform the in-situ experimental monitoring, while the researchers occupied the other one facing east. The distance of the Visual Display Terminal (VDT) to the window is equal to 150 [cm] . To avoid any bias, the type of furniture and setting, such as the chair's height, distance of the tables to the walls as well as the interior design of the two offices, were amended so as to be as similar as possible. The VDT are Eizo-FlexScan L557 terminals and were tuned to the same display settings: their full brightness is equal to $250 \text{ [cd.m}^{-2}\text{]}$ according to their technical manual. The following main VDT parameters were used: positive polarity thus categorized as high luminance screen, Case A according to Table 4 of Standard EN12464-1 [142], $6'500 \text{ [K]}$ color temperature,

gamma 2.4, 97% gain for red, 100% for green and 98% for blue. An overview of the equipment installed in each office room is given in Table 3.1.

Equipment/ algorithm	Reference Room	Advanced Room
Controller	Best practice controller based on E_{desk}	Fuzzy logic based controller taking into account DGP, E_{desk} and sun profile angle
Movement filter	Time- and magnitude based	
Desk illuminance meter	Ceiling mounted luminance meter Siemens GE252	HDR vision sensor IcyCAM
Glare sensor	None	HDR vision sensor IcyCAM
Electric lighting	2 LED luminaires (23 [W]/2400 [lm], 4000 [K])	
Sun shading	2 motorized external blinds	
Energy meter	3 Phase electricity meter, for lighting, heating and plug loads	
Data acquisition system	KNX communication system	Ad-hoc platform merged into KNX system

Table 3.1 – Overview of the equipment installed in each office room of the experiment in LESO building.

The illuminance in the reference office room is measured by a ceiling mounted 'brightness sensor' (Siemens GE252), located at a distance of 3.5 m from the facade elements (Figure 3.2); according to their technical manual, the latter measures the luminance in an angle of $(-20, +38)$ degrees from the vertical. A Minolta CL-100 illuminance meter was placed right beneath the sensor before starting the monitoring to obtain a calibration curve by comparing the measured illuminance and the readings of the brightness sensor.

3.1.1.1. Presence Detection Algorithm

In the advanced office room, the ceiling mounted HDR vision sensor has two purposes: i) evaluating the horizontal work plane illuminance and ii) presence detection (Figure 3.4). The horizontal illuminance on the workstation is evaluated by assuming that the work plane surface is an ideal diffusive surface (e.g. Lambertian). The procedure for horizontal illuminance monitoring from the ceiling is presented in Appendix G. On the other hand, the presence detection algorithm features negligible false positive and false negative detections and captures images with a frequency of ~ 1 [Hz]. In this section, this algorithm is fully elaborated and its performance is demonstrated and validated.

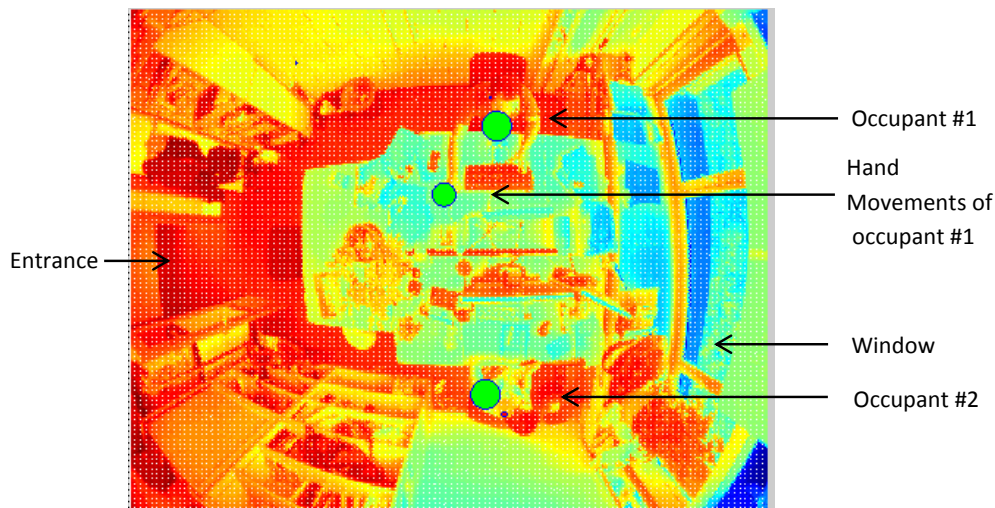


Figure 3.4 – Present detection algorithm implemented on a ceiling-mounted HDR vision sensor. Green circles show the detected "present" objects. Subtle movements of occupant's hand are also detected as a separate object.

3.1.1.1.1. Introduction

A ceiling mounted HDR vision sensor is installed basically for measuring the horizontal illuminance on the workplane. The same sensor may be readily used for detection of the presence.

This section is basically a technical description of a computing routing implemented in the MATLAB software and consists of a detailed explanation of the image processing algorithm. The main idea is to use a ceiling-mounted High Dynamic Range vision sensor (Figure 3.5), equipped with a fisheye lens with data acquisition frequency (f_{DAQ}) of 11 [Hz], as a presence detection sensor.

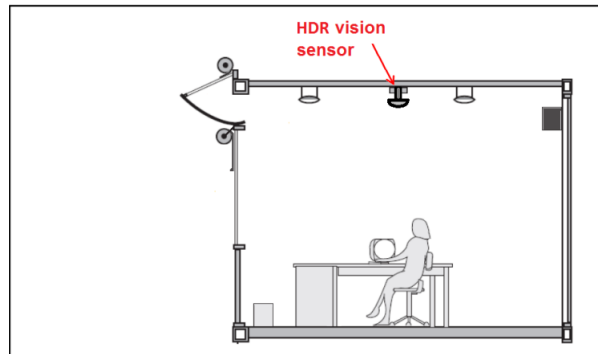


Figure 3.5 – Arrangement of the sensor with respect to the office occupant.

3.1.1.2. Problematic

The main challenge is to develop a system that has negligible FP and FN detections. This goal is not reachable by simple comparison of the difference between the values of the pixels of two consecutive captured images, as shown in Figure 3.6. The edge of the window as well as some highly reflexive points inside the office are considered as moving objects (FP) while alteration of their values are mainly due to alteration in solar radiation.

Increasing the static threshold would, on the other hand, lead to a high rate of FN detections since small movements of the occupant leading to small luminance alterations would remain undetected.

3.1.1.3. Objective and Specification of the Detection System

It is required to develop a robust, self-deliverable, reliable system with negligible False Positive and False Negative (refer to Section 3.1.1.4 for the definition) that is capable of detecting a new office occupant within 2-3 seconds and can keep the occupant detected even if s/he does not exhibit any detectable movement for 60 seconds. The system should be robust to the sudden variation of illumination conditions in the office room. However, reporting the exact number of the occupant(s) and their precise location, distinguishing between human and animal or a rotating fan (object recognition) is not the goal of this system. This system should be self-deliverable; regardless of the configuration of the office and the location of the entrance or building envelop opening it should be able to detect reliably the office room occupant(s).

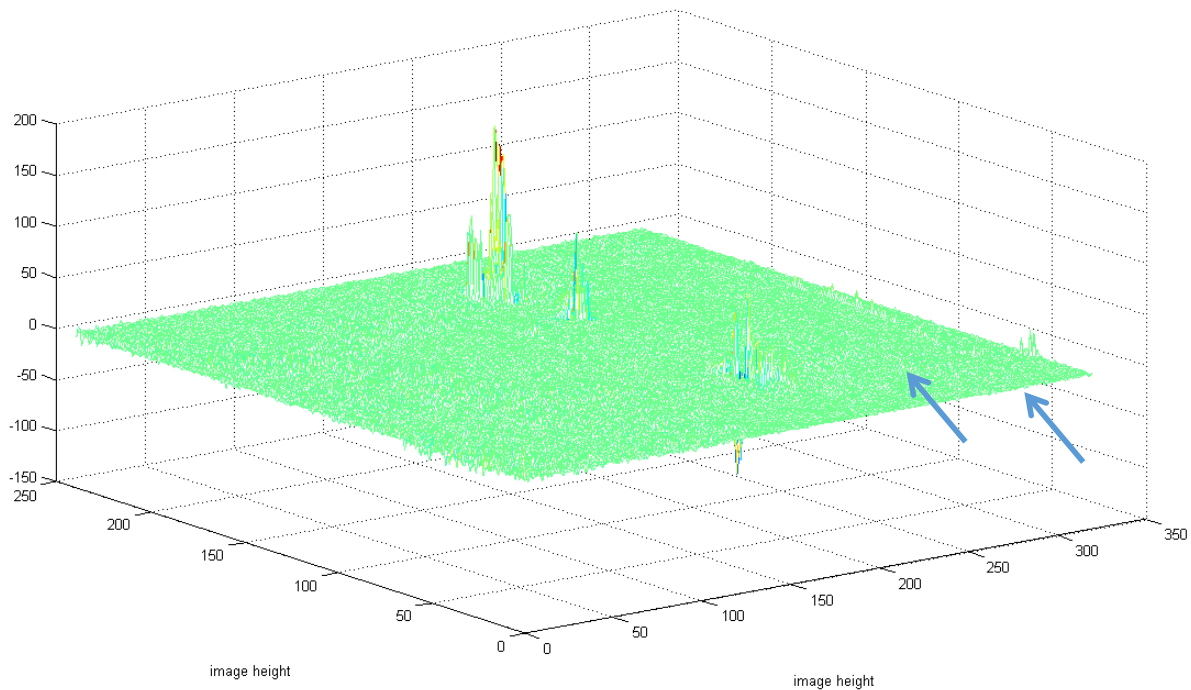


Figure 3.6 – Difference between two consecutive images. Failure in application of image differentiating for detecting moving object. Edges of the border of the window (pointed by the arrows) is also considerable.

At this stage, the object recognition (e.g. distinguishing between a human and a pet or rotating ventilator) is not required. Moreover, the parts of the image that correspond to the office room surroundings are not in the first instance removed from the image, assuming that there is not any person outside the office room that remains in the field of view of the vision sensor for long enough to be detected.

3.1.1.4. Terminology

DAQ: Acronym for data acquisition that is performed by a remote computer through the MATALB software. As a result of DAQ, a 2D matrix of [240, 320] ([rows, columns]) is produced by the vision sensor, used for further image processing steps.

Background: The part of the image (pixels) that is stationary and does not normally move during office detection by the image sensor. Some objects might be displaced by the office occupant who leads to temporal classification of corresponding pixels as “non-background”; however ideally they will be re-classified as background shortly after their displacement

Foreground: Part of the image (pixels) that is not classified as background. It might correspond to moving objects, or to the noise from the environment or intrinsic noise of the imaging device.

Ghost movement: This is the subtle movement of the hand, head or even finger of the office occupant when he is at work. Due to the small nature of these movements, there is a tendency of classifying the office occupant as background pixels.

Blob: Blob stands for **B**inary **L**arge **O**bject and refers to a group of connected pixels in a binary image. The term “Large” indicates that only objects of a certain size are of interest and that “small” binary objects are usually noise. They are basically built by regrouping the pixels in the foreground and might include the noisy detections.

Objects: These are the blobs that have a high probability of being associated with a real “office occupant”. In other words, they are noise-free trackable blobs.

Blob Associating: The action of associating the newly found blobs with the existing objects. This action is essential for object tracking and updating the probability of correctness of the blob.

Object Tracking: The action of tracking the existing objects and updating the coordinates of each object with the associated blobs.

False Positive (FP): An undesirable action of detecting a “moving object” while in reality it is false. This might be created by the noise in the environment or the imaging device.

False Negative (FN): undesirable phenomena of eliminating previously detected “moving object(s)”. This phenomenon occurs normally when office occupants exhibit ghost movements.

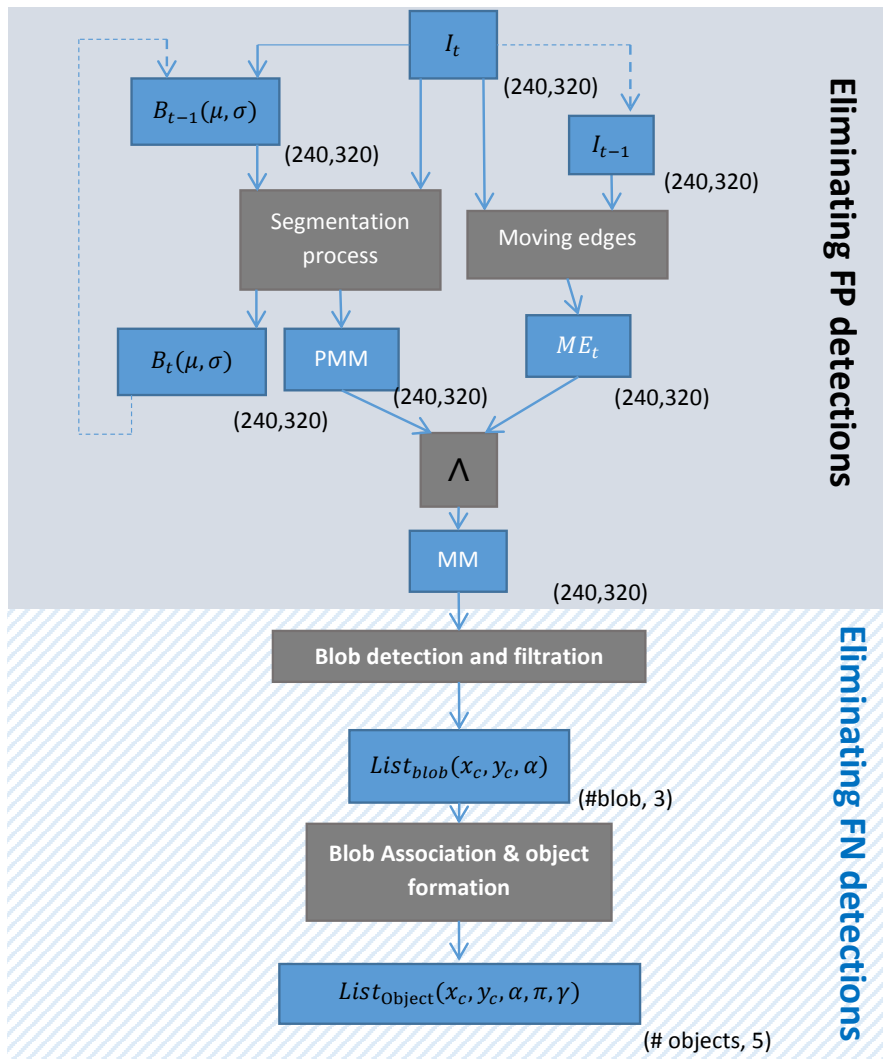


Figure 3.7 – Overview of the procedure of detecting objects.

3.1.1.5. Solution

In this section, an algorithm used for reaching the mentioned objective is elaborated in detail.

3.1.1.5.1. Overview of the Algorithm Flowchart

In Figure 3.7, the image processing after n^{th} DAQ is explained. The variables are shown with blue rectangles, the actions/process with red rectangles. The dimensions of the variables are shown next to them in parenthesis.

The first part of the algorithm (with solid gray background) detects the blobs and is responsible for reducing the FP detections by filtering out the noisy detections. The basic idea is to get the border of the moving objects (so called *edges*) by the interception of two methods:

- i) the edges extracted from the result of absolute difference between the current image I_t and the previous one I_{t-1} ;
- ii) the edge computed with the difference between the stochastic model of the background and the actual image.

The second part of the algorithm is responsible for reducing the FN phenomena by keeping the history of the activity of the office occupant and updating the existing objects with newly found blobs.

The FP detections are preferred to FN detections, since they have direct impact on the automatic system acceptance. In other words, it is preferable to have few FN detections in exchange of several FP detections. Practically speaking, it would be pointless if the office occupant's presence was not detected (FN) and the lights were turned off. Keeping the light on for a further couple of seconds after occupant's departure (FP) is not negatively perceived and has negligible effect on the electric lighting energy consumption.

3.1.1.5.2. Edge Detection by Background Subtraction

With a static vision sensor, the search space can be reduced by detecting regions of interest in the image where the probability of finding a person is high. The first step is through background subtraction; only the changes are detected. For this purpose, among several existing approaches, the one that proves to be the most promising through a comparative study [161] is chosen: **One Gaussian**. In this method each pixel of the background is modeled with a probability density function (PDF) learned over a set of training frames. In this case, the background subtracting problem is turned into a PDF-thresholding problem. For instance, to take noise into account, some authors [162] model every background pixel with a Gaussian distribution $\eta(\mu_{p,t}, \sigma_{p,t})$ where $\mu_{p,t}$ and $\sigma_{p,t}$ stand for the average background value and covariance matrix over pixel p at time t . If for a pixel the value $\sigma_{p,t}$ is high, it signifies that there is an uncertainty regarding the mean value of that pixel in the background model. As somebody passes through the image, the σ of the corresponding pixels in the background increases. This simple model is a compromise between quality of detection, computation power and memory requirement. In this context, the distance metric can be the log likelihood:

$$d_{G_{p,t}} = \frac{1}{2} \log((2\pi)^3 \cdot |\sigma_{p,t-1}|) + \frac{1}{2} (I_{p,t} - \mu_{p,t-1}) \cdot \sigma_{p,t-1}^{-1} \cdot (I_{p,t} - \mu_{p,t-1})^T \quad (3-1)$$

Where d_G is the distance between the value of pixel p captured at time t ($I_{p,t}$) with the same pixel from the background map from the previous step. In the original formulation, $\eta(\mu_{p,t}, \sigma_{p,t})$ is calculated for RGB values while in our application, a single grayscale value is produced by the imaging system and used.

To allow for illuminance variation or any change in the position of the stationary objects in the office room (e.g. displacement of the telephone after a call), the mean and the covariance of each pixel iteratively updated as follows:

$$\mu_{p,t+1} = (1 - \alpha_{update}) \cdot \mu_{p,t} + \alpha \cdot I_{p,t} \quad (3-2)$$

$$\sigma_{p,t+1} = (1 - \alpha_{update}) \cdot \sigma_{p,t} + \alpha_{update} (I_{p,t} - \mu_{p,t})(I_{p,t} - \mu_{p,t})^T \quad (3-3)$$

Where α_{update} is the learning rate for updating B : the larger it is, the faster the history is eliminated and the result of edge detection by background subtraction will get similar to edge detection by consecutive image subtraction (Section 3.1.1.5.3). The smaller it is, the more the history is taken into account and the less the image is updated with new measurements. In this case, a new stationary object in the field of view remains as "present object" for a larger duration. The updating action is represented by a dashed line in Figure 3.7.

The output of this algorithm is called primary motion mask (PMM) and defined as follows:

$$PMM_{p,t} = \begin{cases} 1 & d_{G_{p,t}} > \tau_{distance} \\ 0 & d_{G_{p,t}} < \tau_{distance} \end{cases} \quad (3-4)$$

where $\tau_{distance}$ is the threshold for detecting the edges based on the distance between the new readings and the background model.

3.1.1.5.3. Edge Detection by Consecutive Image Subtraction

This algorithm is inspired by [163]. A simple yet efficient edge detection algorithm that does not significantly exceed the time requirements for our application is chosen. It compares each pixel value with its 4 connected neighbor pixels. If the difference between the pixel and one of its neighbors is higher than a given threshold (τ_{edge}), the pixel is marked as an edge. Based on this description, $D(x, y)$ is defined as follows:

$$D_t(x, y) = I_t(x, y) - I_{t-1}(x, y) \quad (3-5)$$

And the following function defines the output of this algorithm, called binary matrix of the Moving Edges ME_t :

$$ME_{t,x,y} = \begin{cases} 1 & \text{if } |D(x, y) - D(x-1, y-1)| > \tau_{edge} \vee \\ & |D(x, y) - D(x-1, y+1)| > \tau_{edge} \vee \\ & |D(x, y) - D(x+1, y-1)| > \tau_{edge} \vee \\ & |D(x, y) - D(x+1, y+1)| > \tau_{edge} \\ 0 & \text{if } \textit{otherwise} \end{cases} \quad (3-6)$$

The larger τ_{edge} , the more robust the system is to environment noises, and it also becomes less sensitive to the small movements of the office occupants. Thus, the choice of this parameter is a trade-off between the robustness to the noise and sensitivity to an occupant's movements. It is static and experimentally chosen for the time being.

The final result of foreground, the so called Moving Mask (MM), is created by intersection of the result of two edge detection algorithms:

$$MM_t = PMM_t \wedge ME_t$$

3.1.1.5.4. Blob Formation and Filtration

Now that the noise free foreground is formed, the blobs are extracted. The blobs will be used later as input for the object tracking algorithm. For each blob, three characteristics are registered: x_c (center of its pixels in x direction), y_c (center of its pixels in y direction) and α (total number of pixels).

For creating the blobs, the grass-fire algorithm is applied. In this algorithm, the foreground is firstly swept. If the detected pixel already belongs to an existing blob (e.g. a blob labeled β), the algorithm starts to search in its vicinity to find any foreground pixel that does not belong to any blob yet. As soon as an uncategorized pixel is found, it is labeled as Blob β . The coordinates of the Blob β are updated with the coordinates of the newly categorized pixel. In the case where the initial pixel does not originally belong to any blob and there is not any other categorized foreground pixel in its vicinity, a new blob is created and labeled and its coordinates are equal to the coordinates of the single pixel. For more efficient vicinity search, the categorized pixels are registered in a list so as to be referred to rapidly if needed.

The searching radius is predefined by the user (τ_{blob}). The larger it is, the higher is the risk of regrouping the noisy measurements and passing them to the next step as an input for the tracking algorithm. The smaller it is, the larger the number of blobs that will be detected and the tracking part of the algorithm will require more computation.

In the next step, the blobs with the sizes smaller than a threshold (τ_{blob}) are eliminated. This is an important filter for reducing the number of FP detections.

3.1.1.5.5. Object Formation

Here is the core part of the algorithm for eliminating the FN phenomena. This step relies on an important fact: an office occupant is continuously moving and does not disappear/reappear in the image captured from the ceiling. Thus, his movement is trackable from one frame to another. Based on this fact, the notion of an "object" is introduced. Objects, as explained in Section 3.1.1.4, are the blobs with a *probability* of being correctly associated with a part or the whole projection of an office occupant on the imaging system. In other words, the notion of probability reflects the certainty of the tracking algorithm with regard to its decision.

As an office occupant appears as a moving object in an image, the probability of the associated object(s) should increase since the algorithm will find a proof of his or her detection. Conversely, as the same office occupant does not appear as a moving object in an image (remaining still for couple of seconds), the probability of his appearance will be reduced. Although reduction of the probability of presence of an office occupant does not seem logical, it is needed, however, for eliminating any FP detected objects.

In order to translate the notion of probability to two binary states of *absence* and *presence*, two thresholds are defined: $\tau_{presence}$ above which the object is labeled as present; $\tau_{absence}$ below which the object is labeled as absent. In the case where the probability remains between these two boundaries from one step to the other, the state does not vary.

$$\gamma_t(obj) = \begin{cases} 1 & \pi_t(obj) > \tau_{presence} \\ 0 & \pi_t(obj) < \tau_{absence} \\ \gamma_{t-1}(obj) & otherwise \end{cases} \quad (3-7)$$

Moreover, following what is explained in the previous paragraph, two multipliers ($\rho_{increase}$, $\rho_{decrease}$) are introduced for increasing/decreasing the probability upon confirming/rejecting the presence of a tracked object. This concept is summarized in Eq. (3-8)

$$\pi_t(obj) = \begin{cases} \pi_{t-1}(obj) \times \rho_{increase} & if \exists blob \leftrightarrow obj \\ \pi_{t-1}(obj) \times \rho_{decrease} & if \nexists blob \leftrightarrow obj \end{cases} \quad (3-8)$$

where $\pi_t(obj)$ is the presence probability of object *obj* at time step *t*. The process of blob association is done by taking into account the center of the *obj* and the *blob*. If the Euclidean distance between the center of the existing *obj* and the newly found *blob* is less than a predefined threshold (r_{obj}), the blob association takes place, the presence probability of the *obj* increases and the *blob* is eliminated from the blob list.

At the end of the blob association process, the remaining unassociated blobs are added to the end of the object list with the initial probability of the $\tau_{absence}$. If in the following frames, any blob can be associated with them, their probability would increase.

The value of the multipliers $\rho_{increase}$ and $\rho_{decrease}$ depends on two factors:

i) how fast a new occupant's *arrival* is detected; namely the time that the presence probability (π) of an object is increased from $\tau_{absence}$ to $\tau_{presence}$. This duration is parameterized as $T_{arrival}$. Based on the objectives of this project, $T_{arrival} = 2 - 3$ [s]. The longer this duration, the slower the system perceived by the occupant;

ii) for how long the occupant may remain still while working at his desk or reading something off the screen. During this duration, the algorithm should "remember" the presence of the office occupant. This duration ($T_{remember}$) should be enough time for the presence probability of an object to decrease from $\tau_{presence}$ back to $\tau_{absence}$. Based on the objectives, $T_{remember} = 60$ [s].

Knowing the frequency of DAQ (occasionally $1.5 - 2$ [Hz]), $T_{arrival}$ and $T_{remember}$ are translated to a number of DAQ cycles. ($\omega_{arrival}$ and $\omega_{remember}$ respectively). Finally, based on Eq. (3-8) and knowing the DAQ frequencies and threshold for absence and presence, one is capable of deriving $\rho_{increase}$ and $\rho_{decrease}$ by Eq. (3-9).

$$\rho_{increase} = \omega_{arrival} \sqrt{\frac{\tau_{presence}}{\tau_{absence}}} \quad (3-9)$$

$$\rho_{decrease} = \omega_{remember} \sqrt{\frac{\tau_{absence}}{\tau_{presence}}}$$

The detected "present objects" are not combined in the current version of the algorithm since, as stated in Section 3.1.1.3 this is not necessary. In other words, even if there are two detected blobs per office occupant (e.g. one for hand

and one for head), they are not unified since knowing the number of people in the office does not have any priority for the time being.

3.1.1.5.6. Robustness to Sudden Change to Lighting Condition

In the office environment, several phenomena lead to a considerable amendment in the lighting condition, such as lighting or shading movements and sudden changes in the sun coverage. In these cases, the background model $B(\mu, \sigma)$ should be updated so as to avoid any misdetection. For resetting the background model, if the number of pixels with considerable difference ($\tau_{robustness}$) in values with respect to previous captured images exceeds a certain amount (e.g. one fifth of the total number of pixels), the background model is reinitiated after a pause of 20 seconds. This pause is meant to allow the lighting condition to re-stabilize once again.

3.1.1.5.7. Tuning the Parameters

The main difficulty of implementing such algorithms in an office environment is that the final performance depends on the appropriate selection of the thresholds. Dynamic selection of the parameters based on the collected data is more favorable than use of static parameters (i.e. predefined constants), since the former lead to a more robust system that requires fewer adjustments when installed in a new environment. In the current version of the algorithm (v4.5), the parameters are mostly static. In this section, the logic behind choosing the static and dynamic thresholds and parameters are elaborated. Some of the parameters are tuned by simply performing a sensitivity analysis.

- α_{update} [—]: The values are amended between 0.01 and 0.5 (maximum is 1). The smaller α_{update} is, the more static the background model remains. The larger the value; the faster the office occupant is recognized at the expense of exhibiting more FP. A reasonable compromise is 0.3.
- r_{obj} and r_{blob} [pixel]: The larger this value, the smoother the tracking functionality. In other words, in this case, the algorithm is capable of following a walking occupant without forming numerous blobs and objects. However, a large search radius leads to considerable FP and is computationally more demanding. Since the goal of this project is to perform robust and fast presence detection, smooth tracking has less priority. Thus, the option has been taken to keep this parameter relatively small at 30 pixels.
- τ_{blob} [pixel]: This parameter defines the minimum number of pixels allowed for each blob; blobs with pixels fewer than τ_{blob} are eliminated. The bigger this value, the smaller the FP. However, in this case, the subtle movements of, for example, the fingers or head of the occupant are eliminated although detected as blob. On the other hand, the smaller this parameter, the more FP detection.

The solution for remaining sensible to subtle movements of the office occupant and keep the system as robust to noise as possible is to tune τ_{blob} , r_{obj} and τ_{edge} simultaneously and accordingly: τ_{blob} is chosen to be small so that the small movements are detected, r_{obj} is also chosen to be small so as to avoid noisy blob associations. In this case, although the risk of creation of noisy blobs is higher, the risk of being associated to an object and gain high presence probability is low. Finally, τ_{edge} is increased to be higher than the noise level of the vision sensor (~ 15 [grayscale]). A suitable balance between these three parameters allows reaching τ_{blob} values as small as 2 pixels, small enough to detect finger movements.

- Image trimming: Not all of the image pixels belong to the office room environment; there are some pixels belonging to the corridor and some capture the movement through envelop openings. The solution is to define a region confined to the office environment. This solution is not aligned with the “self-commissioning objective of this project”, however between this solution and a more sophisticated one, e.g. developing a *recognition* strategy in order to distinguish between humans and moving plants outside the window, the former is chosen for the sake of simplicity and effectiveness.

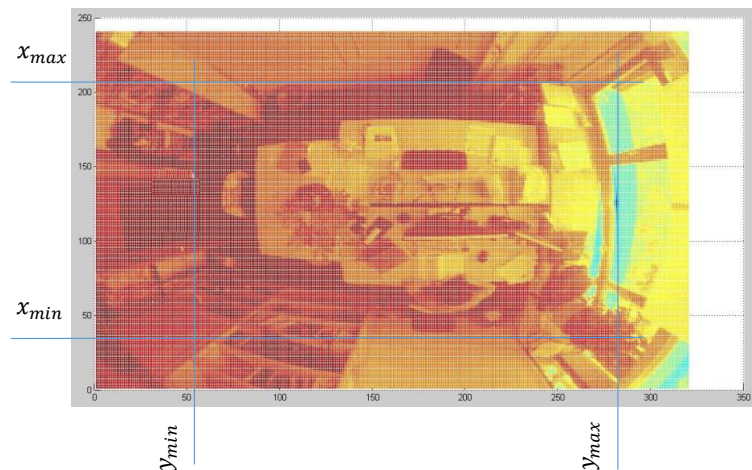


Figure 3.8 – Defining the “interest region”, a region that corresponds to the interior environment of the office room.

3.1.1.6. Experimental Results

A visualization system is developed for debugging purposes and for more insight into the importance and role of parameters such as thresholds and searching radii. As mentioned in (3-3), the presence detection algorithm consists of two sections: i) FP elimination; and ii) FN elimination. A data visualization panel is developed per section to allow for rapid intuitive verification of the algorithm outputs. Figure 3.8 shows the visualized data at the end of first phase and Figure 3.9 shows the data at the end of the second phase, namely the output of the whole algorithm.

The raw input is shown in the top left image and an office occupant is encircled with a green cycle. The background model is shown next to it (middle corresponds to mean values and top right to the standard deviation (SD) of the model). Obviously, the background mean map is similar to the input raw data except for the pixels corresponding to where the office occupants have previously passed. The SD map of the background image shows high values for where the occupant is present.

The output of background subtraction (*PMM*) is shown in the bottom left image, where noisy movement detections are observed from where the occupant is located as well as where the window is located.

In the bottom middle the output of Moving Edge detection (ME) is shown where we observe high constant noise created by the border of the window. This is the reason why simple consecutive image subtraction would not lead to reliable presence detection.

Finally, in the bottom right image, the intersection of ME and PMM is evaluated, which shows the moving mask encircled in green. The foreground also consists of some pixels in the top left corner remaining from faulty edge detection generated by the border of the window. As explained in Section 3.1.1.5.7, even if these pixels are passed to the next steps, due to their random nature, they would not consistently influence the amendment of presence probability (π) of an object and consequently they would be rapidly eliminated from the object list.

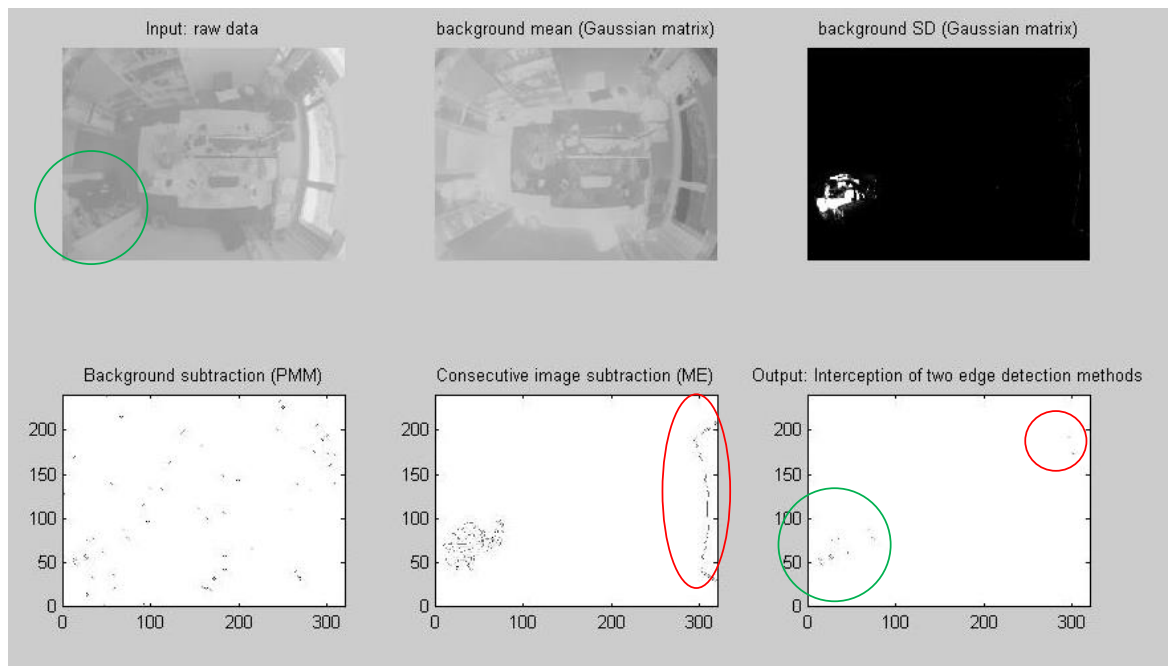


Figure 3.9 – Validation of the first part of the algorithm (FP detection elimination).

These pieces of data show the success of the foreground detection algorithm to reduce the FP detections considerably in such a noisy environment and to return as foreground merely the pixels which correspond to the office occupant.

The result of the next step is shown in Figure 3.10. The location of the objects is superimposed on the input data using circles. The size of the circle represents the presence probability of the object: the larger it is, the higher the presence probability. The color of the circle shows its state: $\gamma = 1 \rightarrow$ green; $\gamma = 0 \rightarrow$ red. In Figure 3.10, two present objects are shown, of which one is a real office occupant and the second one is his reflection by the window glass.

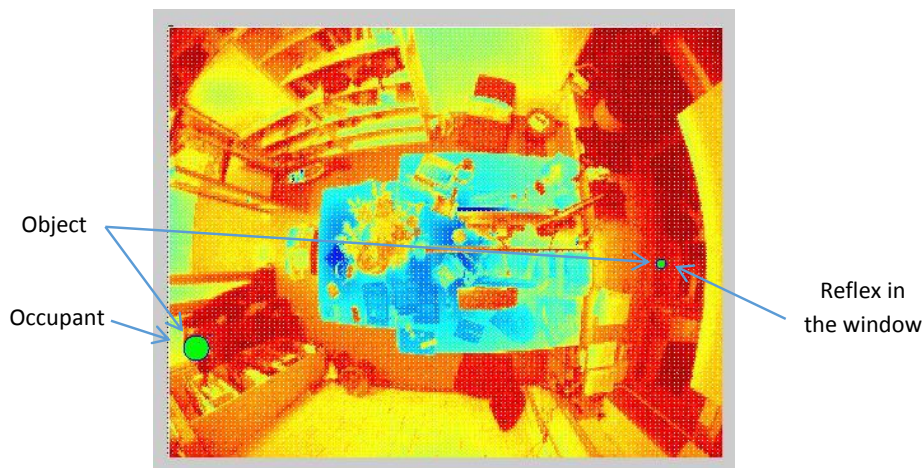


Figure 3.10 – Validation of second part of the algorithm (FN phenomena elimination).

Figure 3.11 shows how the system behaves after being launched. At the beginning, several small objects with low presence probabilities are created. Upon confirmation/absence of presence in the next frames, the probability of each object is increased/decreased. Finally, two objects are detected as present after 3 seconds.

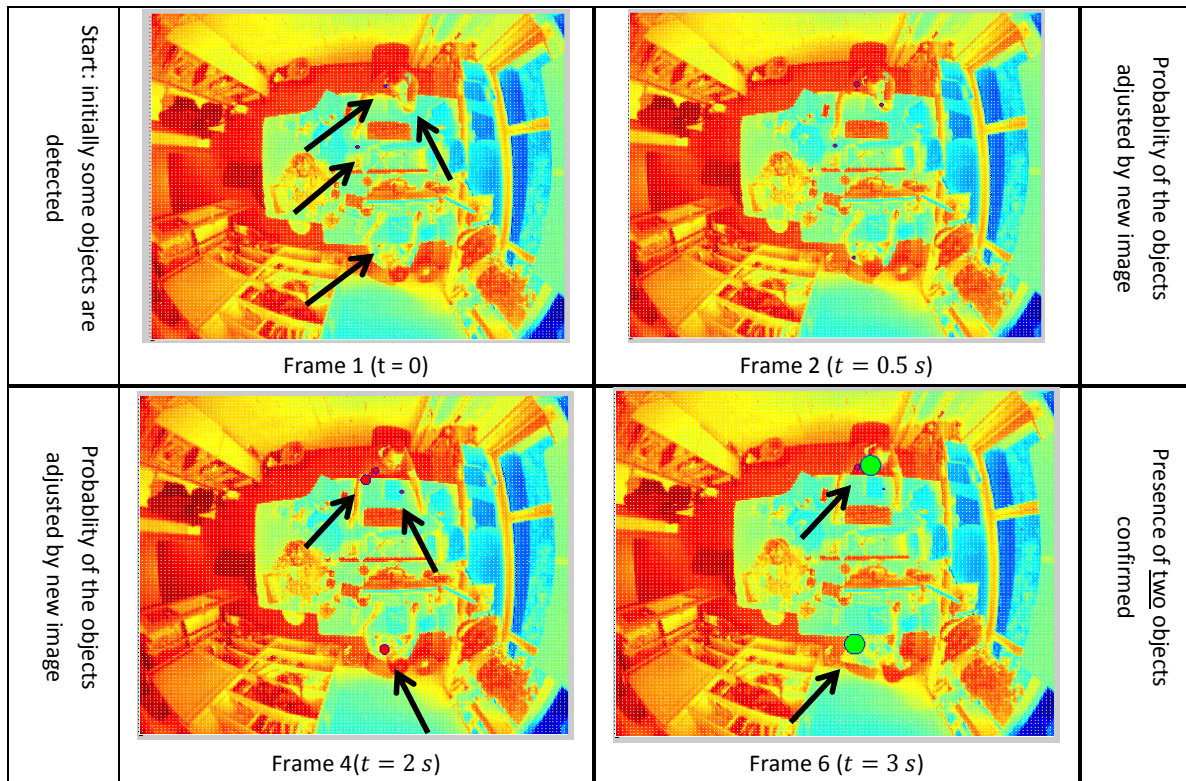


Figure 3.11 – The moment when the algorithm is activated and the office occupants are both present.

In Figure 3.13, the process of detecting the presence of a new occupant is elaborated. The most explanative frames are selected. It takes 4 seconds for our algorithm to detect the presence of a new occupant. Since s/he moves too fast for the tracking system, a new object is created as s/he moves from the entrance to the workstation (Frame 129). The probability of the old object (#1 in Frame #131 and #161) is reduced as its existence is not reconfirmed by new measurements in the next frames; it is turned to red (not present) and is finally removed.

The result of solving the ghost movement detection is explained below. In Frame 197, the probability of Object #2 is lower than the one in Frame 161 (smaller green circle) since it might have remained unmoved or undetected. However, in Frame #225 (after 27s), it is moved once again and its presence probability is increased accordingly.

Figure 3.12 shows that two separate objects are associated to the movements of the hand and the head of the occupant.

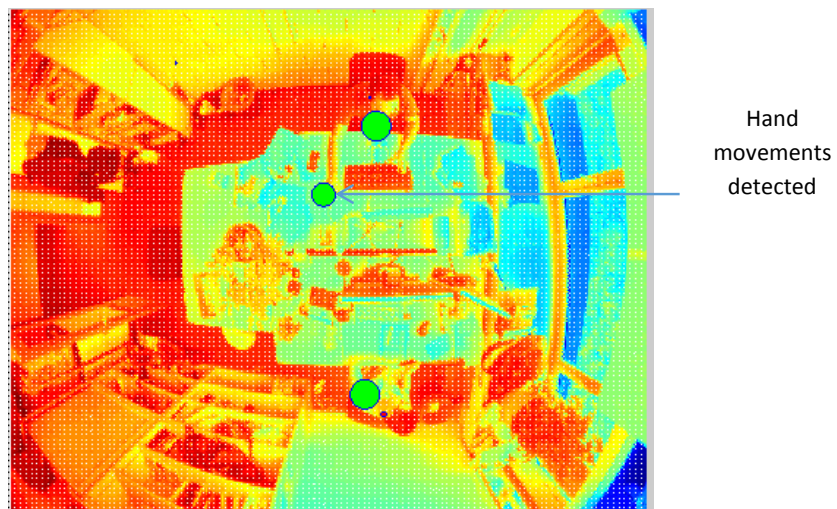


Figure 3.12 – subtle movements of occupant’s hand is also detected as a separate object.

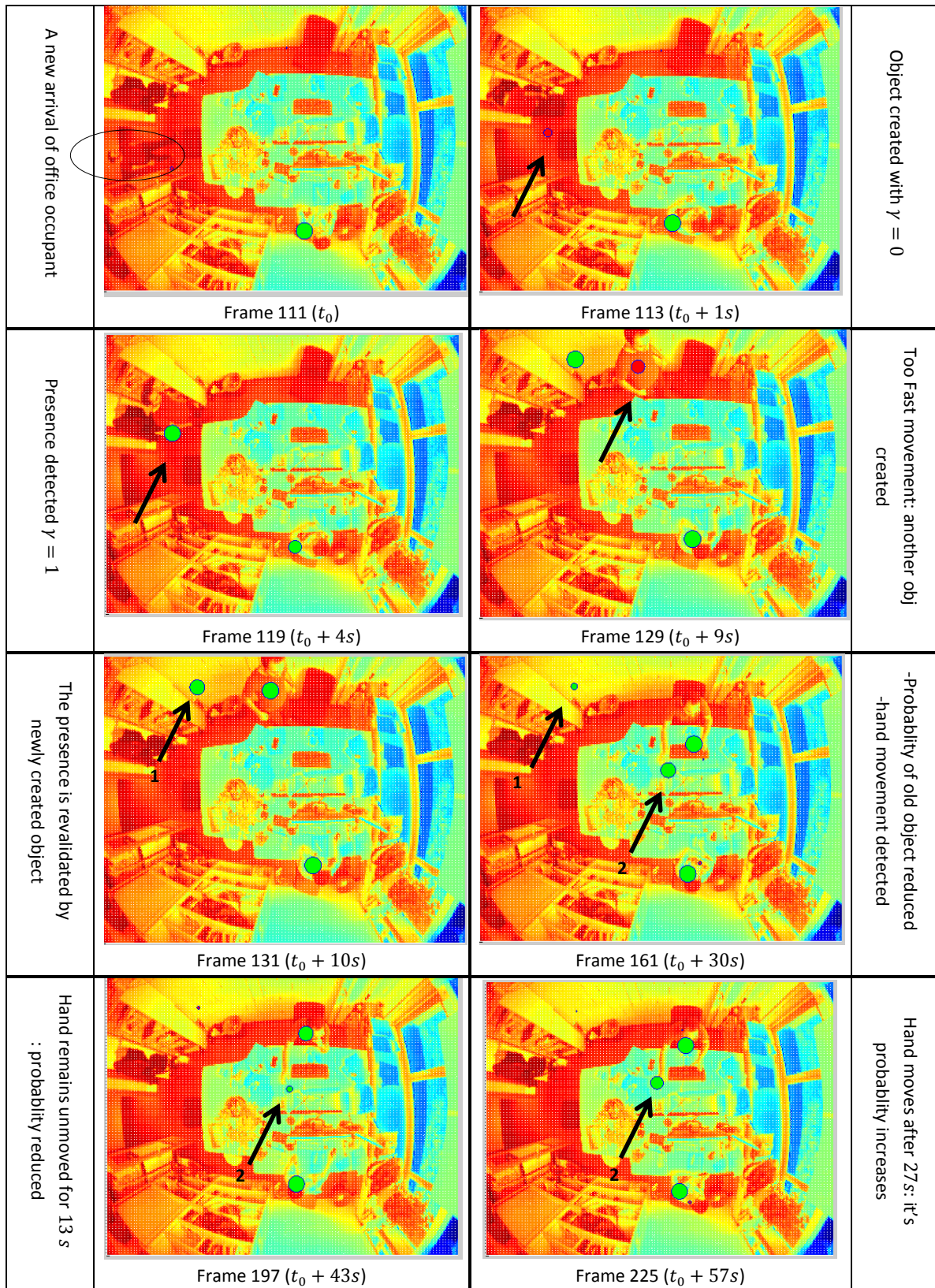


Figure 3.13 – Process of detecting a new arrival and continuation of detecting him or her even if s/he exhibits “ghost” movements.

3.1.1.7. Validation

On May 18, 2016, a full day experiment is carried out and the results of the proposed solution are validated against ground true data. The occupants of the office are asked to note their arrival and departure on a piece of paper hung up at the entrance. The data are captured from 9 AM till 5:30 PM. The office LE001 in the LESO experimental building has two office occupants that stay in the office room during the normal working hours.

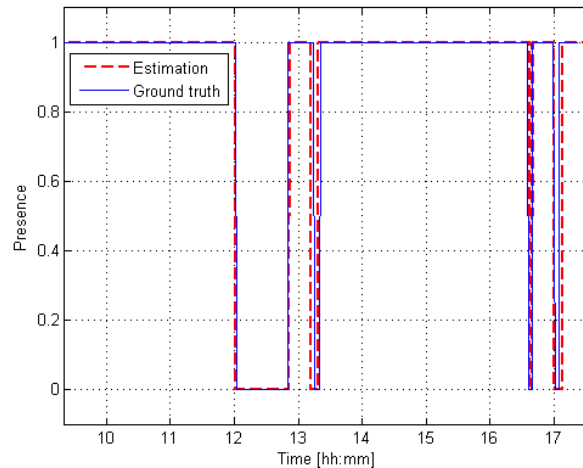


Figure 3.14 – Validating the presence detection algorithm by means of comparison with the ground truth.

3.1.2. Electric Lighting

The electric lighting system is identical in the two office rooms. It consists of LED based dimmable lighting fixtures and can be commanded manually or automated. It was designed to complement the daylight during early morning and late afternoon working hours. The offices are not foreseen to be occupied outside working hours: for this reason, the maximum horizontal illuminance provided by the lighting system alone corresponds to the lowest recommended value in the norms [142] and delivers around 300 [lx] in the work plane at full power. The control algorithm for the dimming of the electric lighting is detailed in Appendix D. The dimming feature is applied for the long-term experiments (Section 5.3); while for the short-term subjective assessment (Section 5.2), the on/off approach is adapted.

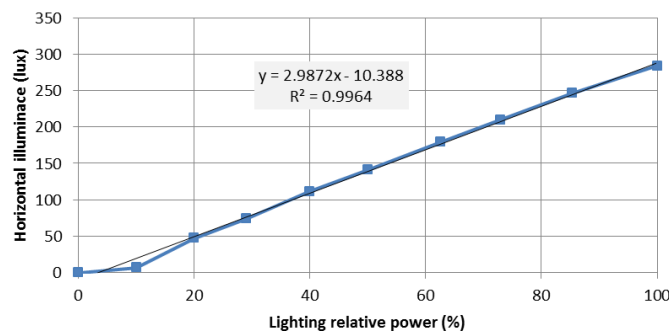


Figure 3.15 – Horizontal illuminance in the advanced office room as a function of relative power. The error of the illuminance readings is 1% (Table 4.5).

Based on the simulation performed by Regent Lighting, the UGR index in the intended office rooms remain below 18.9 measured at the height of 1.2 [m].

3.1.3. Control Platform

The KNX network communication protocol, a standardized EN50090 network developed based on a European Installation Bus (EIB), was first installed in the LESO building in 1999; as reported by Lindelöf [20], 240 connected devices were integrated in the communication system as of August 2004. Today, this building features 237 sensors and actuators that generate information on 716 different logic addresses on the KNX field bus. For each room of the building, these

inputs control or give information on [157] air temperature, occupant presence, lighting level, shading, heating, electric lighting and occupant interactions with switches.

3.1.3.1. Communication Platform Layout

An ad-hoc control platform was set up by the author to guarantee appropriate data acquisition and logging, flawless initialization as well as actuator commanding. The topology of this system is shown in Figure 3.16: it is installed on a PC labeled “Control Platform” (#1 in Figure 3.16). This PC performs the on-the-fly data acquisition, hosts the controller, sends the commands to the actuators and finally, logs the corresponding data. In other words, the whole procedure described in Figure 3.17 is hosted by this *Control Platform*. The data transfer between relay units and the control platform is carried out through the “mapped drive” technique provided by MS Windows; it is the most robust method for data synchronization between different Windows platforms through internet. The ad-hoc system shown on the left communicates with the buildings KNX system shown on the right through a data bridge named MyHomebox manufactured by Ergo3 [164].

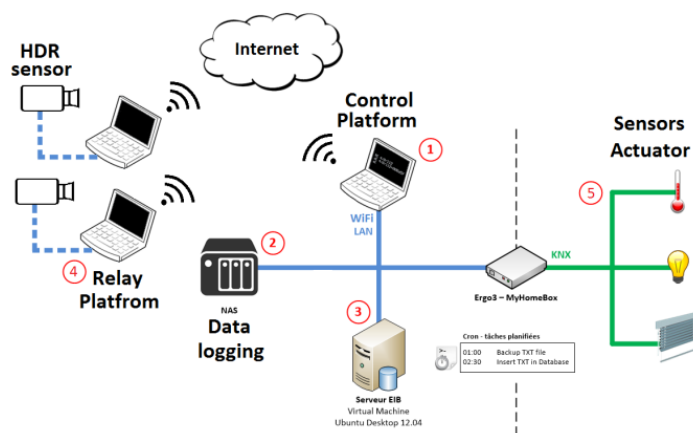


Figure 3.16 – Layout of communication platform for the experimentations in LESO building. The ad-hoc system on the left communicates with the building’s KNX system, in the right, through a data bridge named MyHomebox manufactured by Ergo3 [164].

This ad-hoc system is suitable for rapid prototyping of the control algorithms in MATLAB environment in a laboratory setup. However, for integrating the HDR vision sensor in the BMS in a marketable format, direct integration of the sensor (without dependency on any relay platform) is indispensable. Development of such system is out of the scope of this research study and is postponed to the further development phases of the project, potentially in collaboration with an industrial partner.

3.1.3.2. Control Platform Execution Block Diagram

The control platform was designed and set up based on the following principal strategies:

- Data should be registered as received by the master platform in order to avoid a loss of information if any unforeseen problem occurs. They should be stored in a folder with an easily recognizable label.
- The platform should be flexible enough to allow for the introduction of any type of new control strategy. In other words, the platform should manage the input data to the controller and retrieve the output data from the latter in a structured standard format. This flexibility allows the platform user to introduce his controller in a time efficient manner by including only one file (the controller) in the predefined location and to readily evaluate its functionality. On the other hand, masking the physical and logical addresses of the actuators and the sensors with “user-friendly labels” eases the utilization and reduces ambiguity; this feature allowed an easy installation of the control system in the Fraunhofer ISE daylight testbed (Chapter 6).
- The platform should be flexible enough to accommodate a timely efficient introduction or elimination of a sensor and/or an actuator.

- The control platform should have a “control panel” with an accessible code location (evidently at the beginning) so that the user has the opportunity to modify the key parameters of the platform in a straightforward way without exploring the whole platform.

Finally, an appropriate structure and classification for the files managing sensors and actuators is needed to lead to faster debugging and tuning of the control platform.

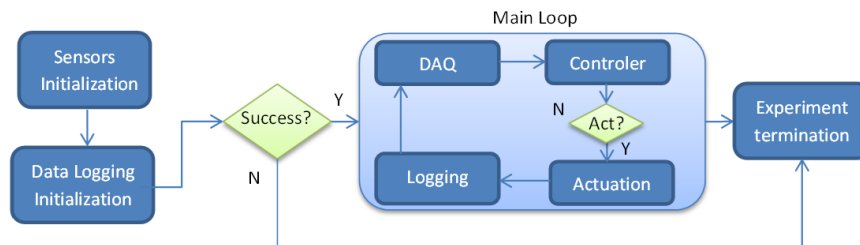


Figure 3.17 – Block diagram of the control platform for advanced and reference controller in both short term (Section 5.2) and long-term (Section 5.3) experimentations.

The *sensor initialization* block illustrated in Figure 3.17 allows the platform to verify if all sensors are operating and that an access to the sensor readings is established. The control platform requests a sample to the relay platforms and by examining it determines whether the HDR vision sensors are properly functional. On the other hand, the shading system is initialized and fully raised to mark the initial state. The status of the electrical lighting is also recorded.

The *main loop* block contains four action blocks and a conditional one. The DAQ block prepares the input data for the control block. This block verifies the data correctness by comparing them with the expected ranges. In the next step, the control block generates the appropriate command for the building actuators based on the algorithm loaded in the initialization section.



Figure 3.18 – *Phobio* module in the LESO building, used basically as dark room for calibration of the HDR vision sensor. The luminous panels (Section 4.6) is designed originally for emulating the daylight through the test room’s window

A decision-making procedure is carried out next to find out if the generated command should be actually executed or not; this process is based on several principles, such as:

- The actuation should not be carried-out more than certain number of times per day, since too many amendments of the lighting and sun shading would annoy the office occupant.

- ii) The controller applies the control action provided that the amendment of the shading position is larger than a given threshold. For instance, if the newly proposed sun-shading relative position differs from the current one by more than 30%, the new command is passed to the shading actuators.

In the actuation phase, the commands are sent through the KNX network insuring that they are consequently executed. In any case, the whole acquisition data and the input and output variables of the controller are stored on a local hard disk. As soon as the conditions for ending the experimentation are met, the main loop ends and the whole data registered on the local hard disk are copied into a database located on an EPFL server so that the risk of data loss is minimized.

3.1.4. HDR Vision Sensor Calibration Test Room

The majority of the HDR vision sensor calibration procedure (Chapter 4) takes place in the a thermally isolated chamber named “Phobio” located in the LESO building (Figure 3.18). This chamber was used principally as a dark room. The luminance panels used in Section 4.6 were originally built for emulating the daylight passing through the chamber’s window for several human centric lighting experiments.

3.2. Daylighting Test Environment in Singapore

In this section, three testbeds that were used during an exchange program in Singapore ETH Center (SEC) are detailed. The objective is to evaluate the influence of different designs on indoor daylighting condition and discomfort glare perception. The results of the experiments carried out in these testbeds are presented in Section 4.7. The role of each testbed in this experiment is listed in Table 3.2.

Role	Reference case	Advanced case
Testbed	SinBerBEST testbed (Section 3.2.1)	3for 2 Building (Section 3.2.2)

Table 3.2 – Label and role of the testbeds in Singapore used for facade lighting performance.

The main difference between these testbed is the design of their facade:

- i) Vertical facade with no shading or any special architectural design, named SinBerBEST, it is considered as reference case and detailed in Section 3.2.1.
- ii) Novel facade design for tropics by Prof. Arno Schlueter and his team [165], tilted facade, named 3for2 and elaborated in Section 3.2.2.

This scientific sojourn was financed by the Zeno Karl Schindler (ZKS) foundation and took place in January 2017.

As sensing equipment, the following sensors are used:

- i) DGP: The recent version of the HDR vision sensor, VIP, presented in Section 4.2.2 is used for these series of experiments.
- ii) Illuminance [lx] : For evaluating the reference illuminance at the height of 1.5 [m] in the inner side of the facade ($E_{h_{facade}}$) in the two environments, a Konica Minolta illuminance meter (T-10A) is used. The horizontal illuminance in the SinBerBEST testbed were measured using an EKO Instruments Co. luxmeter (model ML-020SO) characterized by a measuring range of 0 to 150,000 [lx] and a spectral relative error (f'_1 by Eq. (4-5) [166]) of 2.3%.

3.2.1. Singapore-Berkeley Daylight Testbed

The Singapore Berkeley program (SinBerBEST), funded by the National Research Foundation (NRF) of Singapore and headed by Professor Costas Spanos, is one of two core research programs within Berkeley Education Alliance for Research in Singapore (BEARS). The BEARS was established in 2011 by the University of California, Berkeley as a non-profit company. SinBerBEST is an interdisciplinary group of researchers from UC Berkeley, Nanyang Technological University (NTU), and the National University of Singapore (NUS) who come together to make an impact with broadly

applicable research leading to the innovation of energy efficient and sustainable technologies for buildings located in the tropics, as well as for economic development [167].

In SinBerBEST, there are two identical office rooms equipped with a high performance daylight emulator that has the ability to portray varying weather conditions ($10 \cdot 3 [m^2]$, max $40 [klx]$ and $2'400 - 10'000 [K]$ variable Correlated Color Temperature (CCT)) together with a lighting and shading monitoring and control facility (Figure 3.20). The emulator is composed of 50 LEDs of $2400 [K]$ and 50 LEDs of $10'000 [K]$, each consuming $3W$ at full power, that are placed on a mechanically ventilated panel. The windows of the testbed are covered with diffuse panels so as to smoothen the light sources created by point LEDs.

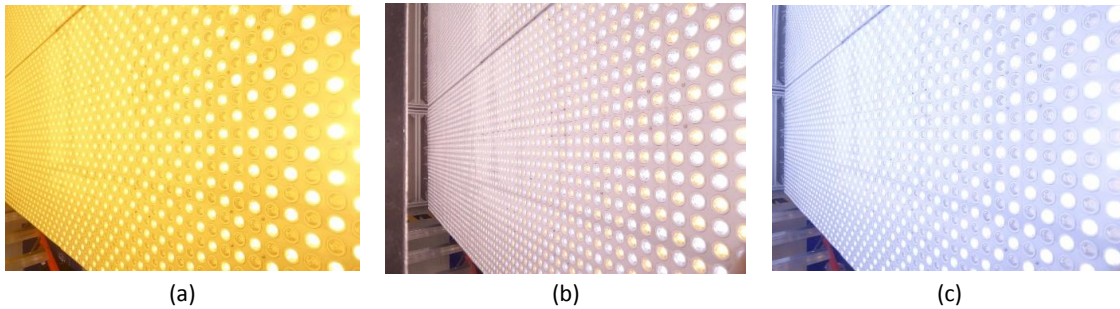


Figure 3.19 – LED-based daylight emulator in SinBerBEST testbed; (a) Only 2400 K LEDs are on in full power; (b) both 2400 and 10000 K LEDs are on in dimming mode; (c) Only 10000 K LEDs are on in full power

One of these office rooms is only used for the present project and equipped with large windows and non-coated glazing; it can be used as baseline for a daylight performance assessment of a facade and compared to the other daylighting facade designs. There is only a table and a chair in the deepest part of the room. The dimming level of the emulator's LEDs are chosen in a way that $E_{h_{facade}}$ and the CCT are comparable to the ones recorded in the advanced case (3for2 board room).

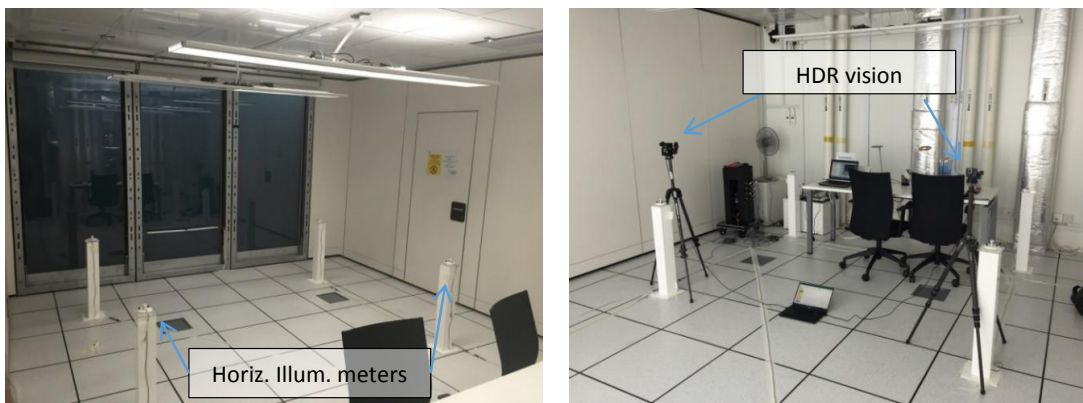


Figure 3.20 – The SinBerBEST daylight testbed equipped with 6 horizontal illuminance meters and two HDR vision sensors.

The position of the stationary horizontal illuminance meters are illustrated in Figure 3.21 by red rectangles and placed at the height of $0.8 m$ from the ground; they are labeled by s_i where $i \in \{1,2,3,4,5,6\}$. The HDR vision sensors, however, were moved from one location to another during the experiment and placed in 9 positions s_i & m_j , $i \in \{1,2,3,4,5,6\}$, $j \in \{1,2,3\}$ and in 4 directions o_k , $k \in \{1,2,3,4\}$. The Konica Minolta illuminance meter was placed horizontally at the height of $1.5 m$, presented by green triangle in Figure 3.21.

Thus, in total $9 \cdot 4 = 36$ luminance maps are captured and 6 horizontal illuminance values are registered.

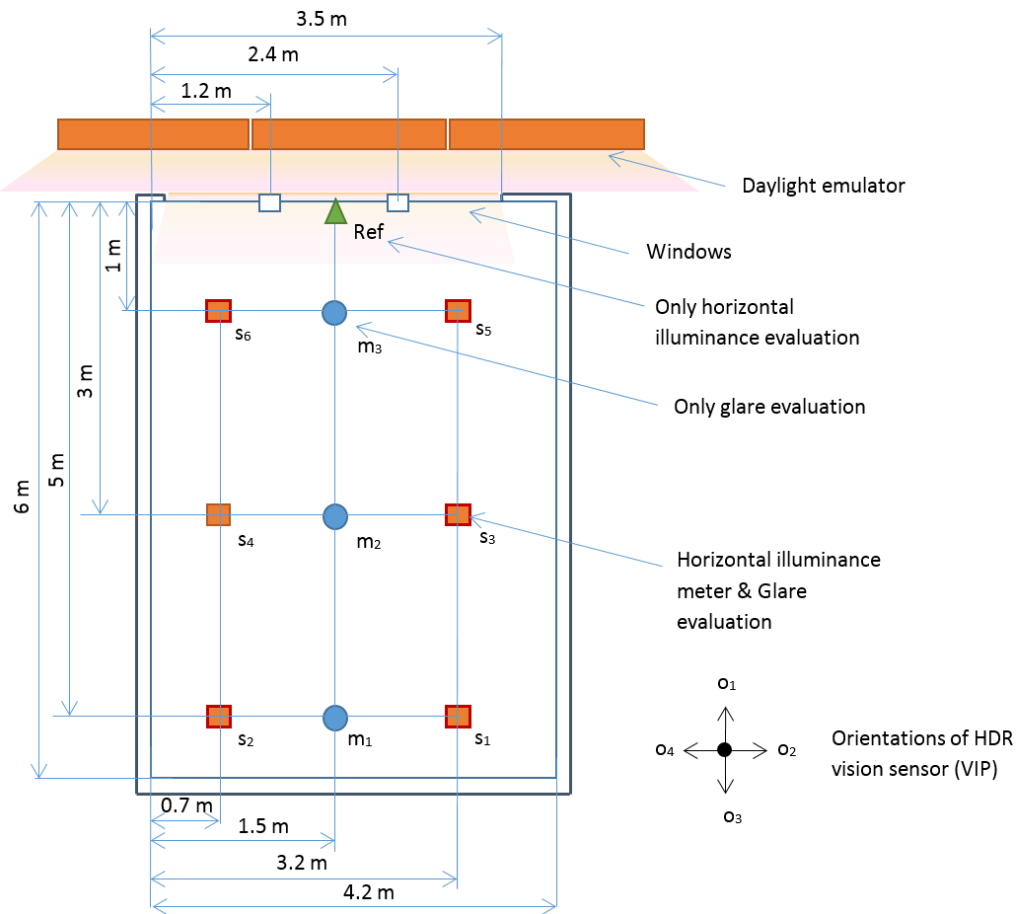


Figure 3.21 – SinBerBEST daylight testbed floor plan; position and orientation of the horizontal illuminance meter (s_i) and HDR vision sensors (m_i & s_i) as well as their labels. The HDR vision sensors take 4 orientations (o_i). The reference sensor is placed next to the window and is represented by a green triangle.

3.2.2. 3for2 Building

With a focus on reducing the necessary size of the services plenum, an alternative paradigm for the optimization of space, material, and energy use in buildings is proposed by Schlueter et al. [168], [169]: a holistic integration of all building systems – structural, mechanical, and electrical. The authors address the increasing pressure on future cities, especially in the dense mix-use developed areas in Singapore, in terms of limited space and resources, by introducing a novel decentralized HVAC concept.

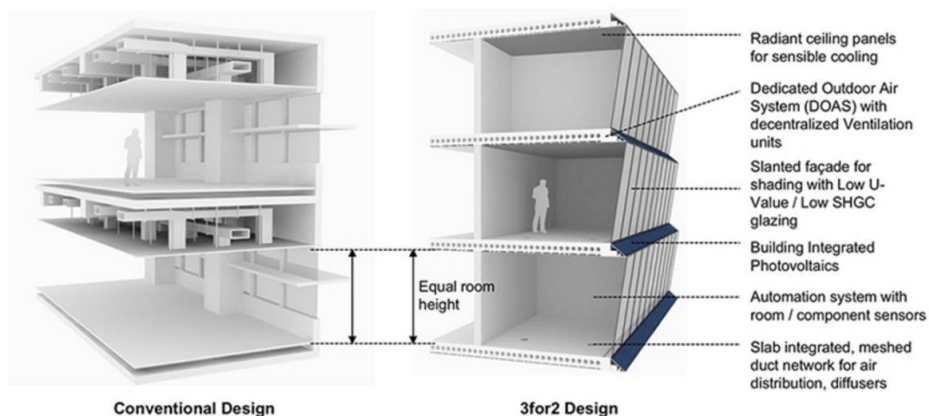


Figure 3.22 – Conceptual schematic of an idealized 3for2 building section compared to a conventional building section [168].

Despite the impact of ceiling plenums shielding a building’s mechanical and electrical installation from the occupants’ view on building material use, space intensity, and energy consumption, this design continues to prevail. In fact, typical floor to false ceiling heights are approximately 2.8 [m] and the height of the ceiling plenum can reach 1.5 [m] on average. One needs only to imagine the alternative to this system to understand the adverse effect of this conventional design: a high-rise building that altogether eliminates any functional need for plenums or dedicated floor spaces for air handling equipment and electric installations, while still providing energy services in an efficient, architecturally-appealing manner. This principle is at the core of the “3for2” design concept for high-rise buildings (see Figure 3.22). The 3for2 pilot building at United World College of South East Asia (UWCSEA) in Singapore was completed in 2015. Rysanek et al. [165] observed in this building that a decentralized ventilation system comprising both recirculating and dedicated outdoor air fan coil units may reduce daily electricity requirements for air-conditioning in Singaporean office spaces by over 15%. The present study, detailed in Section 4.7, evaluates this novel design from the daylight performance point of view.

The concept of using an illuminance ratio to quantify the amount of daylight in buildings has at least existed since around 1909 when Waldram published a measurement technique based on the approach [170].



Figure 3.23 — Outdoor and indoor view of the 3for2 building. The reference horizontal illuminance is at the height of 80 [cm].

The HDR vision sensor (VIP) is placed at predefined positions (m_i & s_i) as shown in Figure 3.24. This room is normally used for meetings in UWCSEA. Four orientations (σ_i), at each measurement point, are covered in this experiment.

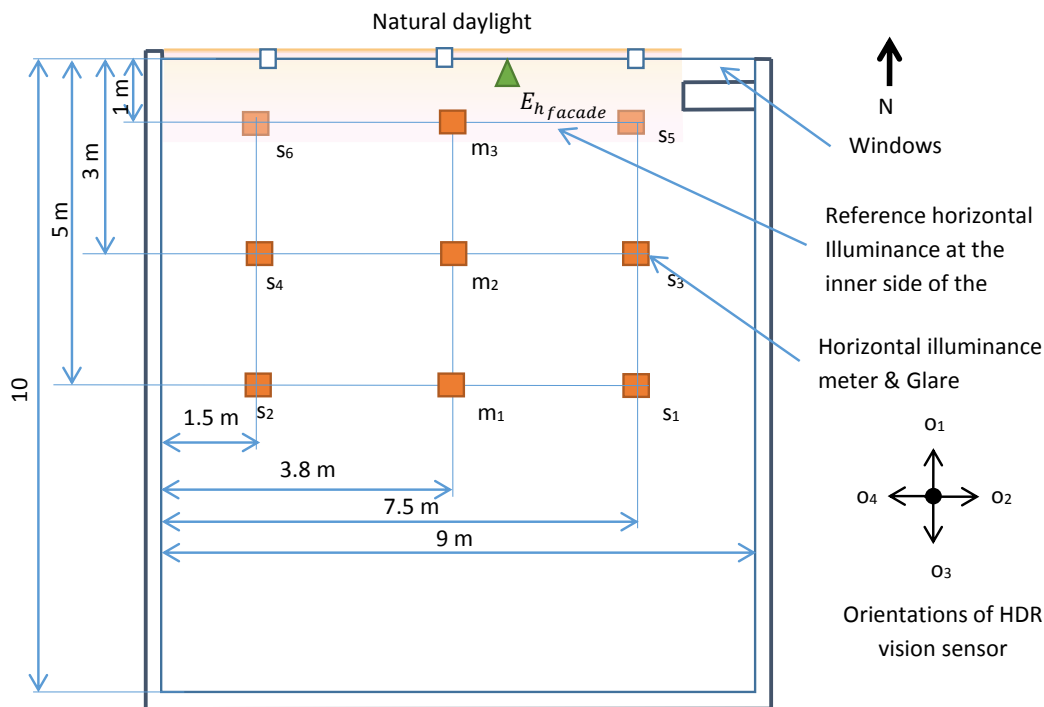


Figure 3.24 – The 3for2 board room (Singapore), horizontal illuminance and DGP index are evaluated at points m_i & s_i . The VIP, used for glare assessment, is placed in four orientations o_i . Reference horizontal illuminance is measured at the inner side of the facade at the height of 1.5 m

3.3. Daylight Testbed in Fraunhofer ISE

In this section, the daylight testbed located at the Fraunhofer Institute for Solar Energy (ISE) in Freiburg i B. (Germany) is presented in detail. This facility was used during the 9 months of an exchange program supported by the ZKS foundation. The control strategy and the experimental results are presented in detail in Chapter 6.

3.3.1. Rotating Testbed

The rotating testbed is located on the rooftop of building H of Fraunhofer Institute for Solar Energy Systems (ISE) at a latitude and longitude of $48.010650^\circ N$ and $7.834241^\circ E$ respectively. It can be rotated *over* 360° to allow the emulation of office rooms with the different facade orientations. The room's facade is fully glazed with a color-neutral sun protecting double glazing with a light transmission of $T_{\perp} = 54\%$, a U-value of $1.1 [W \cdot m^{-2} \cdot K^{-1}]$, and a Solar Heat Gain Coefficient of 29%. The Window to Wall Ratio (WWR) in the configuration shown in Figure 3.25 is *about* 89% [17]. The test facility is split into two identical rooms 3.65 [m] wide and 4.6 [m] deep with a suspended ceiling located 3 [m] above the floor. For a comprehensive description of the testbed, one may refer to a recent publication by Katsifaraki et al. [74].

The floor plan of the testbed and the location of the workstation and sensor are illustrated in Figure 3.27. The monitoring system is based on a fieldbus system connected with the main computer, which operates as both a data logger and the controller. The system is further connected with the Fraunhofer ISE network through an Ethernet connection for weather data acquisition, monitoring and maintenance purposes.

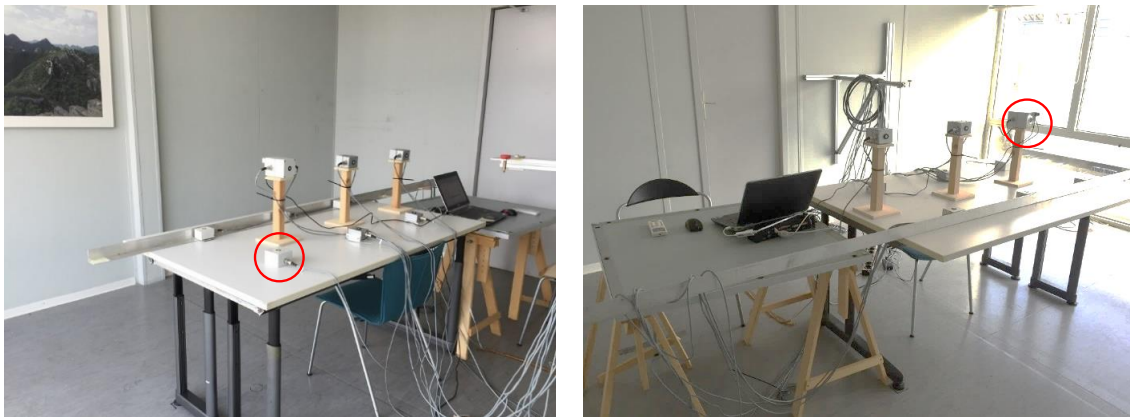
Even though there are two identical office rooms in this testbed, there is only a single shading command available for the two offices. For this reason, the second room is not used during this experimentation. One of the advantages of the testbed is that it is unoccupied allowing for experimental testing without perturbations and improvement of prototypes of the controller without the concern of disturbing the occupants or neighboring offices.



(a)

(b)

Figure 3.25 – The testbed at Fraunhofer ISE composed of two identical rooms. The experimentation was carried out only in the left one.



(a)

(b)

Figure 3.26 – Daylight testbed, equipped with horizontal and vertical illuminance meters. The one used in this experiment is encircled in red; (a) horizontal luxmeter; (b) HDR vision sensor for *DGP* index assessment.

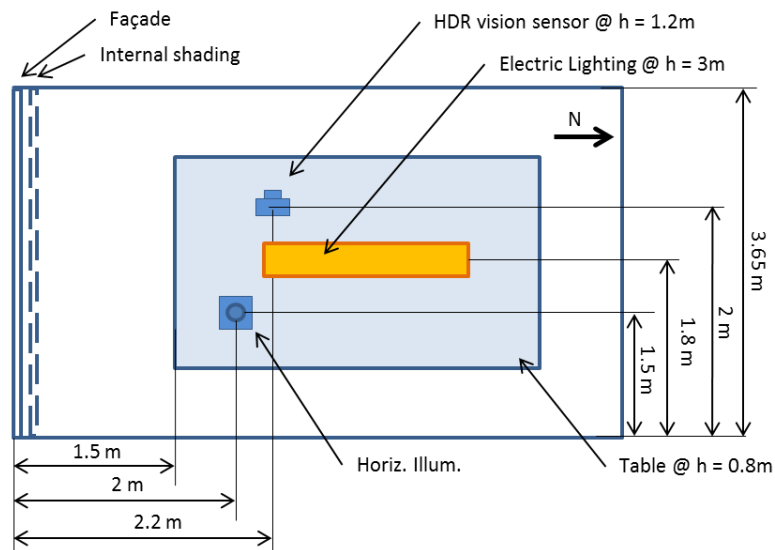


Figure 3.27 – Floor plan of the daylighting testbed on a building rooftop at Fraunhofer ISE. Only the sensors and actuators of this experiment are depicted.

3.3.2. Sensors of Daylight Testbed

The HDR vision sensor is located at the position shown in Figure 3.28 (b): the latter is close to one of the possible locations and orientations of an HDR vision sensor in the day-to-day life (e.g. on the VDT), once operating in a working environment. Moreover, in such an environment, the horizontal illuminance may be evaluated by a ceiling-mounted HDR vision sensor facing downward: a setup similar to the one used for a long-term monitoring in the LESO building.

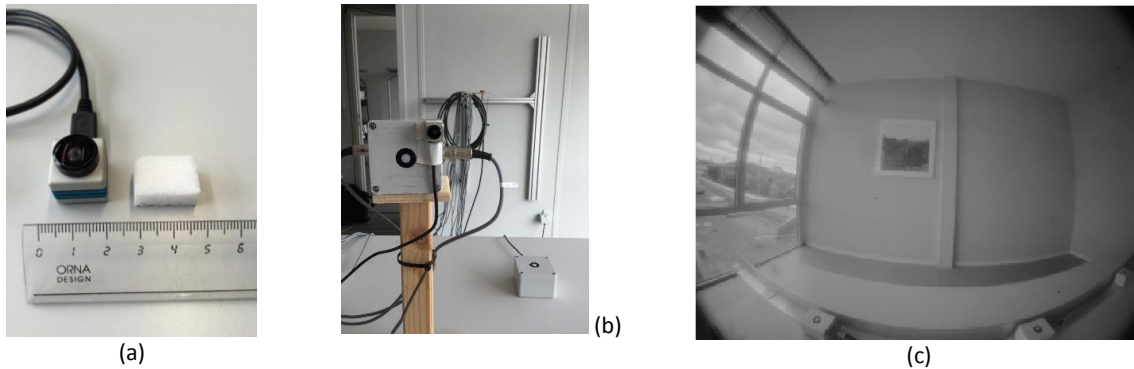


Figure 3.28 – (a) The HDR vision sensor (VIP); (b) Installation location of the VIP during the experimentation at Fraunhofer ISE; (c) sample images captured by VIP from its installation location in daylighting testbed;.

The testbed provides the following set of information in real time: shading position, six horizontal and six vertical illuminance values at numerous points scattered over a table. The illuminance meters are manufactured by Hagner (model SD2); their accuracy, as reported by the manufacturer, is equal to 3%. Considering the whole system including the signal amplification, the accuracy of monitored illuminances is about 5%. The global and diffuse horizontal irradiance are measured by a pyranometer manufactured by DeltaT (model SPN1), whose relative accuracy is estimated to be equal to $\pm 10\%$ over the 0.4 to $2.7 \mu\text{m}$ range. The slat angle of the venetian blind is not measured in the testbed. An internal variable keeps however track of the slat angle and is updated when a movement is recorded.

3.3.3. Actuators of Daylight Testbed

The control system commands the following actuators: shading position and shading slat angle as well as the dimming of the ceiling mounted electric lighting. The slat angles after a raising movement is equal to zero. Knowing this when the controller is launched for the first time, the blinds are slightly raised, i.e. at 5% of total height. Accordingly, the internal variable for slat angle is initialized to zero. The shading system, in its completely retracted state, covers still 30 cm of the window height. This configuration is visible in Figure 3.28 (c).



Figure 3.29 – The slat profile of venetian blind in the daylight testbed at Fraunhofer ISE.

A dimmable direct/indirect pendant luminaire equipped with two T5 fluorescent tubes with a nominal power of 98W is installed in each test cell. Connected to a Hager light actuator, a control signal is applied simultaneously to both cells. A dimming curve was drawn for the testbed based on the readings of illuminance Sensor #2 (Figure 3.26 (a)). The curve

and the corresponding equation, shown in Figure 3.30, are used as command by the controller for the lighting system knowing the horizontal illuminance shortage with respect to the target illuminance $E_{h_{ref}}$ (Eq. 3.10).

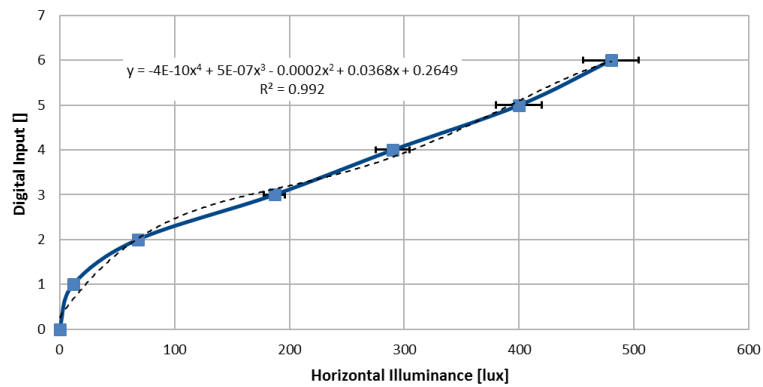


Figure 3.30 – Electric lighting dimming level with respect to the horizontal illuminance. Error bars are equal to 5% of the sensor reading (Section 3.3.2).

Chapter 4

HDR Vision Sensor

In this chapter, the first research question raised in the Section 1.3 is addressed:

- *How the notion of visual comfort and specially glare rating indices can be introduced to the BMS?*

In order to answer this question in a scientific manner, we had to perform sensor characterization, calibration and validation. The history of the HDR vision sensor in the course of this project is explained in Section 4.1. In the following section, 4.2, the most recent version of the sensor, named Vision-in-Package (VIP), is characterized and calibrated. The calibration result is validated in a joint project with Laboratory of Integrated Performance in Design (LIPID) [171] and elaborated in Section 4.3. The author implemented the DGP index evaluation on the embedded processor of the two generations of the HDR vision sensor. The details of this development is presented in Section 4.4. Robustness and accuracy of the embedded software is demonstrated in Sections 4.5 and 4.6. In Section 4.7, the use of HDR vision sensor as a building facade characterization device is demonstrated. Finally, in Section 4.8, the author assesses how realistic it is to consider the readings from a stationary HDR vision sensor, installed in the vicinity of an office occupant, as an indicator of the actual exposure of the occupant to daylight.

This chapter is very technical in nature. At the end of this chapter, the reader is expected to know the sensor's characteristics and to understand the mechanism of a glare index evaluation through an embedded image processing algorithm.

4.1. Introduction

In this section, the adaptation of the HDR vision sensor to our use-case is explained. An overview of the collaboration between the Solar Energy and Building Physics Laboratory of EPFL (LESO-PB) and the Centre Suisse d'Electronique et de Microtechnique (CSEM), who developed the sensor hardware, will help the reader to better understand the instrumentation and experimental set-up used in this thesis.

This sensor offers a 132dB intra-scene dynamic range encoded logarithmically with 149 steps per decade while achieving a fixed-pattern noise (FPN) of 0.51 Least Significant Bit (LSB). Besides, its powerful system-on-chip (SoC) platform combines a front-end pixel with a time-domain logarithmic encoding and a variable reference voltage, a 32b processor, a graphical processing unit (GPU), 128KB of SRAM, and several communication interfaces allows performing concurrent image processing for calculating discomfort glare indices [172]. Each HDR image therefore provides a complete record of the magnitude and spatial variation of the luminance in the field-of-view [80].

Such system allows for on-the-fly capture and embedded analysis of the images without any dependency on an external agent for data analysis. Consequently, no sensitive information from the building leaks outside and accordingly the concern about the occupant's privacy can be properly addressed.

The first version of the HDR vision sensor, named IcyCAM (Figure 4.1 right), was delivered to LESO-PB in 2008. Apiparn Borisuit and her colleagues [38] calibrated and characterized the device and equipped it with a fisheye lens. The vision sensor available at the beginning of this doctoral thesis was able to perform some basic photometric measurements such as glare rating thanks to an ‘ad hoc’ software package running on a connected PC. The direct robust implementation of a glare rating software on a processor embedded in the IcyCAM was one of the main tasks achieved during this thesis, allowing to carry out the main experiments described in Chapter 5.

The author received the second version of the sensor, VIP, illustrated in Figure 4.1 left, from CSEM in September 2016. The VIP was already equipped with a fisheye lens. A complete calibration, programming and adaptation of the device to our control platform were carried out during this thesis. The exchange programs in Singapore ETH Centre (SEC) and Fraunhofer ISE benefitted from this new version of the HDR vision sensor. A summary of the experiments and the corresponding HDR vision sensor is given in Table 4.1.



Figure 4.1 – Left: new version of the HDR vision sensor named VIP; right: previous version, named IcyCAM.

Section	Experiment/activity	Testbed/location	Sensor
4.2	Sensor characterization & calibration	LESO	VIP
4.3	Validation of sensor calibration	LESO-LIPID	VIP
4.4	Embedded glare assessment development	LESO	IcyCAM
4.5	Robustness and accuracy test	LESO	IcyCAM
4.6	Uniformity and accuracy verification	LESO	IcyCAM
4.7	Sensor as characterization device	SinBerBEST, 3for2 (Singapore)	VIP
4.8	Optimal location of the sensor	LESO	IcyCAM
5.1	Short-term experiment	LESO	IcyCAM
5.3	Long-term experiment	LESO	IcyCAM
6	Self-commissioning efficient shading control	Fraunhofer ISE (Germany)	VIP

Table 4.1 – List of the experiments reported in this thesis and their corresponding HDR vision sensor.

4.2. Sensor Calibration

The new version of the HDR vision sensor, VIP, is equipped with a High Dynamic Range (HDR) photo sensor (S2 manufactured by Analogue Devices Corp.) identical to the one of IcyCAM. It benefits accordingly from a logarithmic response; it is equipped with a more powerful processor, is more compact and feature a fisheye lens with a wider opening angle. The sensors’ embedded system specifications are listed in Table 4.2.

Sensor	Year	CPU	Memory	Photosensor	Inertial sensor	Software
IcyCAM	2008	50 MHz, 32b [172]	128 Kb of SDRAM	S2 (132 dB)	-	Devise
VIP	2016	Cortex-M4 180 MHz	64 MB of SDRAM	S2 (132 dB)	ST LSM9DS1	uKOS

Table 4.2 – Specifications of HDR vision sensor prototyped by CSEM. IcyCAM is shown in Figure 4.1 on the right and VIP on the left.

4.2.1. Purpose of the Calibration

The sensor is not calibrated at all; its output does not quantify any physical properties of the captured light. For visual comfort indices assessment and building control application, it is essential that each pixel of the sensor returns the luminance of the observed part of the field of view regardless of the type and intensity of the light source and the position of the pixel on the image. To this end, the sensor needs to be calibrated spectrally, photometrically and geometrically.

4.2.1.1. Calibration Procedure

The steps for performing this calibration, inspired from Andersen [173], are as follows:

- i) The VIP output [grayscale] is mapped to radiance [$W \cdot sr^{-1} \cdot m^{-2}$] by means of a white light source in order to derive a mapping function (calibration curve).
- ii) The VIP raw spectral sensitivity function is obtained, using the previous curve, and employed to determine optimal photopic filter combinations.
- iii) The “Spectral calibration” is achieved using three gelatin-based organic filters manufactured by Roscolux following a procedure defined by Borisuit et al. [38]; they were previously tested with IcyCAM and verified with VIP to check their accuracy.
- iv) The “Photometric calibration” is performed to obtain the equivalent luminance from grayscale values.
- v) The “Geometric calibration” accounts for the vignetting effect and eliminates the light fall-off in the border of the image.

A list of sensors, light sources and light treatment devices is shown in Table 4.3. Their accuracies are based on those reported by the manufacturers.

4.2.1.2. List of Equipment

Device/Equipment	Application	Role	Output/Range/Accuracy
Vision In- Package (VIP)	Device to be calibrated, 4 devices at disposal	In all the steps	(320 × 240) pixel image [grayscale], 0 to 1024, to be determined
Halogen quart-tungsten lamp	Stable light source	Spectral calibration	Light beams
Monochromator	Transmitter of a mechanically selectable narrow band of wavelengths of light	Spectral calibr.	Wavelength 380-780nm; ±5%
Integrating sphere	Providing white reflecting surface as target	Spectral & photometric calibr.	-
Spectroradiometer JETI Specbos 1201	(il)luminance and (ir)radiance meter	Reference for Photometric calibr.	Luminance [$cd \cdot m^{-2}$], 2-7e+4, ±2% (1000 $cd \cdot m^{-2}$ and 2856 K)
Minolta LS-110 luminance-meter	Luminance meter	Reference for Photometric calibr.	Luminance [$cd \cdot m^{-2}$], 0- 999'900, ±2% of reading
Followspot KORRIGAN HMI 1200	Powerful Light source	Photometric calibr.	Light beams, 0 – 1.5e6 cd @ 7° beam range
Konica Minolta cr-210 Chroma-Meter	Organic filters sizing	Spectral calibr.	Chromaticity coordinates (x, y) 0 to 1; intensity 0-160% of reflectance; ±1%

Table 4.3 – List of the equipment used during the calibration process of HDR vision sensor.

4.2.2. Preliminary Testing

These tests were performed before the calibration procedure in order to have a better understanding of the functionality and performance of the VIP sensor.

4.2.2.1. Field of View

The field of view (FoV) of the vision sensor is essential to be determined for further image processing purposes. Moreover, the mapping function, which converts the pixel coordinates to angular distance from the optical axis, is needed for evaluating the size, location and luminance of the glare sources.

The FoV of the VIP sensor is equal to 167° vertically times 132° horizontally. The captured image has 320 pixels (columns) and 240 pixels (rows). In other words, in the horizontal direction, the resolution is equal to $167[^\circ]/320 [\text{pixels}] = 0.5218 [^\circ/\text{pixel}]$ and in the vertical direction is $132[^\circ]/240 [\text{pixel}] = 0.5513 [^\circ/\text{pixel}]$. In comparison to the IcyCAM, VIP has a larger field of view ($FoV_{IcyCAM} = 102^\circ \cdot 136^\circ$) with the same image size ($320 \cdot 240$), thus a lower resolution.

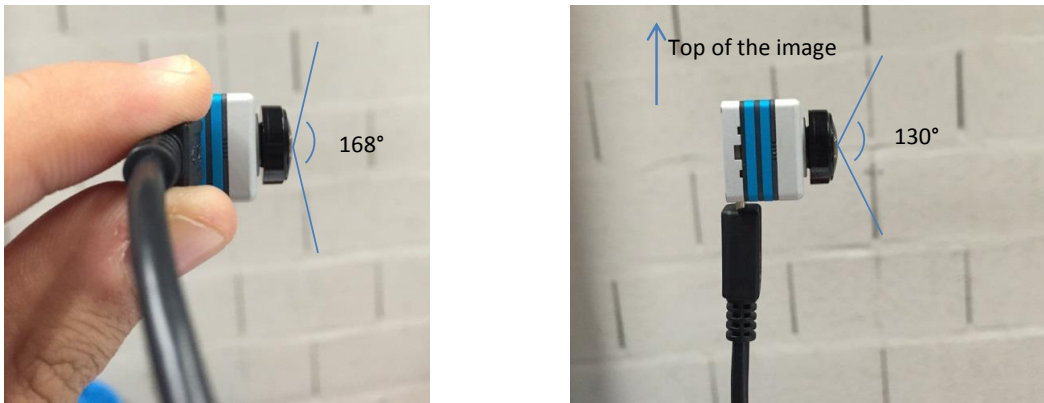


Figure 4.2 – Field of View of the VIP.

In order to measure the field of view of VIP, the HDR sensor was placed in front of a checkerboard of 10×8 B/W squares (Figure 4.3). The width and the height of each squared form on the checkerboard is $9 [\text{cm}] \cdot 9.6 [\text{cm}]$ ($H \cdot V$). The captured images, corresponding to two distances between the sensor and the checkerboard, are shown in Figure 4.4.

The sensor is placed in a way that the corner of a checkerboard's square is located on the optical axis (i.e. distortion center) of the sensor. In this case, the vertical and horizontal lines on the checkerboard passing through that corner (and the center of distortion of the image) remain straight lines. In this configuration, the calculation of the center of distortion, horizontal and vertical FoV is feasible.

The angular distance between the optical axis and a measurement point is determined by using Eq. (4-1), where $D [\text{cm}]$ is the distance between the sensor and the checkerboard. An example of $L [\text{cm}]$ is shown in Figure 4.4. The distance on the image, on the other hand, is measured in pixels and is calculated from the distortion center of the distortion.

$$\theta = \text{atan}\left(\frac{L}{D}\right) \quad L \in \{X_t, X_r, Y_t, Y_b\} \quad (4-1)$$

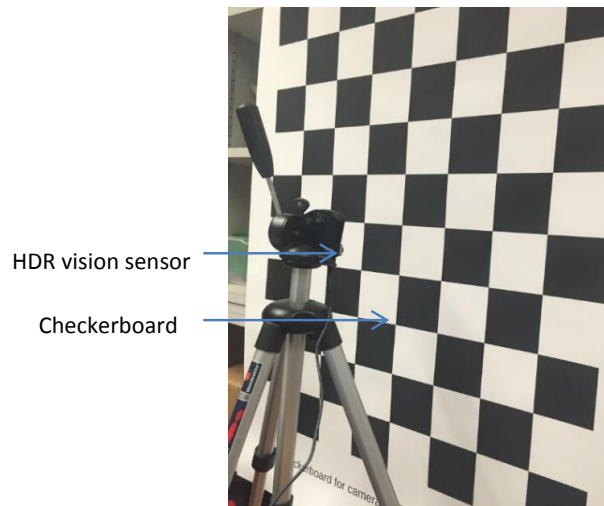


Figure 4.3 – Mounting the sensor on a tripod in front of the checkerboard for measuring its field of view and deriving the mapping function to convert pixel positions on the digital image to the angular distances from optical axis

The distance was varied between the checkerboard and the sensor so that a different angular distance could be produced. The result of the calibration is shown in Figure 4.5. These fitted curves are used later in the embedded software development to determine the angular distance from the optical axis by knowing the pixel position on the image. The curves intercept is not nil, e.g. -0.0394 in the vertical direction and $+0.7222$ in the horizontal direction. The misalignment between the image center and the optical axis of the lens was extracted using this information. This intercept corresponds to the equivalent of -0.07 pixels in the vertical and 1.38 pixels in the horizontal direction; these values suggest that the misalignments in the vertical ($\frac{0.07}{240} = 0.029\%$) and the horizontal ($\frac{1.38}{320} = 0.38\%$) directions are negligible.

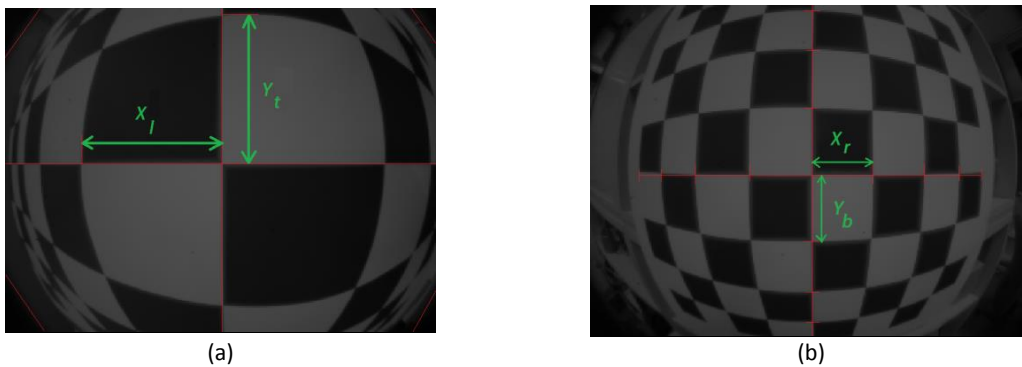


Figure 4.4 – Image captured by VIP for extraction of the mapping function, conversion of pixel coordinates to angular distances from the optical axis to determine the field of view; (a) small distance; (b) large distance between the sensor and the checkerboard. The red and green lines are added in the post-processing.

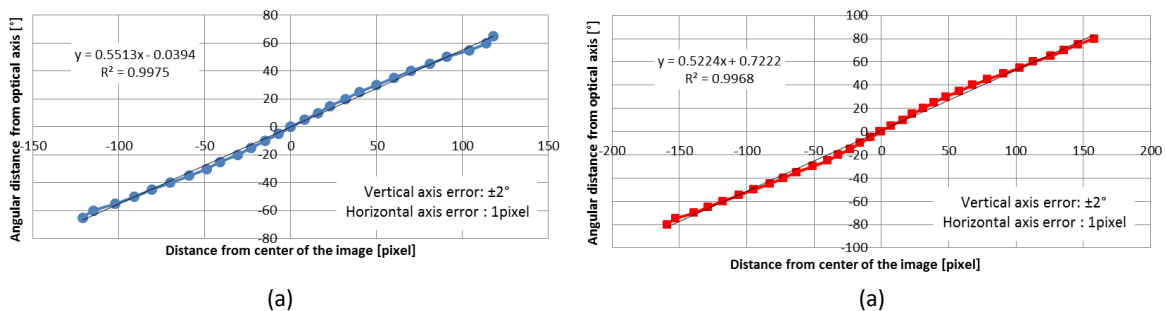


Figure 4.5 – The mapping function to convert pixel positions on the digital image to the angular distances from optical axis; (a) vertical; (b) horizontal.

4.2.2.2. Image Output

The output of the HDR vision sensor can be visualized in Figure 4.6. The organic filters used, issued from the spectral calibration, are, in this case, placed on the VIP sensor: the image comprises accordingly luminance values in a 10 *bit* mode.

It is essential to monitor pixel values in absolute darkness since the latter are used, as presented in Section 4.2.3, to derive the grayscale to radiance raw calibration function. In other words, it is essential to measure the pixel value corresponding to zero radiance.

It was observed that the temperature of two VIP sensors (VIP #1 and #3) in operation increases and stabilizes up to 58 °C. This phenomenon, per se, is not a real issue if the drift of the sensor, defined as the average values of all pixels monitored when the sensor is absolute darkness, does not vary significantly. This is not the case for the aforementioned devices as there is a temperature induced drift, even if the sensor's Digital Signal Processor (DSP) is during 98% of time in idle mode. The noise, defined as the standard deviation of the pixel values in absolute darkness, also rises in these cases; it is outlined using error bars in Figure 4.8. On the other hand, the temperature of the other two sensors (VIP #2 & #4) remains below 43 [°C] after stabilization; no temperature induced drift is accordingly observed (Figure 4.8, blue curve).



Figure 4.6 – Sample image captured by HDR vision sensor (VIP).

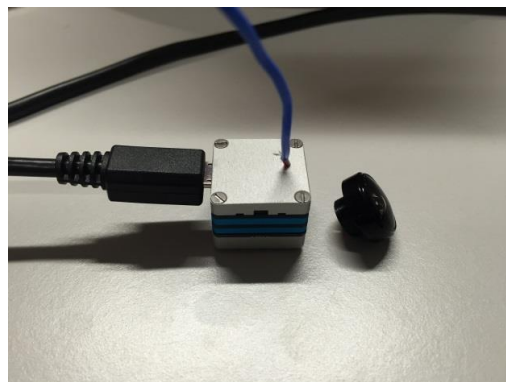


Figure 4.7 – Measuring the temperature of the VIP in absolute darkness; the sensor's fisheye lens is removed. It is placed against a flat surface (table).

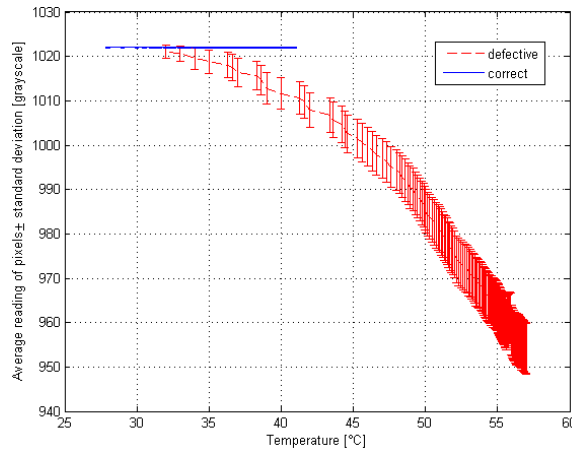


Figure 4.8 – Comparison of the drift in two VIPs, defective vs correct. Defective ones are subsequently repaired CSEM.

The upcoming stages of the calibration procedure were carried out using VIP #2 and #4, showing no temperature issues. The observed problem for VIP #1 and #3 was reported to CSEM. They received the defective sensors and returned them after repairing. The grayscale value equivalent to zero radiance is equal to 1022 for all devices. This is an important point that will be referred to for deriving Eq. (4-3).

VIP index	Steady state (after 20 minutes)			Current at idle mode(mA)	Board
	temperature (°C)	Average drift (grayscale)	Standard deviation of the noise		
1	58	68 (1022 → 954)	5.7	228	
2	40	0 (1022 → 1022)	0.03	92	
3	47	18 (1022 → 1004)	3.84	166	
4	41	0 (1022 → 1022)	0.15	107	

Figure 4.9. – Summary of overheating issues and problem statement for VIP #1 & #3.

4.2.3. Spectral Calibration

In this section, the steps applied for modifying the spectral sensitivity of the VIP are elaborated. To adapt its spectral sensitivity to human eyes, the raw spectral response of the device must first be determined and a combination of gelatin-based color filters selected according to it.

4.2.3.1. Grayscale to Radiance Function

Two sets of measurements were carried out by means of the setup illustrated in Figure 4.10. In a first step, the halogen light source emit a polychromatic light toward the input port of the monochromator, which filtered out all the visible radiations except for the user defined one within a 7 [nm] spectral range (Figure 4.12). The wavelength increment of 10 [nm] is chosen for this step based on the reason provided in Section 4.2.3.2.1. The quasi-monochromatic beam was

then projected on the internal surface of the Ulbricht sphere. The VIP sensor (e.g. #4) and the spectroradiometer were aiming at the same surface area labeled as target in Figure 4.10. By varying the power of the light source from 400 [W] to 1000 [W], radiance (R) of the target and grayscale value (GS) of the corresponding pixels were varied and recorded.

Figure 4.11 depicts the recorded data and the curve fitted to the data. Due to the high stability of the light source and the VIP sensor, the measurement error is lower than 0.1 % F . The correlation between the VIP pixel value and radiance measured by the spectroradiometer is given by Eq. (4-2):

$$R_{VIP} = 10^{-05} \times GS^2 - 0.0166 \times GS + 6.5055 \tag{4-2}$$

where R_{VIP} is radiance corresponding to a pixel of image captured by VIP [$W \cdot m^{-2} \cdot sr^{-1}$] and GS is the grayscale value [-] that pixel.

Although the correlation coefficient of the fitting curve is satisfying, this quadratic function does not return zero radiance for the grayscale of the absolute darkness ($GS = 1022$). This discrepancy would be problematic especially in the next step (spectral sensitivity) where the radiance of the quasi-monochromatic beam is considerably lower than the one of white light.

To address this issue, a “zero radiance” is introduced as one of the data points in order to ‘force’ the calibration curve to nil. Since the best fit of the new data set is a power function (thanks to trial-and-error and comparison of r^2 -correlation coefficient), the nil radiance couple of variables is introduced as $(GS, R)_{near\ zero\ radiance}$ equal to $(1022, 0.0003)$. The new fitting curve is depicted in Figure 4.11 (b).

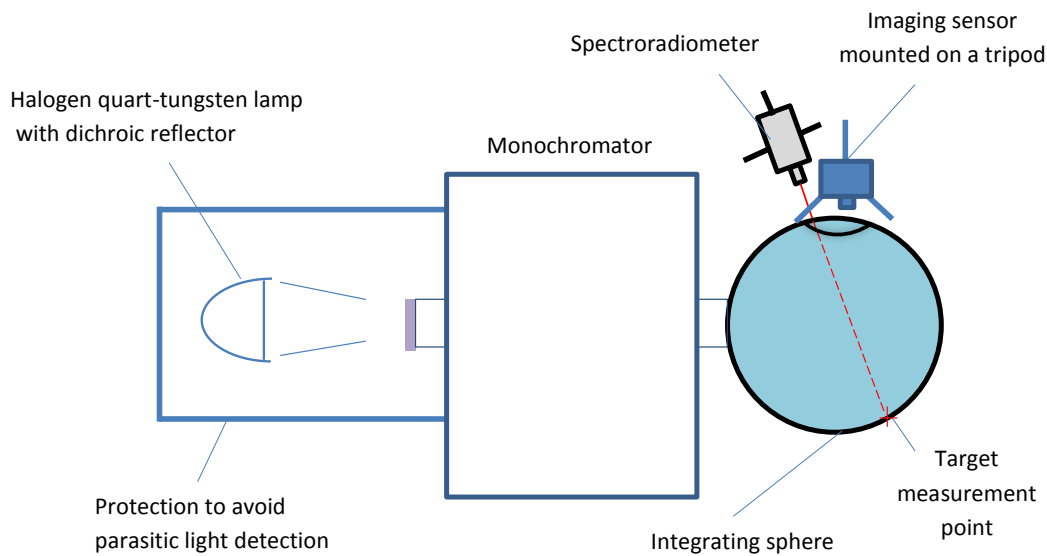


Figure 4.10 – Schematic representation of the experimental setup for spectral calibration, comparable to the setup used by Andersen [173].

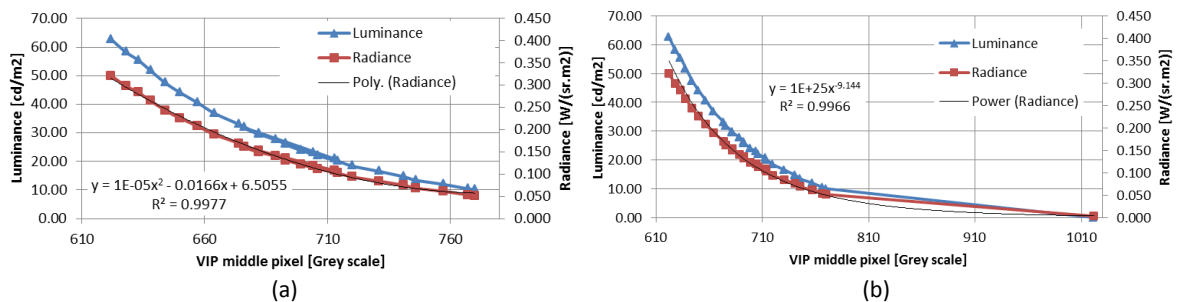


Figure 4.11 – VIP sensor #4 fitting curve in equivalent radiance and luminance. In this figure, the data point corresponding to 0 radiance is not considered; (a) without zero radiance; (b) modified with zero radiance.

Eq. (4-3) is the correlation between the grayscale value [–] of a pixel of an image captured by VIP and its corresponding radiance [$W \cdot m^{-2} \cdot sr^{-1}$] by including the ‘zero radiance’ value.

$$R_{VIP} = 10^{25} \times GS^{-9.144} \quad (4-3)$$

where R_{VIP} is radiance corresponding to a pixel of image captured by VIP [$W \cdot m^{-2} \cdot sr^{-1}$] and GS is the grayscale value [–] that pixel. This equation was used for curve fitting in the next step for determining the raw and corrected spectral sensitivity of VIP.

4.2.3.2. VIP Raw Spectral Response

4.2.3.2.1. Wavelength Increments

As shown in Figure 4.12, the Full Width at Half Maximum (FWHM) of the quasi-monochromatic beam measured by the spectroradiometer is 14 [nm] (peak ± 7 [nm]). Based on this observation, the wavelength increment for scanning the visible range was set to a slightly conservative value of 10 [nm] which leads to larger spectral overlap of consecutive beams.

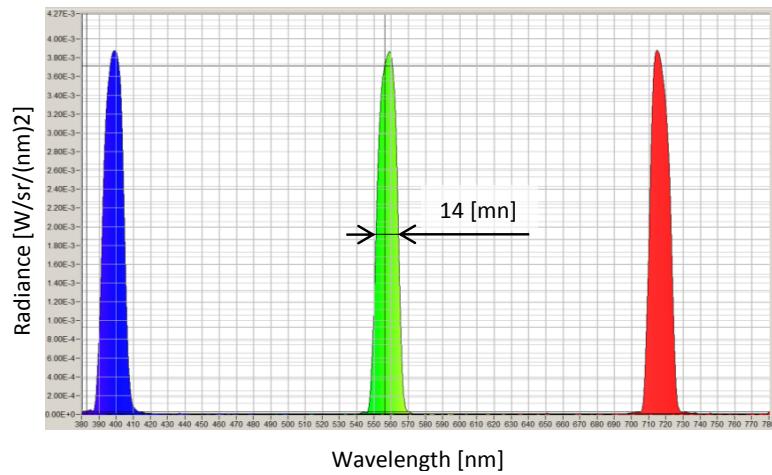


Figure 4.12 – Spectral distribution of the quasi-monochromatic beam measured for three different wavelengths. the Full Width at Half Maximum (FWHM) of the beam is 14 nm.

4.2.3.2.2. Spectral Sensitivity of the VIP #4

In this stage, the raw spectral sensitivity of the VIP #4 is evaluated. For this purpose, the monochromatic delivered a quasi-monochromatic light beam in the visible range of 380 – 780 [nm] with an increment of 10 [nm] while its corresponding radiance (R) and equivalent radiance (R_{VIP}) were experimentally determined using a spectroradiometer and a VIP sensor respectively. R_{VIP} is derived from Eq. (4-3) on the basis of the average of 15 pixel values corresponding to the target area. To compensate for the lower radiance of the monochromatic light flux, compared to white light, the entrance point of the light beam was taken as target in this case (Figure 4.13). The normalized spectral sensitivity $S_{raw}(\lambda)$ is determined using Eq. (4-4); it is illustrated in Figure 4.14 (b).

$$S_{raw}(\lambda) = \frac{(R_{VIP}(\lambda)/R(\lambda))}{(R_{VIP}(555 [nm])/R(555 [nm]))} \quad (4-4)$$



Figure 4.13 – Experimental setup for spectral calibration. The VIP and spectroradiometer are pointing toward the entrance of the integrating sphere so that sufficiently high luminances can be measured.

4.2.3.2.3. Correction Filters

A combination of colored correction filters was chosen to adapt the raw spectral sensitivity of the VIP sensor to the human eye response (photopic response curve).

To quantify the agreement between the corrected response of the VIP sensor $S(\lambda)$ and the photopic response curve $V(\lambda)$, the function f'_1 , defined by CIE [174] as “the degree to which the relative spectral sensitivity $S(\lambda)$ matches the $V(\lambda)$ or photopic action curve”, was used and evaluated according to Eq. (4-5).

$$f'_1 = 0.0093584 \sum_{n=1}^{N_\lambda} |S(\lambda_n) - V(\lambda_n)| \cdot \Delta\lambda_n \quad (4-5)$$

The constant 0.0093584 is valid for wavelengths expressed in $[nm]$; $\Delta\lambda_n$ represents the wavelength step between λ_{n-1} and λ_n .

Several filter manufacturers, such as Konica Minolta, PRC and LMT, were contacted to purchase organic $V(\lambda)$ correcting filters. It turned out that they only use glass filters due to their higher stability and precision, being less prone to drift due to high temperatures and moisture as well as their precisely controllable spectral transmittance. Moreover, their filters are customized and optimized for their type of sensors and do not necessarily meet our requirements. Moreover, these glass filters are not suitable for our own technical developments due to the compactness of the VIP design: there is only $1.3 [mm]$ of available space between the photosensor chip and the optical lens to implement the correcting filters while the minimum thickness of a glass filter is $1.2 [mm]$ and most probably, a combination of three glass filters is needed. On the other hand, for facilitating further a possible commercialization of this device, organic filters were also preferred for cost reasons.

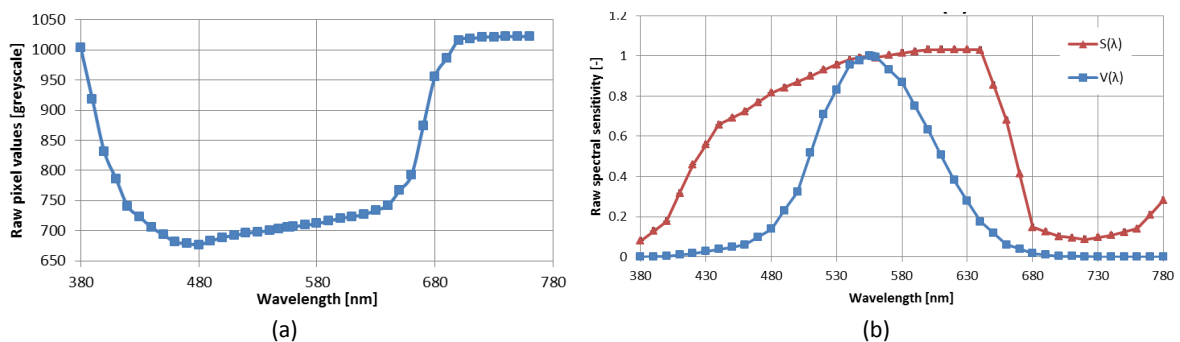


Figure 4.14 – (a) Raw spectral response of VIP #4 in grayscale; (b) normalized raw spectral sensitivity in comparison with photopic curve.

Borisuit [38], designed a glass-based filter with optimal thicknesses to correct the spectral sensitivity of the IcyCAM, reaching an error estimation f'_1 of 8.3%. She applied an optimization algorithm to derive the thickness of the three glass filters; as the VIP photosensor has the same spectral response as IcyCAM, the three glass filters were taken as starting point for developing the organic filters.

Several filters manufactured by Kodak, Roscolux and Gossen Filters were chosen and tested. Although the usual approach for filter dimensioning is to *optimize* their thickness so as to adjust their combined transmittance with the $V(\lambda)$ photopic response [173], [175], a trial-and-error method has proven to be faster and more effective than the optimization approach. The reasons are as follows: i) the transmittance curve of the organic filters would have to be manually introduced in the optimization software owing to the fact that their transmittance data are not available; this is a time consuming and inaccurate process, ii) Secondly, these data do not often correspond to the measured transmittance of filters, leading to undesirable errors and (iii) finally, the existing routine for filter thickness optimization [175] cannot be directly used since the thickness of the organic filters is fixed; the only remaining option is to include and/or remove them from the filter combination.

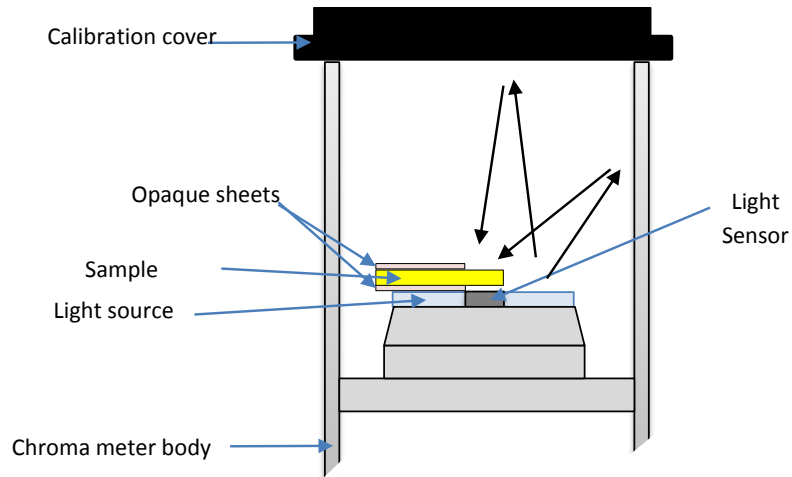
The option finally adopted was to select a combination of off-the-shelf available Roscolux filters. The company produces filters with 200 + colors made of two types of organic plastics. More than 65% of the product line is made of co-extruded polycarbonate foils; the remaining 35% are made of deep dyed polyester.

The main idea is that two filters with similar spectral transmittance have the same apparent color while exposed to white light. In other words, the author wanted to identify three Roscolux organic filters that had the same “color” and “transmittance” as the glass filters originally used for the correction of the IcyCAM sensor developed by Borisuit [38]. A comparison of these filters’ features could not rely only on human eyes due to the lack of precision, and metamerism of the experimenter’s eyes.

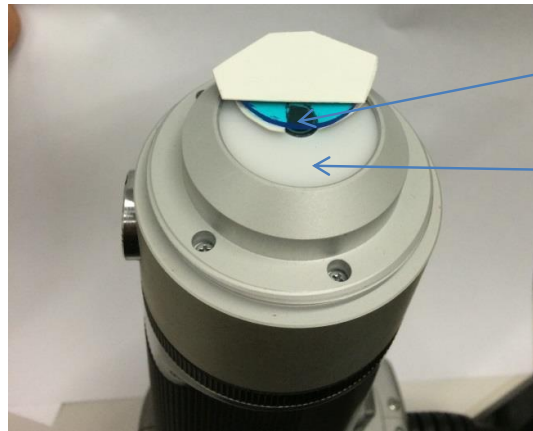
To address this issue, a calibrated cr-210 chromameter (last sensor listed in Table 4.3) was used as depicted in Figure 4.15. This device was originally employed for an accurate assessment of the color coordinates and reflectance factor of a given sample. In this experiment, the sample filter (gelatin- or glass-based) was placed between two opaque sheets covering its surface except for the part that is located right on the top of the photosensor. Finally, a calibration cover made of a bright white surface was used to close the device’s chamber. The white light flux generated by the light source was reflected by the calibration cover, passes through the sample filter and was perceived by the photosensor. Its output consisted of the CIE XYZ chromaticity coordinates (x, y) with triple significant digits and the luminance (Y) sensed by the photosensor; Y is directly proportional to the transmittance of the sample filter.

Table 4.4 summarizes the color matching procedure. The chromaticity coordinates of the reference filters as well as a combination of newly found organic filters (e. g. Roscolux filters R14+R3316+R386) are given in the same table. It shows an acceptable coherency between the CIE XYZ coordinates of glass filters (reference) and the organic filters (usable for the VIP sensor).

The filters were placed in front of VIP #2 sensor and its corrected spectral response was measured as illustrated in Figure 4.17. The f'_1 CIE error estimator is equal to 10.3%, which is slightly larger than the corresponding value observed with glass-based filters fitted on the IcyCAM ($f'_1 = 8.3\%$). It is worth noting that the overall response of the spectrally corrected VIP is significantly reduced in comparison with a plain VIP sensor; the equivalent radiance measured at 555nm ($R_{VIP555nm}$), close to the most sensitive part of the curve, corresponds only to 12% of the response obtained with a VIP sensor without filters. This low sensitivity might limit the applicability of a VIP in an equivalent case, such as presence detection in a low illuminance environment for instance. However, for glare rating, this low sensitivity might not be a problem as glare sensations are generally caused by very bright surfaces or light sources, such as the presence of the sun or reflections in the field of view.



(a)



(b)

Figure 4.15 – Setup for dimensioning the gelatin filters based on Glass filters optimized by Borisuit [38]. Minolta chromameter is used for finding out the color of the filters.

Filter	Borisuit [38]			R14+R3316	R386
	Blue	Yellow	Brown		
Y	34.2	46.5	29.0	31.2	41.2
x	0.237	0.391	0.441	0.445	0.229
y	0.304	0.443	0.435	0.451	0.3559
Comment	References filters			x and y match but still too transparent	Mixture of blue and yellow

Table 4.4 – Summary of color matching of the reference glass-based filters and the combinations of organic filters.

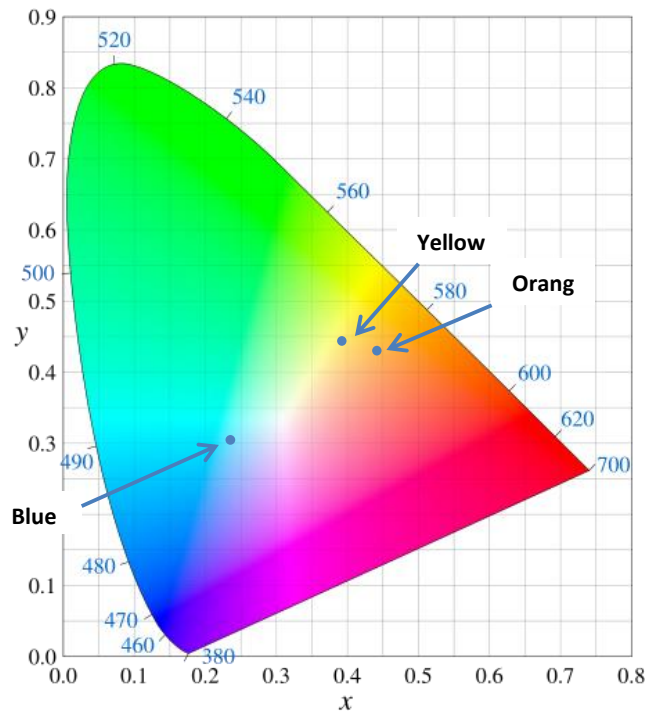


Figure 4.16 – Color coordinates of the blue, yellow and orange filters on the CIE chromaticity diagram.

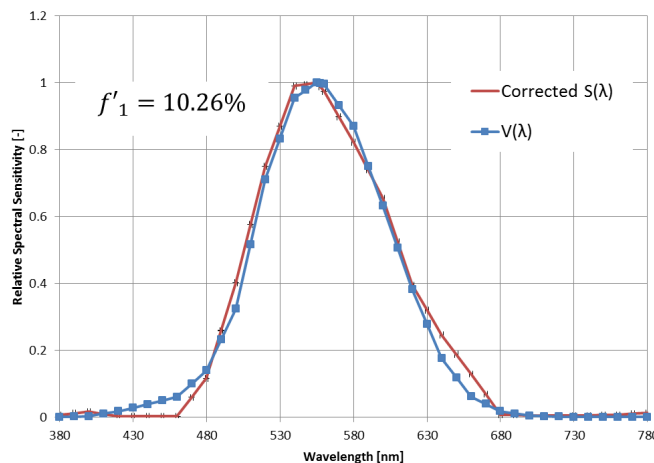


Figure 4.17 – Spectral sensitivity of the VIP #4 equipped with 3 organic filters: compared to $V(\lambda)$.

Finally, according to several experiments, the author observed that the temperature rise of the VIP does not influence the transmittance of the organic filters and that the variation of the f'_1 factor is lower than 2%.

In spite of the advantages of the organic filters in terms of high interchangeability and cost, this approach has certain limitations. For example, they may bleach over 10'000-100'000 hours of light exposure and heating depending on the conditions. Moreover, as the organic filters reduces the overall sensitivity of the photosensor, it might not be applicable in low illuminated environments. The direct implementation of plasmonic filters on the VIP chip is one of the promising solutions that would lead to longer durability, features even more accurate spectral sensitivity and does not reduce the overall sensitivity of the sensor. This follow-up project is sketched in Section 7.4 as an important step for better technology transfer toward industrial application/product.

4.2.4. Photometric Calibration

The photometric calibration is intended to provide the functions mapping the pixels' grayscale values (from 0 to 1022 digits) to the corresponding luminance [$cd \cdot m^{-2}$]. The calibration procedure was performed in two steps in order to

cover a large luminance range corresponding to a daylight environment and to minimize the calibration error. The following experimental set-up for the light sources was used accordingly:

- i) Low luminance range ($l < 67 [cd.m^{-2}]$) using a halogen quart-tungsten lamp;
- ii) High luminance range ($76 [cd.m^{-2}] < l < 9'500 [cd.m^{-2}]$) using a followspot KORRIGAN HMI 1200.

For the first stage, the VIP #2, sensor, a luminance-meter (Minolta LS-110) and spectroradiometer (Specbos 120) are placed at the entrance of the integrating sphere (Figure 4.18). Due to the setup, it is not possible to use the light entrance aperture as the target; all devices are accordingly pointing toward the same target area in the Ulbricht sphere. The power of the light sources varies between 400 and 1000 [W].

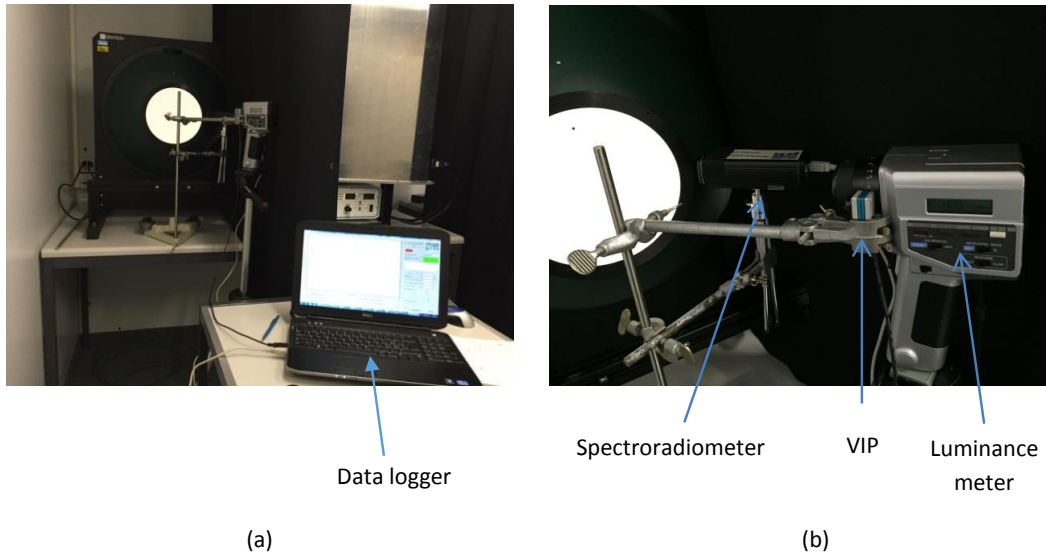


Figure 4.18 – Experimental setup for photometric calibration of HDR vision sensor (VIP) in “low” luminance ranges ($0 - 67 [cd.m^{-2}]$).

For the second stage, a high power followspot device fitted with a 1200W HMI discharge lamp was used as light source. A white diffusive surface was placed at 5 meters distance of the light source, the sensors pointing toward this surface (Figure 4.19). The reflecting surface must be large enough in order to obtain a homogenous luminance distribution on a sufficiently large area. It is worth mentioning that, as opposed to the halogen quart-tungsten lamp, this light source does not provide a very stable illumination even after 20 minutes of operation due to the inherent discharge phenomena. To overcome this problem, the VIP and the spectroradiometer performs automatically a continuous measurement of the white surface luminance: the average and standard deviation of 20 measurement samples were then taken into account to derive the calibration curve.

The result of the photometric calibration is illustrated in Figure 4.20 for both low and high luminance ranges. The calibration function is shown in Eq. (4-6).

$$L_{VIP} = 952302e^{-0.01 \times GS} \quad (4-6)$$

where $L_{VIP} [cd.m^{-2}]$ is the luminance obtained from the VIP and $GS [digits]$ is the pixel value in grayscale.

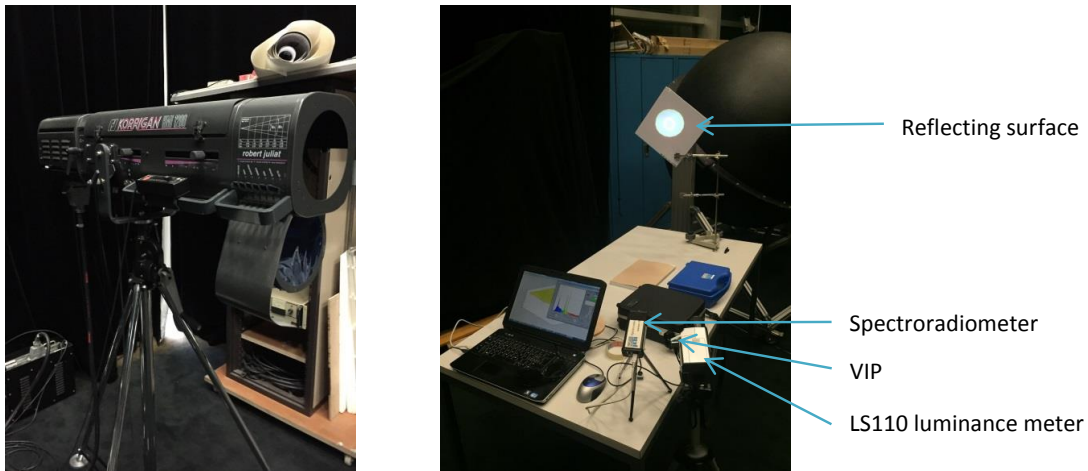


Figure 4.19 – Experimental setup for photometric calibration of HDR vision sensor (VIP in high luminance ranges ($76 - 9'500[cd.m^{-2}]$)).

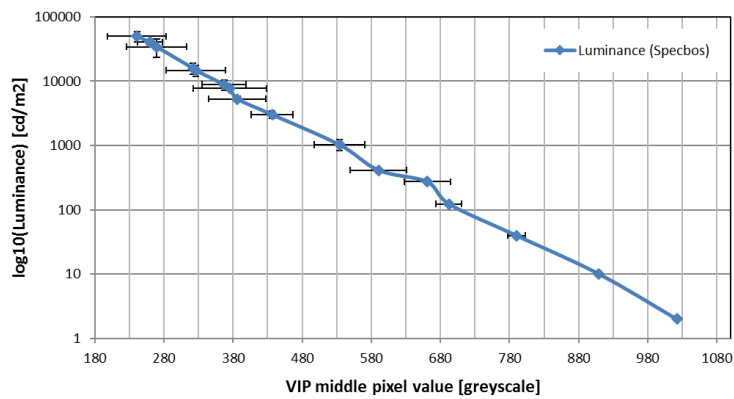


Figure 4.20 – Photometric calibration curve (mean \pm SD) of HDR vision sensor (VIP). Vertical error bars are barely visible.

4.2.5. Geometrical Calibration

In this section, the stages of the geometric calibration are presented. The VIP sensor is equipped with a fisheye lens, which is known for exhibiting noticeable light falloffs at the border of the captured image, known as vignetting effects. In other words, there is a luminance loss for pixels located far from the optical axis. This calibration procedure was carried out in collaboration with Marta Benedetti, an MSc student at LESO-PB supervised by the author.



Figure 4.21 – Experiment set-up for geometric calibration of HDR vision sensor (VIP). Courtesy of Marta Benedetti.

An experiment was designed (Figure 4.21) in order to evaluate and counterbalance the vignetting effects of the fisheye lens. Sensor VIP#2 and a steady-state white light source were used for this purpose.

The VIP sensor was mounted on a tripod with the possibility to rotate horizontally and positioned perpendicular to the light source. Figure 4.22 shows a grayscale map captured by the sensor when it is directed towards the light source, thus the latter is in the center of the image.

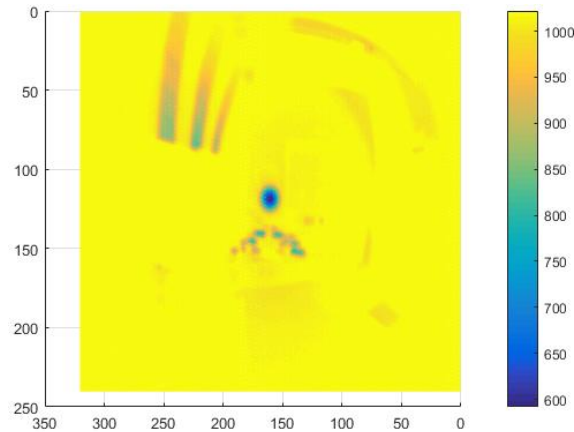


Figure 4.22- Grayscale map captured by the sensor when in front of the light source during the geometrical calibration.

The tripod was progressively rotated by 5° steps and snapshots were taken at each position, as shown in Figure 4.23.

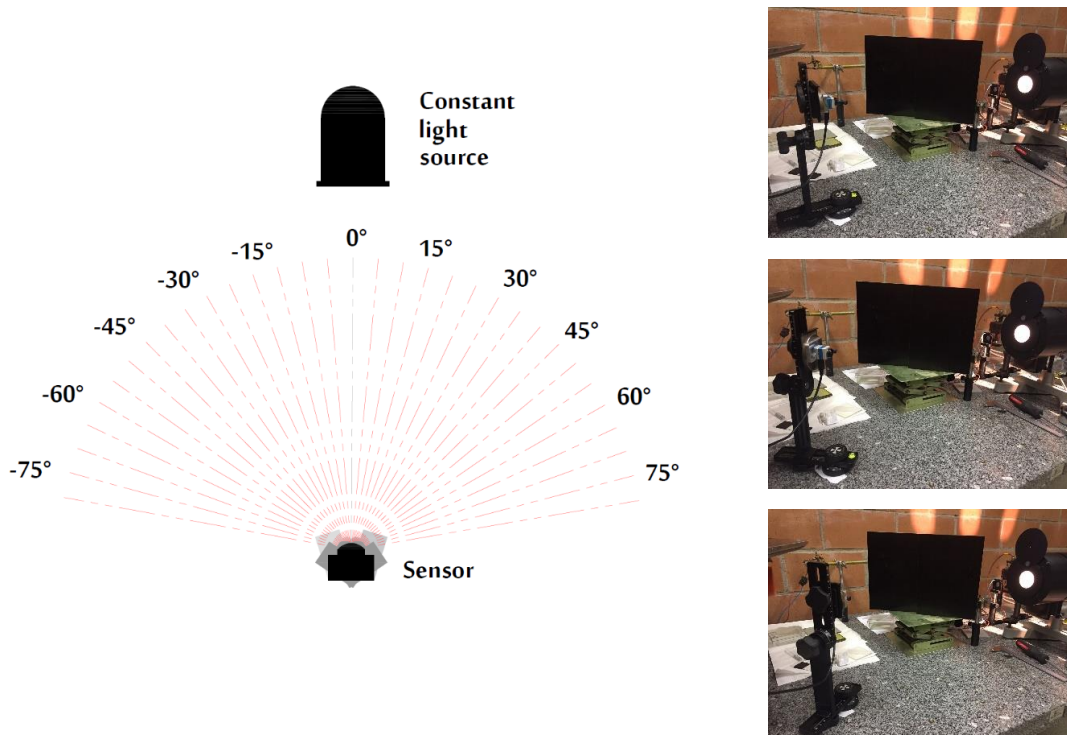


Figure 4.23 — Experimental set-up for geometric calibration of VIP sensor. The sensor is rotated around its axis by 5° steps using a rotating tripod. Courtesy of Marta Benedetti.

At each angle, the grayscale value of the pixel corresponding to the light source – i.e. the lowest grayscale value in the image - was extracted, and each pixel position recorded. Since vignetting effects are noticeable in both horizontal and vertical extension of the captured image, the procedure was repeated for both directions, i.e. by placing the sensor in the two different positions shown in Figure 4.24.

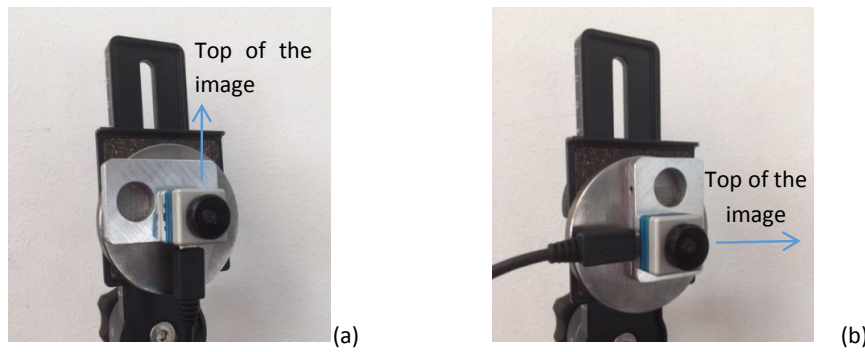


Figure 4.24 – HDR vision sensor (VIP) mounted on tripod in two positions in order to consider both (a) horizontal and (b) vertical angle.

The lowest grayscale value of the captured map was plotted for each rotation angle; the results are shown in Figure 4.25 for horizontal and vertical directions.

Horizontal error bars denote observational errors ($\pm 1^\circ$), whereas vertical error bars are negligible, the light source being very stable, thus the luminance constant. In order to test the stability of the light source, a luxmeter was placed in front of it and illuminance measurements were taken continuously for 15 minutes. For the entire duration of the test, a constant illuminance was observed by the instrument with a precision equal to 0.1 [lx]. Both sets of data were fitted to 5th order polynomial functions.

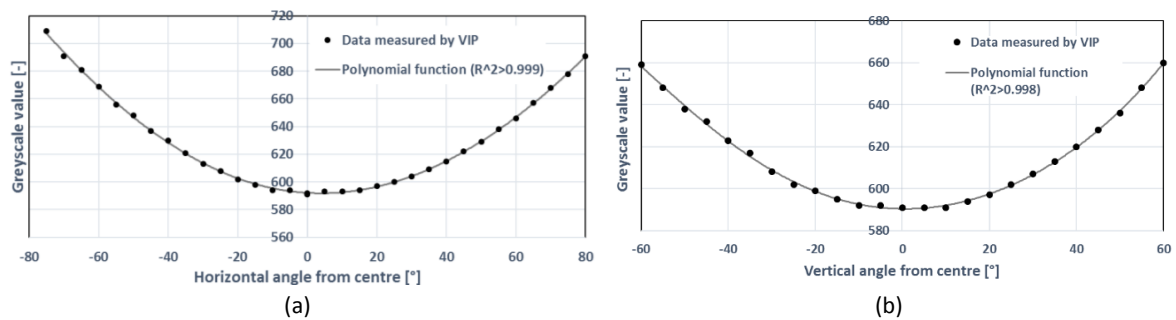


Figure 4.25 – Grayscale value of light source in the captured map vs. (a) horizontal (b) vertical angle of rotation of the sensor. Error bars in the horizontal direction indicate the observational error due to reading the angle on the rotating tripod. Horizontal error bars denote observational errors ($\pm 1^\circ$), whereas vertical error bars are negligible.

Eq. (4-7) and (4-8) present the polynomial functions fitted to the data depicted in Figure 4.25 for horizontal and vertical rotation directions, respectively.

$$GS_{horizontal}(\vartheta) = 9 \cdot 10^{-10} \cdot \vartheta^5 - 1 \cdot 10^{-7} \cdot \vartheta^4 + 1 \cdot 10^{-5} \cdot \vartheta^3 - 0.0188 \cdot \vartheta^2 + 1.477 \cdot \vartheta + 592.09 \quad (4-7)$$

$$GS_{vertical}(\vartheta) = 9 \cdot 10^{-9} \cdot \vartheta^5 - 1 \cdot 10^{-7} \cdot \vartheta^4 - 2 \cdot 10^{-5} \cdot \vartheta^3 + 0.0194 \cdot \vartheta^2 - 0.023 \cdot \vartheta + 590.36 \quad (4-8)$$

where $GS_{horizontal}$ and $GS_{vertical}$ is the grayscale value of the pixels recorded when the VIP sensor was rotated horizontally and vertically respectively (Figure 4.24) and ϑ is the VIP rotation angle as shown in Figure 4.23.

By carefully observing the graph in Figure 4.25, it can be noticed that the curve is not perfectly symmetrical. A further analysis of the field of view of the sensor allowed observing a misalignment between the center of distortion and the center of the image, which causes the FoV to be asymmetrical. In order to obtain only one single function, the two curves were overlapped and the curve related to the vertical angle shifted by 3.5 degrees (equivalent to 7 pixels) in order to adjust the misalignment of the two curves (Figure 4.26). On the y-axis, the grayscale value difference with respect to the center is considered. A 5th order polynomial function was fitted to the whole set of data, resulting in Equation (4-9) with a goodness of fit $R^2 > 0.998$:

$$GS_{normalized}(\vartheta) = -3 \cdot 10^{-9} \cdot \vartheta^5 - 2 \cdot 10^{-7} \cdot \vartheta^4 + 10^{-5} \cdot \vartheta^3 - 0.1736 \cdot \vartheta^2 + 1.3214 \quad (4-9)$$

Where $GS_{normalized}$ is the difference in grayscale value with respect to the center and ϑ is the rotation angle.

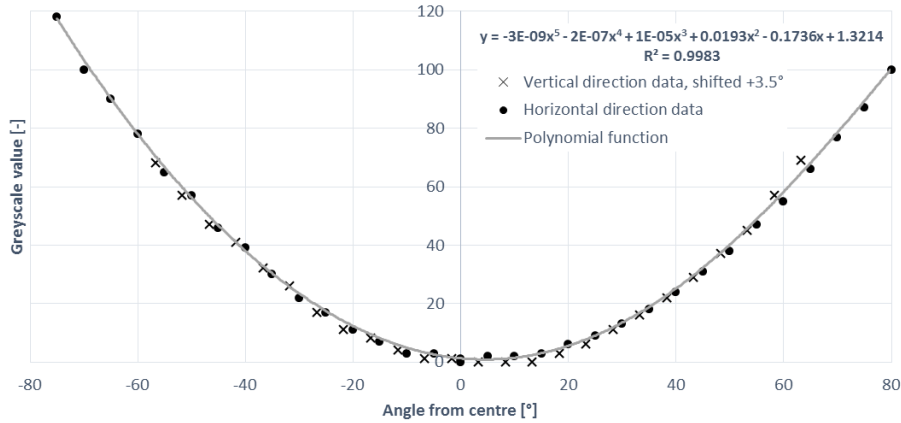


Figure 4.26 – Relative grayscale values of pixels of HDR vision sensor (VIP) in horizontal and vertical direction, as a function of the rotation angle (ϑ).

For the implementation of the vignetting correction, it is necessary to convert grayscale values in luminance and angles into pixels. To convert the grayscale value in luminance [$cd \cdot m^{-2}$], Eq. (4-6) presented in the previous section was introduced: the result are shown on Figure 4.27.

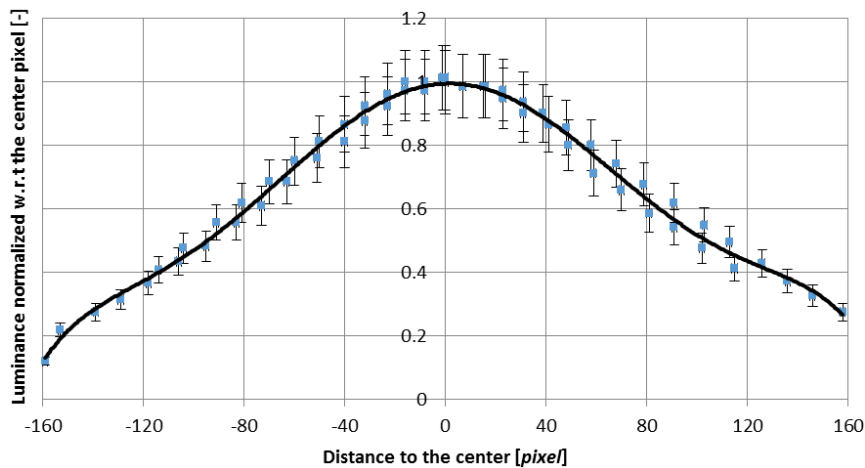


Figure 4.27 – Normalized luminance of HDR vision sensor (VIP) versus distance [$pixel$] from center of the image. This figure shows the normalized luminance for vertical and horizontal rotation.

As a final step, the function allowing a vignetting correction was found by taking the inverse of the normalized luminance plotted versus the distance to the center in pixels and fitting the polynomial function illustrated in Figure 4.28.

The function for the vignetting correction is expressed by Equation (4-10):

$$V_{VIP} = 10^{-13} \cdot d_p^6 - 6 \cdot 10^{-12} \cdot d_p^5 - 10^{-9} \cdot d_p^4 - 3 \cdot 10^{-8} \cdot d_p^3 + 0.0001 \cdot d_p^2 - 0.0002 \cdot d_p + 0.9956 \quad (4-10)$$

where V_{VIP} is the geometric (vignetting) correction factor as a function of the distance (d_p [$pixel$]) of the pixel p to the image center. This function is implemented on the embedded processor of the VIP.

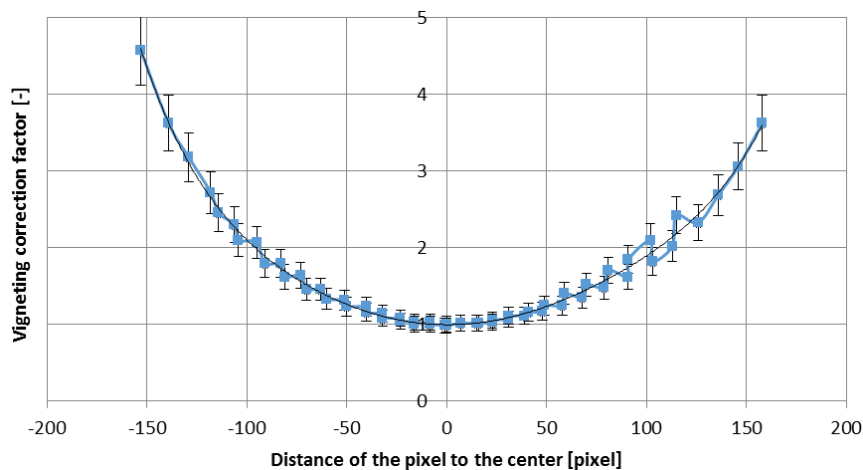


Figure 4.28 – Geometrical calibration curve as a function of the distance [*pixel*] of the pixel to the center of the image. Vertical error bars correspond to 10% error of the measured data.

4.3. Calibration Checking

Several photometric sensors were calibrated with respect to the reference sensors listed in Table 4.5. This verification of the calibration was performed in collaboration with the LIPID scientists, e.g. Jan Wienold and Peter Hansen [171]. Peter Hansen prepared the sensing platform (Figure 4.29), chose and ordered the target surfaces (Figure 4.30) and performed the post-analysis of the images captured by LMK 98-4 to create the luminance maps. The author participated in the ideation session held in LIPID for determining the location of the measurement scenes, participated in carrying out the measurements. Finally, the author performed independently the post processing of the images captured by the HDR vision sensor, carried out the comparison between the readings of reference sensors and ones of the HDR vision sensor drew the conclusions and finally wrote the present section of the thesis.

4.3.1. Photometric Sensors

Six sensors are mounted horizontally on a tripod, at the approximate height of 120 *cm* from the floor. Two spirit levels were used to guarantee horizontality of the viewing directions. Three of them serve as reference sensors, the other three being calibrated according to the reference sensors. They are listed in Table 4.5 and the setup is illustrated in Figure 4.29.

Index	Sensor	Type	Task	Accuracy
1	Kenmerken van de LMT LUX2	Luxmeter	Reference	Not reported
2	LMK 98-4	Imager	Reference	3%
3	Konica Minolta LS-110	Luminance meter	Reference	0.2%
4	VIP	Imager	Calibrated	To be figured out
5	Canon EOS 70d (#1)	Imager	Calibrated	To be figured out
6	Canon EOS 70d (#2)	Imager	Calibrated	To be figured out

Table 4.5 – List of sensors used for calibration checking procedure.



Figure 4.29 – Sensor setup for calibrating checking experimentation. Courtesy of Peter Hansen.

During each experiment, the handheld luminance meter is pointed toward 5 target samples shown in Figure 4.30. The HDR vision sensor (VIP) was included in this setup and compared to three reference photosensors; LIPID researchers were interested in calibrating two Canon digital cameras.



Figure 4.30 – Target samples for luminance evaluation for calibration checking.

4.3.2. Illumination Conditions

The experiments were performed in three indoor locations in Building LE on the EPFL main campus in Lausanne as well as outdoors in front of Building LE. The images from the testbeds are listed in Appendix F.

A first scene was captured on the 6th June 2017. However, the sky condition during this day was not steady; ergo the results were not reliable and consequently disregarded. Second round of the measurement campaign (Scene 2 to 6) was executed during the afternoon of the 7th June 2017 during stable sky conditions. At each indoor location, several series of measurements were performed for various lighting conditions. Amending the sun shading and the electric lighting status produced different lighting conditions. A summary of the experimental protocol is listed in Table 4.6.

Scene index & location	Condition index	Uniformly illuminated targets	Non-uniformly illuminated targets	Explanation
Scene 4, LE001 (S4)	C1			Top and bottom shading open, el. light. off
	C2	1, 2	3, 4, 5	Top shading closed, bottom one open, el. light off
	C3			Top and bottom shading closed, el. light off
	C4			Top and bottom shading closed, el. light on
Scene 5, LE001 (S5)	C1			Top and bottom shading open, el. lightings off
	C2	1, 4	2, 3, 5	Top shading closed, bottom one open, el. light off
	C3			Top and bottom shading closed, el. light off
	C4			Top and bottom shading closed, el. light on
Scene 2, LE1 (S2)	C1			Shading open, el. light. off
	C2	1, 3	2, 4, 5	Shading half open, el. light. off
	C3			Shading completely closed, slat horiz., el. light. off
	C4			Shading completely closed, slat horiz., el. light. on
Scene 3, LE1111 (S3)	C1			Shading open, el. light. off
	C2	3, 5	1, 2, 4	Shading half open, el. light. off
	C3			Shading completely closed, slat horiz., el. light. off
	C4			Shading completely closed, slat horiz., el. light. on

Table 4.6 – List of testbeds, indoor conditions and targets surfaces for calibration checking experiment.

Five target samples (Figure 4.30) showing a uniform reflection coefficient were placed in different locations in the field of view of the sensors.

The sensors' accuracy was derived according to the two following criteria:

- i) Luminance values [$cd \cdot m^{-2}$] of the target samples measured by all the instruments (except for N°1, see Figure 4.29);
- ii) Illuminance values [lx] measured by all the instruments (except for N°3, see Figure 4.29).

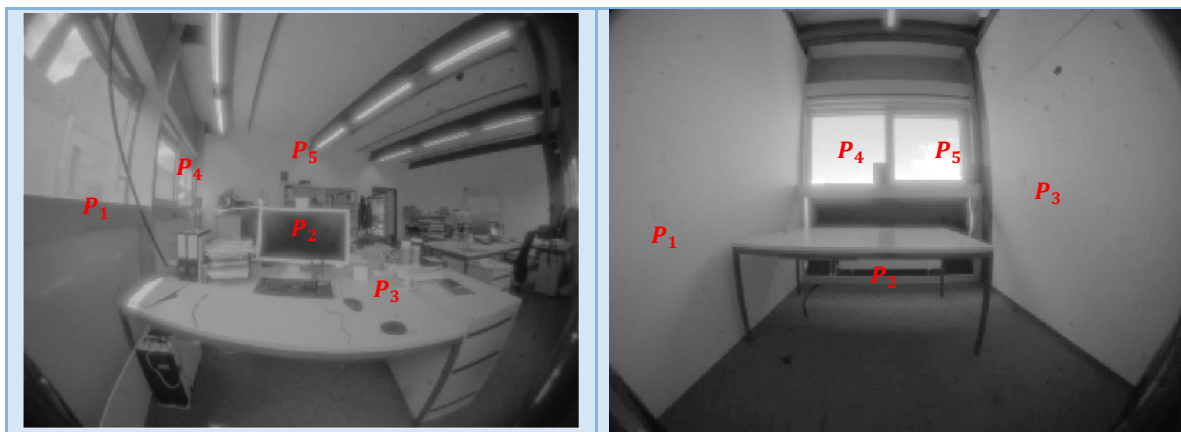
The accuracy was evaluated using the average normalized relative error from the reference value expressed in [%].

$$\epsilon_{relative} = E \left(\left| \frac{\hat{y} - y}{y} \right| \right) \cdot 100 \text{ [%]} \quad (4-11)$$

where \hat{y} is the variables measured by the VIP and y is the one measured by reference sensors.

4.3.3. Experimental Results

Table 4.7 presents the grayscale images captured by the VIP from different scenes. The target samples are shown as red labels P_1, \dots, P_5 . The locationa of the target samples are illustrated with more details in Appendix F.



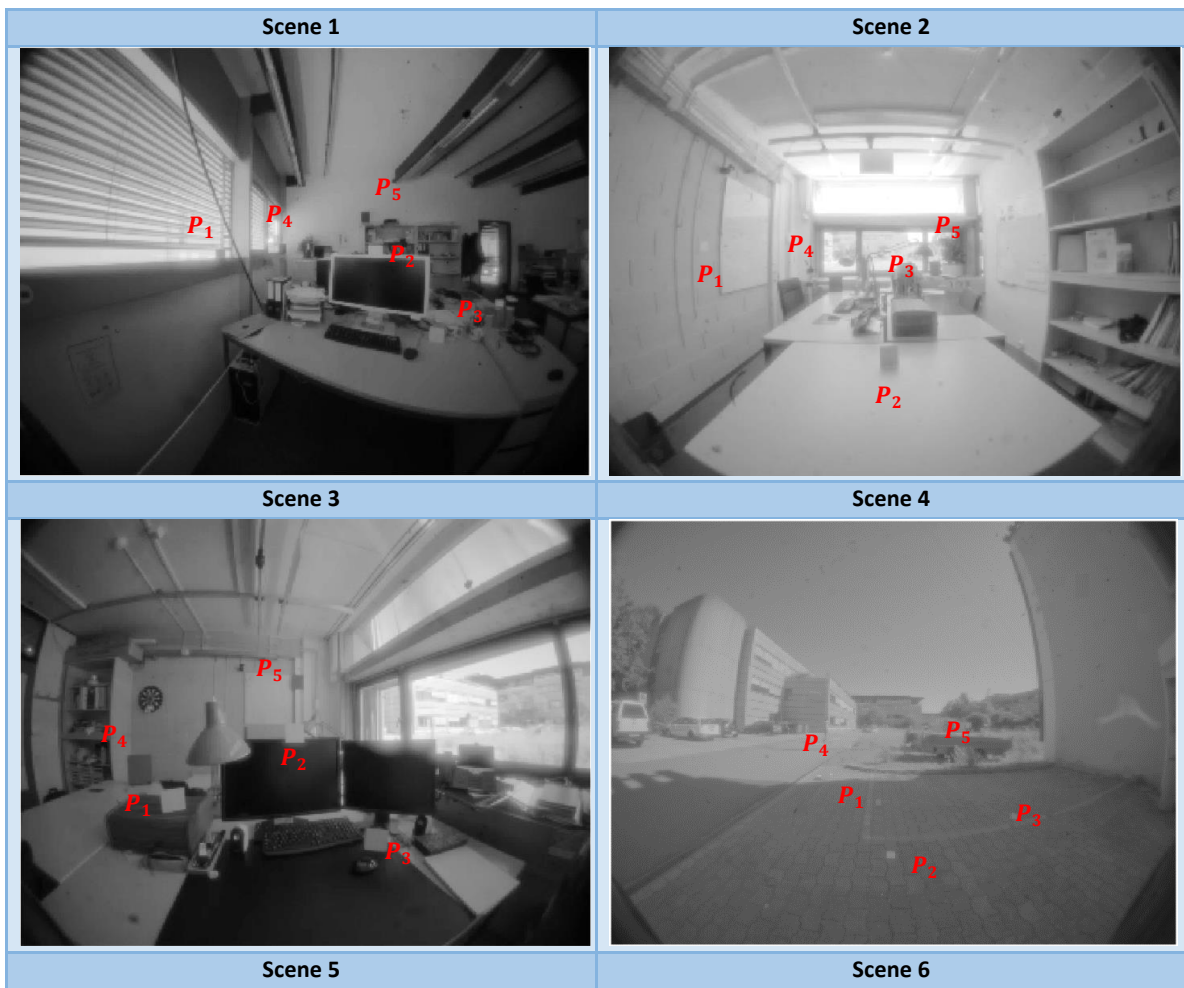
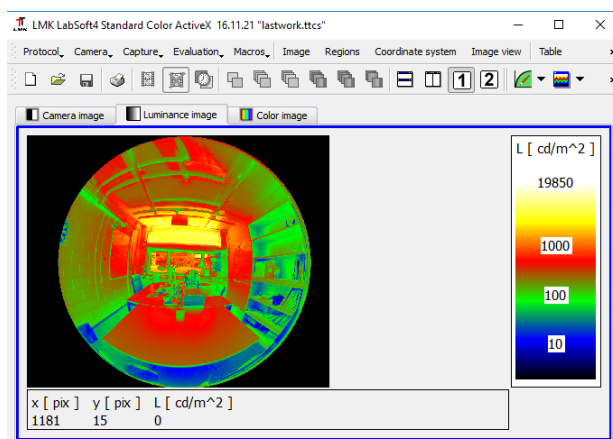


Table 4.7 – Rendering of grayscale maps measured by HDR vision sensor (VIP) during calibration checking experiments. Current rendering of the images does not reflect the actual gray scale value.

During each experiment 5 luminance maps were produced by means of the VIP. For each lighting condition in each scene, two series of measurements were carried-out: different aperture sizes were chosen for the digital cameras.



(a)



(b)

Figure 4.31 – (a) Example of LMK imager’s user interface and an HDR sample image captured at Scene 4. Courtesy of Peter Hansen.

4.3.3.1. Luminance Monitoring

Pointwise luminance measurements were performed using a Konica Minolta LS-110 luxmeter. This measurement is prone to errors: firstly, because it is a handheld device, the experimenter’s ability influences the measurements and secondly, there is an offset between its viewpoint and the other sensors.

A luminance map captured by the VIP was accordingly analyzed in order to characterize the pixels corresponding to the target samples. The luminance corresponding to these pixels was determined [$cd. m^{-2}$].

A detailed study of this luminance map shows that the relative variation of the pixel values of the targets placed close to the facade is larger than 200%, even at the center of the target sample. The targets located further than 2 [m] from the facade show a more uniform surface luminance (Figure 4.32). For this reason, the samples located close to the facade were disregarded for reasons of accuracy: all over 32 evaluations from uniformly illuminated target samples were collected.

The normalized relative error between a VIP and LMK monitored luminances for the homogeneously lit surfaces is equal to 19.6%. The corresponding error between LMK and Konica Minolta LS-110 luminance meter is equal to 8%.

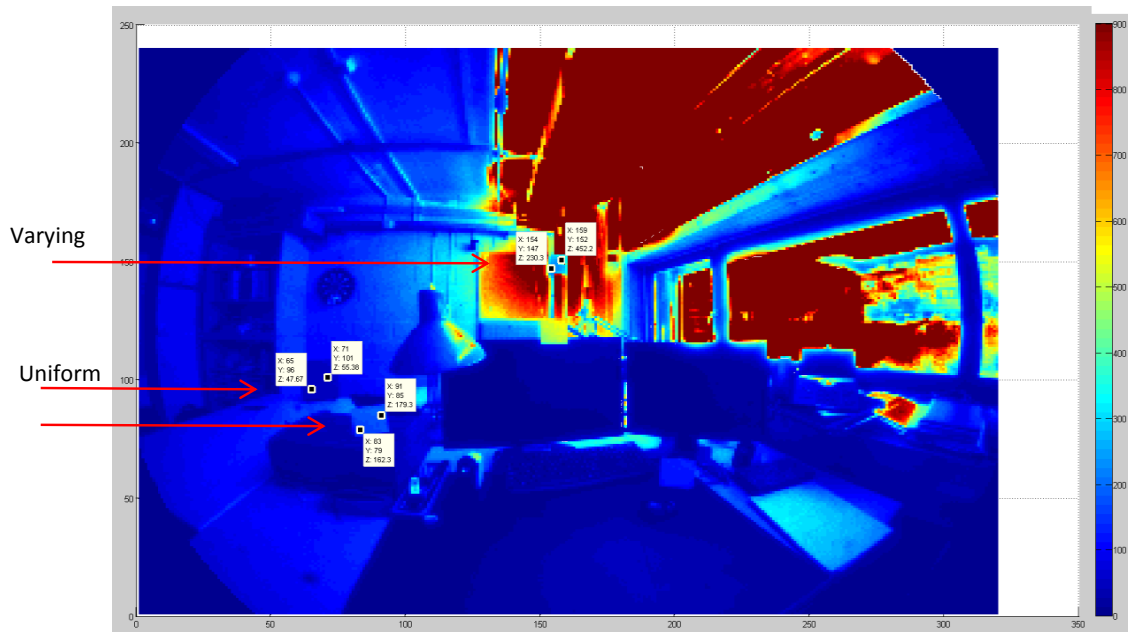


Figure 4.32 – Example of considerable variation of apparent luminance of the target surface located close to the facade. (X, Y) are the pixel coordinates and Z is the luminance.

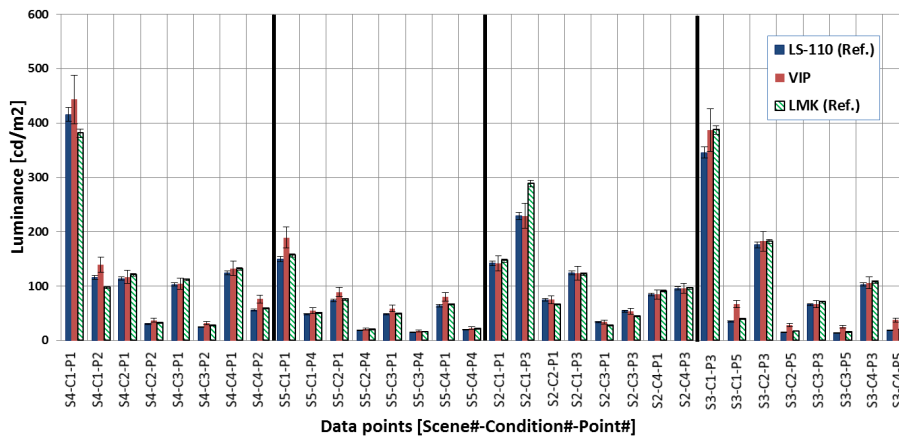


Figure 4.33 – Pointwise luminance comparison between VIP, LMK imager & Konica Minolta handheld luminance meter.

4.3.3.2. Illuminance Monitoring

The luminance maps created by the VIP are transformed to illuminance values by means of Eq. (4-16) as detailed in Section 4.4. Thus, the author may compare their readings with the illuminance values recorded by LMT luxmeter as well as LMK 98-4, i.e. Sensors 1 and 2 in Table 4.5 and Figure 4.29. It is worth noting that the field of view of the VIP (*e.g.*, $167^\circ \cdot 132^\circ$) is smaller than a full hemisphere, thus is not capable of capturing the light rays arriving from the regions out of its own range. The VIP field of view represents accordingly 89% of the full hemisphere (Section 4.2.2).

The LMK imager is the most accurate photosensor among all the reference sensors. The relative accuracy of the VIP in regards to LMK is 10.1% and with respect to the LMT luxmeter it is 12.9%. For comparison, the accuracy of the LMT luxmeter in regards to the LMK imager is 7.9%. This shows that the HDR vision sensor is only 2.2% less accurate than the standard product LMT luxmeter (10.1% vs. 7.9%) with regard to the most accurate photosensor at hand, the LMK imager. Thus, the HDR vision sensor's accuracy can be deemed acceptable.

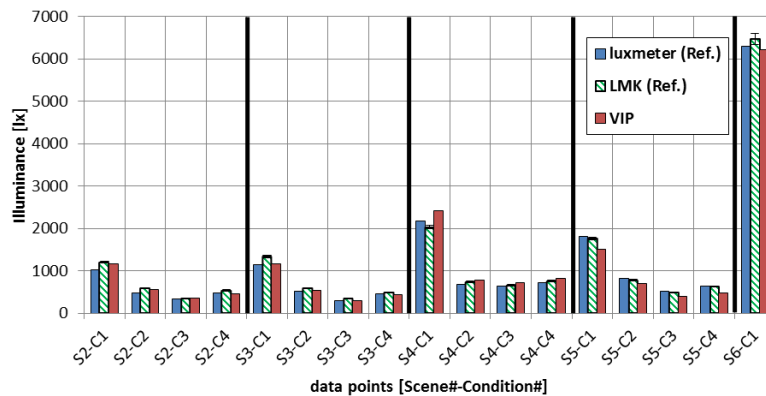


Figure 4.34 – Illuminance comparison between VIP, LMK imager and LMT LUX2 illuminance meter.

4.4. Implementation of DGP Rating in the Embedded System

In the previous section, the VIP has been characterized and calibrated. In this section, the implementation of the glare index rating software in the VIP embedded system is presented step-by-step. The theoretical background is covered in Section 2.1 whereas the practical subtleties are covered in this section. The specifications of the embedded system are listed in Table 4.2.

The flow chart of the data processing is illustrated in Figure 4.35. The processing starts with the reading of a grayscale matrix (raw image) by the software and ends with a glare rating, using the *DGP*, *DGI* or *UGR* indexes, as output.

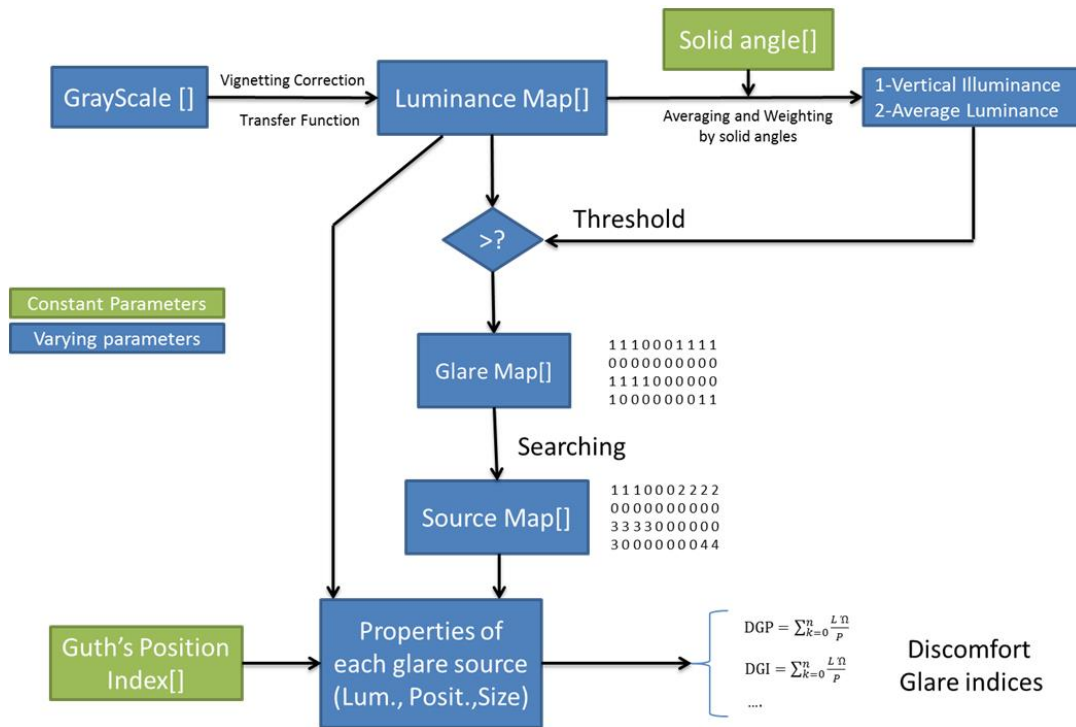


Figure 4.35 – Schematic representation of flow chart of embedded glare rating software. Raw data [grayscale] monitored by the VIP sensor (top left) is transformed to discomfort glare indices [–] (bottom right).

4.4.1. Illuminance and Average Luminance

The empirical valuation of the illuminance and average luminance by the VIP requires first to determine two main variables: i) the angular distance from the optical center and ii) the solid angle sustained by each pixel. The way the latter are assessed is explained in the following section.

4.4.1.1. Angular Distance from the Optical Axis

The angular distance from the optical axis or image center is calculated based on the “pixel to degree” ratio that was found during the VIP characterization in Section 4.2.2.1. The latter has shown that the fisheyes lens projection is an *equidistant* or *linear scaled one*. More details on this subject are given in Appendix E, the corresponding “pixel to degree” relation being:

$$\alpha_{VIP}(x, y) = \rho \cdot \sqrt{(x - x_c)^2 + (y - y_c)^2} \tag{4-12}$$

Where $\alpha(x, y)$ is the angular distance from the optical center and $(x_c, y_c) = (119, 159)$ is the coordinate of the center of the image and ρ is the angle to pixel ratio [$^\circ/\text{pixel}$] equal to 0.533. In Figure 4.36, the correlation between the angle and distance to the center for both directions are superimposed.

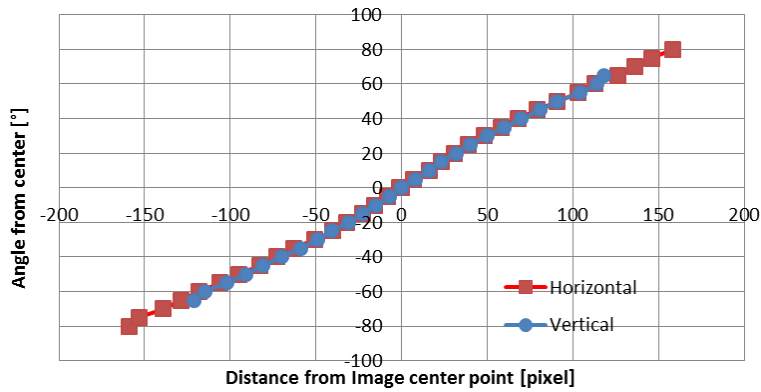


Figure 4.36 – Conversion from the pixel coordinates to angle to the optical axis (center of image) in vertical (blue) and horizontal (red) direction. The slope of these curves defined the parameter ρ in Eq. (4-12) which is equal to $0.533 [^{\circ}/pixel]$.

4.4.1.2. Solid Angle Subtended by each Pixel

The objective of this subsection is to present the way the solid angle that is subtended by each pixel is calculated. Knowing the type of projection, one can obtain this relation by means of a procedure that is presented below.

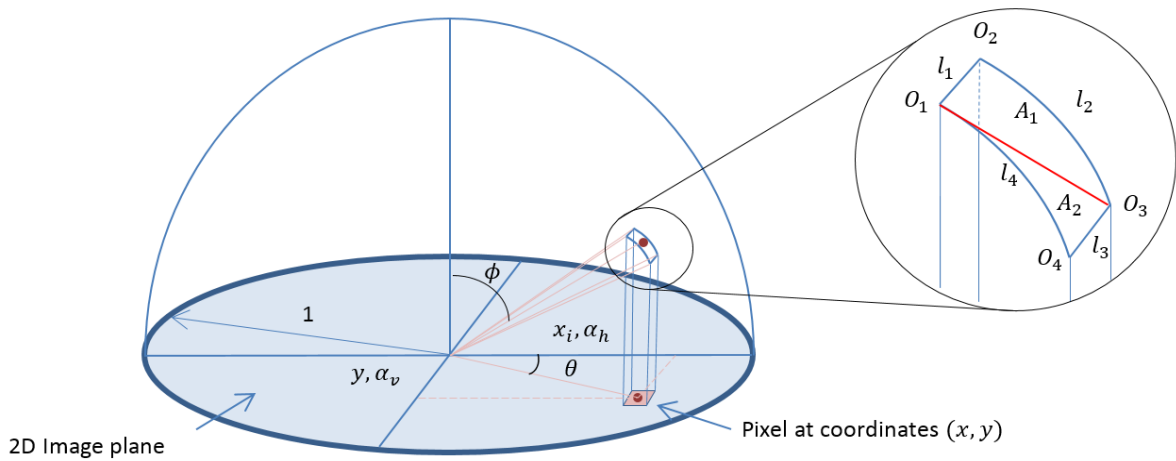


Figure 4.37 – Schematic representation of procedure for calculating the solid angle subtended by a pixel on a captured image. The variables refer to the coordinates of the pixel center; the principles are applicable to the corners of the pixel.

The procedure used for calculating the solid angle subtended by a given pixel is schematically depicted in Figure 4.37. For the sake of simplicity, the variables referring to the coordinates of the pixel center are illustrated. The annotation for the pixel corners follows the same convention:

- I. The coordinates of each image pixel expressed in the Cartesian coordinates system (x, y) are assigned to the center of a pixel. Each pixel having four corners, their coordinates are calculated by finding the mid-point between the centers of neighboring pixels. Thus, four pairs of Cartesian coordinates for four corners are obtained $(x_i, y_i) i \in \{1,2,3,4\}$.
- II. In the next step, the angles in the horizontal and vertical direction corresponding to the Cartesian system axis are found by applying Eq. (4-12) $(x_i, y_i) \rightarrow (\alpha_{h,i}, \alpha_{v,i}), i \in \{1,2,3,4\}$.
- III. Thirdly, the corners angles are transformed from Cartesian coordinates to spherical coordinates assuming that the radius of the sphere is one and that projection is orthogonal $(\alpha_{h,i}, \alpha_{v,i}) \rightarrow (\phi_i, \theta_i, \rho_i), i = \{1,2,3,4\}$ where $\rho_i = 1$.

- IV. Knowing the spherical coordinate, one can calculate the length of each side of the projected rectangle by applying the Euclidean distance in 3D. The length of the rectangle diagonals can be determined similarly. For example $l_j = \overline{O_i O_{(i+1)}}$
- V. Knowing the length of each side and one diagonal, one may find the area of two triangles forming the projected rectangle (A_1, A_2) . The area of the rectangle is equal to the sum of the area of the each triangle: $A(x, y) = A_1 + A_2$.
- VI. Since the rectangle is projected on a unit sphere, the area of the rectangle is by definition equal to the solid angle of the original pixel: $\omega(x, y) = A(x, y)$. By repeating the procedure for the whole image, a matrix of solid angles can be created.

This process is computationally too heavy to be implemented on the embedded DSP of the VIP sensor. Given the field of view, the image dimensions and the type of projection, one may pre-calculate the matrix of solid angles offline and burn the whole matrix on the flash memory of the VIP. Since the available onboard memory is limited, another solution was applied: a polynomial function was fitted in order to be able to reproduce the matrix of solid angles. The calculation of this function is by far less CPU intensive and does not require any storage resources.

A curve given by Eq. (4-13) was fitted to this data to approximate the solid angles with high accuracy ($R^2 = 0.9998$ and $RMSE = 1.042 \cdot 10^{-07}$). Thanks to the symmetry, a quarter of the solid angle matrix is sufficient to be modeled this way.

$$\omega(x, y) = 4.326 \cdot 10^{-5} + 2.351 \cdot 10^{-7} \cdot x + 2.03310^{-7} \cdot x - 7.319 \cdot 10^{-10} \cdot y^2 + 1.242 \cdot 10^{-10} \cdot y \cdot x - 8.749 \cdot 10^{-10} \cdot x^2 \quad (4-13)$$

where ω is the solid angle [sr] and coefficients are derived with 95% confidence bounds. The total solid angle covered by the fisheyes lens is equal to 5.5985 [sr] which is about 89% of the solid angle of an hemisphere (2π [sr]).

4.4.1.3. Grayscale to Luminance Mapping

The raw output data of the imager represent a matrix $M_{grayscale}$ of grayscale values

$$M_{grayscale} = \left(m_{grayscale}(x, y) \right)_{0 \leq x \leq 239, 0 \leq y \leq 319}, m_{grayscale} \in \mathbb{N} \leq 1022.$$

Through the characterization procedure, the sensor has been photometrically, spectrally and geometrically calibrated so that the grayscale value of each pixel can be converted to luminance. Thus, a luminance map $M_{lum} = m_{lum}(x, y)_{0 \leq x \leq 239, 0 \leq y \leq 319}$ and $m_{lum} \in \mathbb{R}^+$ can be derived based on Eq. (4-14):

$$\begin{aligned} M_{lum} &= \Psi_{lum}(M_{grayscale}) \cdot V_{VIP} \\ m_{lum}(x, y) &= \Psi_{lum}(m_{grayscale}(x, y)) \cdot V_{VIP}(x, y) \end{aligned} \quad (4-14)$$

where M_{lum} is the luminance map (or matrix), $\Psi_{lum}(M_{grayscale})$ is the conversion function derived through the photometric calibration and V_{VIP} is the vignetting correction factor derived through the geometric calibration. For further information on these functions, one may refer to Section 4.2.

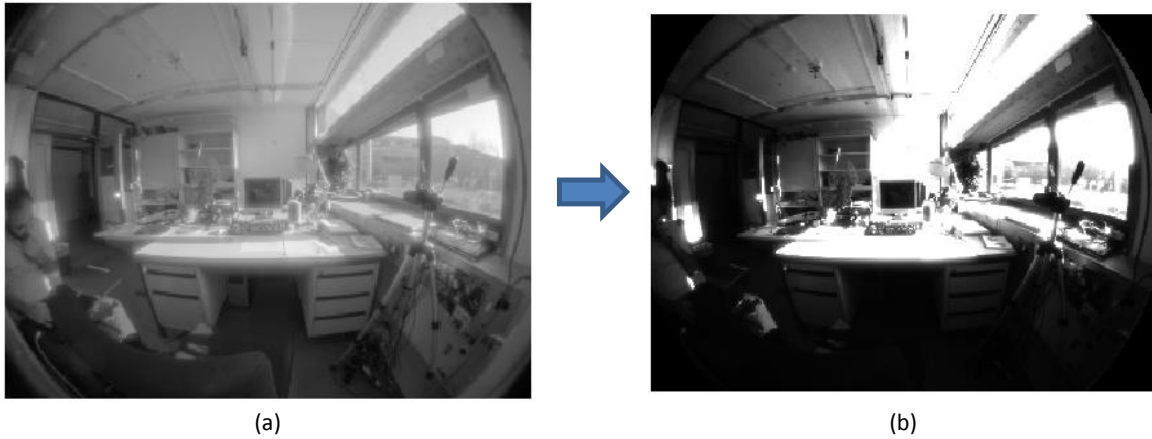


Figure 4.38 – (a) Example of raw grayscale map evaluated by VIP; (b) luminance map obtained from the grayscale map.

The illuminance and average luminance are finally derived by applying Eq. (4-15) and (4-16).

$$L_{average} = \frac{\sum_{x=0}^{239} \sum_{y=0}^{319} (m_{lum}(x, y) \cdot \omega(x, y))}{\sum_{x=0}^{239} \sum_{y=0}^{319} \omega(x, y)}, \text{ if } \alpha_{VIP} < 90^\circ \quad (4-15)$$

where $L_{average}$ is the average luminance of the scene and “ \cdot ” symbol is an element-wise multiplication of two matrices.

$$E_v = \sum_{x=0}^{239} \sum_{y=0}^{319} (m_{lum}(x, y) \cdot \omega(x, y) \cdot \cos(\alpha(x, y))), \text{ if } \alpha_{VIP} < 90^\circ \quad (4-16)$$

where E_v is the illuminance in lux.

4.4.2. Glare Pixel Map

All pixels with angles to the optical axis larger than 90° are filtered out and set to 0.

The threshold for glaring pixels detection can be found based on the recommendation by [17] as shown in Eq. (4-17).

$$T_{glare} = 5 \cdot L_{average} \left[\frac{cd}{m^2} \right] \quad (4-17)$$

Another approach consists in applying the contrast thresholds corresponding to near and mid peripheral regions in the field of view [175], [176], such as:

- For a 30° angle around the line of sight, corresponding to the ergorama, if the ratio of the pixel luminance to the one of the pixel on the line of sight (pixel in center of the image) is larger than 1:3 or smaller than 3:1, the pixel is labeled as glaring;
- In the region between a 30° and 60° angle around the line of sight, corresponding to the panorama, if the ratio of the pixel luminance to the one of the pixel on the line of sight is larger than 1:10 or smaller than 10:1, the pixel is labeled as glaring;

Both approaches were implemented in the embedded software of the VIP. The first one was used in the framework of this doctoral thesis. A glaring pixels map, which is made of binary items, was defined for that purpose as follows:

$$M_{glare_pixel} = \left(m_{glare_pixel}(x, y) \right)_{0 \leq x \leq 239, 0 \leq y \leq 319}, m_{glare_pixel} \in \{0, 1\}$$

The elements of this matrix are defined as follows:

$$m_{glare_pixel}(x, y) = \begin{cases} 1 & \text{if } (m_{lum}(x, y) > T_{gs} \ \& \ \alpha(x, y) < 90^\circ) \\ 0 & \text{otherwise} \end{cases} \quad (4-18)$$

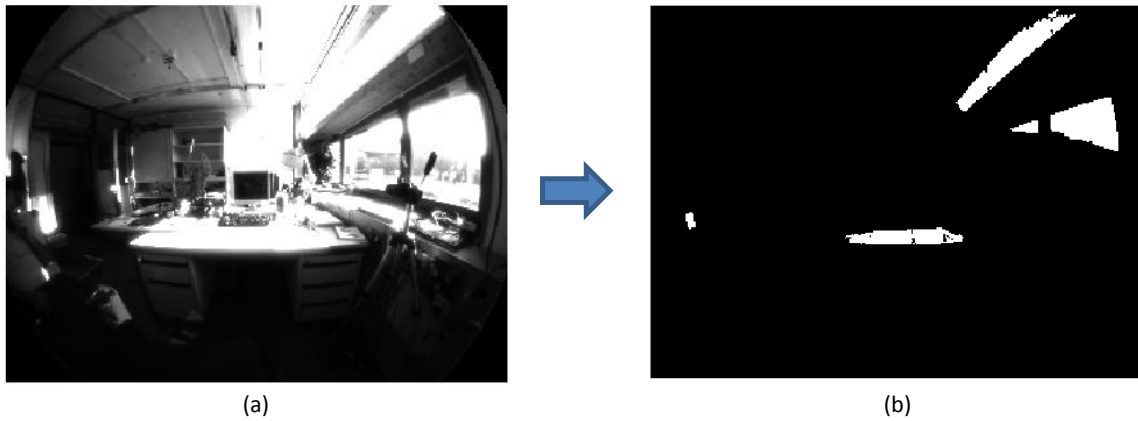


Figure 4.39 – (a) Luminance map [$cd.m^{-2}$] (b) potential glaring pixels map found by application of Eq. (4-18). White pixels are the glaring pixels and the black area is the background.

4.4.3. Glare Source Map

A glare source map consisting of a matrix defined as follows is created at this stage.

$$M_{glare_source} = \left(m_{glare_source}(x, y) \right)_{0 \leq x \leq 239, 0 \leq y \leq 319}, m_{glare_source} \in \mathbb{N} \quad (4-19)$$

At the previous stage, a glaring pixel map was created. In this step, the glaring pixels are regrouped to form the glare sources if they are within a given radius. The *Grass fire* algorithm is applied for grouping the pixels; this algorithm is inspired by the natural spread of fire in a plane partially covered with grass. The fire is initiated from a corner of the plane (image); if there is unburnt grass in the vicinity of the fire, the fire is naturally spreading to that region of grass. The fire spreads to the region until there is no more unburnt grass within a specific distance from the fire. A new fire is set as soon as a new distant unburnt grass point (pixel) is detected, the fire spreading to the neighbors in the same manner. The process is going on until all grass is burnt (e.g. no unburnt grass remains).

Using this analogy, one may explain in simple words how the glare sources are formed. The implemented algorithm is however more elaborated than this explanation to guarantee the robustness and computation simplicity.

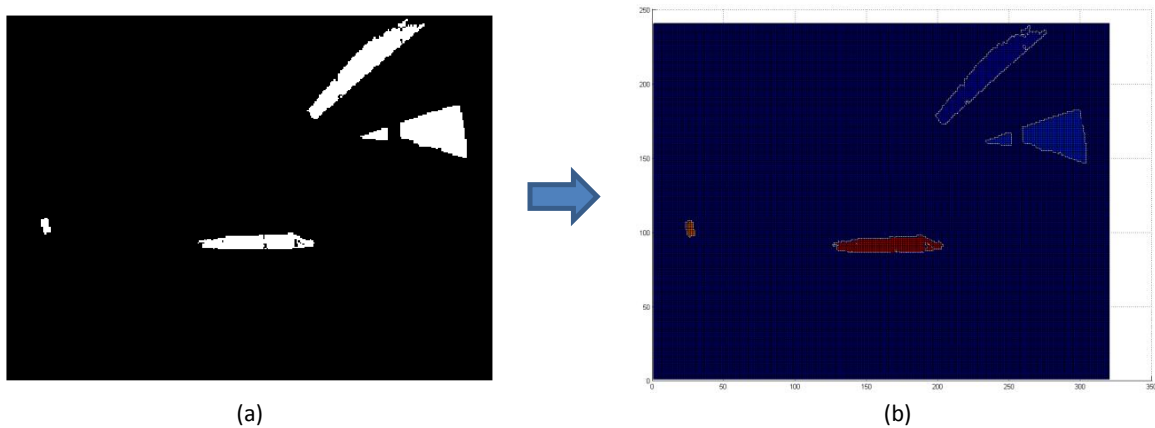


Figure 4.40 – Glaring pixels, i.e. white pixels on the left image (a), are grouped to form three glare sources shown in the right image (b). The image on the right is called glare source map.

The M_{glare_pixel} is swept and as soon as the first glaring pixel is detected (if $m_{glare_pixel}(x, y) = 1$), the corresponding pixel in the glare source map is indexed to 1 ($m_{glare_source}(x, y) = 1$). At this point, the neighborhood search for finding unindexed glaring pixels starts (equivalent to near unburnt grass in the analogy above). Each pixel in the window defined by $(x \pm 20, y \pm 20)$ is checked. Thus, the width and height of the search window are equal to $2 \cdot 20 + 1 = 41$ pixels. When the whole neighborhood is indexed, the sweeping process continues. In this process, if a new unindexed glare pixel is found, a neighborhood search starts to look for already indexed pixels. If none is found, it means that a new

glare source has been detected; this pixel is indexed as a new glare source: $m_{glare_{source}}(x, y) = I + 1$ where I is the number of glare sources already found. In other words, a *new* fire is set.

Figure 4.40 illustrates how the grass fire algorithm is grouping the glaring pixels in order to identify potential glare sources.

4.4.4. Analyzing the Glare Sources for Features Extraction

In this step, the features of glare sources, such as their luminance, angular size and location, are extracted from the digital image. The list of the corresponding parameters is shown in the following table.

Variable	Description
L_s	Luminance of glare source s [$cd.m^{-2}$]
P_s	Guth's position index for source s
ω_s	Solid angle subtended by the source s [sr]
Ω_s	Solid angle subtended by the source, modified by the position of the source [sr]
$(L * \omega)_s$	Luminance of glare source s , pixel-wise weighted by solid angle [$cd.m^{-2}.sr^{-1}$]
$\sum L_s$	Sum of the luminance of all glare sources [$cd.m^{-2}$]
$\sum \omega_s$	Solid angle subtended by all the glare sources [sr]
$\sum (L * \omega)_s$	Luminance of all the glare sources, pixel-wise weighted by solid angle [$cd.m^{-2}.sr^{-1}$]
E_d	Direct vertical illuminance at eye due to all sources [lx]
L_b	Background luminance [$cd.m^{-2}$]

Table 4.8 – List of glare sources features extracted from the digital image. These features are used for calculating glare indices based on Eq. (2-1) to Eq. (2-5).

4.4.4.1. Position Index Calculation

In order to take into account the effect of angular displacement of the glare source relative to the observer line of sight in the glare indices formula, a *position index* P-index known as the Guth position index is determined for each pixel of the glare sources [17]. The analytical equation of the position index depends on the location of the glare source or the glaring pixel. If the pixel is above the line of sight, it is given by Eq. (4-20); if below by Eq. (4-21).

$$P_{Guth}(\tau, \sigma) = \exp([35.2 - 0.31889 \cdot \tau - 1.22 \cdot \exp(-2\tau/9)] \cdot 10^{-3}\sigma + [21 + 0.26667 \cdot \tau - 0.002963\tau^2] \cdot 10^{-5} \cdot \sigma) \quad (4-20)$$

$$P_{Guth}(R, D) = \begin{cases} 1 + 0.8 \frac{R}{D} & R < 0.6D \\ 1 + 1.2 \frac{R}{D} & R \geq 0.6D \end{cases} \quad (4-21)$$

where $R = \sqrt{H^2 + Y^2}$, H is the vertical distance between the source and the viewing direction, Y is the horizontal distance between the sources and the viewing direction and D is the distance from the eye to the source in the viewing direction. Figure 4.41 illustrates the angular variables that must be taken into account in the calculation of the Guth position index.

To derive the P-index for each pixel, one needs to convert the pixel Cartesian coordinates to the angles τ and σ . To perform this conversion, two new variables, α_h and α_v are introduced corresponding to the horizontal and vertical angles measured in respect to the line of sight, given by Eq. (4-22).

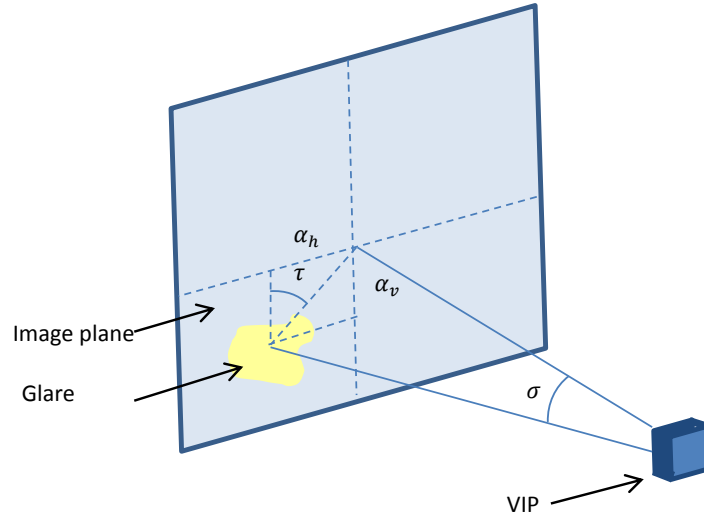


Figure 4.41- Schematic representation of the angles τ and σ used for calculating the P-index.

$$\begin{aligned}\alpha_h &= \alpha_{h,min} + \frac{\alpha_{h,max} - \alpha_{h,min}}{W_{image}} * y \\ \alpha_v &= \alpha_{v,min} + \frac{\alpha_{v,max} - \alpha_{v,min}}{H_{image}} * x\end{aligned}\quad (4-22)$$

where $\alpha_{h,min} = -83.5^\circ$, $\alpha_{h,max} = +83.5^\circ$, $\alpha_{v,min} = -66^\circ$, $\alpha_{v,max} = +66^\circ$, $W_{image} = 320 \text{ pixels}$, $H_{image} = 240 \text{ [pixel]}$ and $(x, y) \in ([0,239], [0,319])$ are the pixel Cartesian coordinates.

The angular variables τ and σ can be determined as follows:

$$\begin{aligned}\sigma &= \sqrt{\alpha_h^2 + \alpha_v^2} \\ \tau &= \text{asin}\left(\frac{\alpha_h}{\sigma}\right)\end{aligned}\quad (4-23)$$

4.4.4.2. Calculation of Selected Glare Sources Features

Characterizing the glare sources is a tricky task: their luminance L_s and sustained solid angles Ω_s must be weighted pixel-wise in some cases. The following equations provide the exact definition of these variables:

$$L_s(s) = \frac{\sum(L \cdot \omega)_s}{\sum \omega_s}\quad (4-24)$$

$$L_b = \frac{\sum \omega \cdot L_{average} - \sum(L \cdot \omega)_s}{\sum \omega - \sum \omega_s}\quad (4-25)$$

$$\Omega_s(s) = \frac{\omega_s(s)}{P_s(s)^2}\quad (4-26)$$

4.4.5. Evaluating the Glare Source Indices

In a final stage, the glare indices are evaluated on the basis of the glare sources' main features. Eq. (2-1)(2-4)(2-2)(2-3) can be directly applied. However, for *DGP* calculation some subtle modifications to the original formula have been suggested by Wienold, the inventor of this index, for low illuminance scenes; these are given by Eq. (4-27).

$$DGP = \begin{cases} DGP \cdot \frac{e^{(0.024 \cdot E_v - 4)}}{1 + e^{(0.024 \cdot E_v - 4)}} & E_v < 100 \text{ lx or } DGP < 20\% \\ DGP & \text{otherwise} \end{cases} \quad (4-27)$$

In the example presented in Figure 4.39 (a), a DGP value of 37% was drawn, corresponding to a “Disturbing” discomfort glare sensation according to Table 2.1.

4.5. Robustness and Accuracy Tests

This section is based on work the author has presented and published in 2015 at the CISBAT 2015 International Conference on Future Buildings and Districts – Sustainability from Nano to Urban Scale at EPFL Lausanne (Switzerland) [80].

Today the Evalglare software, a Radiance based tool for glare rating developed by Wienold [118], is a reference for assessment of glare indices using luminance maps. An embedded program inspired by the Evalglare software has been developed in order to perform glare indices calculation on the HDR vision sensor. The essential features of the embedded program are: i) its computational efficiency (each cycle takes approx. 12 seconds); ii) accurate image processing in spite of limited embedded RAM memory and iii) a telemetry transmission feature of whole records of a visual comfort analysis over LAN to a remote machine (MATLAB based interface).

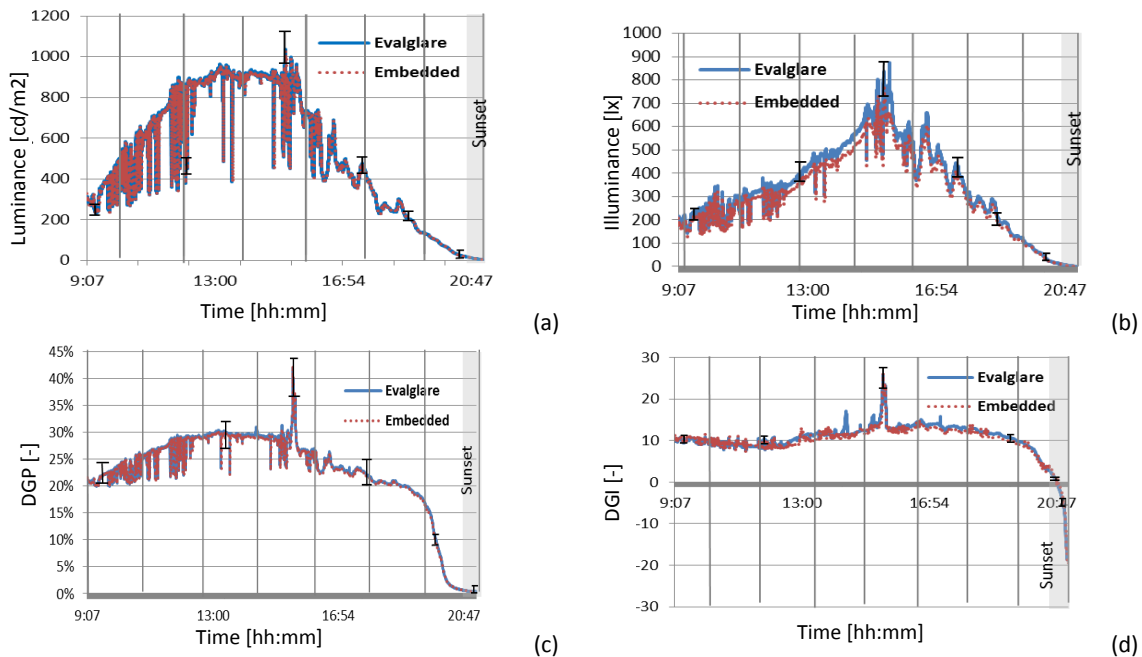


Figure 4.42 – Validation of HDR vision sensor embedded glare indices calculation versus Evalglare software calculations [17].

The software was validated through comparison of 5400 measurements captured under clear sky conditions during approximately 18 hours from 9:20 AM to 6:10 AM on March 16 and 17, 2015. As shown in Figure 4.42, a reasonable matching was observed between the photometric variables (average luminance and direct illuminance of the glare sources) and glare indices (DGP and DGI) monitored with the HDR sensor and those calculated with Evalglare. The relative discrepancy for the average luminance, the direct illuminance of glare sources, the DGP and DGI shows Root Mean Square Error (RMSE) values of 0.9%, 8.9%, 2.5%, 6.7% respectively. According to Borisuit et al. [175], the accuracy i.e. in terms of RMSE of the HDR vision sensor for daylight conditions with respect to a luminance meter (Minolta LS 110) was estimated at around 20%.

In order to verify the robustness of the functioning of the HDR vision sensor, it was positioned on a tripod at a west-facing workstation in the LESO solar experimental building, similar to the setup shown in Figure 4.60 (a) in Section 4.8, for more than 33 hours; the blinds were completely open and the office occupied for regular office tasks during that period. The electric lighting was turned on from 6:45 PM to 8:55 PM on the first day. The sky was partially cloudy on the first day and sunny during the second day. During the latter, the sun disk was perceived by the sensor: very high vertical pupilar illuminance values for some moments of the day were accordingly observed. These illuminance values were properly reflected in the *DGP* (and to some extent in the *CGI*) while the other indices return values comparable to those monitored for overcast sky conditions. This observation is due to the strong linear relation of the *DGP* with the vertical pupilar illuminance.

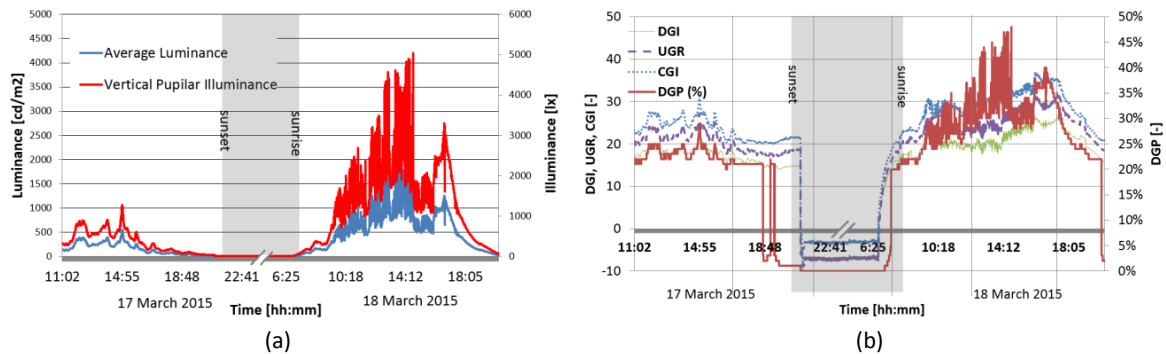


Figure 4.43 — Proof of functionality robustness of the HDR vision sensor during approx. 33 hours; (a) principal photometric variables: vertical pupilar illuminance [lx] and average luminance [$cd \cdot m^{-2}$]; (b) glare indices *DGI*, *UGR*, *CGI* and *DGP*.

4.6. Uniformity and Accuracy Verification

4.6.1. Introduction and Goal

This experiment was designed and performed in order to verify the uniformity and accuracy of luminance measurements throughout the field of view of two High Dynamic Range (HDR) vision sensors. These sensors return a luminance map (a 2D matrix of 320x240 pixels) where the value of each pixel corresponds to the luminance of a part of the field of view.

The reason for performing this verification process is as follows: two HDR vision sensors are equipped with photopic filters adapting the spectral response of the photoreceptor to the human eye relative sensitivity expressed by the $V(\lambda)$ function (Figure 4.44 (b)). These filters were designed and fabricated based on the raw spectral response of the middle pixel of the first sensor (pixel [160,120]). With the correction filters installed, the first sensor is photometrically calibrated based on the response of the same pixel. In the final stage, the sensor was geometrically corrected in order to eliminate the vignetting effect based on the value of the same middle pixel. These calibrations were made only for the middle pixel of the first sensor. However, it is not sure if the rest of the field of view is also accordingly calibrated. Moreover, the applicability of the calibration results to the second vision sensor is also uncertain.

Thus, two questions can be raised and must be answered:

1. Is the luminance measurement of the first HDR vision sensor accurate enough for the whole field of view?
2. Is the *second* vision sensor accurately enough calibrated based on the results of the calibration of the *first* sensor?

In this section, the experimental setup procedure used for that purpose is described, the results are presented and the questions are answered.

4.6.2. Experimental Setup

Three customized photopic filters are depicted in Figure 4.44. The thicknesses of these filters were optimized in order to adapt the spectral sensitivity of the HDR vision sensor to the photopic curve $V(\lambda)$; for further explanations the reader is referred to [38].

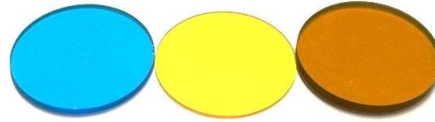


Figure 4.44 – Three customized photopic filters (colored glasses) placed between the fisheye lens and the photosensor chip.

The luminance Meter LS-110 is a hand-held device with a measurable luminance range of 0.01 to 999900 $cd.m^{-2}$; it shows a $1/3^\circ$ acceptance angle and is TTL (through-the-lens) viewing and sensing (Figure 4.45 (a)).

The dimensions of the luminous panel, shown in Figure 4.45 (b), are 152 cm x 118 cm. These panels are originally built for emulating the daylight through the window of the phobio test chamber (Figure 3.18). Its light flux can be controlled through a command box (Figure 4.45 (c)). The intensity of the panel is controllable by a potentiometer knob. The potentiometer setting can be chosen between 0 (lowest luminous intensity slightly higher than nil) and 1000 (maximal intensity). The relationship between the luminous intensity of the luminous panel and the reading on the potentiometer is not linear. The internal light sources are grouped into halves and can be switched on/off independently: during our experimentation the both halves were switched on.

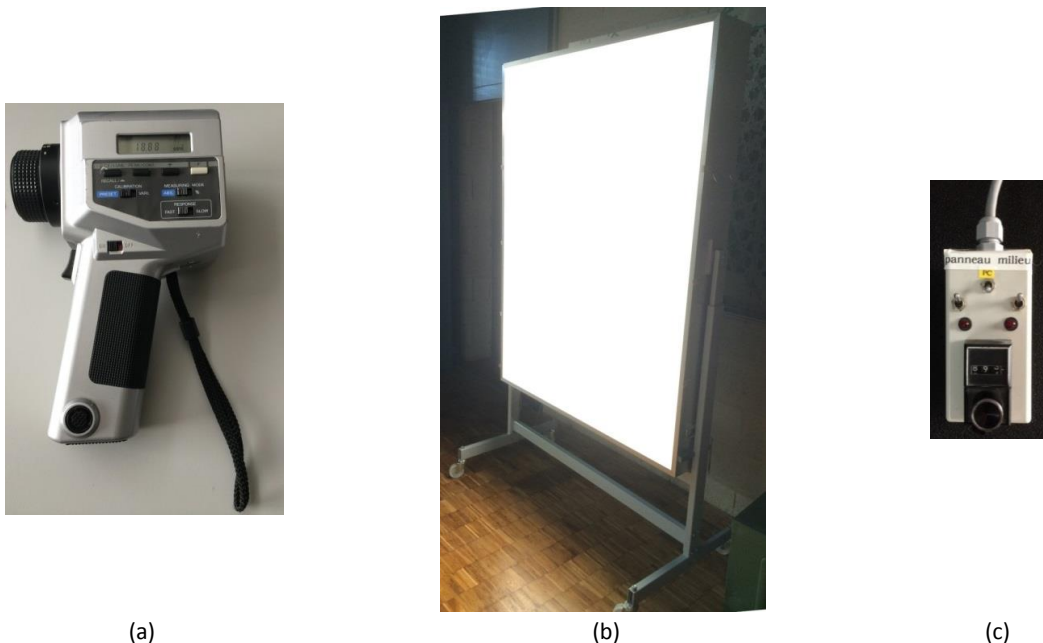


Figure 4.45 – (a) Handheld LS-110 luminance meter (Konica Minolta); (b) (quasi-)uniform luminous panel; (c) The command box used for regulating the intensity of the light (circular button in the bottom with the counter) and for switching on/off the interior lighting fixtures (three buttons on the top).

In order to eliminate the influence of the ambient light, the whole setup was placed in a dark room available in the LESO building for lighting experiments.

4.6.3. Experiment Procedure

The luminance meter and the HDR vision sensor are located as indicated in Figure 4.46. The view point distance from the panel (60 [cm]) is chosen in a way that the whole panel fits into the luminance map (image) of the HDR vision sensor. The luminance of the zone encircled with 9 rings was also measured for the sake of luminance comparison. The

inner diameter of each ring is equal to 4 [cm]. The luminance of each ring is calculated by taking the average values of the corresponding pixels in the luminance map. The rings at the border of the luminance map, i.e. the rings numbered 1, 3, 7, 9 in Figure 4.46, correspond to the at least four pixels. The rings in the middle of the image correspond to a larger number of pixels.

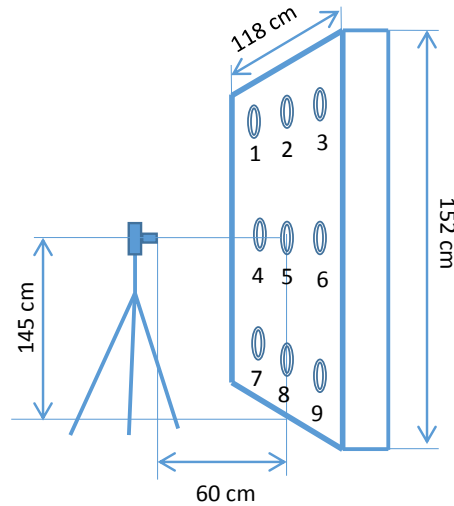


Figure 4.46 – Schematic representation of the experimental setup for uniformity verification. The relative position of the HDR vision sensor (IcyCAM) with respect to the luminous panel is depicted. The inner diameter of each circle on the panel is 4 [cm].

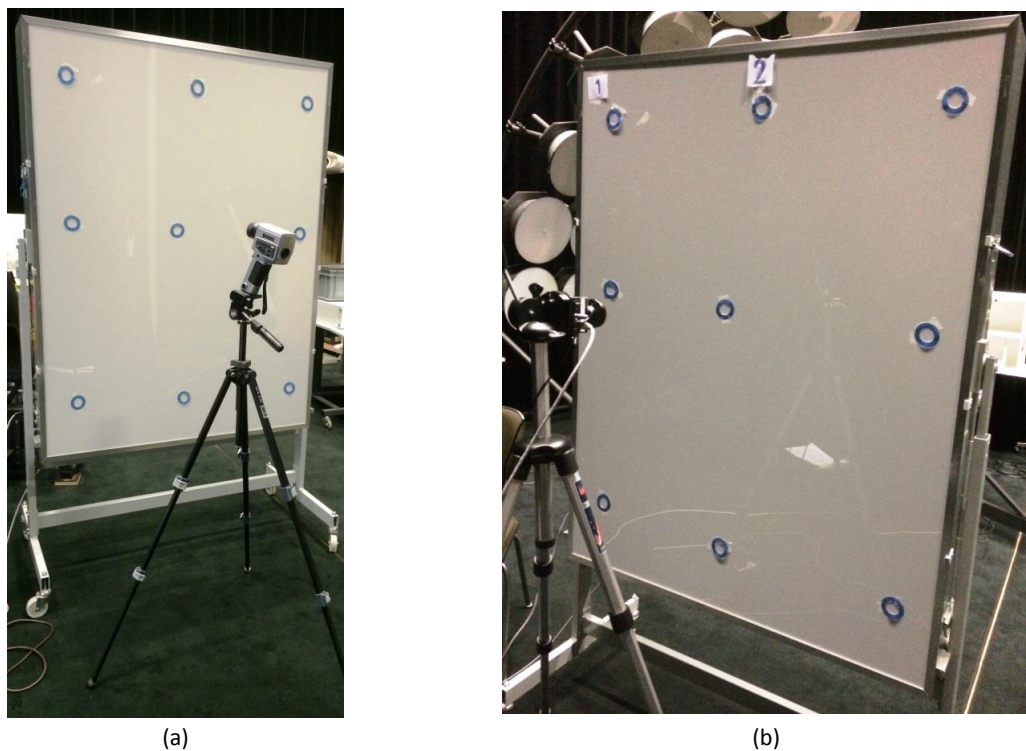


Figure 4.47 – Experiment procedure: (a) measurement of luminance by Minolta luminance meter. For measuring the luminance in the middle point of each circle the luminance is aimed at that point; (b) measurement done by installing the HDR vision sensor. The orientation of the sensor does not vary and it is fixed.

The luminance of the area located in the middle of each circle was measured first by the luminance meter. The panel setting was set to 000, 500 and 1000 by means of the potentiometer on the command box, corresponding respectively to a luminance of 251, 2148 and 4350 [$cd \cdot m^{-2}$] luminance of ring #5, measured by Konica Minolta LS-110, installed at the view point depicted in Figure 4.46. The setting of the potentiometer, which adjusts the dimming level of the electric lighting system of the panel, will be called “panel setting” in this text. The vision sensors were placed in the reference position; a digital image (luminance map) was created for each panel setting.

4.6.4. Experimental Results

In this section the results of the experimentation are presented. An example of luminance mapping is shown in Figure 4-48; the 9 circles located on the luminous panel are clearly visible.

Figure 4.49 shows the values obtained with the first sensor. Figure 4.50 illustrates the measurements of the second sensor. The author observed that the discrepancy between the measurements of the luminance meter (reference instrument) and the HDR vision sensor is negligible and almost constant throughout the whole field of view.

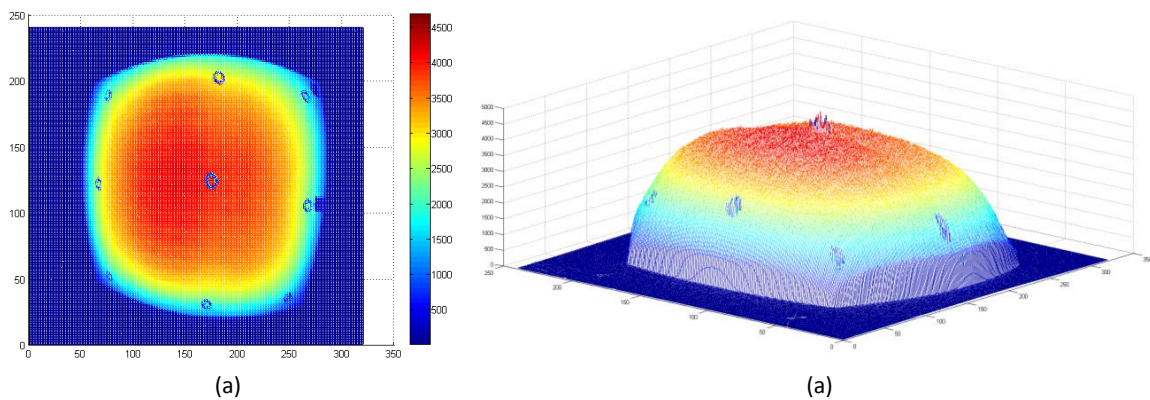
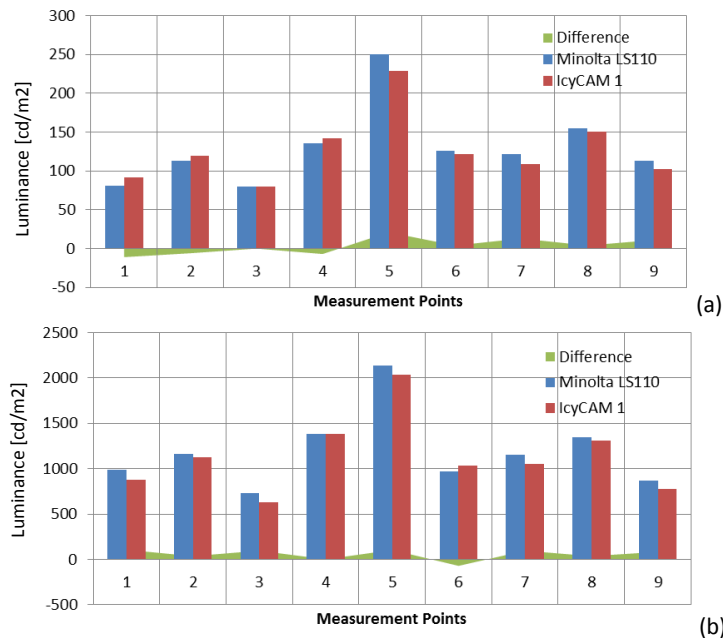


Figure 4-48 – Luminance map generated by the HDR Vision Sensor (IcyCAM) #1 with a luminous panel setting equal to 1000.



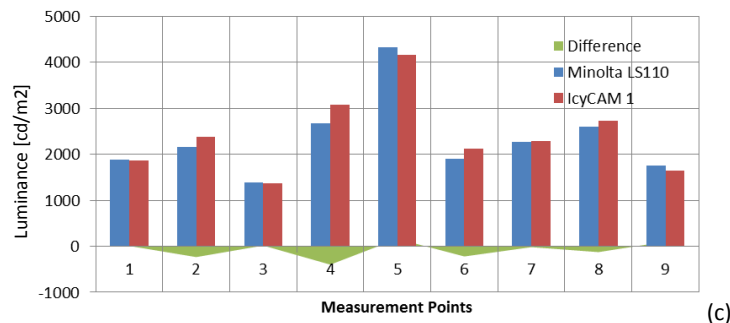


Figure 4.49 – Comparison of the luminance measurement captured by HDR vision sensor (IcyCAM) #1 and Minolta luminance meter ; (a) light panel setting :000; (b) light panel setting : 500; (c) light panel setting : 1000.

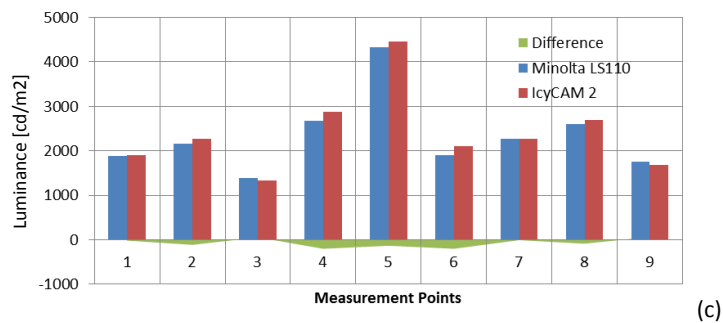
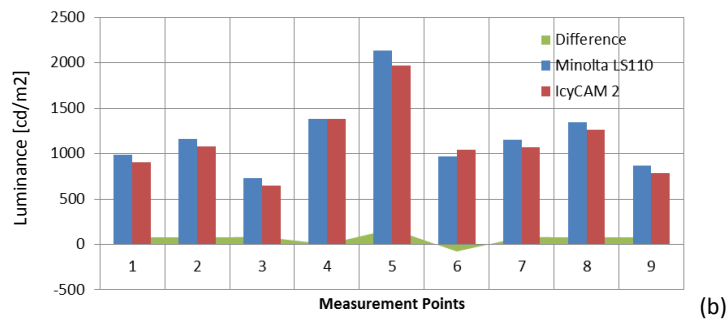
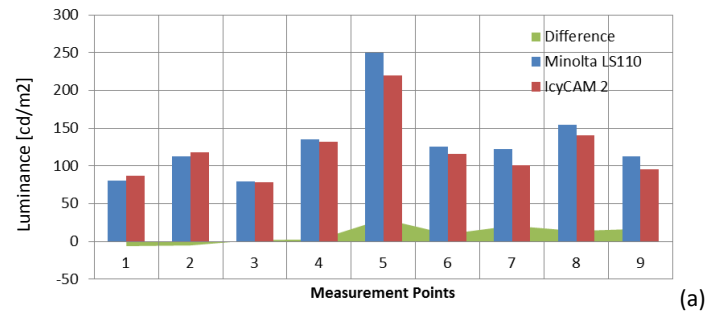


Figure 4.50 – Comparison of the luminance measurement captured by HDR vision sensor (IcyCAM) #2 and Minolta luminance meter ; (a) light panel setting:000; (b) light panel setting: 500; (c) light panel setting: 1000.

To summarize the depicted figures, the root mean square error of difference between the luminance measurements of HDR vision sensor and the Minolta luminance meter is calculated and summarized in Table 4.9.

$$RMSE = \sqrt{\frac{\sum_{i=1}^9 (L_{HDR,i} - L_{minolta,i})^2}{9}} \cdot 100 \quad [\%] \quad (4-28)$$

Where $L_{HDR,i}$ and $L_{minolta,i}$ are the luminance of i th circle on the light panel measured by respectively HDR vision sensor and Minolta luminance meter.

Light Panel Setting	IcyCAM #1	IcyCAM #2
000	7.80%	6.22%
500	7.86%	7.78%
1000	7.71%	8.98%
Average	7.79%	7.65%

Table 4.9 – Root mean square of percentage of relative error of luminance measurements by HDR vision sensor (IcyCAM) #1 and Sensor #2 for three different lighting panel settings.

Table 4.9 shows that there is a negligible discrepancy between the RMSE of measurements of two sensors.

The average of root mean square errors (average of all 6 values in Table 4.9) is 7.72 %. This value can be used for error indication in the charts resulted from HDR vision sensor measurements.

4.7. HDR Vision Sensor as Characterization Device

4.7.1. Introduction

For decades, work-plane illuminance has been used in many forms in the daylight factor and daylight autonomy, for characterizing the daylight performance of a building façade. However, this metric is not sufficient to assess the daylight performance while an occupant is present in the built environment. The reason is that, based on the experienced visual discomfort, the occupant may amend the shading position; the fact that influences the daylight performance of the façade considerably. In this case, the daylight autonomy or daylight factor would deviate significantly from the one predicted by the building designer. Thus, there is a need for a more comprehensive criterion for such intrinsically complex environment which is introduced in Section 4.7.2.

In this section, the experiments carried out during an exchange program in Singapore ETH Center (SEC) are detailed. The goal of this study is to experimentally quantify the *daylight performance* of a facade concepts named 3for2 concepts, utilized in the tropics. It is compared with a reference case, a normal facade with no shading installed in a testbed with daylight emulator. Daylight performance of a facade in this context is defined in terms of:

- i) the magnitude to which a facade provides the daylight to the deeper part of the building;
- ii) to what extent a facade creates glare conditions for occupants in a sitting position at different distances from the facade and different orientations.

The main difference between the testbeds is the design of their facade:

- 1) A vertical facade with no shading or any special architectural design, named SinBerBEST, which is considered as reference case and detailed in Section 3.2.1.
- 2) A novel facade design for tropics by Prof. Arno Schlueter and his team [165], i.e. a tilted facade named '3for2', which is described in Section 3.2.2.

In this work, three evaluation metrics were used to assess the lighting performance of the '3for2' building:

- i) The horizontal illuminance monitored at the height of a workstation (80 [cm]), normalized with respect to the horizontal illuminance measured in the interior close to the facade;
- ii) The vertical illuminance assessed at the eye level for a seated office occupant (120 [cm]);
- iii) The Daylight Glare Probability (*DGP*) assessed from the view point of a seated office occupant (120 [cm]) according to Figure 3.21 and Figure 3.24 by means of an HDR vision sensor (version VIP).

As reference, the horizontal illuminance at the facade is recorded. For the sake of equivalent comparison, this reference values is used to normalize the horizontal illuminances, shown in Figure 4.56.

In the next section, the result of the evaluations is presented and followed by two sections of discussion and conclusions. This scientific sojourn was financed by the Zeno Karl Schindler (ZKS) foundation and took place in January 2017.

4.7.2. Experimental Results

Sample images taken at position m_2 (according to Figure 3.21 and Figure 3.24) for four orientations in three different environments are shown in Figure 4.51.

The DGPs index and vertical illuminances are collected for 4 orientations. Their orientation of the vertical plan of measurement is indicated by (o_1, o_2, o_3, o_4) when o_1 is the vertical plan perpendicular to the facade. The definition of the orientations can also be found in the testbed description in Section 3.2. For more effective recognition of the correlations between the collected data, radar charts are suggested. These chart are presented in a 3 by 3 arrangement as shown in Figure 4.53 and Figure 4.55. The first row of the chart depicts the vertical illuminance. The second one is the DGP index and the last one is the normalized vertical illuminance.

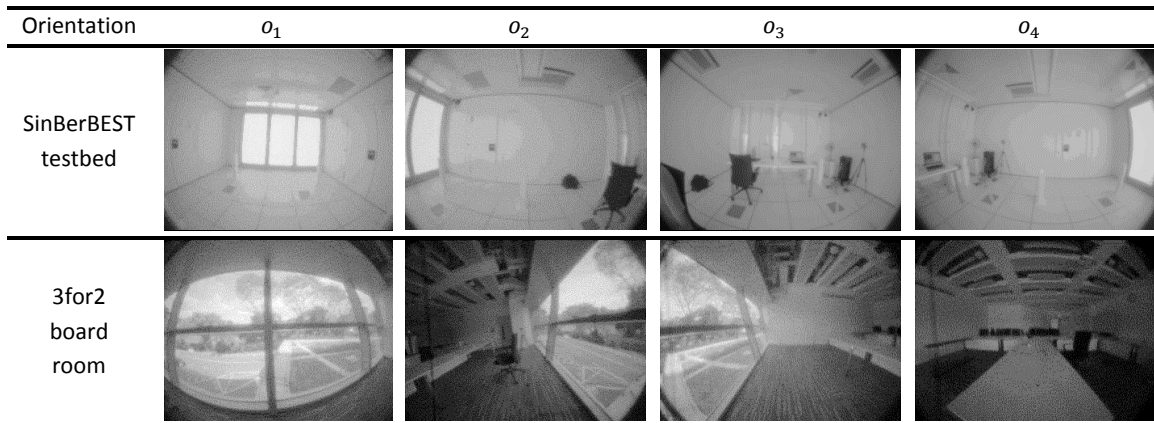


Figure 4.51 – Digital image captured by HDR vision sensor (VIP) for 4 orientations at position m_2 in three office working environments.

For the reference case, the SinBerBEST testbed, the horizontal illuminances (E_h) are shown in Figure 4.52. The figure shows that E_h is sufficiently high, i.e. more than 500 [lx] according to [142], in the measurement point at a distance of 1 and 3 [m] from the facade. Based on this piece of information, one may conclude that the lighting situation is favorable for a representative office occupant to performance normal office paper-based tasks. However, in practice this is not the only relevant criterion. The office occupant should be visually comfortable too. Figure 4.53 shows that the DGP index at a distance of 1 m from the facade for orientations o_1, o_2, o_4 exceeds 35%, the threshold for “perceptible” discomfort glare sensation defined in Table 2.1. This implies that, in such a condition, a representative office occupant would take appropriate measures, such as lowering a shading system, to mitigate the glare sensation. Consequently, the horizontal illuminance would be reduced with respect to the present situation, leading potentially to insufficient E_h and necessity for the use of electric lighting.

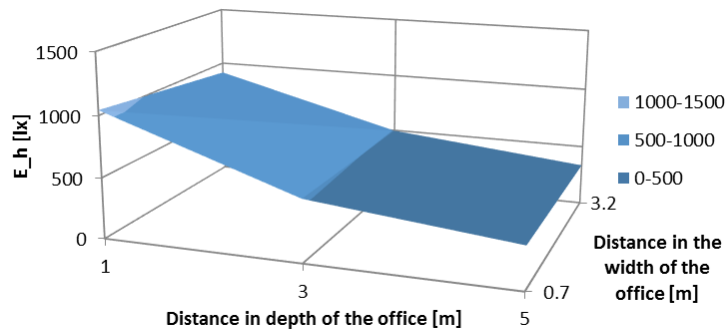


Figure 4.52 – Horizontal illuminance at the different distances from the facade of SinBerBEST testbed.

One observes in Figure 4.53 that the measurement values are relatively larger in the orientation perpendicular to the facade (o_1). Moreover, the measurements are attenuated as the measurement points are at the distance of 3 and 5 [m] from the facade (deep part of the building). The vertical illuminances (last row) are normalized with respect to $E_{h_{ref}}$.

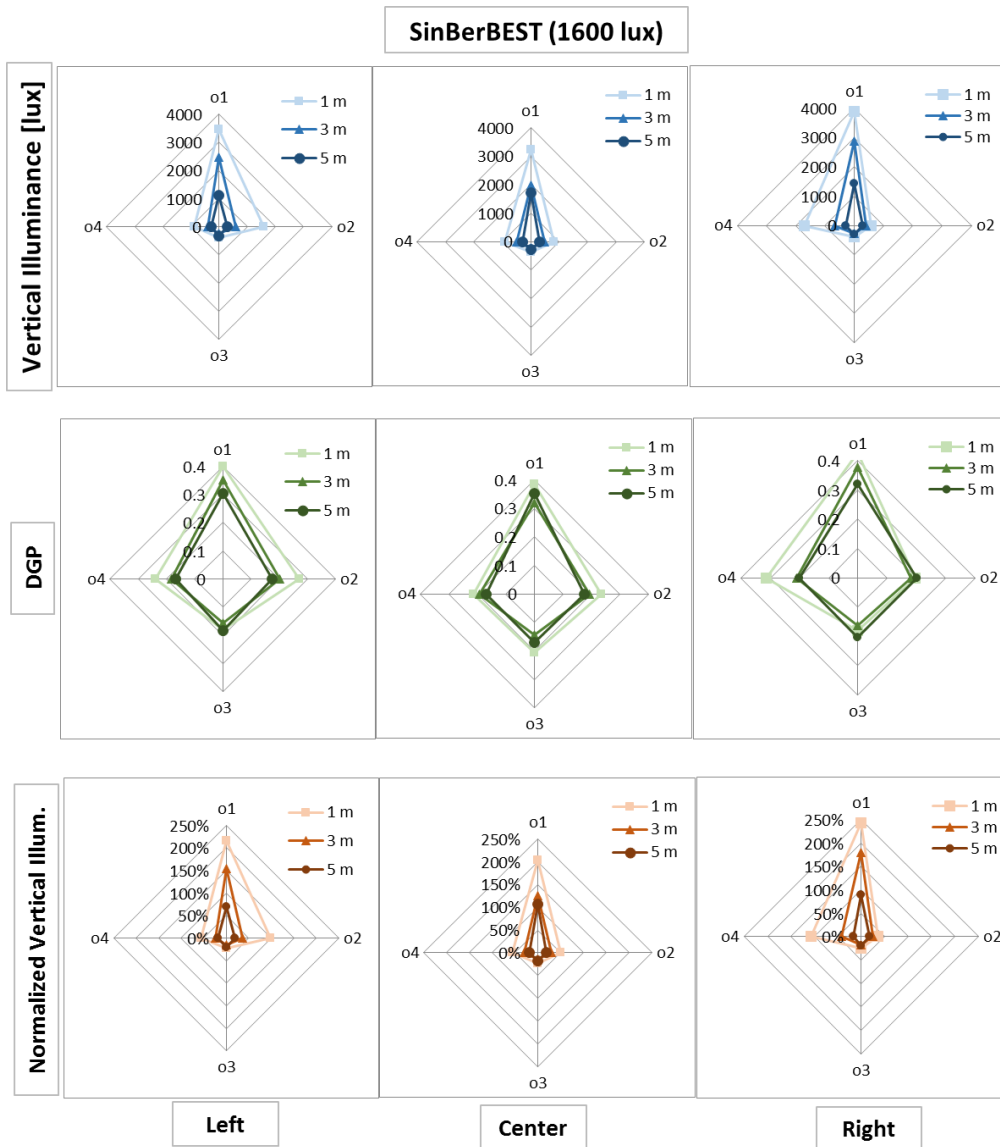


Figure 4.53 – HDR vision sensor readings summarized in radar charts for SinBerBEST testbed (reference case). The reference horizontal illuminance monitored at the inner side of the facade is 1600 [lx].

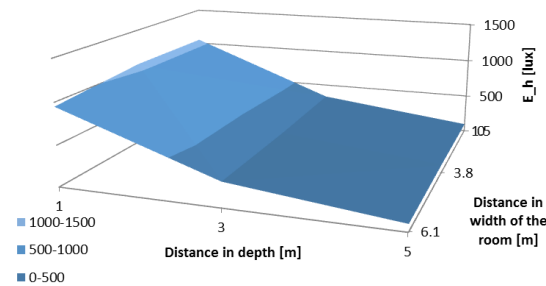


Figure 4.54 – Horizontal illuminance [lx] for 3for2 board room (advanced case), for 9 measurement points a shown in Figure 3.24.

In the advanced case, the situation is interestingly different. In the 3for2 board room, E_h at the measurement points at 1 m from the facade are higher than 500 [lx], which is sufficiently high for performing normal paper-based office tasks. Meanwhile, the DGP index for these measurement points is inferior to 30%, sufficiently small to be categorized as “imperceptible” discomfort glare (Table 2.1). In other words, in this building, an office occupant sitting at a workstation placed at a distance of 1 [m] from the facade finds the illumination conditions sufficient and comfortable.

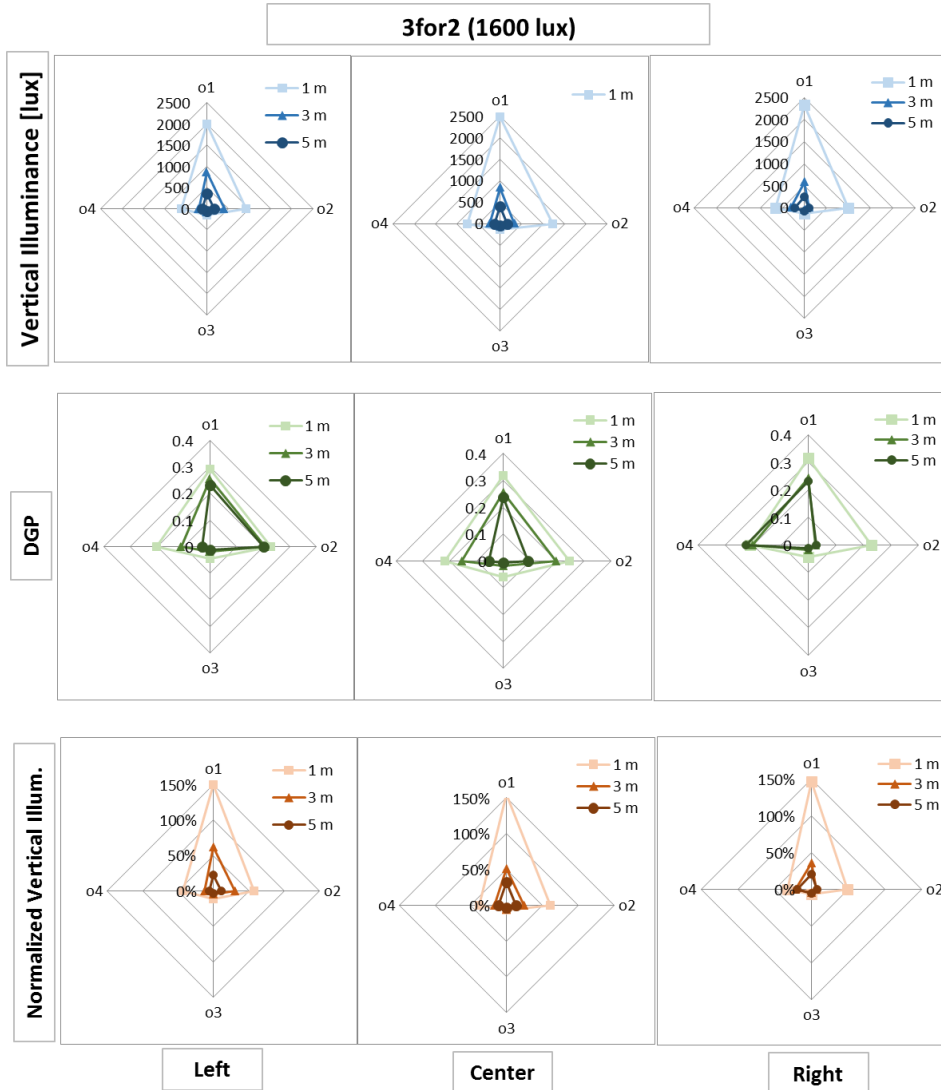


Figure 4.55 – HDR vision sensor readings for 3for2 board room(advanced case) summerized in radar charts.

Nonetheless, the situation in the deep part of the building, furthest from the facade, is more favorable in the reference case and there is deeper daylight penetration. To study this phenomenon, the horizontal illuminances normalized by $E_{h_{ref}}$ are compared in Figure 4.56. This figure is extracted from Figure 4.52 and Figure 4.54, by averaging the values in width of the rooms. This shows that, for comparable $E_{h_{ref}}$, which is 1600 lx for both cases, the horizontal illuminance in the 3for2 building is lower than the one in SinBerBEST. In other words, E_h diminishes when moving from 1 m to 5 m from the facade by 68% and 90% in the SinBerBEST testbed and 3for2 building respectively. This fact implies that the new facade design, due to smaller sky view factor, reduces the daylight penetration into the building in comparison with the traditional design.

In order to report the observed situations more clearly in a single figure, two new ratios are suggested: $\rho_{DGP,o1}$ and $\rho_{E_h,o1}$ according to Eq. (4-29) and Eq. (4-30).

$$\rho_{DGP} = \frac{DGP_{3for2,o_1}}{DGP_{SinBerBEST,o_1}} \tag{4-29}$$

$$\rho_{E_h} = \frac{E_{h_{3for2}}}{E_{h_{SinBerBEST}}} \tag{4-30}$$

where ρ_{DGP,o_1} is the ratio between the DGP indexes recorded in the advanced and the reference case for orientation o_1 [-]; DGP_{3for2,o_1} and $DGP_{SinBerBEST,o_1}$ are the DGP index recorded for orientation o_1 in the 3for2 board room and in the SinBerBEST testbed respectively [-]. Accordingly the ρ_{E_h} is the ratio between the horizontal illuminances in the advanced and the reference case [-]; $E_{h_{3for2}}$ and $E_{h_{SinBerBEST}}$ are the horizontal illuminances recorded in the 3for2 board room and in the SinBerBEST testbed respectively [-].

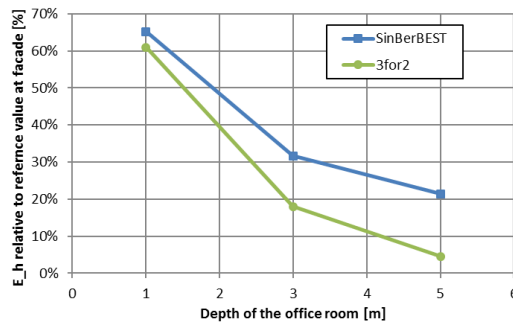


Figure 4.56 – Comparison of the normalized horizontal illuminances for SinBerBEST testbed (reference) and 3for2 board room (advanced), as a function of depth of the room [m].

These ratios are depicted in Figure 4.57. The average ρ_{DGP} obtained for nine measurement points is equal to 73%; suggesting that the lighting condition in the advanced case is more comfortable than that in the reference case. On the other hand, the horizontal illuminance at a distance of 5 [m] from the facade is reduced considerably, on average by 56%, in the advanced case with respect to the reference case. The latter suggests that daylight in the advanced board room penetrates less efficiently into the deep part of the building.

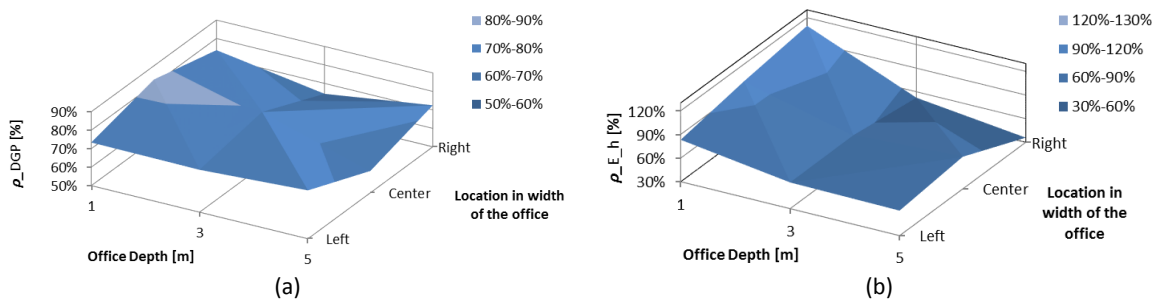


Figure 4.57 – ρ_{DGP} and ρ_{E_h} , evaluated based on Eq. (4-29) and Eq. (4-30). The location of 9 measurement points are depicted in Figure 3.22 and Figure 3.24.

4.7.3. Discussion and Conclusion

From the presented experiments, it can be observed that considering horizontal illuminance as a sole criterion for evaluating the daylight performance of a facade may not be sufficient for some situations when the visual comfort plays an important role. The reason is that, in practice, if the occupant experiences visual discomfort, he would amend the facade configuration, by using a shading system, so as to guarantee their visual comfort. In this case, even if the horizontal illuminance by daylight was sufficient (based on standards) for a paper-based task on a horizontal plan, the visual comfort constraints would urge the occupant to close the shading system and consequently use electric lighting to compensate the lack of daylight. In the 3for2 building, the occupants would probably not lower the blinds as they do not experience any discomfort glare, which leads to higher daylighting performance.

As shown in this case study, the innovative facade design provides comfortable and sufficiently lit spots for placing the workstation perpendicular to the window. However, the daylight penetration is worsened with respect to the reference case and electric lighting may be needed for the deepest part of the building.

The results of this study reveals the necessity for a more comprehensive criterion for evaluating the daylight performance of a facade, which encompasses not only the daylight sufficiency (e.g. daylight autonomy), but also the notion of the occupant's visual comfort. Especially with the recent improvements in technology and simulation, a vast number of designers and practitioners have access to appropriate tools for discomfort glare assessments.

It is worth mentioning that the interior design and the reflectance properties of the indoor surfaces are not necessarily equal in the three considered environments. In the 3for2 boardroom, for example, the ceiling is not white and has a dedicated plenum for the cooling installation; compared to the SinBerBEST testbed, the boardroom has a darker ceiling.

4.8. Optimal Location for HDR Vision Sensor

The goal of this study was to assess how realistic it is to consider the readings from a stationary vertically mounted sensor, installed in the vicinity of an office occupant, as an indicator of the actual exposure of the occupant to the daylight. To answer this question, four conceivable locations for the stationary sensor were chosen: on a tripod, on the desk lamp, on the visual display terminal and on the back wall.

This section is partly based on a work presented by the author in 2017 at the CISBAT 2017 International Conference on Future Buildings and Districts – Energy Efficiency from Nano to Urban Scale at EPFL Lausanne (Switzerland) and published in Energy Procedia [177].

4.8.1. Foreword

A correct measurement of the indoor lighting conditions is an essential aspect of a human centric approach in building automation [53]. Several wearable photosensors (Figure 4.58) have been studied showing that illuminance monitoring strongly depends on the position of the sensor on the body and on the lighting conditions (indoor vs. outdoor) [178]. An extremely low power CMOS glare sensor with a $32 \cdot 64$ pixels resolution was developed by Bhagavathula et al. [179]. Each pixel is activated if the impinging light ray intensity is larger than a user-tunable threshold. This equipment, however, considers glare rating on a pixel-based image and does not envisage it neither as an excessive vertical illuminance nor as contrast in the Field of View (FoV). A lightweight head-mounted device was developed to record radiation exposure estimates for both the visual and circadian systems [180]. It can record the illuminance in $[lx]$ and/or $[melanopic\ lx]$ with a frequency of 0.1-1 $[Hz]$. A multi-element subtractive glass filter matches the silicon photodiode response to the photopic luminous efficiency function.

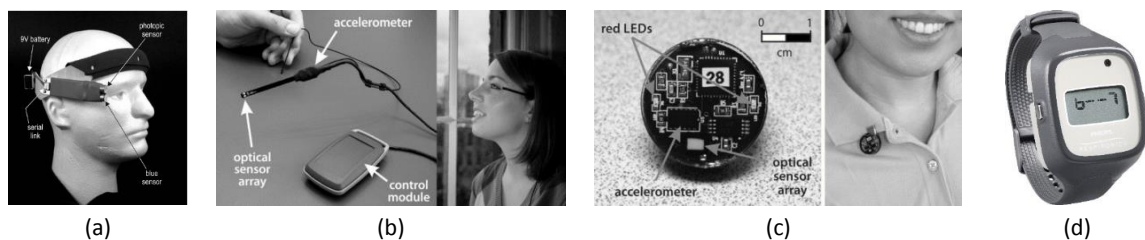


Figure 4.58 – (a) Daysimeter old version at 2005 [180], (b) Version S (2013); (c) version D (2013) [181]; (d) Actiwatch Spectrum by Philips.

The wearable equipment presented above has been shown to be an appropriate research tool but has clear limits for a practical marketable application in the built environment. For this reason, it remains preferable to use a stationary sensor located as close as possible to the occupant's eyes.

The HDR vision sensor measurements however inevitably differ from what the office occupant's eyes perceive. The main reason is due to the fact that the location and orientation of the sensor is fixed in the working space while the occupants FoV varies due to their natural movements. Appropriate placement of the sensor plays a crucial role in the performance

and acceptability of a sun shading and lighting control system whose main input is the glare rating from the user's view point.

On one hand, it is necessary to assess a possible discrepancy between the HDR vision sensor rating and the light flux perceived by the occupant; and on the other hand the optimal position and orientation for a steady sensor must be determined in order to minimize the geometrical offset between the HDR sensor and the occupant.

The goal of this field study is to quantify the covariance between the two instruments and consequently find the optimal position and orientation for the stationary HDR vision sensor.

This experimentation was carried-out during a one-year sabbatical sojourn of a Brazilian Researcher, Dr. Maíra Vieira Dias, at LESO-PB in 2016-2017. The reference *Oculux*™ sensor (Figure 4.59 (b)), was developed at University of Campinas, Brazil and was calibrated at EPFL. The relative accuracy of the RGB sensor is equal to 23% with respect to a calibrated illuminance meter (T-10 by Konica Minolta, Japan) for measurements in the range of 0 – 2500 [lx]. The author of this thesis contributed in an equal way to the Oculux calibration, to the performance of this experimentation as well as to the writing of a related article [177].

4.8.2. Methodology

4.8.2.1. Experimental Setup

The field studies were carried-out at the LESO solar experimental building in an office room located on the ground floor (room LE001). During the monitoring campaign, the shading system and the artificial lighting were managed automatically to guarantee the visual comfort of the occupant (by minimizing glare risks) and sufficient illumination on the workstation (by optimizing the work plane illuminance). The subject, on the other hand, was allowed to manually control the blinds using hand switches located in the room in order to tune the lighting conditions.

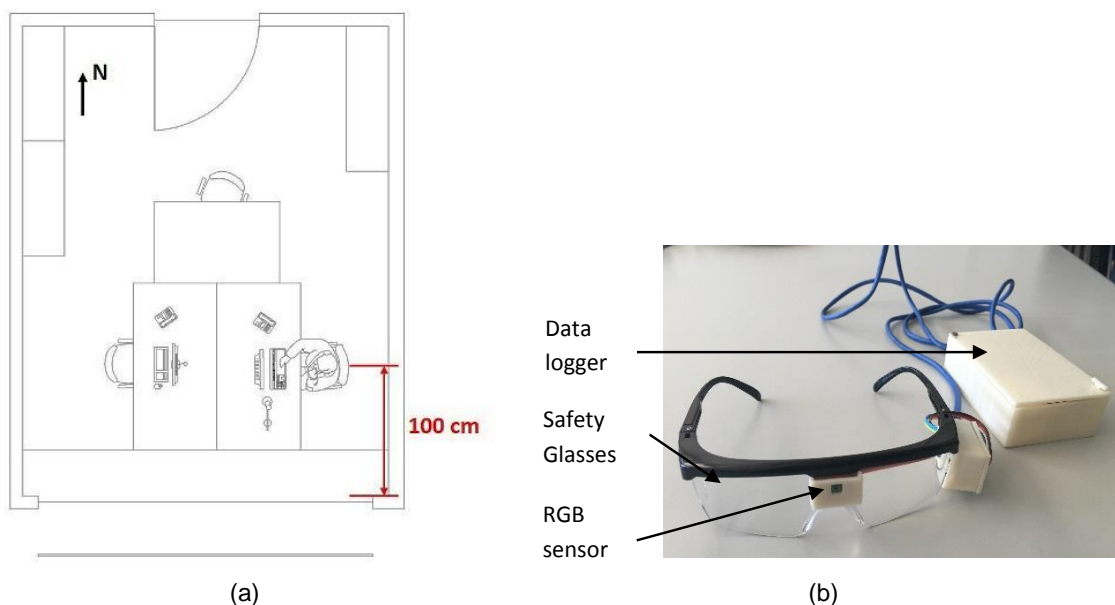


Figure 4.59 – (a) West-facing workstation occupied by the subject during the measurement campaign (plan to the scale); (b) “OcuLux”, wearable sensor evaluating real-time frontal illuminance. Courtesy of Maíra Vieira Dias.

4.8.2.2. Design of Experiment

The HDR vision sensor (version IcyCAM) was placed at four different locations as illustrated in Figure 4.60:

- i) On a tripod placed at 1.2m height (eye level) between the office occupant and the facade facing forward;
- ii) On the desk lamp between the occupant and the facade, slightly above eye level;
- iii) On the Visual Display Terminal (VDT) located on the workplane in front of the occupant;

iv) On the back wall at eye level behind the occupant and shifted toward the window.

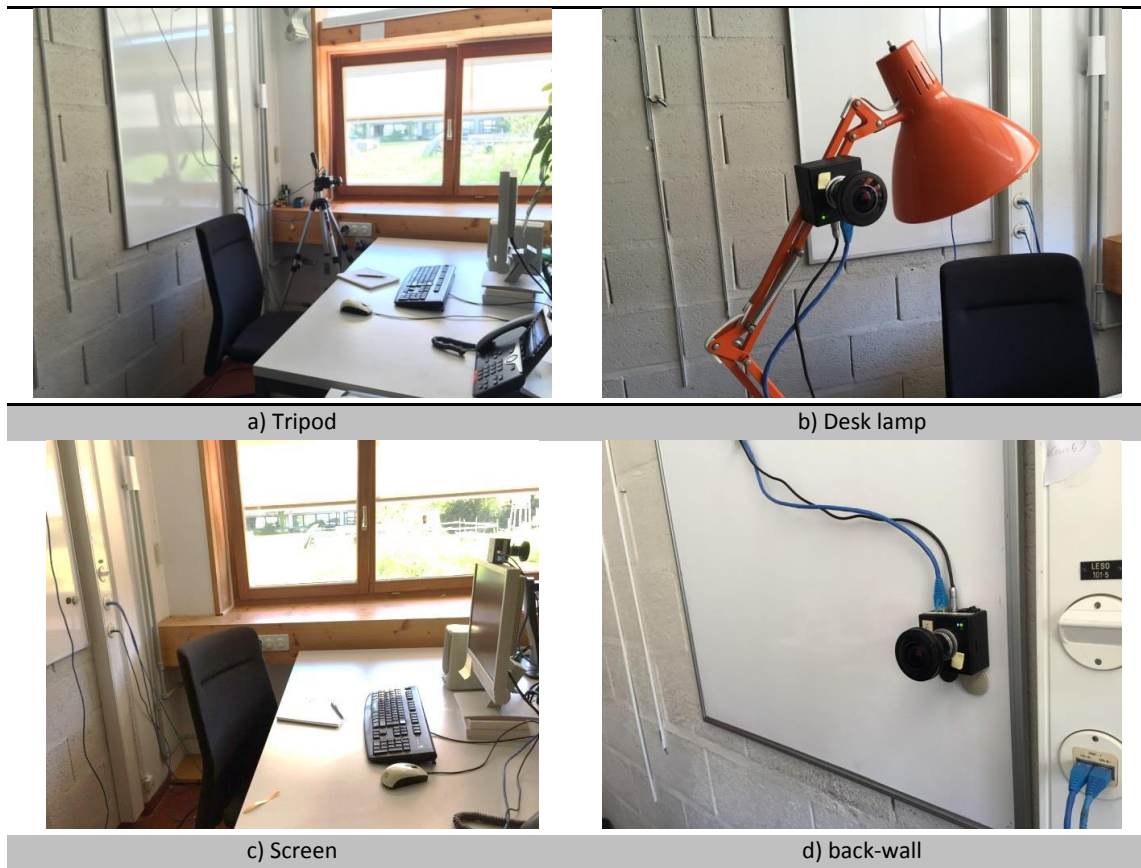


Figure 4.60 – Four locations of the HDR vision sensor during the experiment for evaluating its optimum location.

The precise locations of the HDR vision sensor with respect to the southern facade and the back wall are depicted in Figure 4.61.

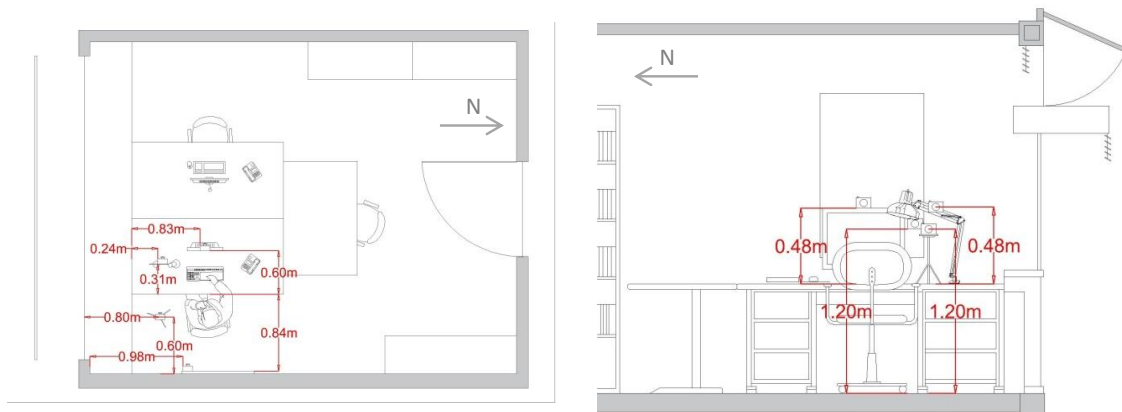


Figure 4.61 – Precise location of the HDR vision sensor during the experiment for evaluating its optimum location. Courtesy of Maira Vieira Dias.

The duration of the monitoring for each configuration was 5 days. This was long enough to cover all three sky conditions: clear (C), intermediate (I) and overcast sky (O). The weather conditions are classified based on the Sky Ratio (SR) model by Fakra et al. [182]. This model is elaborated in details in Section 6.2.2 (Eq. (6-8) and (6-9)). A thirty-year-old female human subject with normal vision (no corrective glasses) wore the OcuLux device for 20 full days from 8 AM to noontime as well as from 1 PM to 5 PM. The dates and the weather conditions are listed in Table 4.10.

Location	(a) Tripod					(b) Desk lamp				
Date [dd.mm.2016]	26.10	27.19	28.10	31.10	2.11	8.11	9.11	5.12	6.12	7.12
Weather	I	C	C	O	I	O	O	I	I	C

Location	(c) VDT					(d) Backwall				
Date [dd.mm.2016]	14.11	15.11	16.11	28.11	19.01 .2017	10.11	11.11	17.01 .2107	18.01 .2017	02.12
Weather	O	O	P	P	C	O	O	C	I	C

Table 4.10 – The weather condition during the experiment.

The criterion for comparing the reference sensor (e.g. the Oculux closer to the subject eyes) and the HDR vision sensor is the vertical illuminance [lx]. In order to compare the sensors, two parameters were used:

- i) Root Mean Square Error (RMSE) given in Eq. (4-31).

$$RMSE = \frac{\|X_{ref} - X\|}{N \cdot \text{mean}(X_{ref})} \cdot 100 \quad [\%] \quad (4-31)$$

This parameter can be used to find out the accuracy of the measurements by the HDR vision sensor.

- ii) Goodness of fit between the HDR sensor and the reference data incorporated in routine `goodnessOfFit` in MATLAB. The cost function is chosen to be Normalized RMSE and reported in relative fraction. NRMSE costs vary between $-\infty$ (bad fit) and 1 (perfect fit) [183]. If the fit is equal to zero, then the HDR vision sensor evaluation is worse than a straight line at matching the ones of Oculux.

$$G_{fit} = \left(1 - \frac{\|X_{ref} - X\|}{\|X_{ref} - \text{mean}(X_{ref})\|}\right) \cdot 100 \quad [\%] \quad (4-32)$$

where $\|\cdot\|$ indicates the 2-norm of a vector. This parameter can be used for estimating the appropriateness of the sensor location.

4.8.3. Experimental Results

A total of 18616 samples were collected by the Oculux and the HDR vision sensor during the whole experiment, i.e. on average 930 samples per day.

A sample of the gray-scale images taken by the HDR vision sensor at each location is illustrated in Figure 4.62. The window fraction visible in each image differs and should lead to discrepancies in the illuminance sensing anyway.



Figure 4.62 – Sample images captured by HDR vision sensor at (a) tripod; (b) desk lamp; (c) screen; (d) backwall .

Figure 4.63 shows two monitoring samples of the two sensors. In the first one, dated on 19 January 2017, the HDR vision sensor was placed on the VDT screen: an acceptable accordance between the two measurements is noticeable. The G_{fit} and $RMSE$ are relatively small.

During the 28 October 2016, while the sensor was installed on the tripod next to the occupant, the discrepancy between the readings of the two sensors is considerable. Since the HDR vision sensor is closer to the facade, it senses larger illuminances in comparison with Oculux data.

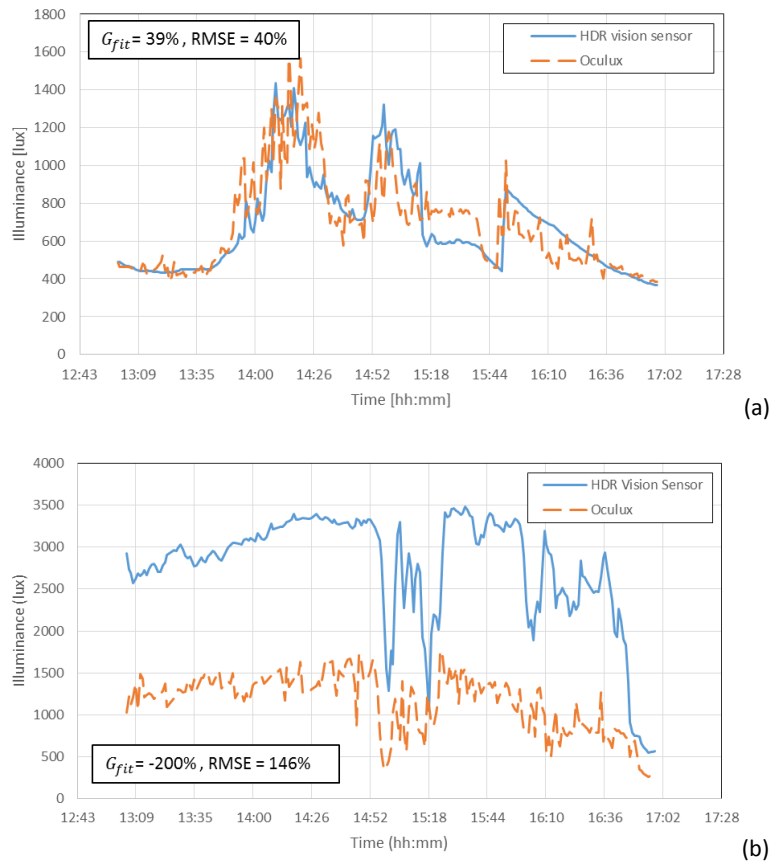


Figure 4.63 – Comparison between HDR vision sensor and Oculux monitoring data; (a) with a large goodness fit while the sensor is mounted on the VDT screen; (b) with a small goodness fit while the sensor is installed on a tripod. Accuracy for Oculux is 23% and for HDR vision sensor is 10%.

Figure 4.64 shows the goodness of the fit for the HDR vision sensor installed at four locations. For each one, ten bars are plotted, depicting the G_{fit} for a half-day period: the first bar corresponds to the morning of the first day, the second one corresponds to the afternoon of the first day and so on. This figure shows that the fit for the HDR vision sensor on a tripod is the lowest (worst) among those of four locations. The average of all fit values for each location is illustrated in Figure 4.68 (a).

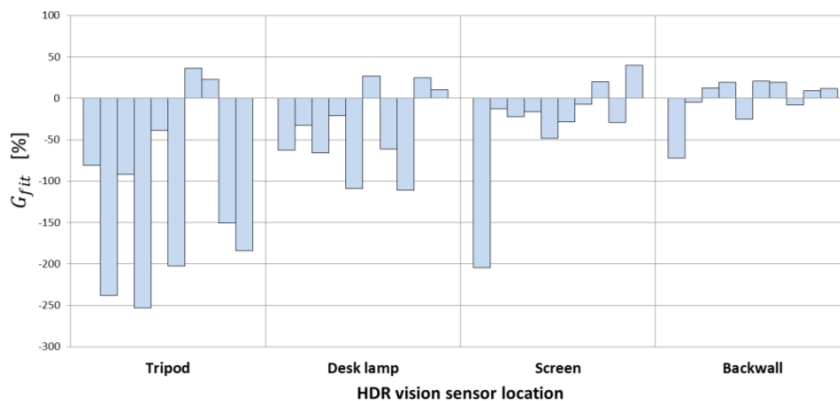


Figure 4.64 – Goodness of fit for different locations of HDR vision sensor (IcyCAM) . Each bar corresponds to half a day (morning/afternoon) of experiment.

Figure 4.65 shows that the RMSE of the measurement of the sensor located on the back wall is not significantly lower than the ones of the sensor placed on the VDT screen or the desk lamp. The average values, illustrated in Figure 4.68(b), reveal that the RMSE standard deviation for the desk lamp, screen and back wall are matching.

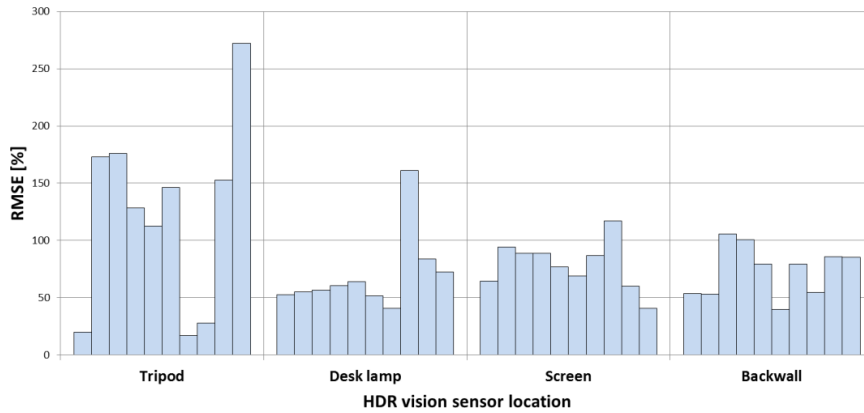


Figure 4.65 – RMSE for different locations of HDR vision sensor (IcyCAM). Each bar corresponds to half a day (morning/afternoon) of experiment.

As a second step, the effects of the *time of the day* on the evaluation criteria are evaluated. In Figure 4.66 (a), the average of the RMSE between the evaluation of HDR vision sensor and Oculux are demonstrated for 4 positions of the HDR vision sensor, categorized by morning and afternoon. Thus, each bar shows the average of *RMSE* for 5 mornings/afternoons and the error bars show the Standard Error of Mean (SEM) for a 95% confidence interval during the corresponding period. (Eq. (4-33))

$$SEM = 1.96 \cdot \frac{\sigma}{\sqrt{N}} \quad (4-33)$$

where σ is the standard deviation of the data set and N is the number of the samples per data set.

As the RMSE bars are matching during the morning, there is not a significant difference due to the location of the HDR vision sensor. However, the average *RMSE* for the tripod is larger than the ones registered for the other cases during the morning.

The situation during the afternoon is different: there is a statistically significant difference between the RMSE of the tripod and the HDR vision sensor locations. The p-values of two-tailed distribution for a two-sample unequal variance (heteroscedastic) are 3.56% for the tripod-desk lamp, 3.91% for tripod-VDT screen and 2.1% for tripod-back wall. On average, the back wall setup leads to lower RMSE in comparison to other cases.

For the goodness of the fit during the afternoon, shown in Figure 4.66 (b), the same trend is observable: the G_{fit} in the morning does not differ in statistically significant way for different locations of the HDR vision sensor. Nevertheless, in the afternoon, the same t-test leads to significant differences between the tripod configuration and other cases: p-values are 4.1% for tripod-desk lamp, 2.44 for tripod-VDT screen and 2.27% for tripod-back wall. On average, the back wall configuration leads to higher G_{fit} .

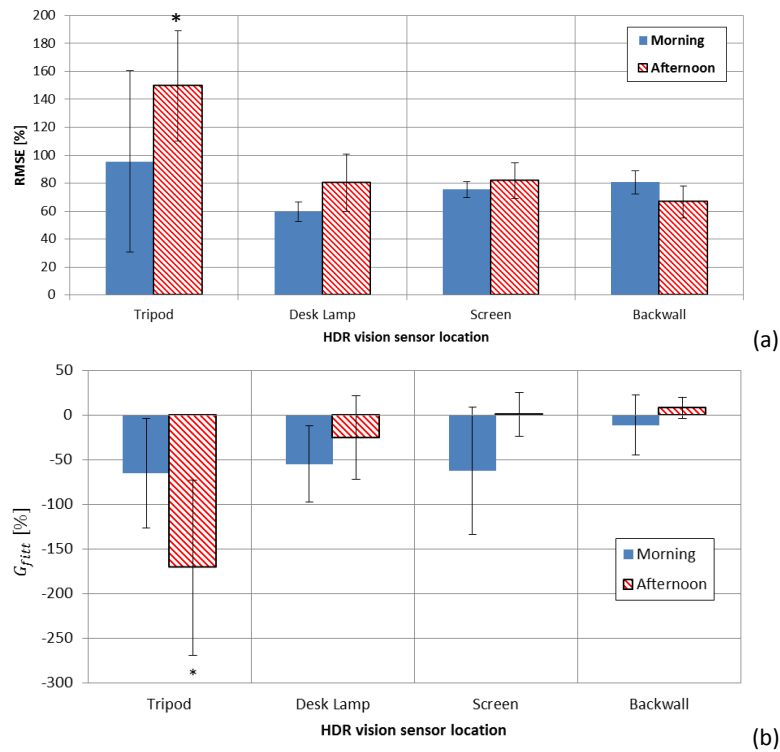


Figure 4.66 – Comparison of HDR vision sensor and Oculux illuminance evaluation for morning and afternoon. (a) RMSE; (b) G_{fit} .

In the next step, the effect of sky conditions on the comparison criteria was studied. The criteria are categorized into three sky conditions: clear, intermediate and overcast skies; the RMSE and G_{fit} are illustrated in Figure 4.67. The results show that for an overcast sky, the differences between goodness of fit between the different HDR sensor locations are not statistically significant. However for clear and intermediate sky conditions, the tripod configuration shows the lowest G_{fit} in comparison to other configurations and the difference is significant: p-values for clear sky conditions (t-test, 95% confidence interval, double tail, unequal variance) is 3.16% for tripod-VDT screen and 5% for tripod-back wall. For intermediate skies, the situation is similar: the goodness of fit for the tripod configuration is significantly lower than those of the other cases: p-values are 0.87% for tripod-desk lamp, 0.70% for tripod-VDT screen and 0.76% for tripod-backwall.

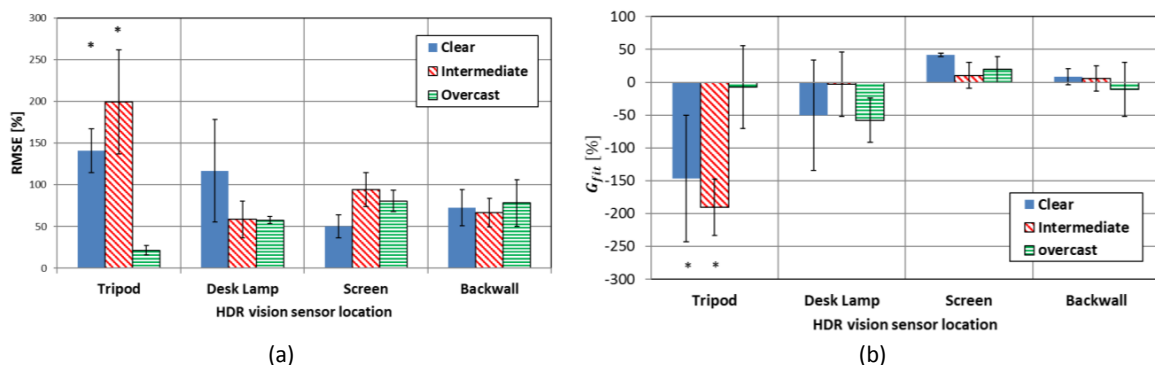


Figure 4.67 – Influence of the weather condition on the goodness of fit for different positions. (a) RMSE; (b) G_{fit} .

A summary of the two criteria for four HDR vision sensor locations is given in Figure 4.68. It shows that on average the best fit is obtained by placing the vision sensor on the back wall. This location is significantly more accurate than the sensor on tripod (p-value = 0.6%). For the RMSE, there is no significant difference between the configurations, but the back-wall case reveals on average to have the lowest RMSE among four configurations.

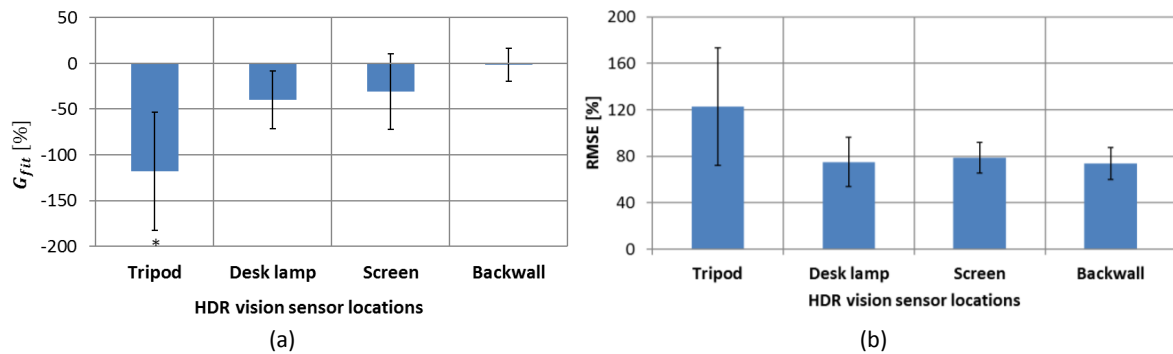


Figure 4.68-Summary of (a) G_{fit} values (b) RMSE for four locations of HDR vision sensor.

4.8.4. Discussion and Conclusion

The Oculux sensor is basically an RGB sensor that approximates the illuminance: it leads to a considerably low accuracy with respect to the reference illuminance meter (Konica Minolta CL-200). However, as it takes into account the head movement of the occupant, it offers a unique opportunity to capture the lighting dynamics perceived by the occupants. Moreover, the Oculux RGB sensor does not provide any quantitative information regarding glare sensations leading to a limited investigation field, which includes the vertical and frontal illuminances.

The tripod configuration shows generally larger values than the Oculux device. The distance of the HDR vision to the facade is 80 [cm], while in the other configurations, it reaches 87 [cm], 98 [cm] and 118 [cm] for the desk lamp, the VDT screen and the back wall respectively. The sensitivity of the distance from the window on the goodness of fit is large: the closer the stationary HDR sensor is to the occupant's view point, the better the goodness of fit of the estimation is.

During the overcast sky condition, as the diffuse daylight is predominant indoors, the geometric offset effect is reduced. Nonetheless, for clear and intermediate sky conditions, where the directionality of the incident daylight flux on the facade becomes important, the tripod configuration loses its accuracy in estimating the actual light perceived by the occupants.

The back wall configuration leads to a largest G_{fit} with respect to the Oculux data since a fraction of the HDR sensor view field is obstructed with the occupant. It is worth noting that in this case, the windows remain fully visible by the vision sensor (Figure 4.62 (d)). Daylight penetration through the windows contributes in a major way to the illuminance sensing; as the window remains fully exposed to the HDR sensor, the goodness of fit remains relatively better with respect to other configurations.

On the other hand, although the vision sensor on the VDT screen is placed almost at the same distance from the window as in the back wall configuration, the goodness of fit for the VDT screen configuration is better (Figure 4.68(a)). This difference is however not statistically significant: it may be due to the fact that for the VDT screen, the window is not fully visible from the HDR sensor (Figure 4.62 (c)).

As a conclusion, the author found out that, among four HDR vision sensor locations, installation on the back wall leads to the highest accuracy and best goodness of fit. It can also be noticed that the closer the stationary HDR sensor is to the window, the lower the accuracy of vertical illuminance as indicator of the actual exposure of the occupant to daylight. The time of the day and sky condition have a statistically significant impact on the accuracy of the measurements.

Having performed the calibration process and the preliminary experiments, one can answer the first research question raised in Section 1.3 by stating that "by means of a calibrated, adapted HDR vision sensor, visual comfort indices can be integrated in BMS."

Chapter 5

In-situ Monitoring in LESO building

In this chapter, two different in-situ experiments are considered to address the second and third research question raised in Section 1.3:

- What is the impact magnitude of such a novel system on electric lighting energy demand and user acceptance in a single occupied office room?
- *Is it possible to improve the energy performance of a building, to reduce its CO₂ emission and to mitigate a possible performance gap without jeopardizing the occupant's visual and thermal comfort?*

In Section 5.1, the principles of fuzzy logic control are presented. In Section 5.2, a short-term in-situ experiment performed during 15 afternoons in October and November 2015 is described. An overview of the results of this section was published as a journal paper by Motamed et al. [79] and the concept of “fuzzy logic control reliability” was patented [184]. Section 5.3 details long-term in-situ experiment carried out in the same office rooms from August 2016 to March 2017. In both sections, the approach and experimental results are presented and discussed. For a complete description of the characteristics of the LESO Building testbed, one may refer to Section 3.1.

5.1. Fuzzy Logic

The advanced controller in both our short-term and long-term experiments with human subjects relies on Fuzzy Logic Control (FLC) and a patented concept (i.e. “reliability”), expressed in Section 5.2.1 by Eq. (5-3), is based on a Fuzzy Logic Inference System (FIS) [185], [186]. A brief introduction to fuzzy logic was given in Section 2.3.5. In this paragraph, the approach is elaborated in more detail.

5.1.1. Fuzzy Sets

We assume that the horizontal workplane illuminance in an office room is an indicator of the lighting conditions offered to the occupant. Consider the problem of classifying indoor lighting conditions based on the horizontal desk illuminance in two different sets, expressed by the linguistic terms “*Too Bright*” or “*Comfortable*” related to visual comfort. A classical set theory would consider an element is either a member of a set or not. In this case, if one defines comfortable lighting conditions by a workplane illuminance lower than a threshold of 2000 [lx], an office room with a horizontal desk illuminance of 1000 lx can be assigned to the set *Comfortable*. However, pleasant lighting conditions with a workplace illuminance slightly higher than the threshold, e.g. 2100 [lx], would be assigned to the same set *Too Bright* to which a desk illuminance of 10'000 [lx] would also belong. Thus, by applying a fixed numerical threshold for classification, such as the classical logic theory, there is no distinction in a set and all members belong equally to the same group.

Fuzzy sets do not face the same difficulty: two lighting conditions may belong to the same set but to a different degree. As an example, an office room with a 2100 [lx] workplane illuminance would be member of the set *Too Bright* to a degree of 0.05; while the one with 10'000 [lx] has a membership degree of 0.90.

5.1.2. Fuzzy Inference System

The fuzzy set concept, firstly introduced by Zadeh [135], is applied throughout the present study. For a brief introduction to the Fuzzy Inference System (FIS), as a system that is built upon the fuzzy set concept, the reader is referred to [185], [187], [188].

A FIS is composed of five steps to map the inputs to the output and it is depicted by a simple example in Figure 5.1.

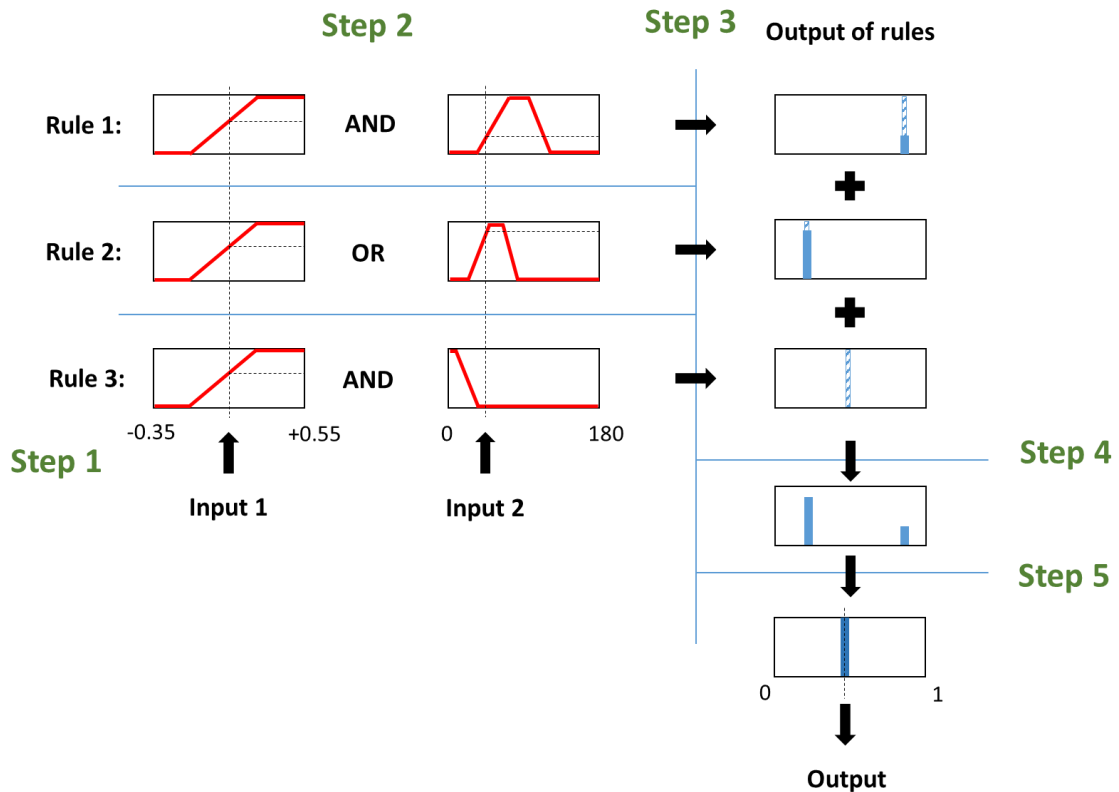


Figure 5.1 – The principle of Fuzzy Inference System (FIS), adopted from [187].

Step 1) Fuzzify inputs: Input values are examined and their membership degree to each of the appropriate fuzzy sets is determined. *Membership functions* are used in this step. The inputs values to membership functions are crisp numerical values limited to their universe of discourse. For the present example, the membership functions are shown by a red solid line. The first input is bound to $[-0.35, 0.55]$; the second input acceptable range is $[0, 180]$. The outcome of this step is a fuzzy degree of membership of an output in the qualifying linguistic set. This membership degree is always comprised between 0 and 1. For more details on membership functions one may refer to Mamdani et al. [189]. The membership functions for this doctoral thesis are listed in Appendix A.

Step 2) Apply fuzzy operators: Having fuzzified the inputs, the magnitude of influence of the various inputs on each rule of the FIS is found. Any logical operator such as AND, OR and NOT, can be used for obtaining one number that represents the result of the antecedent for that rule. The rules may have different weightings (ranging from 0 to 1). The weighting for each rule is multiplied by the output of the rule. In Figure 5.1, each row corresponds to one fuzzy rule. On the left hand side, the antecedent of a rule and on the right the consequent are shown. In this example, each rule has 2 inputs and 1 outputs. Unlike input values, the output can feature membership functions in the form of fuzzy sets (formulated for the first time by Mamdani et al. [189]) or crisp constant values (formulated for the first time by Sugeno et al. [190]).

The latter is computationally more efficient than the former. In the examples shown in Figure 5.1, the outputs are crisp numerical values represented by vertical blue hashed/solid blocks.

Step 3) Apply implication method: Once the result of applying fuzzy operators on the antecedent is obtained and multiplied by the weighting of the rule, the implication method is applied for that rule. By this method, the output fuzzy set is truncated according to the result of the antecedent. This method, illustrated in Figure 5.2 by a simplified example, is demonstrated on the right hand side of the image where the green horizontal dash line (result of the operators on the antecedent) truncates the *output crisp function* to find out the final implication result (solid black block). The fuzzy value of the truncated crisp output (height of the solid black block in the right-hand chart in Figure 5.2) shows the degree to which this rule is accountable for its output (decision): the larger the truncated output value is, the more the decision is justified and the rule is applied. This notion will be recalled later in the definition of FIS reliability, Eq. (5-3).

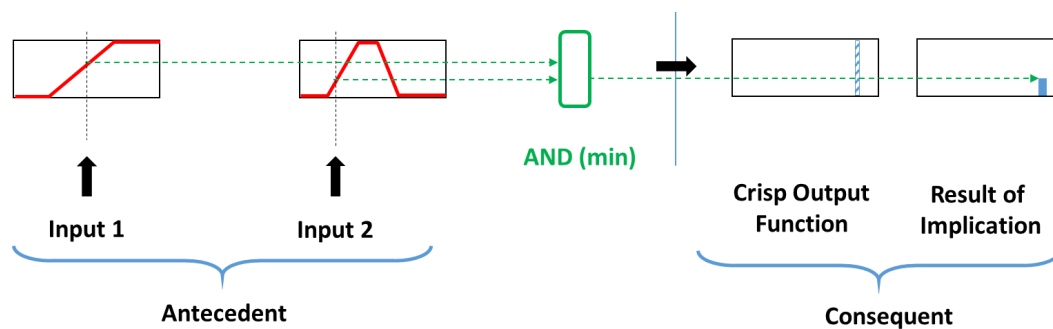


Figure 5.2 – Schematic example of the implication method representing the third step of FIS.

Step 4) Aggregate all outputs: In the fourth step of the procedure, all outputs of the rules are combined. They should be combined in a way to be able to draw a final decision. This process is called *aggregation*, where the outputs of each rule are merged into a single value. The input of the aggregation process is the list of truncated output functions returned by the implication process for each rule. The output of the aggregation process is one fuzzy set for each output variable. The rule order in this procedure is not important. In Figure 5.1, this step is symbolized by “+” signs on the right hand side of the figure. In the current example, the rules outputs are summed up to form the aggregated output value. The fuzzy sets of outputs are used in Section 5.2.1 by Eq. (5-3) to derive the “reliability” of the FIS.

Step 5) Defuzzify: In this step, the final output value of the FIS is generated. The input to this step is the fuzzy set, resulting from the aggregation step; the output is a single crisp value for each output of the whole FIS system. Different method can be applied at this step, such as the centroid and dissector methods. In the present work, the centroid method is utilized, demonstrated by Eq. (5-2). As shown in Figure 5.1 in the bottom corner of the figure, by applying this last step a single output value is produced in the form of the weighted sum of the output fuzzy rule sets.

5.1.3. Fuzzy Logic Control

One of the applications of fuzzy logic is system control. As opposed to a classical control approach based on differential equations, a Fuzzy Logic Control (FLC) is control with sentences, e.g. based on linguistic terms. Mamdani and Assilian [189] applied this control approach for the first time in 1975 to a steam engine. This method provides an effective means of modeling the inexact nature of the World and therefore is much closer to the way a human thinks and describe reality. This control strategy is summarized in Figure 5.3 according to Daum [191]. In the present work, the system under fuzzy control is composed of the HDR vision sensing and actuating systems installed in the advanced office room of the LESO building (Section 3.1.3). FLC is the block labeled as “FLC” in Figure 5.4 (b) as well as the block labeled “Shading Controller” in Figure 5.15 for the advanced control.

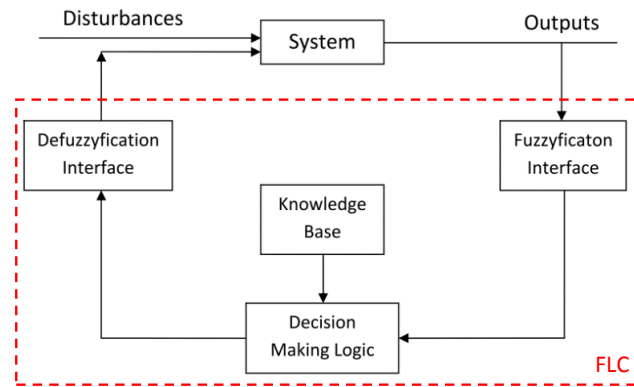


Figure 5.3 – Schematic block diagram of Fuzzy Logic Control (FLC) [191].

5.2. Short-term Experimentation

In this section, the methodology and results of the short-term experimentation are presented and discussed.

5.2.1. Reference and Advanced Controllers

A reference control system has been implemented in one of the office rooms: a ‘Best-practice’ controller, currently used by the Swiss lighting industry, was chosen for that purpose in order to set up a sound and fair reference system for an objective comparison of control approaches (Figure 5.4(a)). It relies only on a ceiling-mounted luminance meter located beneath the LED luminaries: both shading devices and artificial lighting system are managed by the controller. In the other office room, an advanced control system was installed. This Fuzzy Logic Controller (FLC) uses the Daylight Glare Probability (*DGP*), the work-plan illuminance E_{desk} and the solar profile angle to determine the optimal shading position in the upper window as well as the electric lighting dimming status. The two different controllers are presented in the following paragraphs.

The ‘Best-practice’ control system considers the variable measured by a ceiling mounted low cost luminance meter as input signal for the controller. The control rule base is as follows:

$$(\gamma_{light}, \gamma_{top}, \gamma_{bottom}) = \begin{cases} (1,1,1) & \text{if } E_{desk} < 200 \text{ lx} \\ (0,0,1) & \text{if } 2000 \text{ lx} < E_{desk} < 3000 \text{ lx} \\ (0,0,0.5) & \text{if } E_{desk} > 3000 \text{ lx} \end{cases} \quad (5-1)$$

where γ_{light} is the electric lighting status, γ_{top} is the opening fraction of the shading system of the anidolic window, γ_{bottom} is the opening fraction of the shading system of the plain window. The thresholds were chosen by trial and error before the main subjective assessment campaign was initiated. The dead-bands should be sufficiently large to avoid any instability issues and to prevent too frequent shading and lighting operations.

A time dependent filter, explained in the next section, is applied to the output control signal (e.g. the command). The bottom window area is not occulted more than 50% in order to allow a visual contact with outdoors. The control signal is directly sent to the actuation system moving the blinds without passing through any command filtration process.

The advanced controller is designed and based on three principles:

- **User comfort:** The visual comfort of the users is a first priority for the control of the shading system and the artificial lighting. The number of sun shading and lighting amendments during work hours is kept as low as possible;
- **Electricity demand:** The second priority is given to the daylighting flux; the electric lighting being used as a complement;
- **Flexibility and robustness:** The control strategy is kept as simple and flexible as possible in order to facilitate its implementation in other office buildings and reduce the number of parameters to tune during commissioning.

The advanced control strategy illustrated in Figure 5.4(b) can accordingly be described as follows. In a first step, the DGP, the work plane (horizontal) illuminance E_{desk} and the current time t are taken into account; the FLC determines the new positions of the top and bottom blinds. Glare sensations due to daylight are avoided and a sufficient work-plan illuminance is provided, if possible. In order to be able to compare the controllers, the thresholds of all FLC membership functions as well as the electric lighting controller are equal to those of the reference controller (Eq. (5-1)). The actuators enforce new positions if they successfully pass the criteria defined in the *time dependent*, *minimum step* and *controller reliability filters*. These filters are explained in the following lines.

The time dependent filter, inspired by Lindelöf [20] and Guillemin [156], prevents too frequent shading amendments by forbidding any movement during 15 minutes after the precedent one. If the command passes the time filter, the command is considered by the minimum step filter, e.g. the movement is executed if it is larger than the minimal value $\Delta\alpha$. In this study, $\Delta\alpha = 30\%$ is equal to, e.g. 30% of the window height; this value is halved if the new window opening fraction is smaller than the current one.

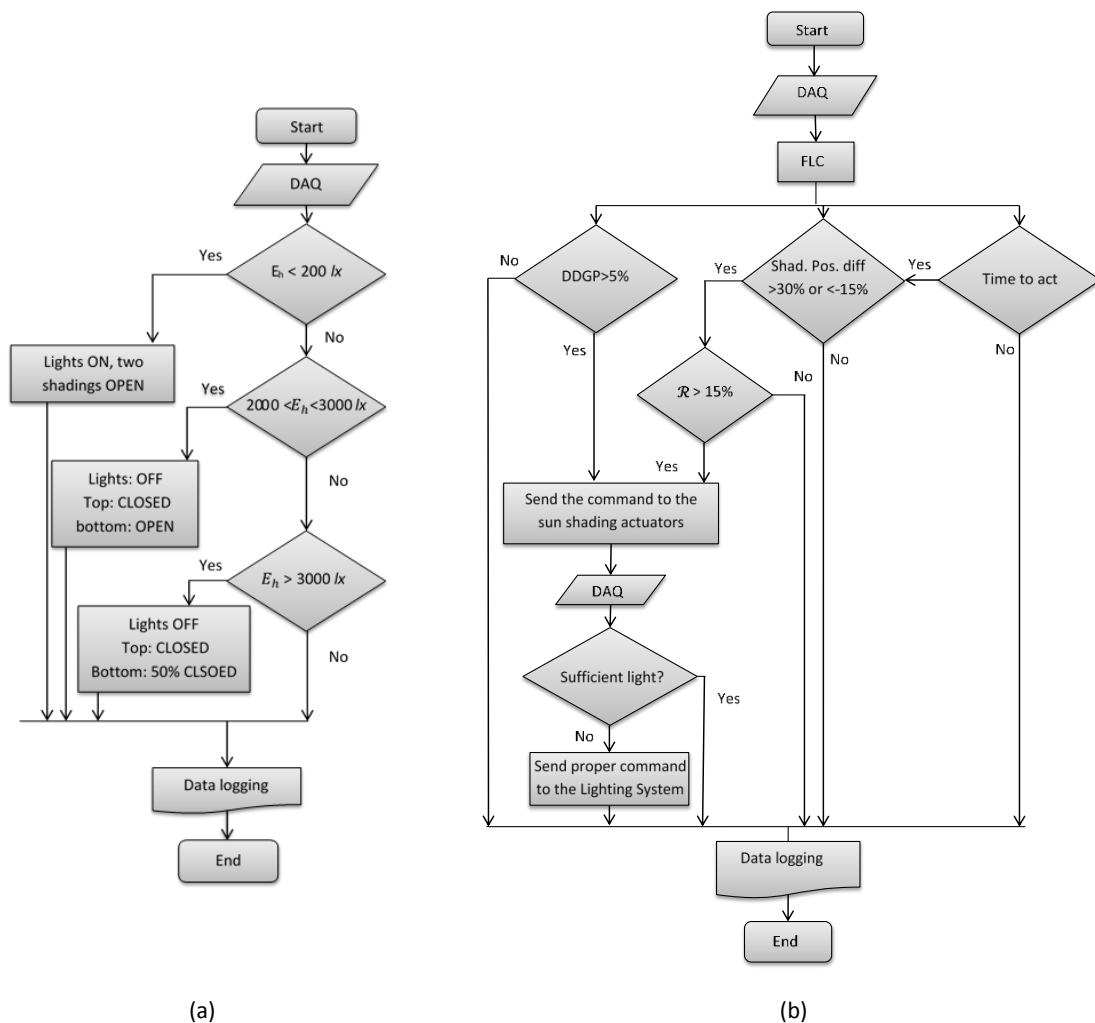


Figure 5.4 – Block diagram of the (a) reference and (b) advanced controller for the short-term experiment.

Finally, a FLC's reliability is taken into account by Eq. (5-3). During the reliability check, it is verified whether the fuzzy logic rules have been sufficiently applied to be accountable for the decision that it has taken.

Fuzzy Logic “Reliability”

The objective of the reliability check is to find out whether the rule base of the fuzzy logic system is sufficiently applied and appropriate for driving the system actuators, i.e. the shading system.

As explained in Section 5.1.2 for the final defuzzification step, the centroid method is applied to return the center of an area under a curve representing the aggregation result. The operation of the centroid method is demonstrated in Eq. (5-2).

$$y_0 = \frac{\sum_{j=1}^F \mu'_B(y_j) y_j}{\sum_{j=1}^F \mu'_B(y_j)} \quad (5-2)$$

where y_0 is the value of the fuzzy inference output; $\mu'_B(y_j)$ is the value of the aggregated truncated output; y_j is the crisp output value of the rule j ; and F is the total number of the rules. The FLC's reliability \mathcal{R} is the denominator of Eq.(5-2), which defines the truncated fuzzy or crisp output sets.

$$\mathcal{R} = \sum_{j=1}^F \mu'_B(y_j) \quad (5-3)$$

where y_j is the crisp output value of the rule j and μ'_B is the truncated value assigned to the outcome y_j of the rule j . If the *reliability* value is close to *nil*, this means that the FLC's decision is not reliable and the rule base is not sufficiently applied for determining the outputs. Practically, the output weightings are provided by MATLAB (IRR parameter, output of `evalfis` command). \mathcal{R} ranges from 0 (not reliable at all) to 1 (completely reliable). In our case, the shading system commands are only applied if the reliability of the FIS output is larger than a predefined threshold σ , equal to 15% in this case. This value is obtained by a trial-and-error method. The higher it is, the more the commands are ignored.

Once shading positions have been amended, it is time to take care of the electric lighting system. Once again, the illuminance E_{desk} is monitored and the electric lighting power adjusted for E_{desk} to reach the recommended workplane illuminance. This two-step approach insures that the daylighting flux is privileged over electric lighting and that the latter is used only as a complementary lighting source. A dimming function is not used in this study: the lights are turned on if $E_{desk} < 200 [lx]$ and turned off if $E_{desk} > 700 [lx]$.

The lower threshold for the workplane (horizontal) illuminance (200 [lx]) is lower than the usual recommendation of the lighting standards [142] for office work (e.g. 300 – 500 [lx]). This is in accordance with the argument of Paule et al. [24], stating that workers may find visual performance conditions sufficient thanks to VDT screens, even if the work plane (horizontal) illuminance is lower than that recommended by lighting standards. Furthermore, as previously mentioned, in the office rooms equipped with an ADS, under certain circumstances, lower illuminances on the work plane seem to be sufficient due to a large daylighting provision during work hours [160], [192].

A more comprehensive filtering algorithm for control systems that includes the arrival and departure of the occupant was developed for long-term experimentation and detailed in Section 5.3.3.5.

5.2.2. Design of Experiment

This section presents the underlying principles and design of the subjective assessment of the two controllers by human subjects and explains the experimental procedure used during this study.

Studies with a human subject start generally with the explanation of the experimental procedure. In this experiment, a graphical user interface has however been developed for time keeping purposes: it announces automatically the different tests that the subject must carry out. In other words, at the beginning of each study, the subject runs the timer and, accordingly at the adequate moments, visual tests pop up on the VDT screen or the program requests the performance of paper-based Landolt tests [193], [160]. Thus, the software reduces the number of interactions of the subject with the examiner, thereby minimizing the risk of bias and non-controlled influence. Furthermore, in order to reduce the risk of errors or superficial answers, the number of tests was first reduced to the minimum (such as only one

paper-based or VDT screen-based task to be carried out per period) to avoid a bothersome experience and consequently superficial answers. Secondly, a user-friendly on-the-screen assistance system clearly explained each test to eliminate any misunderstanding. The examiner was present during the whole experiment for any assistance. Thirdly, by comparing the answers of different subjects, any abnormality and extreme outliers in the answers were detected.

On-line surveys

At the beginning and at the end of a session with a subject, an on-line questionnaire pops up on the VDT screen allowing to perform a subjective assessment of the user's sensations regarding visual and thermal comfort. This questionnaire was set up in French and English; it was inspired by the work of Borisuit [38] and Guillemin [156]. The list of questions is presented in Appendix C, Figure C.1.

Computer-Based Freiburg Visual and Acuity Test (FrACT)

FrACT is a widely used visual test battery in form of a free computer program [194]. It uses psychometric methods combined with anti-aliasing and dithering to provide an automated, self-paced measurement of visual acuity [195], contrast sensitivity and Vernier acuity (ability to discern a disalignment among two line segments or gratings [196]). It complies with the European Norm for acuity testing (EN ISO 8596) and is employed all over the world in vision labs as well as in clinical trials for eye sight evaluation by optometrists and ophthalmologists. In this study, the test was used differently: instead of determining the visual acuity of a subject, their performance in determining the direction of the Landolt rings is measured. The reaction time taken to identify this direction is measured per ring types, the subject performance being evaluated by a performance indicator (η_{perf}) suggested by Linhart et al. [160]. The subject is allowed a maximum of 5 seconds per ring; 18 rings with 8 orientations in total are presented to him/her. The maximum displayed acuity is equal to 1.2 (12/10) due to a limited resolution of the VDT screen as well as limited space in the workplace. During the test, each subject is instructed to keep a distance equal to 120 cm from the screen to their eyes.

Finally, a two-tail paired student t-test with a 95% significance level is applied to detect statistically significant observations. The 95% confidence interval is illustrated in each figure in the Results section. It was obtained from the *Standard Error of Mean* (SEM), which is equal to $1.96 \cdot \sigma / \sqrt{n}$, where σ is the standard deviation of the sample and n is the samples size. If there is no overlap between the error bars (confidence intervals) corresponding to the two control approaches, it can be concluded that a statistically significant difference exists between them.

Human subject Studies

30 healthy subjects (10 females, 20 males) with the age of 21.93 ± 4.52 years participated in 15 days of experiment during the afternoon and just after lunchtime. The subjects had to sleep 6 – 8 hours per day between 23h00 and 8h00 before the experiment. They were asked to sleep according to their circadian cycle for two nights before the day of the experiment. The subjects were requested during the welcome session to read a document explaining the experiment procedure, before asserting their consent to participate in the experiments and for the results and their opinions to be published anonymously for scientific purposes.

Duration and beginning of the experiment were chosen as a function of the following research questions:

- Does the novel system (sensor + controller) result in a lower electric lighting consumption?
- Does its implementation result in a more visually comfortable office environment?
- Does the visual performance of the user vary as a result of the application of this system?

For the performance assessment of the controller with regard to preventing glare sensation, the experiment needs to be carried out during the period when the sun has the chance to potentially jeopardize the visual comfort of the office occupants. As the workstations in both office rooms are facing west, with south-facing windows in the Northern hemisphere, this period occurs theoretically when the sun azimuth is larger than 180° . Although it is possible to perform the experiments all day long, it is more efficient to carry them out when they are really relevant.

On the other hand, the downside of performing the experiments during the afternoon is that some subjects might be more tired and have less tolerance to glare. To address this issue and avoid the effect of interpersonal differences during each period (Figure 5.5), each office room was occupied by two subjects facing each other.

Two critical *periods* of a day were identified in order to evaluate the controllers' performance: the first one at the beginning of the afternoon, during which the glare risks due to direct sunlight for a west-facing workstation are considerably higher. During this period, the controllers' ability to prevent glare is tested. A second period was chosen around sunset, during which an energy efficient combination of daylighting and electric lighting was to provide sufficient workplane illuminance to the users: ergo, the controller performance in accomplishing this task is challenged. On the other hand, in order to eliminate interpersonal differences between subjects, the lighting condition of each office room was evaluated by all subjects during the two *periods*. In practice, subjects were asked to switch from one office room to the other once per period. Finally, the sun azimuth angle (instead of legal time) was used to define the middle point of each period. Taking the azimuth angle as reference eliminates the slight differences due to the different days of experiment. Figure 5.5 shows the layout of the periods and the sessions for each period.

Each day, two experimental studies are launched: i) 30 minutes after the solar noontime ($\alpha_{ref} = 200^\circ$) and ii) 2 hours before sunset ($\alpha_{ref} = 270^\circ$) until the end of civil twilight ($h_{sun} = -6^\circ$), 30-40 minutes after sunset (in total approx. 2.5 hours). The experimental procedure during half a day is also shown in Figure 5.5.

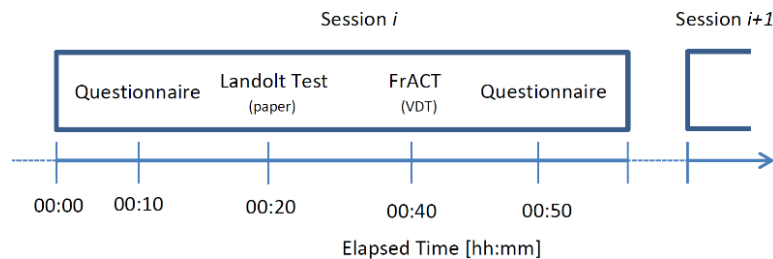


Figure 5.5 – Layout of tests taken during one one-hour session of short-term experiment; online questionnaires (00:10 and 00:50), Landolt paper-based test (00:20) and Fribourg Acuity Test (00:40) [hh:mm].

Study Procedure

After arriving at the laboratory according to an appointment, each subject is offered a quick 5- to 10-minute tour in the LESO experimental building. Moreover, the study is rapidly debriefed, questions are addressed, study participants are offered to use the bathroom and finally they enter the office rooms and begin the experiment. Each participant is asked to perform their usual computer and paper activities and can listen to music, if desired. Each subject answers the online questionnaire twice, once on arrival and once after one working hour in the office room.

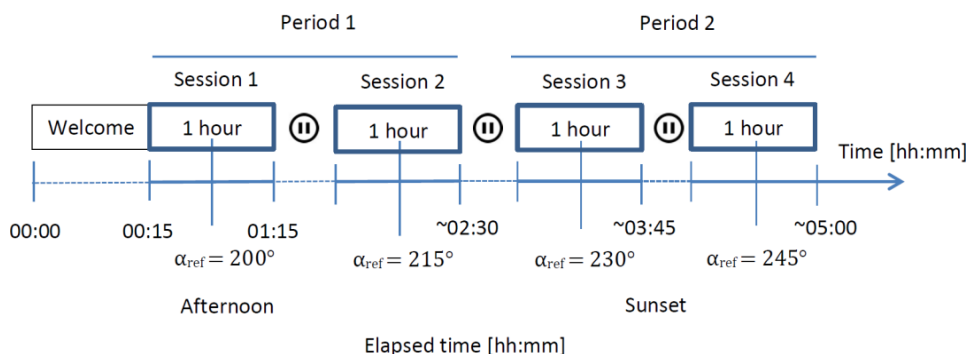


Figure 5.6 – Design of experiment during one day, during short-term experiments, total duration of the experiment is about 5 hours per day. The first period is held in the afternoon and the second during the sunset. Midpoint of the sessions corresponds to sun's azimuth (α_{ref}) equal to 200° , 215° , 230° , 245° .

During each session, two FrACT tests are performed in order to assess the visual acuity of the subject while performing a paper task as well as a computer task. In between two experimental sessions, the participants take a 10-15-minute

break while they are offered light snacks, soft drinks and water; they are also allowed to use the bathroom. The second session then starts and the subjects occupying the two office rooms are swapped. They perform the same procedures, participating in the on-line survey twice, once at the beginning of the session and once at the end. The whole experimental study takes 2.5 hours; the corresponding procedure is schematically illustrated in Figure 5.6.

5.2.3. Experimental Results

The experiments were run during 15 days in the course of November and December 2015; among them there are 5 days with clear sky (9, 16, 18, 26 November and 2 December, marked in yellow on Figure 5.9, Figure 5.10 till Figure 5.14), 3 days by an intermediate sky (12, 13, 23 November; marked in light blue) and 7 days with overcast and rainy skies (the remaining days marked in light gray).

First of all, the subjective survey regarding the visual and thermal comfort was considered. The results of 240 surveys (15 days \times 8 time per day \times 2 offices) are summarized in Figure 5.7. On average, based on Q1 and Q2 (see Figure C.1 in Appendix C), the subjects preferred the lighting conditions in the advanced office room to those of the reference one. However, no significant difference between the two offices in this regard, was found. In addition, there is no statistically significant difference between the answers to the whole 12 questions set, except for Q4 (e.g. 'too much light?') and Q6 (e.g. 'glare feeling?'). The p-values for a 95% confidence interval of the paired two-tailed distribution student test for these 12 questions are 0.501, 0.379, 0.007, 0.095, 0.773, 0.031, 0.433, 0.190, 0.999, 0.603, 0.604 and 0.641 respectively. According to these results, the author assumes that the advanced controller performed noticeably better in avoiding glare and reducing an excessive daylight flux than the reference one. These results confirm that the subjects liked the lighting conditions in both office rooms (Q1) and that they had enough light for performing their tasks (Q3).

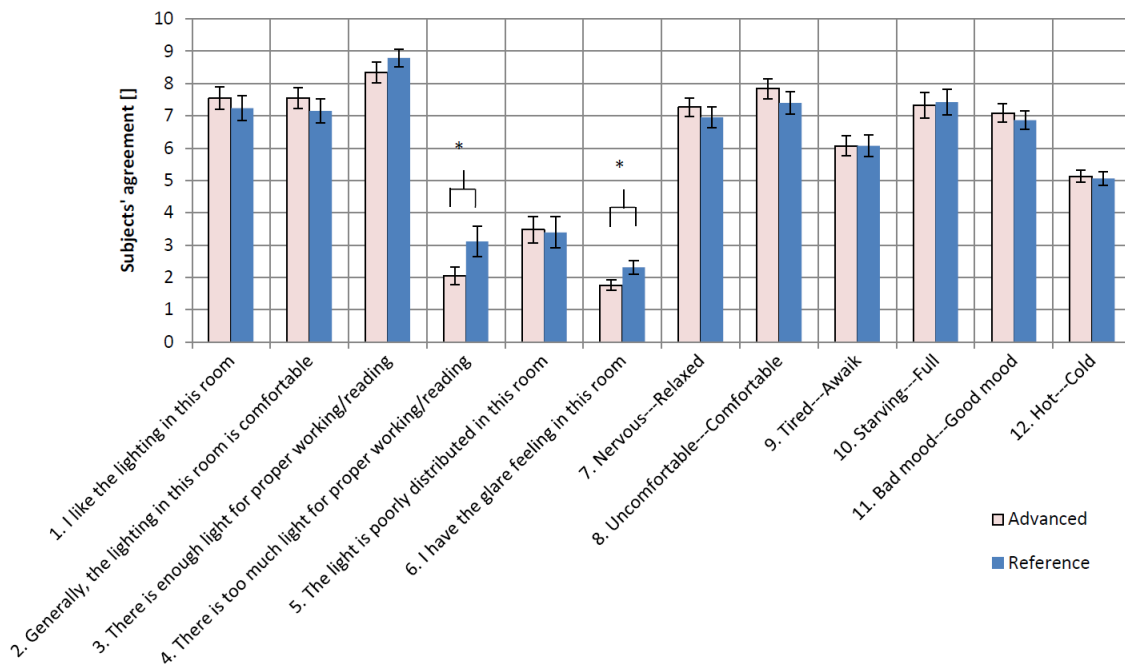


Figure 5.7 – Summary of online survey for the whole short-term experiment. The error bars show the 95% confidence interval namely, Standard Error of Mean (SEM).

A closer look at the two questions Q4 and Q6, thanks to an overview of the hourly-based corresponding answers (illustrated in Figure 5.8), points out a significant difference during the first two sessions (around mid-day), during which the sun azimuth was lower than 220° and possibly created glare sensations. During the two late sessions (close to evening time), the sun was closer to the horizon with $h_{sun} < 10^\circ$ leading the electric lighting to be switched on and the sun shading systems of both office rooms to be fully retracted. Accordingly, no significant difference between the answers of the subjects to these two questions was observed after 15h30.

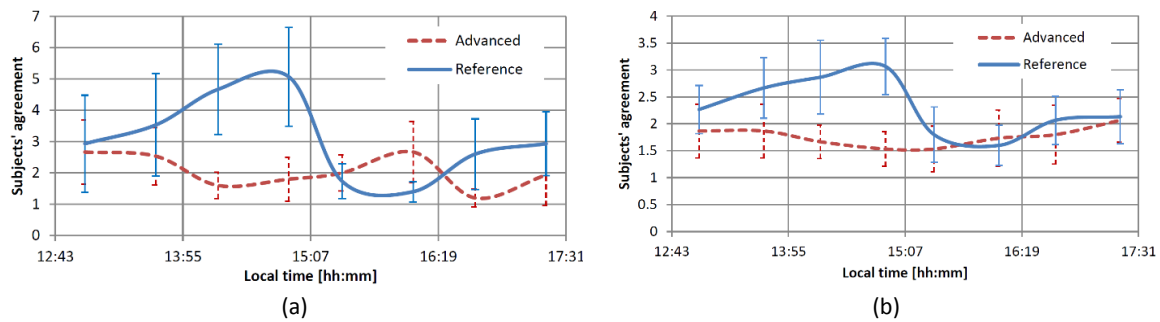


Figure 5.8 – Comparison of subjective answers to a) Q4; b) Q6 along the 4 sessions of the short-term experiment (12:50 PM till 5:30 PM) . The error bars show the 95% confidence interval.

The work plane (horizontal) illuminances monitored in the two offices are reported in the Figure 5.9. This box plot shows that the horizontal illuminance in the advanced office room remains on average higher during most days of the experiment. During sunny days, the horizontal illuminance is higher in both office rooms while during days with overcast sky, such as November 20, the electric lighting is turned on, the work plane (horizontal) illuminance in both offices being relatively lower. DGP values are available only for the advanced office room (Figure 5.10); the average values are lower than 35% (e.g. threshold between imperceptible and perceptible glare).

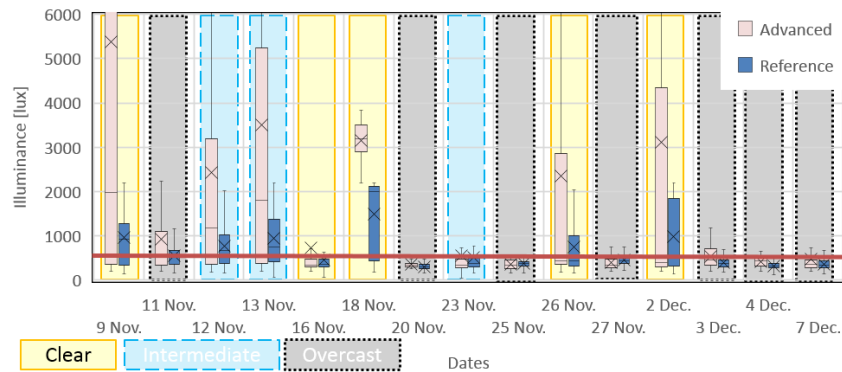


Figure 5.9 – Comparison of the work plane illuminance monitored in the reference and in the advanced office rooms during short-term experiment.

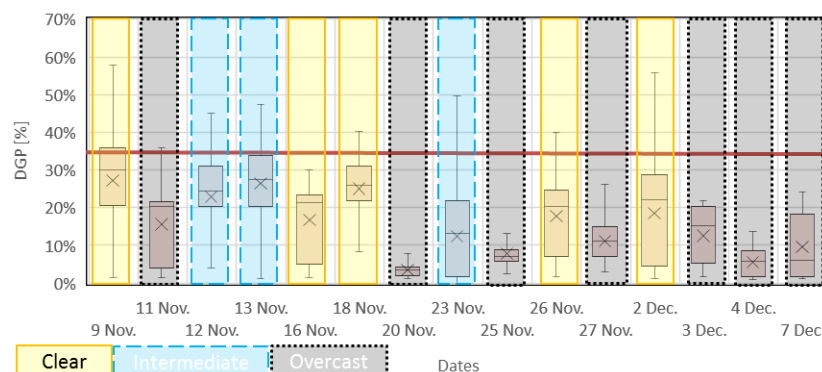


Figure 5.10 – DGP assessed in the advanced office room during short-term experiment.

Figure 5.11(a) gives an overview of the 120 paper-based Landolt tests (15 days × 2 offices per day × 4 tests per office). The average number of mistakes is obtained by summing all the orientations (left) and averaging over all the orientations. Over a total of 384 rings (96 · 4=384), the subjects made on average 36.8 mistakes in the advanced office room and 43.3 mistakes in the reference one. Although these results show that on average, the subjects made relatively fewer mistakes in the advanced office room, no statistically significant difference for the paper-based task was found.

Regarding the computer-based task, the subjects' efficiency in both offices lies between 0.5 and 1 [Hz]; in other words, they correctly determined the direction of the broken Landolt rings every 1 – 2 [s]. On average, in ten days out of fifteen, the subjects located in the advanced office room were more efficient; while for the rest of the time, the efficiency was higher for the subjects in the reference office. However, except on the 4th December, no statistically significant difference between the visual performances of the subjects were found. Moreover, no correlation between the weather conditions and the visual performance of the subjects was observed.

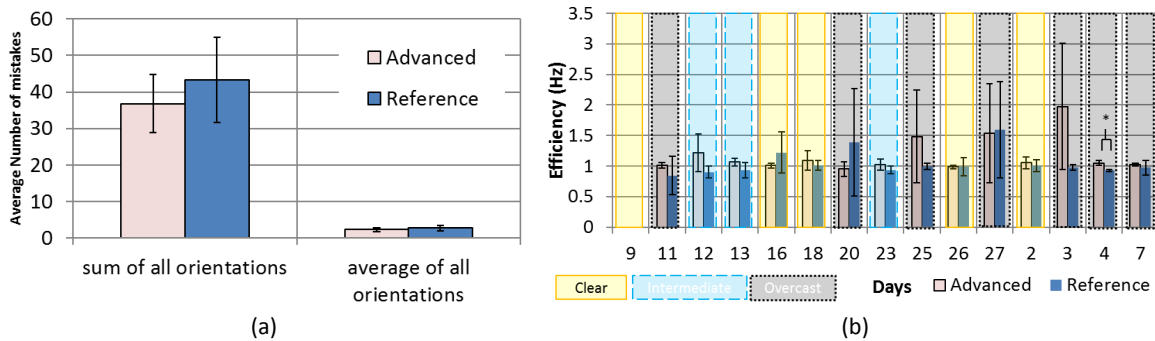


Figure 5.11 — (a) Paper based Landolt Test, (b) Fribourg Acuity Test (FrACT) results for two office rooms during short-term experiment. There is only a significant difference in FrACT on 4th Dec. 2015 For the rest of the time, the results do not show any significant performance impairment.

An overview of the results of the paper-based Landolt test is given in Figure 5.12, which represents the average number of mistakes committed by the subjects for each test; all of them participated in four tests per day. Once again, the number of days during which a statistically significant difference between the subjects' performances can be observed is limited to two days (9th and 20th November). Both days were sunny with an excessive illumination on the horizontal work plane in the reference office; this apparently prevents the subjects from flawless counting of the Landolt rings. In addition, it can be noticed that the subjects make fewer mistakes during the overcast and rainy days in comparison with clear and sunny days.

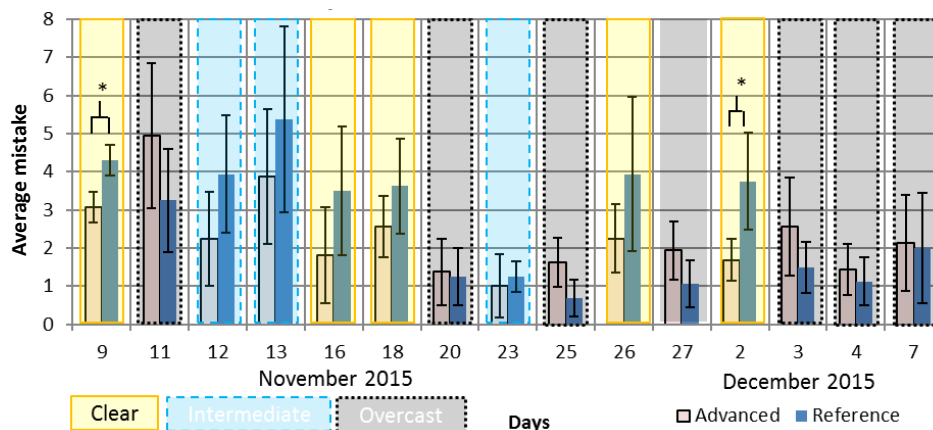


Figure 5.12 — Paper-based Landolt Test for the whole duration of the short-term experiments. The improvements over two sunny days are statistically significant. The error bars show 95% confidence intervals.

The electric lighting consumption is generally lower in the advanced office room with respect to the reference one (Figure 5.13). This difference is more obvious during sunny and intermediate days; while during overcast days (such as 20th Nov. and 4th Dec.) the electricity demand is almost equal, since the electric lighting system was switched on in both offices during the whole day. In total, the electricity demand of the advanced office is 31.4% lower with respect to the reference room; this confirms that the electricity savings potential of an integrated lighting control strategy based on the HDR vision sensor is substantial.

Another criterion for comparing the controllers' performance is the total number of sun shading and electric lighting amendments. In general, the advanced controller implemented 67% more commands during the experiments with

respect to the reference one. Except for one day (18th Nov.), during the remaining days, the daily numbers of amendments were kept below 5 times, meaning an amendment every 40 minutes. This number was acceptable for the subjects: they did not report any dissatisfaction in this regard. Moreover, there is no noticeable correlation between the number of amendments and the weather condition. It is however worth noticing that the minimal electricity demand was recorded on 18th December in the advanced office room; meanwhile the highest number of shading/electric lighting amendments was also recorded during the same day.

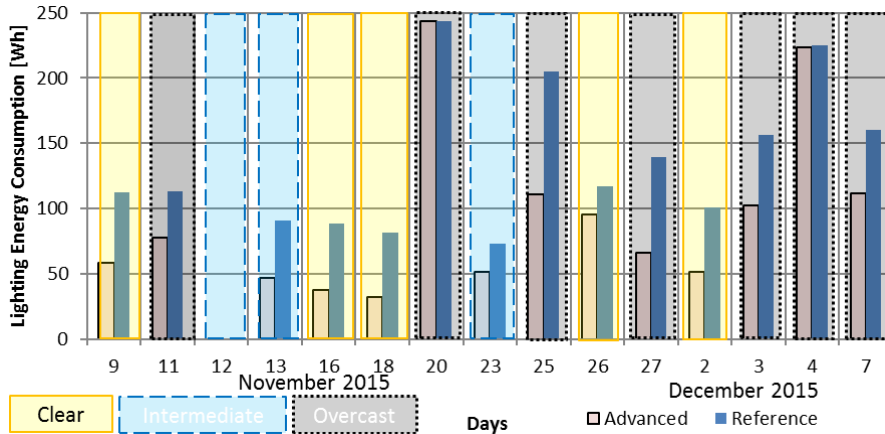


Figure 5.13 – Electric lighting energy consumption comparison during short-term experiment. The advanced office consumes less energy. The energy meters did not function properly on 12th Nov. 2015.

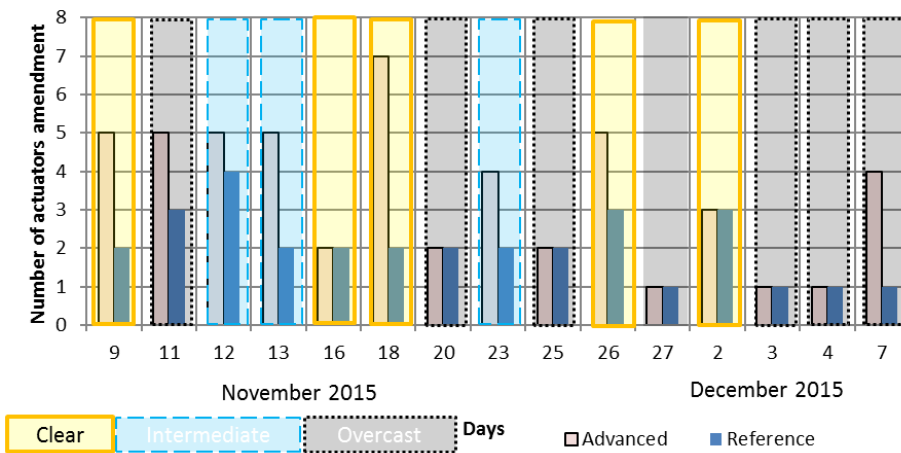


Figure 5.14 – Number of sun shading and electric lighting amendments during each day of experiments. Generally, the advanced office room has relatively more amendments.

5.2.4. Discussion

These results show that the subjects in the advanced office room experienced fewer glare situations during the second part of the experiment. Moreover, the subjects appreciated in an equal way the lighting conditions in both office rooms with a slight preference for the advanced controller. They also described the lighting conditions in both rooms as comfortable (Figure 5.7) although for some moments during daytime, especially at the beginning of the afternoon when the solar altitude was high, they indicated an excess of daylight in the reference office room, accompanied by discomfort glare sensations. The better performance of the advanced controller is very likely due to the *DGP* monitoring and user-centric control at the work space, achieved thanks to the HDR vision sensor, which allows fine tuning of visual comfort for the subject seated at his/her desk.

The *DGP* monitoring shows that the glare sensations remain below the perceptible glare limit in the advanced office room, while the monitored workplane illuminance is by far higher than the thresholds used by the ‘Best-practice’ controller. For instance, on November the 12th and 13th, the average horizontal illuminance equals about 2400 and 3500

lux respectively (Figure 5.9), while the DGP is rated below 35% (22% and 26% respectively in Figure 5.10). The subjects confirmed that they experienced less glare sensations in the advanced office room through their answers to question Q6 of the survey (glare feeling). Moreover, during these two days, they agreed more on Q4 ('Too much light for proper working/reading') in the reference office room than in the advanced one. In other words, if the subjects do not experience discomfort glare, they may even prefer direct sun light falling on the work plane, especially during the winter time.

The subjective assessment of visual comfort related agreement for the first assertion (Q1) 'I like the lighting in this room' yields scores of 72.4% and 75.4% respectively for the reference controller and the advanced one. For both controllers, these values are marginally higher than the ones reported by Akashi and Boyce (i.e. 69%) [197]. The same score is also observed during standard office work hours, as daylighting has a positive impact on a subject's assessment of lighting conditions. Hence, we assume that the two considered control systems offer lighting conditions similar at least to those of standard office rooms.

Moreover, in a recent experiment by Sadeghi et al. [26], the subjects voted on average 4.5 (scale of 1-7, $(4.5 - 1)/(7 - 1) = 58\%$) for the visual condition rating when a fully automated control set-up was in action. This vote is lower than that of the subjects of this experiment to similar question Q2 'Generally the lighting in this room is comfortable' (e.g. 7.3 (scale of 1-10, $(7.3 - 1)/(10 - 1) = 69\%$) for the controller in the advanced office room. We may expect higher comfort and acceptance votes, if an occupant manual control is allowed. Sadeghi et al. have shown that there is a significant improvement of comfort votes if an automated system override is allowed. They also observed that an easy access to control features (e.g. to a web-based interface for shading and lighting system control) leads to increased daylight utilization, which can consequently lead to a lower electric lighting consumption. During the long-term in-situ monitoring in the LESO building reported in the next chapter, the occupants will be allowed to override the BMS commands; they will also rate visual comfort.

The subjects' visual performance for paper-based tasks was absolutely not jeopardized by the advanced control system, since, as shown in Figure 5.11 (a), there is no statistically significant difference between the performances in both office rooms. Thus, the author may conclude that there is no impact of different control strategies on the indoor lighting conditions for paper-based tasks.

On the other hand, the subjects' studies demonstrate that the VDT screen-based tests were not sensitive enough to the lighting conditions to be reflected in the visual performance of the subjects. Alternatively, small differences might be due to the fact that the subjects switch each hour from one office to the other. It can be inferred that the switching rhythm was too fast for the effects to be noticeable. However, the author believes that the impact of lighting on the VDT screen-based tasks occurs shortly after the occupant is seated at the workstation; thus the differences between the control strategies were not large enough to be measured by the current tools.

Moreover, the accurate monitoring of the work plane (horizontal) illuminance, carried out by the ceiling-mounted HDR vision sensor, leads to a fine-tuning of the electric lighting provision on the user desk as well as a lower electricity demand. Besides, the glare rating at occupant's eye level by the other HDR vision sensor, as well as its integration in the control platform, lead to a better protection against glare and improved user satisfaction. These advantages with respect to a best-practice automatic system are inherently related to the more reliable and precise assessment of the indoor lighting condition as well as more accurate integrated control of shadings and lighting system. The author believes that in a typical office room with conventional facade (without anidolic system), such advanced system would lead to even more significant occupant satisfaction and lower electric lighting energy demand with regard to the best practice. The reason is that, as demonstrated by Linhart et al. [192], all the office rooms in the LESO solar experimental building are basically well daylit and feature low lighting power density (LPD). An automatic system whose energy performance surpasses a best-practice system in this building shall certainly outperform it in a conventional building too.

The DGP index cannot predict discomfort glare in an adequate way if the sun is present in the field of view of a subject, due to the extreme values of the solar coronas luminance. Konstantzos et al. [109] showed that the luminance expression of DGP is inflated by this extremely high luminance which is incompatible with everyday practice. The

overestimated DGP when there is direct sunlight in the field of view might lead to unnecessary sun shading amendments, more frequent movements and occupant disturbance. As a solution, different sets of DGP coefficients for different environmental conditions and/or fenestration systems can be used [89].

The advanced controller actions are slightly more frequent than those of the 'Best-practice' one; however, the users did not complain about it. The shading position amendments for the advanced control average 2.5 times per half-day; this was not considered as annoying by the different subjects. The advanced control system leads however to a considerably lower electricity consumption compared to the Best-practice controller (31.4% savings), which is remarkable. The electric lighting saving potential was derived through a comparison of two similar experimental setups with identical control parameters setting evaluated twice by each subject. The overall performance of the advanced controller can even be enhanced by including a presence detection function in the control strategy and through a coupling with thermal regulation.

Another interesting observation is that the subjects were not concerned at all by privacy issues, which might have been raised by having an HDR vision sensor facing their VDT screen. In other words, during these studies they logged into web services and social network accounts without being apparently disturbed by the presence of a digital camera. This can be explained by the fact that the subjects of this study belong mostly to the Y generation, which is used to video camera presences in day-to-day life. Recent studies [198] pointed out an erosion of privacy taking place among this generation; this conditioned erosion is driven by a combination of youthful viewpoint and exuberance and rapid technological advances. Moreover, this development challenges traditional notions of privacy; thus, although privacy concerns regarding the use of HDR vision sensors in the office environment are raised, they do not seem to be such an important issue for young office workers. However, the author acknowledges that these observations has taken place in the context of a scientific experimentation, signifying that the subject's reactions might have different from their in real environment.

5.2.5. Limitations

The main limitation of the present study is the relatively small number of subjects as well as the short duration of the experimental observations carried out per subject. Moreover, the results can likely not be generalized to older adults and elderly people, as most of the subjects are rather young people, such as undergraduate and doctoral students: they are, however, intended to give a first in-depth insight into the expectation and reaction of a specific user group within an office room automated by means of HDR vision sensors. Moreover, during the study, the users did not have the opportunity to modify neither the sun shading position nor the electric lighting power status. Despite this, the assertions regarding visual comfort remained similar to those reported in the literature and standards.

The DGP rating software is already implemented in the embedded Digital Signal Processor (DSP) embedded on the HDR vision sensor. However, the work plane horizontal illuminance is measured from a ceiling mounted HDR vision sensor: the portion of the image corresponding to the work plane should be adjusted in any new environment. FLC membership functions can be designed in a clever way in order to adapt themselves to easy-to-obtain inputs, such as facade and workstation orientations, distance to window, window size and latitude. This is the idea explained and validated in Chapter 6.

5.2.6. Conclusion and Outlook

The performance of a Fuzzy Logic Controller (FLC) commanding both the sun shading system and the electric lighting in an office room through two novel HDR vision sensors was assessed by means of in-situ building monitoring. Thirty human subjects placed during fifteen afternoons/evenings in two identical office rooms of the LESO building on the EPFL campus in Lausanne, Switzerland contributed to the experimental evaluation of the overall performance of this advanced controller in regards to a 'Best-practice' lighting control system (reference controller). Different aspects, such as paper-based visual performance, computer-based visual acuity and efficiency tests, as well as a self-reported subjective assessment of visual comfort by the subjects, were used for that purpose. The experimental results show that the subjects' visual comfort and performance are comparable for both controllers; in some occasions, they are slightly improved in the office room equipped with the advanced controller. Meanwhile, the electricity consumption in the corresponding office room is mitigated by about 31% in comparison to the reference controller. All over this study

has significantly improved our understanding of the performance and application opportunities of novel HDR vision sensors for building management systems (BMS); it also highlighted the subjects' preferences for the advanced controller based on a user-centric control approach.

Having reached this conclusion, one can answer the second research question raised in Section 1.3 by stating that “the BMS, equipped with HDR vision sensor is able to mitigate the electric lighting energy demand of a single occupied office room by 31% while guaranteeing the occupant’s visual comfort.”

In the next section, the long-term effect of this novel control approach during several months on the energy performance of an office room, including the utilization factor of solar gains as well as indoor visual comfort, will be considered. In addition, the occupant’s thermal comfort, which was not considered in this study, will also be taken into account: it plays an important role both for occupant acceptance of BMS and building energy demand.

5.3. Long-term Experimentation

This section presents the methodology and planning of a long-term experimentation regarding an advanced controller based on HDR vision sensors; the experimental results of an eight-month in-situ monitoring campaign in the LESO building will be presented as well. The principal objective of this experimentation is to compare the electric lighting consumption and the energy performance of a passive solar office room equipped with an advanced control system with those of a ‘Best-practice’ electric lighting control system. The advanced controller differs from the one tested during short-term experiments as follows:

- A presence detection based on an HDR vision sensor is integrated in the controller as well as a commands filtering process.
- An occupant presence probability function is integrated in the decision making process.
- A thermal comfort controller is added to the lighting control system to take into account indoor temperature.
- The controller installed on the main control platform is adapted to “event” based cycles rather than a “constant frequency” decision-making process.
- Human building interactions, i.e. the occupant expressing his/her wishes by modifying the sun shading position and the electric lighting power, are taken into account.

5.3.1. Objectives of Control Platform

The goal is to develop a control platform that can run for weeks or months without constant supervision from the facility manager. “Without supervision” does not necessarily mean that the office occupants do not have the right to interact with the electric lighting or the sun shading commands: it means that the control system can operate 24/7 without failures.

5.3.2. Experiment Protocol

The experimentation was carried out in two identical south-facing office rooms of the LESO solar experimental building located on the EPFL campus in Lausanne, Switzerland. The setup is similar to the one of the short term experimentation carried out during winter 2015 presented in [79]. The differences are as follows:

- In both offices, the occupants have the right to interact with the shading and electric lighting system.
- A ceiling-mounted HDR vision sensor performs the presence detection in the advanced office room (Appendix G).

The in-situ monitoring campaign started on the 1st August 2016 and lasted until the 31st March 2017 , except for three weeks in September 2016 (Figure 5.16). The measurements ran in a continuous and autonomous way and did not stop, except during the live data stream issued from the BMS to the data storage medium.

5.3.3. Advanced Controller

The advanced control system is similar to the one used in the short-term experimentation. Some elements were added that will be discussed in more detail.

The reason for using a high frequency data acquisition system (DAQ) and then a command filtration is to keep the control system as agile as possible. The office occupant would obviously reject a control system not able to mitigate visual discomfort in an instantaneous way. The fuzzy logic controller based on the knowledge and skills of the experimenter might not be optimal; a command filtration is accordingly necessary to avoid inappropriate commands reaching the sun shading and electric lighting actuators.

5.3.3.1. Visual comfort controller

In the same way as for the short-term experiment [79], the integrated shading and lighting control system takes into account the workplane horizontal illuminance, the Discomfort Glare Probability (DGP) and the sun azimuth and height; it commands the bottom and top shading systems as well as the electric lighting status. The membership functions, the fuzzy rule base of the controller and the crisp values for the output variables are described in Appendix A.

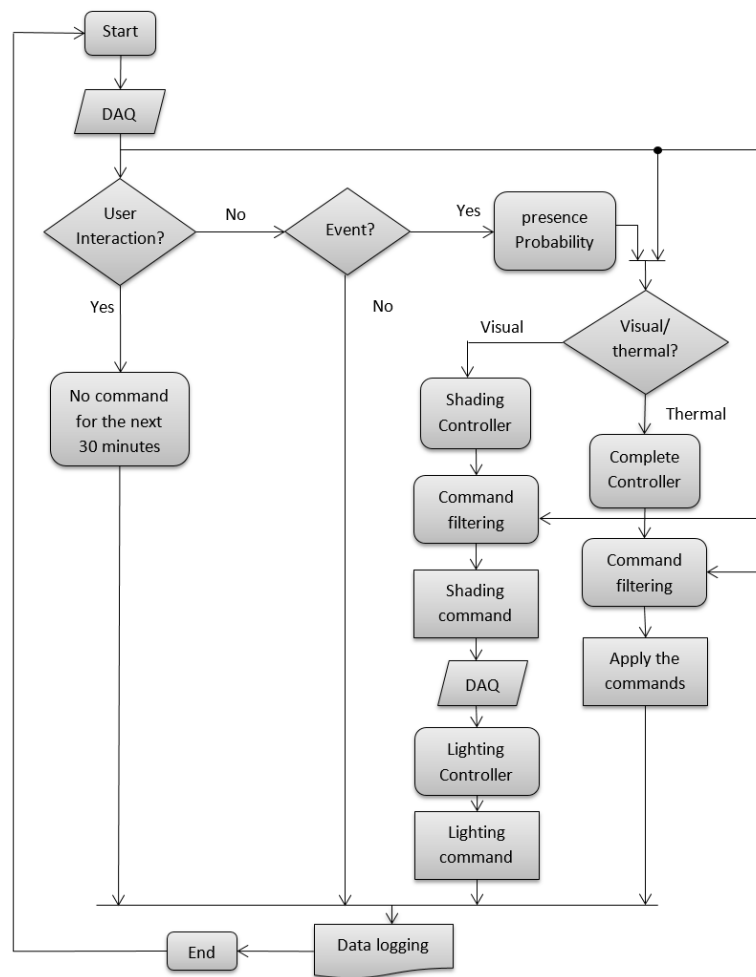


Figure 5.15 – Block diagram of the advanced controller for executing the long-term experiment.

Moreover, the lighting controller is equipped with dimming feature and regulates the horizontal illuminance so as to maintain the target horizontal illuminance with the least possible electric lighting energy demand. The details of dimming level development are elaborated in Appendix D.

5.3.3.2. Thermal comfort controller

When the occupant is not present, the thermal comfort criteria needs to be applied for managing the shading and lighting system so as to avoid overheated or cold environment when they return to the office room.

The back-up heating system is managed by the central BMS of the LESO solar experimental building; the building is not equipped with a cooling system and relies only on natural cooling and thermal mass. The only systems that the advanced controller can command are the shading and electric lighting system. The shading system can be driven based on thermal comfort considerations in case of extreme indoor temperatures. In other words, if the indoor temperature is too high or too low, the thermal comfort benefits from a higher level of priority with respect to visual comfort. During a summer afternoon, for instance, when high indoor temperatures and high indoor illuminances are observed, one can logically conclude that keeping the shading system open would most probably lead to an intolerable overheated space. In this case, even if the visual comfort would not be jeopardized by maintaining the shading system open, it should be closed for thermal comfort reasons. By contrast, during the heating season, if the indoor air temperature is lower than 16 °C, the shading should be opened in order to maximize the passive solar heat gain in the office room. These situations are formulated as thermal comfort considerations in Eq. (5-4):

$$(\gamma_{top}, \gamma_{down}) = \begin{cases} (0,0.7) & \text{if } T_{in} > \tau_{hot} \ \& \ E_h > 1300 \ \text{lux} \\ (1,1) & \text{if } T_{in} < \tau_{cold} \\ (\gamma_{top_{current}}, \gamma_{down_{current}}) & \text{otherwise} \end{cases} \quad (5-4)$$

where T_{in} is the indoor air temperature [°C]; τ_{hot} and τ_{cold} are the upper and lower threshold for prioritizing thermal comfort controller [°C]. $\gamma_{top_{current}}$ and $\gamma_{down_{current}}$ represent the current position of the blinds [-].

5.3.3.3. Human Building Interaction

It is obviously known that a manual override of automated blinds leads to higher user satisfaction regarding indoor lighting [199]; thus, it is crucial that the control system considers human building interactions. In this study, the interactions between the office occupants and the lighting system were detected. If the user changes the blinds position and/or the electric lighting power, a “User-interaction” flag is turned on and no further command is sent to the shading or lighting system during the next 30 minutes. Detecting the human building interactions allows to prevent user irritation by undoing his/her action shortly after its occurrence.

5.3.3.4. Events

The main controller can operate agile, if it takes actions based on events. The event flag is switched on if one of the following cases occurs:

- DGP variation larger than 2%
- Horizontal illuminance variation larger than 30 lux
- Interior temperature variation larger than 1°
- Someone arrives/leaves the office room

By implementing this approach, the loop frequency of the controller can remain high, taking measures as soon as the flag event is turned on. On the other hand, the necessary computational resources are reduced since the controller is not solicited for each cycle.

5.3.3.4.1. Occupancy model

Office occupancy profiles on weekdays and weekend for an office room in the LESO solar experimental building were developed by Jessen Page [200]; the result of his work is summarized in Table 5.1.

Hour	1	2	3	4	5	6	7	8	9	10	11	12
Weekday	0.00	0.00	0.00	0.00	0.00	0.00	0.05	0.10	0.70	0.70	0.70	0.70
Weekend	0.00	0.00	0.00	0.00	0.00	0.00	0.01	0.01	0.05	0.05	0.05	0.05
Hour	13	14	15	16	17	18	19	20	21	22	23	24
Weekday	0.20	0.60	0.70	0.70	0.70	0.70	0.70	0.01	0.01	0.01	0.01	0.00
Weekend	0.01	0.01	0.01	0.00	0.00	0.00	0.00	0.00	0.00	0.00	0.00	0.00

Table 5.1 – Presence probability model developed by Page [200].

5.3.3.4.2. Visual/Thermal Criterion

As stated in Section 2.3.1 based on the thermal comfort model suggested by Fanger [15], at best possible conditions, one may still predict 5% dissatisfied people. Thus, any notion of mathematical discomfort model is, at best case, limited to 95% of the population. Based on Fanger's thermal model, the satisfaction of the occupant depends on six factors namely air temperature, radiance temperature, air velocity, humidity, clothing and level of activity. For engineering application, it is not possible to consider all of these factors to determine the satisfaction degree of the occupant with the current state. For this reason, a simplified model, suggested by Roulet [201] based on ISO 7730 [202], is adopted. This model defines a crisp threshold for thermal comfort zone for an occupant who is seated or standing doing an office work (activity level: 1, 2 [*met*]): the occupant is comfortable if the indoor air temperature is between 18 [°C] and 26 [°C]. These thresholds are used for prioritization of thermal and visual comfort.

The controller should decide thermal or visual comfort criterion must be considered. In other words, the controller should set a higher priority to one of these types of comforts.

The thermal criteria are activated in the following cases:

- i) The office room is vacant AND the probability of user presence for the next 30 minutes is less than 50%.
- ii) The indoor temperature AND the workplane illuminance are too high (e.g. more than 26°C & 800 lx);
- iii) otherwise, a control approach based on visual comfort is applied.

$$Act_{v,t} = \begin{cases} \text{Thermal} & \text{if } (\gamma_{presence} = 0 \ \& \ P(\gamma_{presence}) = 'low') \ | \ ((T_{in} > 26) \ | \ (T_{in} < 18)) \ \& \ (E_h > 800 \ \text{lx}) \\ \text{Visual} & \text{otherwise} \end{cases} \quad (5-5)$$

where $Act_{v,t}$ is the decision regarding the comfort priority [*boolean*], $\gamma_{presence}$ is the occupancy status of the office room [*boolean*]; $P(\gamma_{presence})$ is the probability of the presence in next 30 minutes [-]; T_{in} is the indoor air temperature [°C] and E_h is the workplane illuminance [lx].

5.3.3.5. Commands Filtering Mechanism

The command filter of the advanced controller, partially inspired by [20], [156], [191], is based on the certain considerations leading to the following Boolean rule:

$$Act_x = \begin{cases} \text{TRUE} & \text{if the consideration \#x is valid} \\ \text{FALSE} & \text{if the consideration \#x is not currently relevant} \end{cases} \quad (5-6)$$

The final decision, Act_f [*Boolean*], is based on the logical implication (AND/OR) of these considerations (Eq. (5-7)). If Act_f is equal to TRUE, a command is sent to the shading system and is documented; if not, the command is rejected. These considerations are summarized in three categories illustrated in Table 5.2 : A) Urgent, B) Prohibited and C) Preferred.

The situations of the first category (A) participate in the final decision through the operator OR; namely the flag act_f is switched to TRUE, as these situations occur regardless of categories B or C:

- If the *DGP* value is high, there is a serious glare risk, which should be treated instantaneously (Act_2).
- If the workplane illuminance E_h is low, there is a risk of uncomfortable paper-based work. The commands should be instantaneously sent to the shading and the lighting system (Act_8).

The second category of commands (B) are combined together with an AND logical operator. In other words, if the three following situations are satisfied, the commands are forwarded to the actuators; otherwise, they are ignored. The three situations can be described as follows:

- If the amplitude of the blinds' movement is large enough", then Act_3 (for top shading) and Act_4 (for bottom shading) [*Boolean*] is set to TRUE. A threshold for raising and lowering the blinds is considered for that purpose (Act_3 and Act_4).

- If the fuzzy logic controller is reliable enough, act_0 is set to TRUE (Section 5.2.1). The controller reliability is defined in a second PCT patent recently deposited. If the controller is not reliable”, this flag is set to FALSE avoiding a command sending (Act_0).
- If the duration from the previous shading and/or lighting actuation to the present one is long enough, flag act_1 is set to TRUE; otherwise, it is FALSE. With this flag, sending too frequent commands to the shading and lighting is avoided (Act_1).

Finally, there are situations where shading systems or lighting amendments are preferred since they might be less bothersome to the occupant and he/she is more prone to accept amendments. The flags corresponding to these situations are combined together by the way of an OR logical operator. The cases related to category C are considered as follows:

- The occupant enters after a long absence (Act_9)
- The occupant leaves (Act_{10})
- The occupant arrives (Act_{11})

$$Act_f = (Act_2|Act_8|Act_9|Act_{10}|Act_{11} |Act_1) \& Act_0 \& Act_3 \tag{5-7}$$

Label	A (OR)	B (AND)	C (OR)
	Command should be sent since it is urgent	Avoiding sending command	Sending command preferred in these occasions
Act_2	Urgent risk of glare	Act_3 & Act_4 Amplitude of the shading movements	Act_9 Occupant enters after a long absence
Act_8	Urgent risk of darkness	Act_0 Reliability of the decision	Act_{10} Occupant leaves
		Act_1 Time interval	Act_{11} Occupant arrives

Table 5.2 – Logic rules behind the commands filtering mechanism. The mechanism is applied each time a command is issued from the FLC.

5.3.4. ‘Best Practice’ Controller

The reference controller is based on the current ‘Best-practice’ of the lighting industry. According to the author’s best knowledge, there is no office room on the EPFL campus equipped with occupant presence detectors neither for shading nor for lighting control purposes. A passive infrared sensor (PIR) motion sensor is normally used for hallways and outdoor lighting where a large delay between on/off cycles can be avoided: a too large delay without any occupant presence detection and/or profile would lead to a waste of electricity.

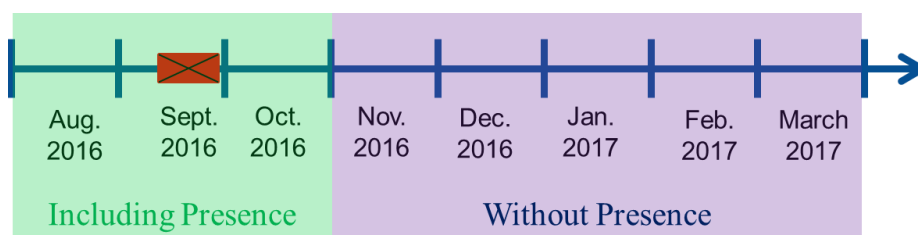


Figure 5.16 – Different control strategies used in the reference office room during two monitoring periods of the long-term experiment.

During the first three months of the monitoring period, occupant presence detection through PIR sensor was implemented in the control algorithm (Figure 5.16, green part; Figure 5.17 (a)). In the last five months, only the luminance meter readings were considered (Figure 5.16, purple part; Figure 5.17 (b)). The control algorithm is fully described in Figure 5.17.

5.3.5. Design of Experiment

An online survey was developed to care for the occupants’ visual and thermal comfort during the experiment. The questionnaire is similar to the one used during the short-term monitoring of November and December 2015 [79]. However, as the subjects of the long-term experiments were unfortunately aware of the project goals, no scientific conclusions can effectively be drawn from these subjective assessments. They are mainly intended to collect feedbacks/suggestions from the colleagues in the case that there is a significant problem with both control strategies. During the experiments, no objection from the colleagues was observed and the control systems were acceptable from their point of view.

The office rooms were occupied by different researchers during the monitoring period. The reference room was occupied until February 2017 by a single person; two persons occupied it during the month of March 2017. On the other hand, the advanced office room was occupied by two people during the whole experiment, except for February 2017, where only a single person was there. During the weekends, the office rooms were partly occupied. The advanced office room was even used during some evenings, leading to a relatively larger electricity demand for lighting. For this reason, and for the sake of a fair comparison of the two office rooms, the daily and monthly electricity consumption for lighting is presented for two time spans: i) The whole monitoring period; ii) Only during office hours between 8 AM and 6 PM.

The author is convinced that the second time span provides a more realistic comparison of the controller’s performance in terms of energy consumption.

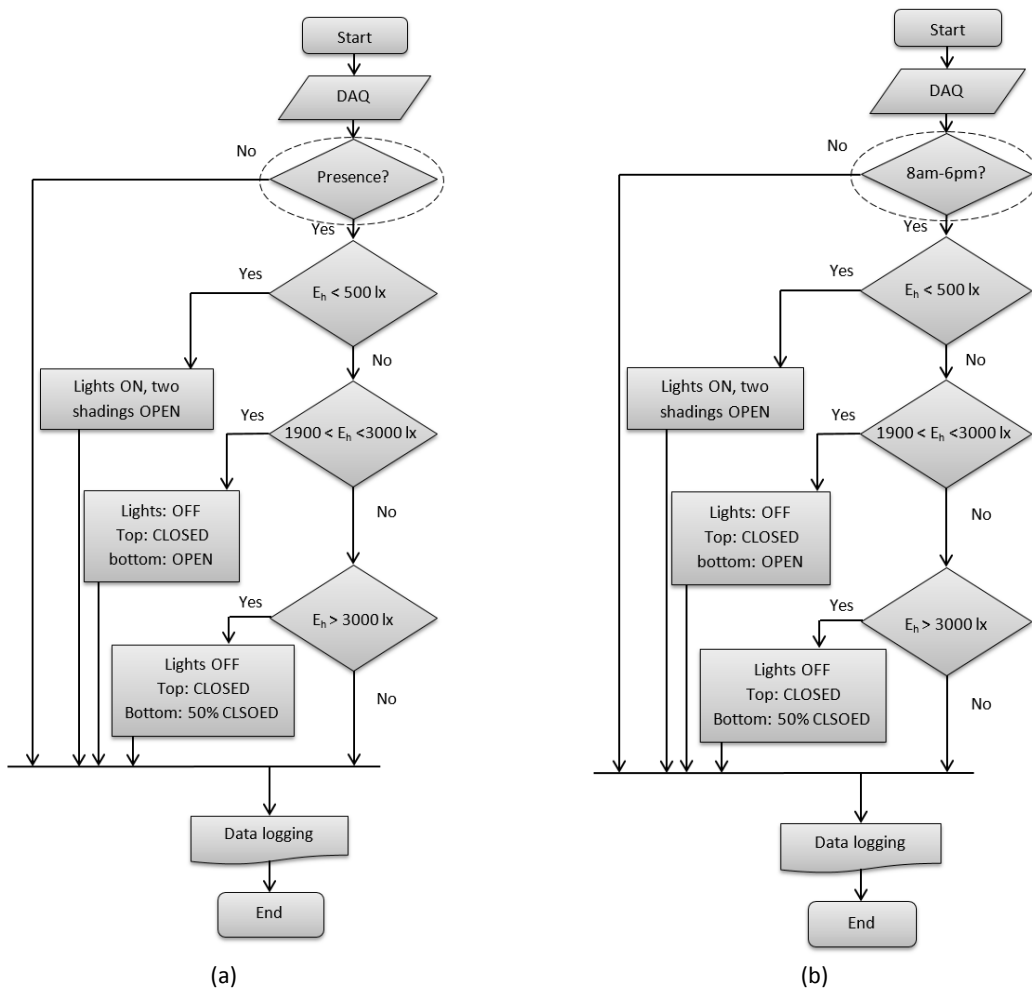


Figure 5.17 – Flow chart of the reference controller; (a) including occupant presence detection (b) without occupant presence detection. The only difference between them is encircled by a dashed oval. The first controller is utilized during the first three months and the second controller is utilized during the remaining five months.

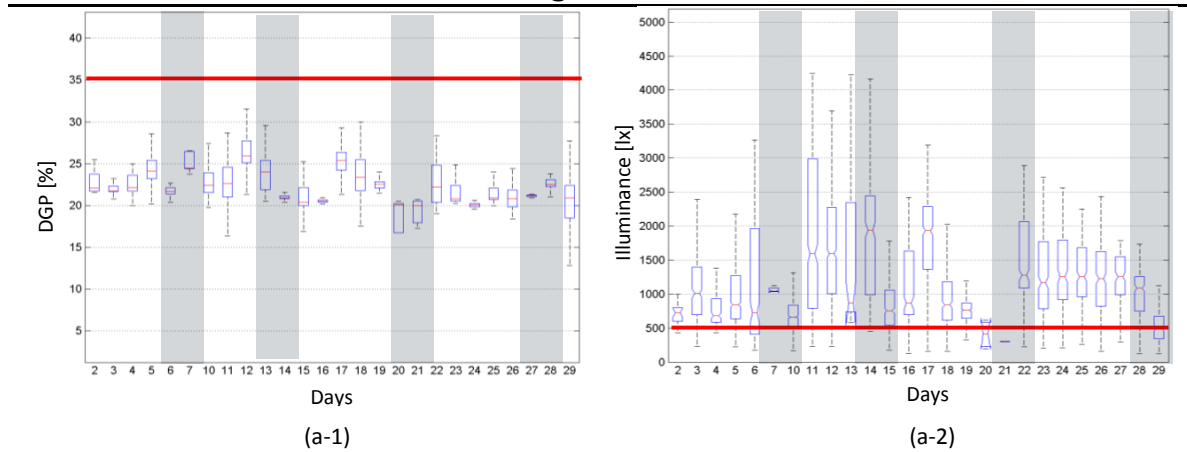
5.3.6. Experimental Results and Post Occupancy Evaluation

The duration of the whole experimentation is 4028 hours, which leads to an average of 18.06 hours/day. The data acquisition unit of the LESO building, involving a KNX network was however not operational during a couple of days; on several occasions, the controller running on an ‘ad hoc’ system programmed in MATLAB stopped. This was mainly due to random errors such as a broken wireless communication channel and/or a malfunction of the DAQ. All over during this 8-month period in both office rooms, 5.15E+08 data were monitored, some of them were used as inputs for the controller, such as the shading position for instance; some other were only used for monitoring purposes, such as the global and diffuse horizontal solar irradiance.

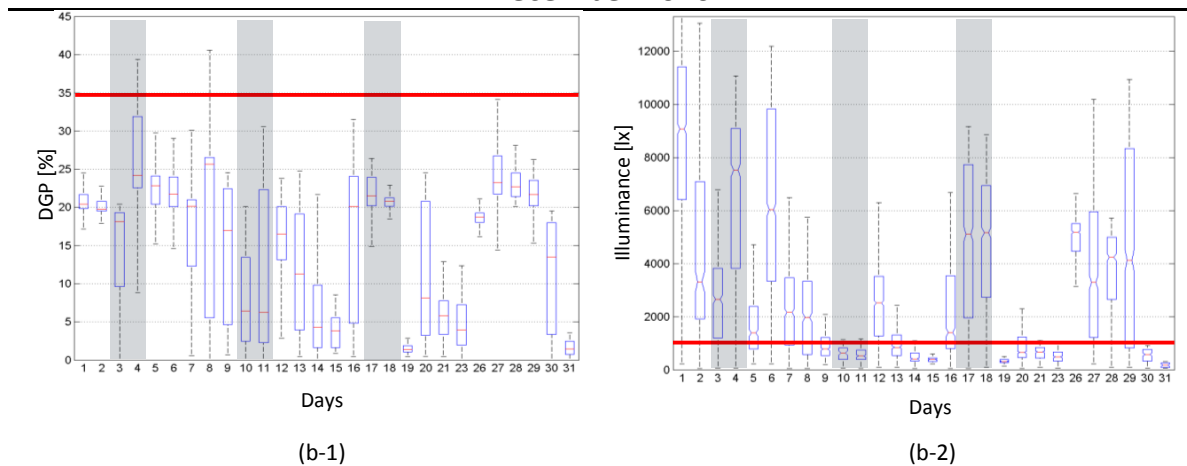
5.3.6.1. Illumination Condition

Firstly, the lighting conditions in each office room were studied. In this section, the representative months during summer, winter and springtime, namely August 2016, December 2016 and March 2017, are considered. Figure 5.18 shows the lighting situation (DGP and E_h) in the advanced office room; Figure 5.19 illustrates the work plane illuminance $E_h [lx]$ in the reference office room. Outliers are removed from the box plot based on the lighting conditions observed during work hours (8 AM to 6 PM).

August 2016



December 2016



March 2017

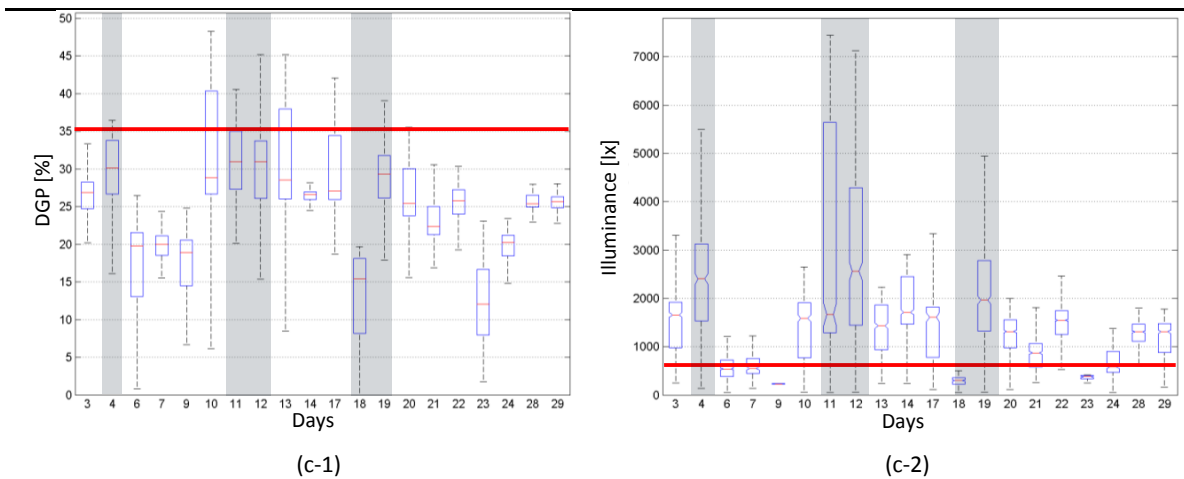
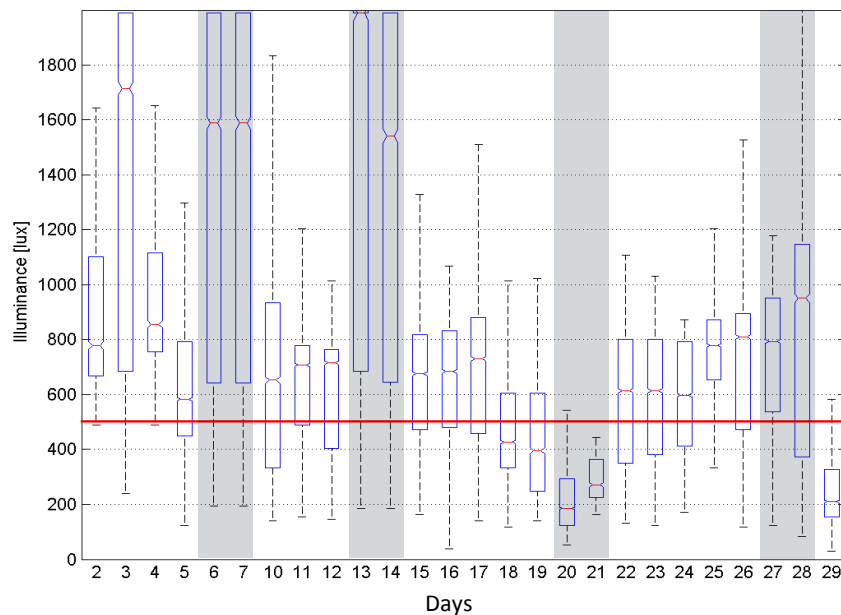


Figure 5.18 – Summary of lighting conditions in the advanced office room between 8 AM and 6 PM in (a) August 2016, (b) December 2016 and (c) March 2017 . In the left column, the boxplot of the DGP values are presented and in the right one, the Horizontal illuminance on the workstation is shown. The gray zones show the weekend periods. The red lines show the visual comfort thresholds.

The horizontal red lines show the visual comfort boundaries. For DGP , the comfortable region is the area below the red line and for E_h , it is above. The vertical gray stripes indicate the weekend periods as the occupant presence probability is lower during the weekends compared to work days. During these days, in case of occupants' absence, only the thermal comfort criteria are considered.

One can observe that, there are some days characterized by DGP readings falling into the discomfort zone above the red line during March 2017. It is possible that the office room was unoccupied during these days; thus only the thermal controller was in action. In another case, it is possible that the DGP exceeded the visual comfort limits and/or E_h readings falls below the threshold value, while the subject is absent for a given time period. In these cases, the performance of the controller cannot be assessed only by considering the DGP or E_h : a new metric is required for that purpose.



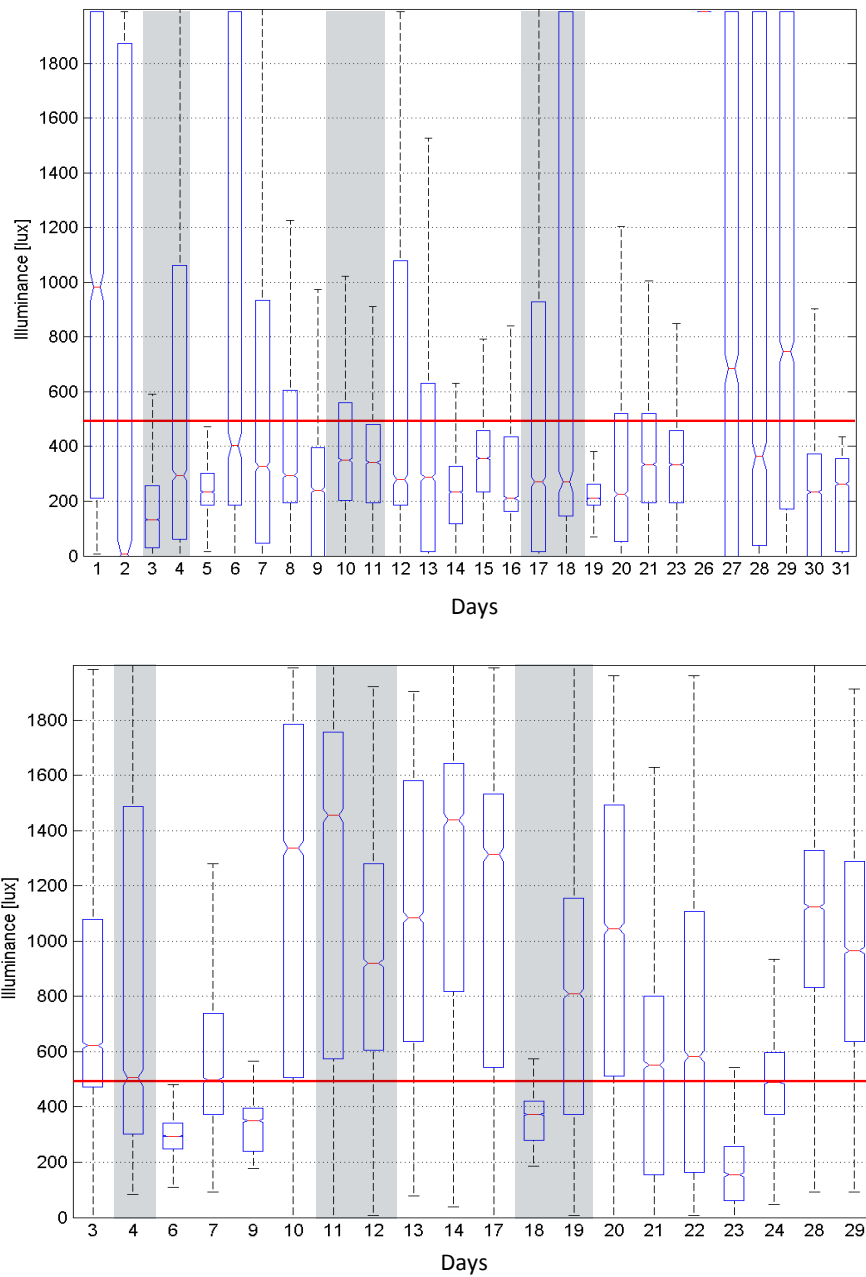


Figure 5.19 – Lighting conditions in the reference office room in (a) August 2016, (b) December 2017 and (c) March 2017. For this room, only the horizontal illuminance [lx] on the workstation is monitored. The gray zones show the weekend periods. The red lines show the visual comfort thresholds.

The DGP values remain below the setpoint of the control system, except for the days when the office occupant is absent and the presence probability is low (e.g., during weekends). In this case, the shading system actuation is based on the indoor air temperature. During December, as this temperature is low, the shading remains open in the office room in order to enhance the passive solar heat gain.

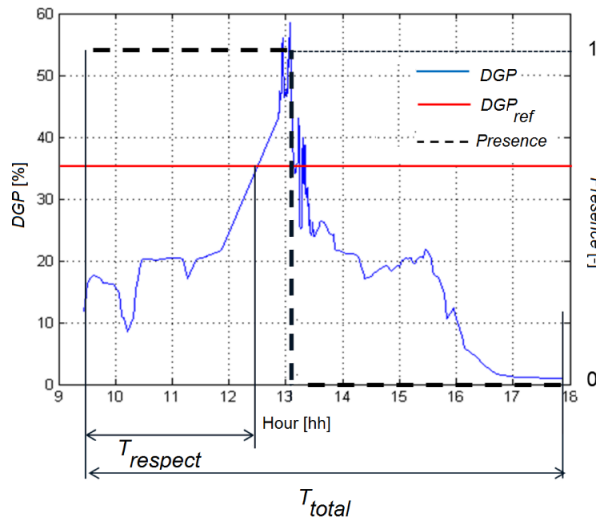


Figure 5.20 – Illustration of the variables used in Eq. (5-8) by a monitoring example on the 6th February 2017. DGP , DGP_{ref} and $\gamma_{presence}$ are depicted.

The analysis of the DGP and horizontal illuminance boxplots provides a global overview of the controllers’ performance. However, the complex nature of the advanced control algorithms, encompassing visual and thermal comfort, necessitates a more comprehensive and universal performance criterion. The performance of the controllers can be evaluated based on their success or failure in respecting the lighting constraints during the time the latter these should have been respected. In other words, the controller performance can be quantified by the relative fraction of time, during work hours, when occupants are present and the visual comfort constraints are respected. The mathematical expression of this criterion is shown in Eq. (5-8); it is called “visual comfort constraints respect ratio” or $\rho_{respect}$.

$$\rho_{respect} = \frac{T_{(respect=1, Presence=1)}}{T_{total}} \cdot 100 \text{ [%]} \quad (5-8)$$

where $T_{(respect=1, Presence=1)}$ is the time step during which both constraints are respected [s], e.g. $DGP < DGP_{ref}$ and $E_h > E_{h_{ref}}$, while the occupant is present ($Presence = 1$); T_{total} is the total duration of the experiment run during work hours (8 AM to 6 PM) [s]. $\rho_{respect}$ can vary from 0 to 100%; 100% corresponds to the most performing controller, as at no time the comfort constraints are violated. The variables of this equation are illustrated by an example shown in Figure 5.20; for the sake of simplicity, only the DGP index is considered.

The constraint respect ratio is evaluated for each month and illustrated in Figure 5.21. On average, the constraints are respected in the advanced office room during 88.1% of the work hours.

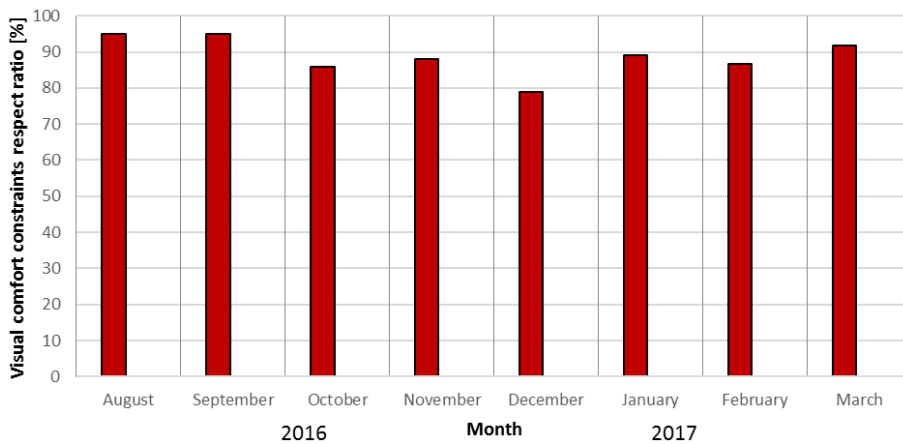


Figure 5.21 – Monthly visual comfort constraint respect ratio ($\rho_{respect}$) for the advanced office room during working hours (8 AM- 6 PM) for long-term experiments.

5.3.6.2. Shading Control Performance

Another criterion for evaluating the performance of the shading and lighting controller is the number of movements: if an automated system is requesting too frequent amendments, the occupant acceptance diminishes.

Figure 5.22 compares the total monthly number of shading and electric lighting amendments. Overall, the blinds in the advanced office room are moved 68% more frequently than in the reference office room. On average, the two shading systems' positions as well as the lighting system status are amended 4.48 and 2.66 times per day in the advanced and reference office room, respectively.

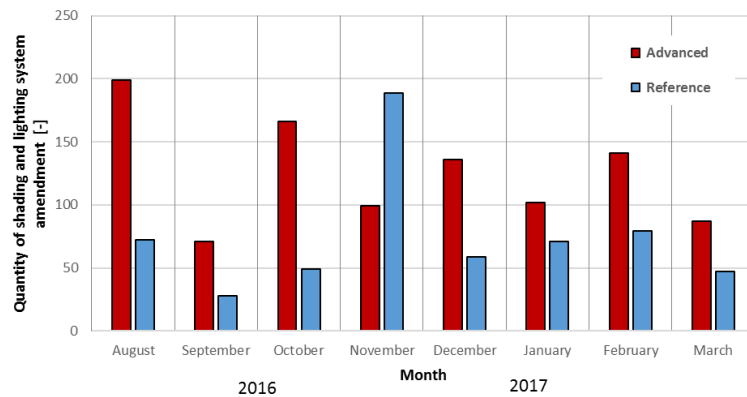


Figure 5.22 – Number of shading and lighting system actuations for reference and advanced office room during long-term experiment.

Figure 5.23 shows the weighted average top shading position for the advanced and the reference room. The definition of the average shading position is given by Eq. (5-9).

$$\bar{\gamma} = \frac{\sum_{i=8am}^{6pm} \gamma_i \cdot \tau_i}{\sum_{i=8am}^{6pm} \tau_i} \tag{5-9}$$

where $\bar{\gamma}$ is the average shading opening fraction [–], γ_i is the shading opening fraction at time step i monitored between 8 AM and 6 PM [s], and τ_i is the duration of the time step i [s].

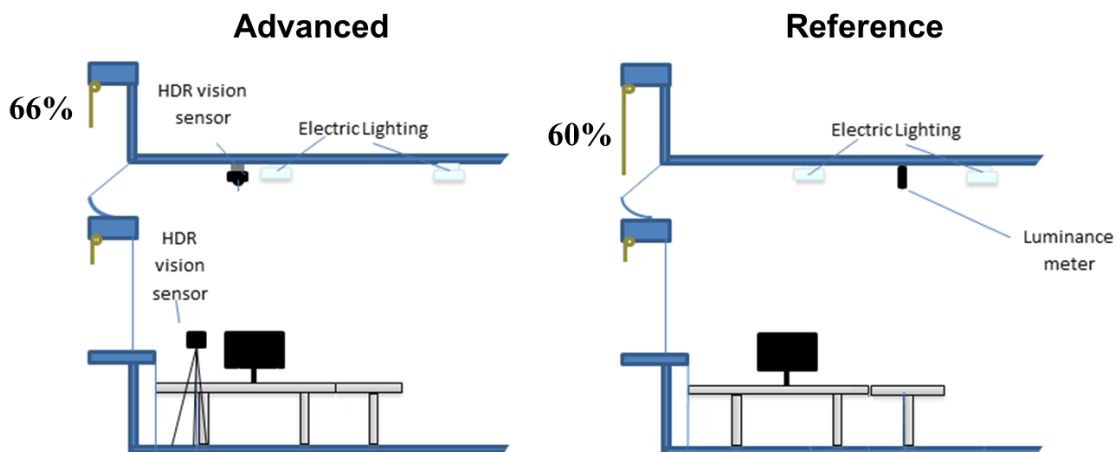


Figure 5.23 – Average shading opening fraction comparison between reference and advanced office room during the working hours (8 AM-6 PM). Top shading is operated differently but bottom shading is rarely used.

On average, the top shading opening fraction during the work hours in the advanced room is 10% larger than in the reference room. However, a close look at the monthly average shading position (Figure 5.24) reveals a seasonal dependence for the top shading control: during the warmer months (August 2016 to October 2016) the opening fraction

of the top shading in the advanced room is smaller with respect to the one in the reference room: this leads to a larger rejection of solar heat gain mitigating overheating risks. By contrast, during the colder months, the opening fraction of the top shading is relatively larger than in the reference room, allowing for larger solar heat gains: this favorable behavior is due to the integration of the solar profile angle in the advanced control strategy.

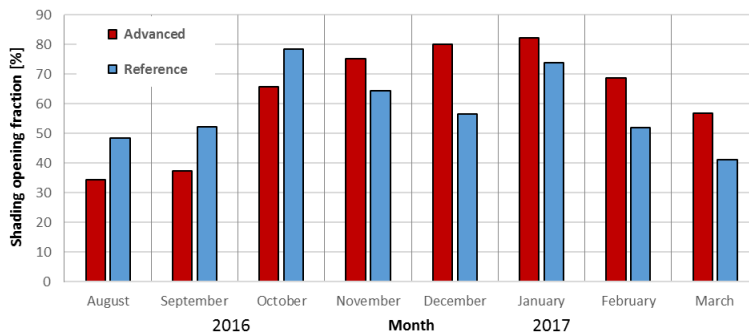


Figure 5.24 – Top shading opening fraction during working hours (8 AM- 6PM) for reference and advanced office room for long-term experiments.

Figure 5.25 illustrates the average opening fraction of the bottom blinds showing that it is more frequently activated in the advanced room; the difference between the two rooms is however not considerable.

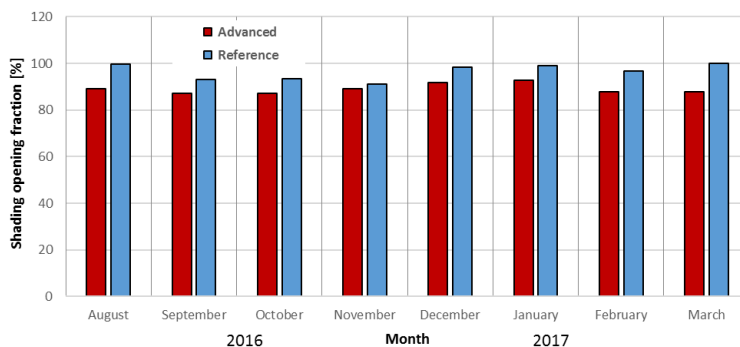


Figure 5.25 – Bottom shading opening fraction during the work hours (8 AM- 6PM) for reference and advanced office room for long-term experiments.

5.3.6.3. Influence of Advanced Shading Control on the Performance Gap

The energy performance gap is defined as the difference between the calculated and measured energy consumption of a building, some authors mentioning deviations of +34% with a SD of 55% based on 62 buildings [203]–[205]. It is stressed that dominant factors related to specification uncertainty in occupant behavior, modeling and poor operational practices have an estimated impact of 10– 80%, 20– 60% and 15– 80% on the energy demand respectively.

Clearly, the difference in shading system management has an impact on the heat demand and thermal comfort of offices. The sun is a free source of energy for buildings; however, the necessity to avoid overheating and maintain indoor comfort for the occupants as well as the mismanagement of shading due to ignorance, can reduce the passive solar gain in a significant way: accordingly, during wintertime, the back-up heating demand is increased and may differ from the value calculated during the building design.

5.3.6.3.1. Goal

A method to quantify the energy performance gap is through comparing the “Useful solar heat gain utilization factor” (FU) of a building equipped with passive solar systems (e.g. e-coated double or triple glazing windows). This variable is simply defined as follows:

$$FU = \frac{Q_{SU}}{Q_p} \quad (5-10)$$

where $Q_{SU}[MJ]$ is the useful solar gain and $Q_p [MJ]$ is the maximal potential solar gain corresponding to an ideal utilization of a building space and facade. The higher the FU is, the more the building benefits from the *free* solar heat gain in order to compensate the thermal losses., reducing accordingly its back-up heating needs.

To fully depict the magnitude of the impact of shading management on the energy performance gap, six different scenarios were considered:

- **Scenario 1:** Unoccupied office room without shading system, maximizing the solar gain to the detriment of visual and thermal comfort (FU_1)
- **Scenario 2:** Advanced office room (FU_2)
- **Scenario 3:** Reference office room (FU_3)
- **Scenario 4:** Manual shading system control by an energy conscious occupant influenced by visual comfort according to Scartezzini et al. [9]: top blinds are closed and bottom blinds set to 75% opening fraction if the vertical solar irradiance on the facade reaches $150 [W/m^2]$. Both are opened when the irradiance falls below the stated threshold and glare risk is reduced. It must be noticed that the person occupying the reference office room behaved in this way (FU_4)
- **Scenario 5:** Manual shading control by an average or standard occupant lowering the top shading to 0% and bottom shading to a 50% opening fraction if the vertical solar irradiance on the facade reaches $150 [W/m^2]$ and does not retract the blinds until late afternoon: this scenario resembles the observations made by Paule et al. [24] on a building of the EPFL Innovation park; the occupants of offices with a south-facing facade keep the shading, on average, with a 26% opening fraction and do not move the blinds more than 1.46 times a week. This vertical solar irradiance threshold is also used in other studies [206], [207]. Most of the people fall into this category (FU_5).
- **Scenario 6:** Manual shading control by an inactive occupant keeping the shading system closed throughout the day regardless of the available daylight; he/she compensates a low workplane illuminance by using the electric lighting (FU_6).

Scenarios 1, 4, 5 and 6 are hypothetical; their labels are inspired from a recent study by Ben et al. [208]. Scenarios 2 and 3 are real scenarios and were monitored during the experimentation. The FU evaluation period corresponds to the heating season, i.e., from October to March.

5.3.6.3.2. Approach

In this section a possible way to determine the “Utilization factor of solar gain” (FU), showing limitations in our case, is presented and discussed. In a next step, a new approach, better adapted to our in-situ monitoring and experimentation is proposed.

Scartezzini et al. [9] evaluated FU by an indirect evaluation of the useful solar heat gain Q_{SU} . Assuming that the internal heat gains and the thermal losses through the external building envelope is known, Q_{SU} can be deduced by applying the energy conservation law by assuming adiabatic conditions between two adjacent office rooms:

$$Q_F + Q_c + Q_{SU} + Q_o + Q_v + Q_e + Q_L = 0 \quad (5-11)$$

where

Q_F is the thermal loss through the facade alone [MJ];

Q_c is the back up heating [MJ];

Q_{SU} is the useful solar gain [MJ];

Q_o is the thermal heat gain from the occupant [MJ];

Q_v is the heat exchange with the neighboring offices [MJ];

Q_e is the heat exchange with outside through the air infiltration [MJ]; and

Q_L is the heat gain from the lighting system and other electric appliances (i.e. computers) [MJ].

In this first approach, the unknown variable is Q_{SU} , which can be determined using monitored data of the remaining variables. On the other hand, the maximal potential solar heat gain (Q_p) is estimated using the *global vertical irradiance on the facade (GVS)* (usually measured) and the *maximal equivalent solar radiation capture surface (S_t)* (estimated using architectural drawings):

$$Q_p = S_t \cdot GVS \quad (5-12)$$

where $S_t = A \cdot g$; A is the net area of the window pane [m^2] and g is the Solar Heat Gain Coefficient of the glazing. [–]

In our case, Q_{SU} is still unknown and can be calculated using monitored data of the remaining variables. The maximal potential solar heat gain (Q_p) is determined in the same way; a building thermal balance calculation software, allowing one or more heated or cooled zones [209], is however employed to determine Q_c . This software, named LESOSAI (2017.0 build 1118) comprises a routine for dynamic simulation of buildings based on the Swiss Standard SIA382/2-SIA2044, which estimates the indoor temperature and power requirements for the HVAC system. The work flow of this approach is illustrated in Figure 5.26.

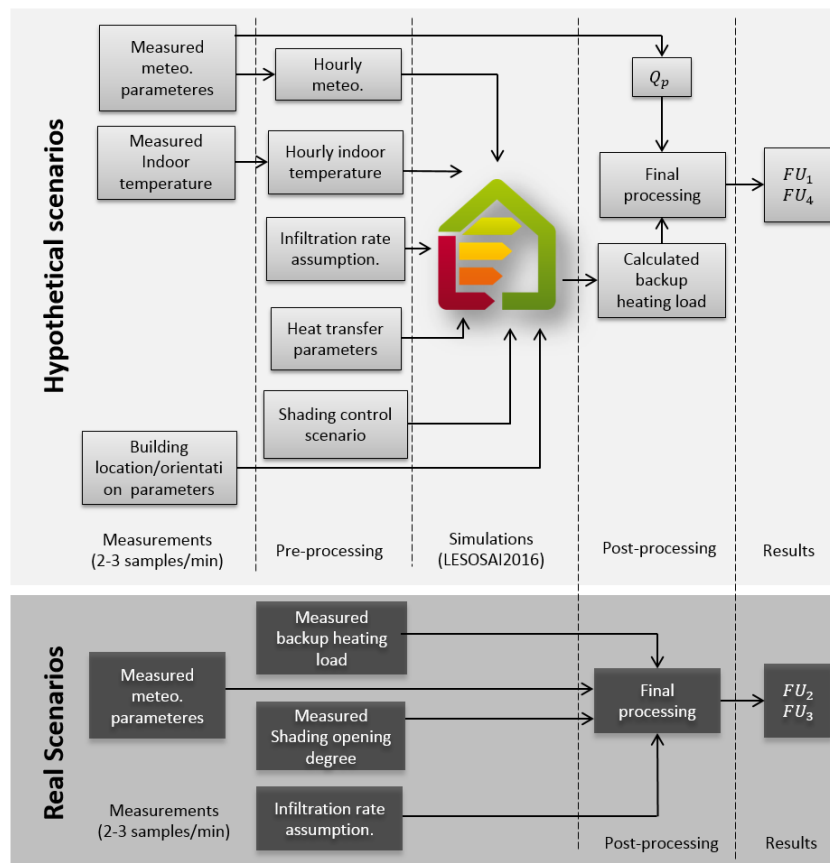


Figure 5.26 – Flow chart of FU evaluation using a LESOSAI-based approach. The block diagram “final processing” refers to Eq. (5-10), (5-11) and (5-12).

In spite of the great potential of this software for estimating the HVAC power requirement, there are fundamental issues with this approach for the current project:

- Without accessing the source code of the LESOSAI, it is not possible to introduce the real shading positions. This field data is essential for simulation of Scenarios 2 and 3 and calculating the backup heating energy;
- Extensive room model tuning is required to obtain the accurate backup heating for hypothetical Scenarios 1,4,5 and 6;

- All the meteorological data required by LESOSAI, such as sky temperature and wind speed are not registered;
- In real scenarios, the setpoints for the backup heating system is adjusted manually by the occupant. These setpoints are difficult to introduce to the software;
- Finally, the internal gains such as occupants and lighting, exchange with neighboring offices and the basement, infiltration rate are approximately implementable in the LESOSAI. The accuracy of this model, as stated in [9], is about 10%.

However, for the current set of experiments, the shading system's opening fraction is monitored in both office rooms by the data acquisition unit (2-3 times per minute) and the thermal transmittance of the fabric blinds is known. At the same time a monitoring of the horizontal global solar radiation is carried out. Knowing the g-value and U-value of the double glazing windows suggests that the Q_{SU} can be calculated *directly*; this approach is schematically represented in Figure 5.27.

This approach is as accurate as the window thermal transmittance value estimation is. The sources of inaccuracy are equal for the six scenarios and may contribute to errors in the same way, thus the results are comparable for all six scenarios.

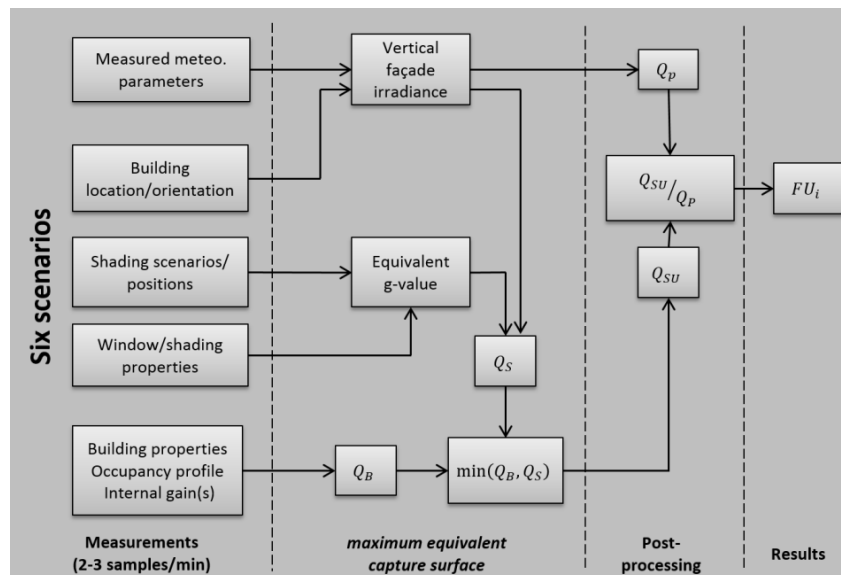


Figure 5.27 - Approach proposed for FU evaluation.

The advantage of this approach is that it does not depend on the assumptions stated previously, except for the air infiltration rate. The FU for the hypothetical and real cases are independent from the indoor temperature setpoint in the office rooms.

According to Guillemin [156], the global vertical irradiance on the facade can be extracted from the sun position, the facade orientation and the global and diffuse horizontal irradiance.

The part of the potential solar heat gain (Q_p) passing through the shading and the fenestration system (Q_s) can be calculated by knowing the shading position. Evaluation of the equivalent g-value of the complex fenestration system depends on the location of the shadings (interior or exterior) and can be systematically calculated by, for example, a method elaborated by Kuhn [210], [211]. The LESO solar experimental building is equipped with an external roller shadings (Section 3.1) with an offset of 20 cm from the facade. For this reason, the interdependence between the shadings and the facade glazing can be neglected. For this reason, the multiplication method elaborated in Eq. (5-13) can be applied:

$$Q_s = GVS \cdot (\gamma_{shading} \cdot g_{glazing} + (1 - \gamma_{shading}) \cdot g_{shading} \cdot g_{glazing}) \quad (5-13)$$

where $\gamma_{shading}$ is the opening fraction of blinds [–].

Q_S is calculated independently for the top and bottom blinds; the corresponding figures are added up.

However, the whole transmitted solar energy is not *useful* as it may lead to an undesirable increase of the indoor temperature. The *usefulness* of the solar heat gain is determined by the “needed heat gain” (Q_B). Q_B is determined by knowing the thermal losses through the southern facade of the office room and the air renewal rate, as well as the internal metabolic gain due to the occupant(s) and the electric appliances. The exact relationship is formulated in Eq. (5-14).

$$Q_N = (Q_e + Q_F) - (Q_o + Q_L) \quad (5-14)$$

where Q_N is the net heat demand [MJ]; Q_e is the heat exchange with the outside, including the air infiltration [MJ]; Q_F is the thermal loss through the facade alone [MJ]; Q_o is the thermal heat gain from the occupant [MJ]; and Q_L is the heat gain from the lighting system and other electric appliances (i.e. computers) [MJ]. In Lausanne, Q_N is positive even through cooling period. The reason is that the raw thermal losses through the façade ($Q_e + Q_F$) are still larger than the internal heat gains ($Q_o + Q_L$) due to the difference between the indoor and outdoor air temperature. According to SIA Documentation 056 [212], the outdoor air temperature during August is 17.2 [$^{\circ}C$] which is lower than the 20 [$^{\circ}C$] room temperature. Consequently, although the backup heating needs in August are nil, the solar heat gain compensating for the net thermal losses of the façade during the same month.

Clearly, during the heating period, the difference between ($Q_e + Q_F$) and ($Q_o + Q_L$) is larger than the one during the cooling one, necessitating larger solar gain for maintaining the heat balance.

The useful solar heat gain is accordingly determined by Eq. (5-15) and illustrated in Figure 5.28.

$$Q_{SU} = \min(Q_S, Q_N) \quad (5-15)$$

The convective heat losses Q_e [MJ], given by Eq. (5-6) were determined using an estimated constant air renewal rate over the heating season implying that windows are closed and only slightly opened in the morning for olfactive comfort reasons. Based on this assumption, the air renewal rate is assumed to be equal to 0.6 [h^{-1}].

$$Q_e = 3.6 \cdot 10^{-6} \cdot \sum 0.6 \cdot V \cdot \rho \cdot C_p \cdot (T_{in} - T_{out}) \cdot \delta t \quad (5-16)$$

where V is the volume of the office room [m^3], ρ is the air density [$kg \cdot m^{-3}$], C_p is the specific thermal capacity of the indoor air at 25 [$^{\circ}C$] and 1 atm constant pressure [$kJ \cdot kg^{-1} \cdot K^{-1}$], T_{in} and T_{out} are resp. indoor and outdoor temperatures [K] and δt is the time laps between each data acquisition [s].

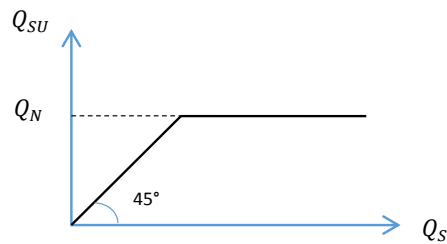


Figure 5.28 – Relationship between useful (Q_{SU}) and potential solar gain (Q_S). The useful solar gain is bound by needed solar heat gain (Q_B).

Thermal loss through the facade (Q_F) is calculated for each sampling interval by knowing the indoor and outdoor temperatures difference and the sampling interval as well as the thermal loss coefficients of the facade elements. A full description of the LESO building facade elements as well as their thermal and geometrical properties can be found in [158].

Thermal heat gain from the occupant (Q_o) is known from Scenario 2, the occupant presence being monitored at each data sampling. Finally, heat gain from the lighting system and other electric appliances (Q_L) is measured by means of a three-phases electrical energy meter providing the electric lighting and plug load electricity consumption.

The uncertainty in the evaluation of the net needed heat gain (Q_N) is mainly due to the assumption regarding the air renewal rate; its relative contribution to the overall thermal losses of the office room is however lower than 5%. The uncertainty regarding the estimation of the potential solar gain is depending on the precision of the weather station; according to Lindelöf [20] it is estimated to 10%.

5.3.6.3.3. Post Analysis Results

The potential solar gain and the needed heat gain are illustrated in Figure 5.29. It shows that during the mid-season the potential gain is large while the needed heat gain is small.

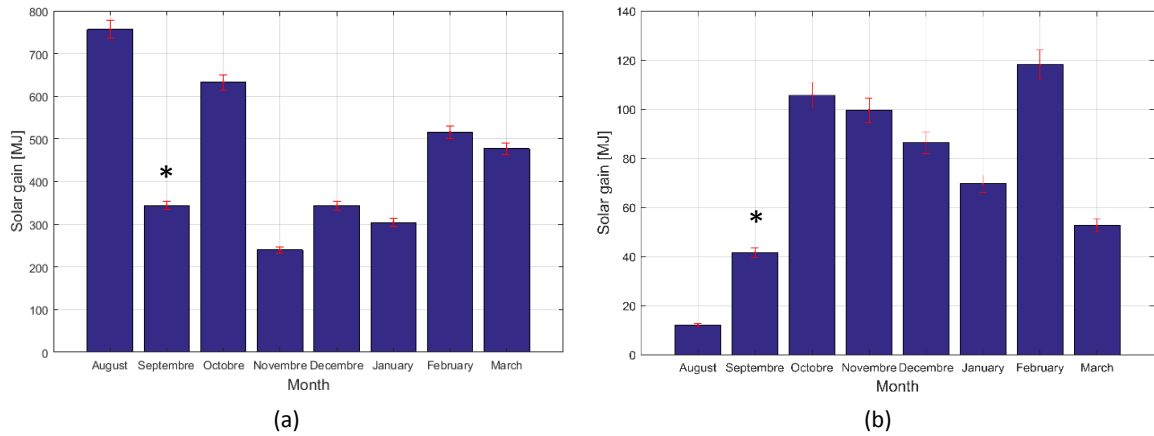


Figure 5.29 – (a) Monthly potential solar heat gain (Q_p); (b) monthly needed heat gain. (*) Data lacking for September 2016.

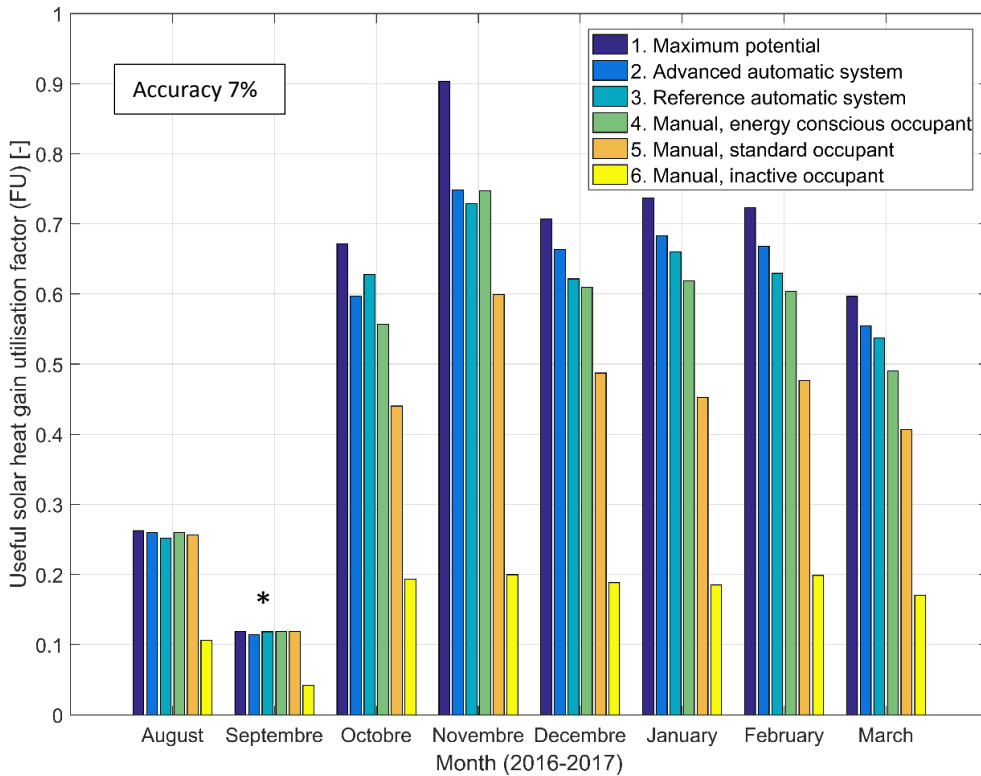


Figure 5.30 – Facade energy performance assessed by comparison of the utilization factor useful of solar gain (FU). (*) Data lacking for September 2016.

Figure 5.30 shows a comparison of the utilization factor of solar gain (FU) for the six scenarios. Scenario 1 leads to the largest FU during all months as by definition no shading is applied in front of the windows. Scenario 4, on the other hand, corresponds to the lowest FU (except for November 2016), the manual control of blinds by a glare sensitive user reducing the useful solar gain in a significant way as demonstrated in [9].

There is no significant difference between the FU during the mid-season: during these months the net heat demand (Q_N) is far lower than the transmitted solar gain (Q_S): the useful solar gain is equal to the needed solar gain ($Q_{SU} = Q_N$). However, during the heating season, the available solar gain is typically lower than the needed one. In these cases, the different shading control strategies lead to substantial differences in useful solar heat among the different scenarios: $FU_2 > FU_3$ from November 2016 to March 2017, the top shading opening fraction in Scenario 2 (advanced control) being larger than in Scenario 3 (Figure 5.24). Thus, the advanced control strategy (Scenario 2) increases the energy performance of the facade and reduces accordingly the energy performance gap.

The upper bound of the performance gap is given by FU_1 , both shading systems being kept open all the time in this case. As most office occupants are very likely standard users, the relative mitigation fraction of the performance gap using the advanced control approach can be found by normalizing FU relative to Scenario 5 during the heating season, by means of Eq. (5-17):

$$\widetilde{FU}(i) = \frac{\sum_m FU(i, m) - \sum_m FU(5, m)}{\sum_m FU(1, m) - \sum_m FU(5, m)} \cdot 100 \quad [\%] \tag{5-17}$$

i : scenarios 1, 2, 3, 4, 5, 6

$$m = \{November, \dots, March\}$$

The results corresponding to the six scenarios are $\widetilde{FU} = \{100, 71.9, 52.7, 50.4, 0, -118.8\}$ respectively. They show that the advanced controller mitigated the performance gap by 71.9% during the heating season with respect to a standard occupant and by 19.2% with respect to the ‘Best-practice’ controller (reference controller). It is worth noting that the overall performance of the automated reference controller does not differ much from that of an energy conscious and active user (e.g. not more than 5%). In order to quantify the backup heating savings for each scenario with respect to the energy-conscious occupant (Scenario 5), the relative useful solar gains given by Eq. (5-18) were determined and illustrated in Figure 5.31 (a).

$$\widetilde{Q}_{SU}(i) = \sum_m Q_{SU}(i, m) - \sum_m Q_{SU}(4, m) \tag{5-18}$$

i : scenarios 1, 2, 3

$$m = \{November, \dots, March\}$$

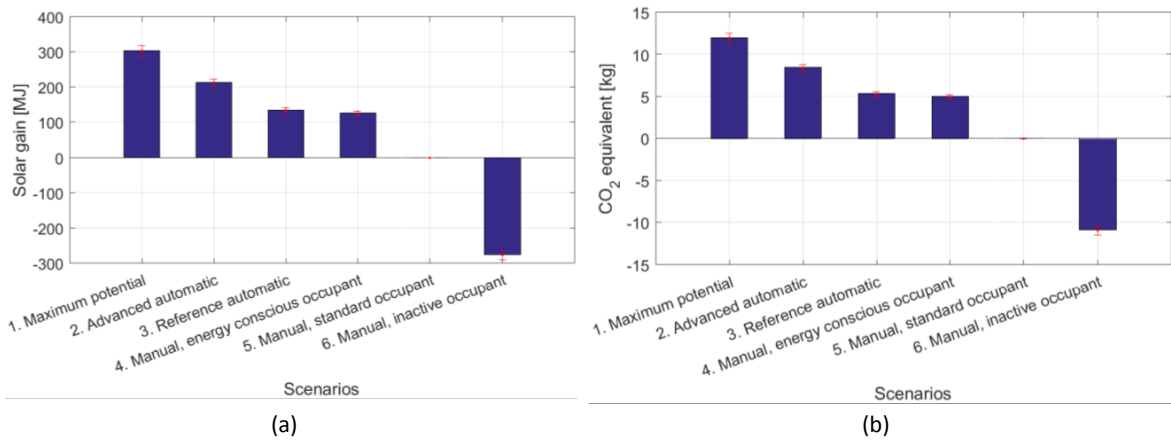


Figure 5.31– (a) Relative useful solar gain improvement with respect to the manual scenario #5 during heating season (November-March); (b) Mitigation of CO_2 emissions due to energy saving in the different scenarios with respect to the manual scenario #5.

According to Dones et al. [213] in Europe, the GHG emissions of natural gas power plants that are ranging from 485 to 991 $[g(CO_2\text{-equiv.})(kWh)^{-1}]$. For Swiss electricity mixes, this value is in average equal to 142 $[g(CO_2\text{-equiv.})/kWh]$. The backup heating is generated by electric heaters for the sake of monitoring flexibility.

The CO_2 emissions related to the energy saving of each scenario is given in Figure 5.31 (b). It shows that the advanced system mitigates the CO_2 gas emission by 8.42 $[kg]$ in comparison with the office room facilities are managed manually by a standard occupant.

5.3.6.4. Electric Lighting Demand

The whole electric lighting consumption in the two office rooms is shown in Figure 5.32. It shows that the electricity consumption during summertime is nil, indicating that daylighting is by far sufficient during the work hours. However, the winter months reveal a difference between the control strategies. The total electric lighting demand is larger during December 2016 and the first three months of 2017. During October 2016, the electric lighting consumption in the advanced office room is larger due to a considerable difference in the occupancy rates of the two office rooms, especially during the evening (Figure 5.33).

A substantial difference between the advanced and the reference office room can be observed in this figure: overall, a 48% energy saving relative fraction with respect to the reference case. Several parameters are accountable for this difference such as different occupancy rate as well as fundamental differences between the integrated shading/lighting control strategies.

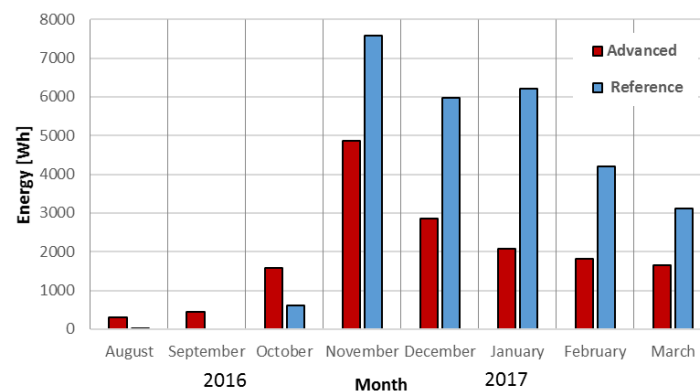


Figure 5.32 – Total electric lighting energy consumption for the two office room during long-term experiment.

Cancelling the effect of the dissimilar office occupation rates would lead to a fairer comparison of the *performance* of the controllers. To this end, the presence profile during this eight-month period is summarized and shown in Figure 5.33 (a). It represents the occupancy rate as the relative fraction of the duration of the in-situ monitoring for each month. This figure shows that there is a substantial difference between the occupancy rate during some months, such as August, November, December 2016 and January 2017. In order to benefit from a clearer idea about the occupancy rate during daytime, the corresponding values between 8 AM and 6 PM are plotted in Figure 5.33 (b). This figure shows that during most of the months, except for the last one, the advanced office room is occupied more frequently; the difference between the occupancy rates is greater in August, November and December 2016.

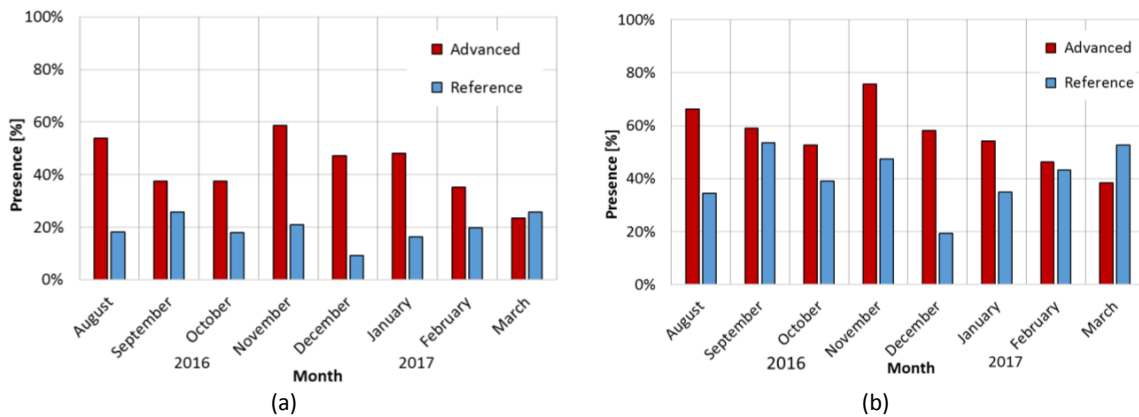


Figure 5.33 – Occupancy profile of the advanced and reference office room, (a) during the whole 24 hours; (b) during only the working hours (8AM to 6 PM).

Consequently, the results presented in Figure 5.32 do not account for the effective differences due to the controller performance and merely reflect the differences between the occupancy rates. It is worth mentioning that the presence-sensitive lighting control was deactivated in the reference room until the beginning of November 2016.

In order to have more precise idea about the differences between the controller performances, the results are analyzed using the following approaches:

Approach 1: Electric lighting energy in *reference office* counted only when the occupant is present and considered only during the work hours (e.g. between 8 AM and 6 PM). In this case, only the electricity demand for lighting is measured in presence of occupants. In other words, this case outlines the electricity consumption in the reference room if the lighting control strategy of the first three months had been kept in place until the end of the monitoring campaign. It is noteworthy that the differences between the occupancy rates are not eliminated by this way.

The corresponding results are presented in Figure 5.34. One can observe that there is a substantial reduction in the electricity demand reported for the reference office room. On the other hand, the hypothetical energy consumption in the reference office room is lower than the corresponding consumption of the advanced one during the first four months. All over, the electric lighting consumption of the advanced office room and the hypothetical case are comparable: 12.3 [kWh] and 11.4 [kWh] for the advanced one and the hypothetical case respectively.

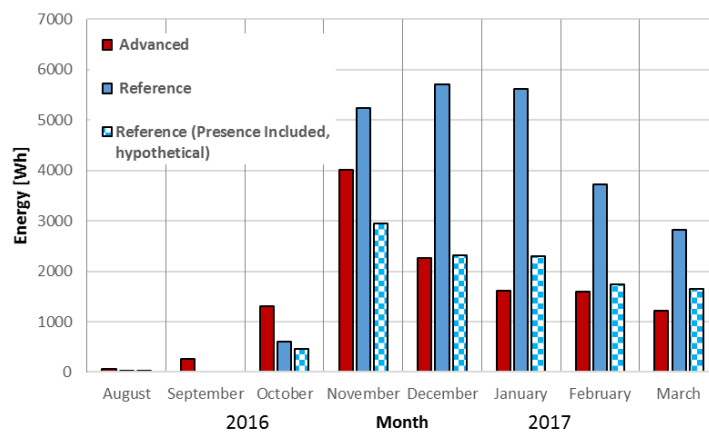


Figure 5.34 – Electric lighting consumption during the work hours compared with the hypothetical case if presence detection would also be accounted for in the reference office room.

Approach 2: Normalized electricity consumption per occupancy rate given by the Eq. (5-19). As mentioned previously, Approach 1 does not eliminate the impact of different occupancy rates. In this approach, this influence is normalized by:

$$P_{el,norm} = \frac{E_{el}}{T \cdot \eta} \left[\frac{Wh}{h_{presence}} \right] \quad (5-19)$$

where E_{el} is the electric lighting consumption [Wh], T is the duration of the monitoring campaign during each month (8 AM-6 PM) [h] and η is the monthly occupancy rate (8 AM-6 PM) [-].

The results are shown in Figure 5.35. Except for September and October 2016, during the rest of the months, the occupancy-normalized electricity demand is smaller in the advanced office room; 93.5 [Wh.h⁻¹] and 272.7 [Wh.h⁻¹] for the advanced and reference office rooms respectively; the largest discrepancy is observed in December 2016.

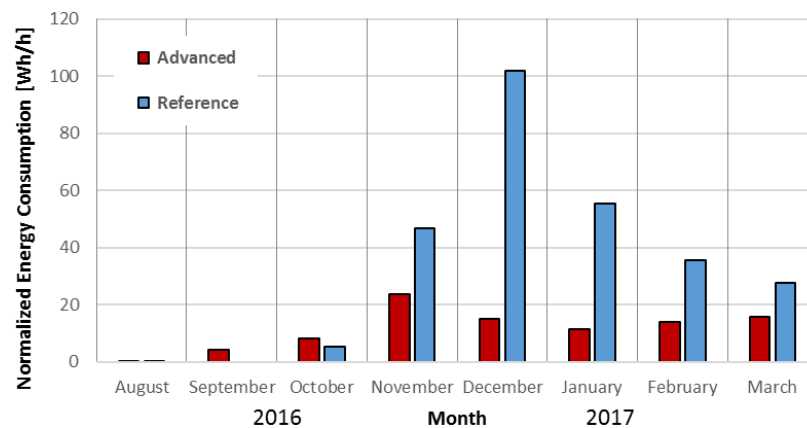


Figure 5.35 – Electric lighting demand normalized by the duration of monitoring and occupation rate, shown for the two office room during the long-term experiment.

5.3.6.5. Heating Demand

The back-up heating system is identical in the two office rooms: a closed-loop on/off controller with manually adjustable setpoints is managing it. The heating demand is compared for the two office rooms in Figure 5.36. The energy consumption for heating during August, e.g. the first month of monitoring is equal to zero. The heating demand is generally larger in the colder months of January and December 2016; it is lower during the mid-season months. This trend is observed for both offices.

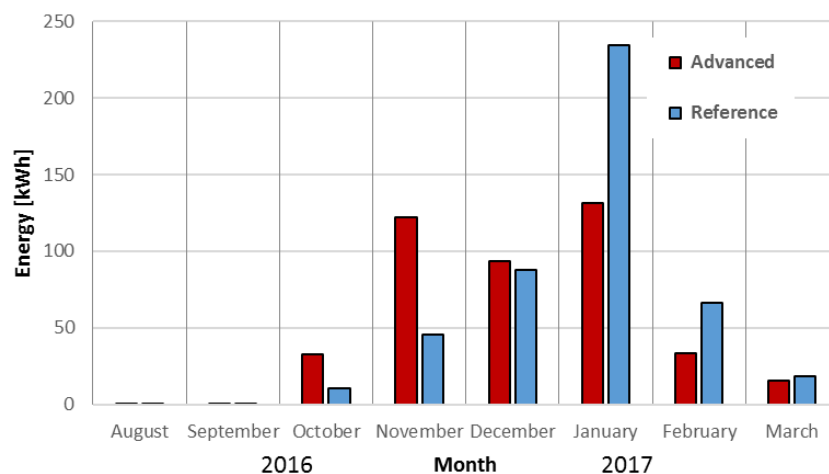


Figure 5.36 – Comparison of the back-up heating demand in the two office rooms during 7 months of long-term experiment.

For a better insight into the back-up heating performance, the indoor temperature setpoints fixed by the office occupants were extracted from the LESO building BMS data: each human building interaction was saved in the BMS database and therefore accessible. Logically, the setpoints remained constant between two interactions; the carpet plot of the heating system setpoints for both office rooms is plotted in Figure 5.37. They are not modified too frequently in September and October 2016; the occupants begin to use the heating system in November 2016. Their interaction rate with the heating system remains high until the end of the monitoring period. It is noticeable that the temperature setpoint in the reference office room is maintained at 24 °C during the whole month of January 2017.

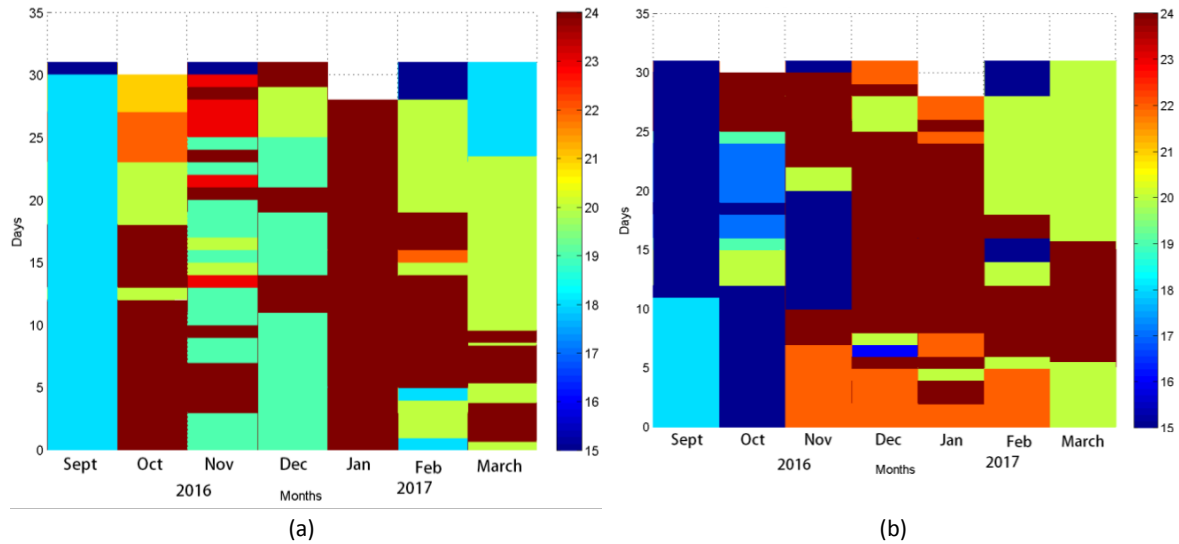


Figure 5.37 – Carpet plot of the heating system temperature setpoints [°C] manually selected by the occupants for (a) reference office room, (b) advanced office room.

For the sake of simple comparison, the heating system setpoint temperatures are represented in boxplots on Figure 5.38 and the average values are drawn in Figure 5.39.

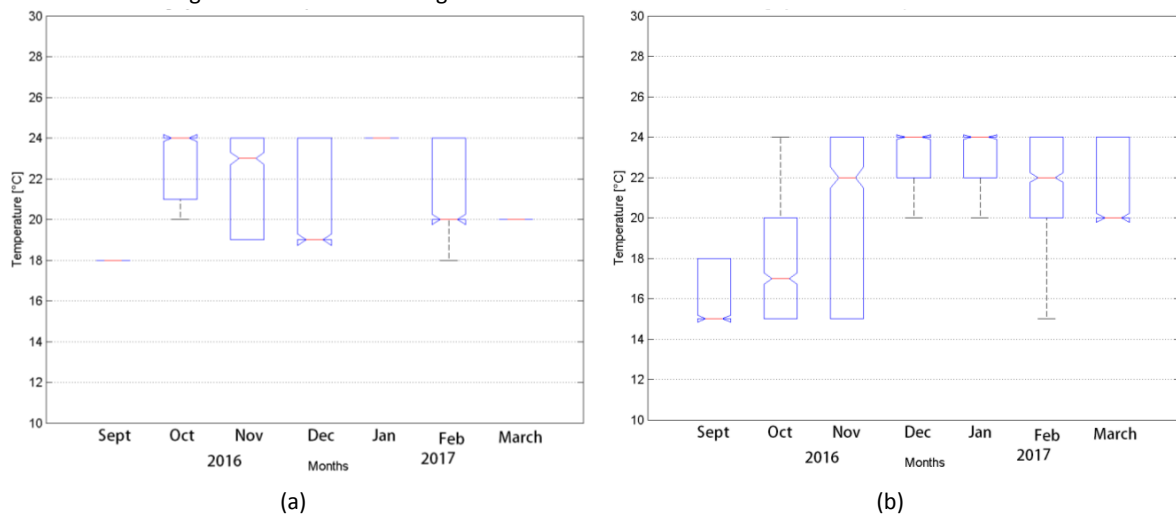


Figure 5.38 – Box plots of the monthly heating system temperature setpoint for (a) reference office room, (b) advanced office room.

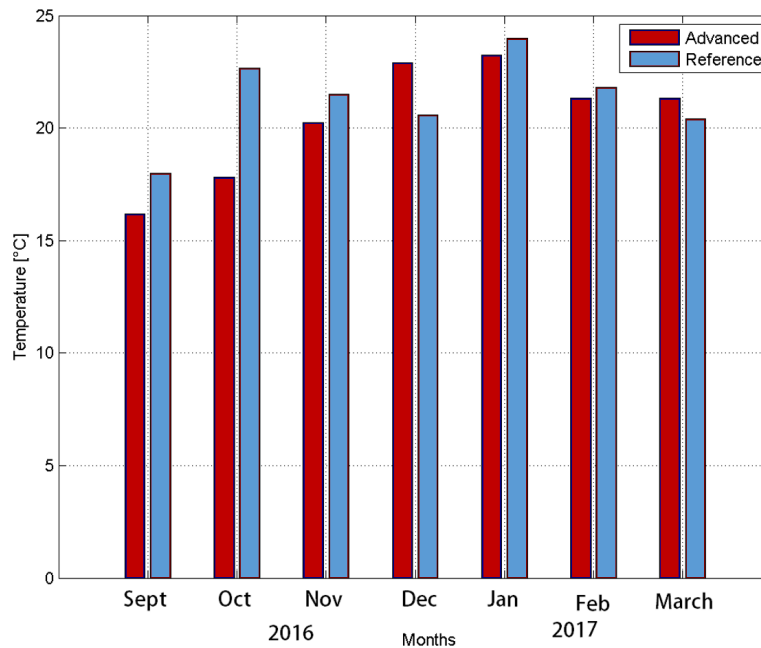


Figure 5.39 – Comparison of average temperature setpoint of heating system for 7 months of long-term experiment.

The back-up heating system in the advanced office room seems to have a malfunction from 14th to 17th October 2016. Even if the indoor air temperature was considerably higher than the temperature setpoint, the heating system remained active: more than 25 [°C] for the indoor air temperature (Figure 5.40 (a)), while the temperature setpoint was set to 19 – 21 [°C] (Figure 5.37 (a)). On October 15th 2016, the temperature setpoint was fixed to be 22 [°C], the heating system consuming more than 12 [kWh] and the indoor temperature reaching 30.4 [°C].

During the other months, the behavior of the back-up heating controller remained more coherent: the indoor air temperature did not exceed the setpoint to a great extent. As the heating controller performance was not the main focus of this work, further investigations are left for further research studies.

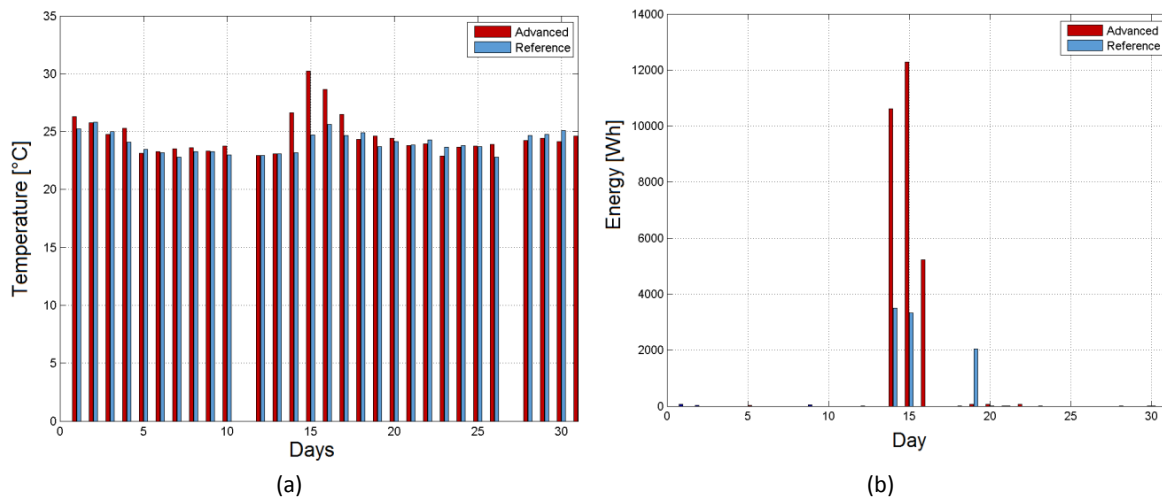


Figure 5.40 – Performance of backup heating system in October 2016: (a) indoor air temperature [°C]; (b) heating energy [Wh].

5.3.7. Discussion

Comparing the lighting conditions in the two offices shows that the thermal comfort is a priority during the month of August: the controller maintains the top blinds closed as soon as the indoor air temperature reaches the upper comfort limit. The visual comfort is directly influenced by this controller decision: glaring sources are practically eliminated by

closing the top shading system. On the other hand, the indoor air temperature remains within the comfort zone most of the time during December 2016, due to the closed-loop control of the back-up heating. In this case, DGP and E_h readings are larger than the ones registered during August 2016.

It is noticeable that the visual comfort constraints respect ratios are high but not close to 100% in the advanced office room. There are several reasons for that:

i) First of all, the commands filtering mechanism guarantees low frequency and meaningful amendments of the blinds and the electric lighting system; there are moments, especially during the mid-season, when the controller is not allowed to react rapidly to the frequent alteration of solar radiation. In other words, the uncomfortable lighting condition is tolerated in favor of less disturbance to the office occupant.

ii) The fuzzy logic controller operates on the basis of 'if-then' rules and was formed according to prior observations and knowledge of the author: this approach is theoretically prone to some limitations. Unexpected glaring sources, such as the sun reflections on neighboring buildings are not foreseen in the rules base: in this case, the control system does not necessarily eliminate the glare sources from the field of view.

iii) The electric lighting system is designed to provide 300 [lx] on the workplane at full power. The reason is that the electric lighting is designed to compensate for the lack of daylight. During the winter season, especially in November and December, sunset occurs around 5 PM. Thus the electric lighting is not capable of providing 500 lx on the work plane after the sunset.

Shading and lighting amendments in both office rooms remains bounded to reasonable numbers. In the advanced office room, they are relatively higher, as the control system takes more refined and delicate actions.

The two offices are not occupied in the same manner during the monitoring period. This discrepancy has a substantial impact on the electric lighting consumption. The electric lighting power (e.g. the electric lighting demand per occupant presence duration) is considerably reduced by implementing an advanced controller equipped HDR vision sensors for glare and work plane illuminance control. The integrated day- and electric lighting control empowered with occupancy presence detection is a key factor to this superior performance.

5.3.8. Limitations

Despite the higher performance of the advanced controller with respect to the best practice automatic scenario and manual control scenarios, the advanced controller has some limitations.

The fuzzy-logic control algorithm might undergo a tuning process once the controller is going to be implemented in a new environment. On the other hand, the controller exerts by principle an open-loop control. If it cannot guarantee visual comfort on some occasions, there is no feedback to take this failure into account. These two limitations are addressed in Chapter 6. On the other hand, evaluation of the E_h from a ceiling mounted HDR vision sensor might not be generalizable. The conversion factor between average apparent luminance of the horizontal plane from the sensor's point of view and E_h (Eq. (G-2)) should be updated when the system is installed in another office room.

The office occupants did not report any dissatisfaction with the automatic control system. Moreover, the visual comfort zone boundaries was respected for 88% of the duration of occupant presence. However, the occupant's acceptability and his/her visual performance are not evaluated through a systematic subjective assessment survey, similar to the one in the short-term experimentation (Section 5.2).

5.3.9. Conclusion

An eight-month measurement campaign was carried out in two identical office rooms in the LESO solar experimental building. It showed that appropriate management of the shading and electric lighting system by the advanced controller mitigated the energy performance gap by 72% with respect to a standard occupant and by 19% with respect to the best practice scenario during the heating season. This improvement is achieved through a larger window opening fraction when the risk of discomfort glare is not present thanks to more refined assessment of visual comfort and

workplane illumination sufficiency. Consequently, the solar heat gain can mitigate the back-up heating needs in the advanced office room leading to a smaller performance gap. It is also shown that the advanced system may theoretically mitigate the CO_2 emission by 42.4 [kg] in comparison with the case when office room facilities are commanded manually by a standard occupant. Meanwhile, the control system managed to confine the indoor lighting condition in the comfort zone during 88% of office occupancy. Based on these facts, the author concludes that it is possible to improve the energy performance of a building, to reduce its CO_2 emission and mitigate the performance gap without jeopardizing the occupant's visual and thermal comfort.

Having reached this conclusion, one can answer the third research question raised in Section 1.3 by stating that “yes, it is possible to improve energy performance of a facade, reduce its performance gap by 71.9% with respect to the standard occupant, reduce the potential CO_2 emission produced because of the energy consumption the heating system, while guaranteeing his visual comfort for 88.1% of working hours.”

Chapter 6

Self-Commissioning Venetian Blinds Controller

This chapter is intending to answer the forth research question raised in Section 1.3:

- *Is it possible to facilitate the commissioning of the enhanced BMS without compromising its performance?*

The main contribution of this chapter, a novel control approach, is presented in Section 6.2. The second contribution, a novel method for visualization and analysis of shading and indoor lighting status is presented in Sections 6.4.1 to 6.4.3.

The sections of this chapter are arranged as follows: In the first section the motivation is elaborated. The control approach is presented in Section 6.2. The preparatory work for the case study is elaborated in Section 6.3. In Section 6.4, the results of experimental implementation in a daylight testbed are shown, followed by a discussion and conclusions in Section 6.5. Finally, suggestions for the further enhancement of the proposed approach are presented.

The control approach was tested through an in-situ experiment, for 22 full days in September and October 2017, in a daylight testbed at Fraunhofer Institute for Solar Energy (ISE). For more details on this testbed, the reader may refer to Section 3.3.

The present work was carried out during 8 months, from March to October 2017, as an outcome of a part time scientific sojourn in Freiburg i B., Germany, financed through a PhD exchange grant by Zeno Karl Schindler (ZKS) Foundation.

6.1. Motivation

In previous chapters, the author proved the benefits of application of a HDR vision sensor in BMS using a Fuzzy Logic Control (FLC) system. However, the previous work has several limitations, namely:

- The design and performance of the FLC depends heavily on the experience of the researchers. Normally a process of fine-tuning is needed before the system is fully functional.
- The FLC system is not easily adaptable to another indoor environment with different facade orientation and distance and position of the workstation. In other words, each time the control system is installed in a new environment, the shape functions of the FLC (Appendix A), needs to be restudied and updated.
- The suggested FLC does not guarantee the visual comfort at any moment since, by principle, it is an *open loop* control. In the case of failure in providing visual comfort, the control system does not have any mechanism to correct its own action.

There are possible solutions to the stated limitations:

i) Closed-loop control: the shading system is amended by small increments until the DGP index is bound below a predefined threshold. This method is not efficient enough for real-world applications due to the large number of shading system movements and consequently disturbance of the occupants it entails.

ii) Model-based control: a room lighting model can be used to estimate the DGP at certain points of the room. Based on this estimation, an optimization routine can find the optimum position of the shading system leading to a DGP below a predefined threshold. The disadvantage of this approach is the necessity of a costly model.

The author suggests a novel *self-commissioning efficient* approach to overcome the stated issues, which outweigh the other possible solutions. *Self-commissioning* in this context means that a non-specialized fitter can install the integrated automatic shading and lighting control system by introducing easy-to-obtain field parameters such as distances and orientations of workstation, for example, by means of hand-held measuring devices and a compass. *Efficiency* in this context means that the system makes the least possible number of blinds' position amendments to guarantee a comfortable environment.

6.2. Control Approach

The control approach is presented in the following paragraphs by an introduction to its main principles, followed by a description of the geometry-based rules. In a next step, the closed-loop control method is detailed; finally, the commissioning procedure based on supervised learning methods is explained.

6.2.1. Main principles

The global concept of the control system is shown in Figure 6.1. The *controller* block takes into account the target setpoints, the measurements from the testbed, the time of the day and the occupancy profile and determines the shading and lighting state.

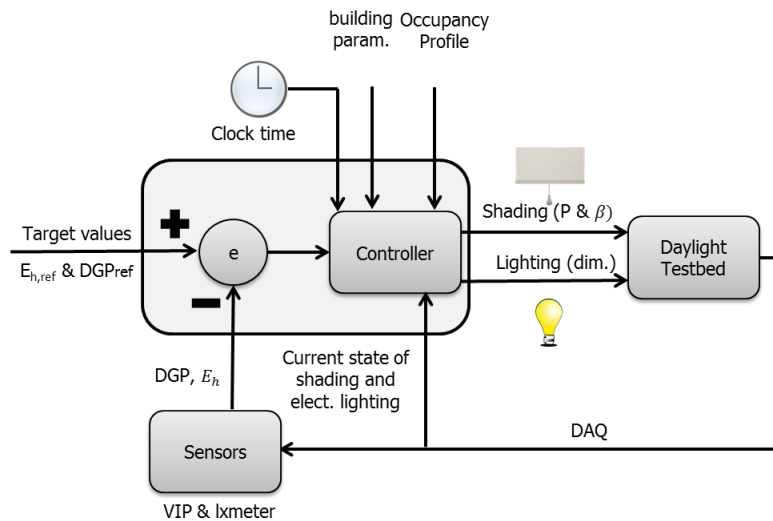


Figure 6.1 – Global block diagram of the controller with respect to the testbed and sensors.

The target values for the visual comfort controller are listed in Eq. (6-1). As one may notice in Figure 3.27, the HDR vision sensor is not placed exactly at the occupant's view point but at the location of a VDT. The value of a DGP index assessed from a VDT (DGP_{VDT}) is smaller than the one assessed from an occupant's point of view ($DGP_{occupant}$), as shown by Motamed et al. [80]. Consequently, the threshold for *perceptible* glare sensation (Table 2.1) for $DGP_{occupant}$, defined by Wienold et al. [17] to be 35%, is reduced to 30%. Thus, in practice, by keeping DGP_{VDT} smaller than 30%, one can assume that the $DGP_{occupant}$ observed by an occupant sitting at a workstation remains smaller than 35%, i.e. in the "perceptible" discomfort glare range. For the current setup, DGP_{VDT} is used as reference value (DGP_{ref}) for the control system. The reference value for the horizontal illuminance is chosen based on recommendations of Standard EN 121464.

The goal is to keep horizontal illuminance on a predefined workplane higher than $E_{h_{ref}}$ and the daylight glare probability, monitored from a predefined point of view, lower than DGP_{ref} , in case the office room is occupied. In the present chapter, this lighting condition is called *acceptable lighting condition* or *comfort zone*.

$$\begin{aligned} E_{h_{ref}} &= 500 \text{ [lx]} \\ DGP_{ref} &= 30\% \end{aligned} \quad (6-1)$$

For daylight privileging, the controller tries first to adjust the shading position in the office room through a command to the shading management system. Once discomfort glare is mitigated, a second control round takes place to adjust the electric lighting in order to guarantee the minimal required work plane illuminance.

Thermal comfort was not considered in this testbed. The reason is that it is a low-mass building construction located on a roof top, with considerable solar heat gains through its opaque walls, larger than in a typical office room located in a regular building. Thus, the testbed actuators driving the sun shading and the electric lighting system do not influence the solar heat gain. Besides, the HVAC system is not adjustable by the controller: it operates in an autonomous way and has its own internal closed-loop temperature-based controller. The HVAC energy demand was not monitored and the indoor air temperature control kept out of the scope of this work.

The DAQ cycle frequency is as slow as the slowest sampling frequency in the sensors of the testbed. In the current setup, the slowest sampling rate belongs to the HDR vision sensor (0.05 Hz, refer to Section 3.3.2). In this way, the controller is updated as fast as the whole data becomes available. However, this frequency is too high for actuating shading and lighting and most of the time the variation of the sensor readings is not considerable. Thus, it is a wasteful allocation of computation resources if the controller calculates its outputs every time the DAQ cycle is completed. To address this issue, the notion of *an event* is introduced (Figure 6.2): whenever the variations of the sensor readings exceed a predefined threshold, an event occurs; consequently, a decision is required to be made by the controller considering the sensor readings and actual state of the actuators. This is formulated by Eq. (6-2).

$$\text{if } (DGP_k - DGP_{k-1} > \epsilon_{DGP}) \text{ or } (E_{h_k} - E_{h_{k-1}} > \epsilon_{E_h}) \text{ or } (\gamma_k - \gamma_{k-1} = \epsilon_{presence}), \text{ then event} = 1 \quad (6-2)$$

where indices k and $k - 1$ signify the monitored variable, i.e. DGP , E_h and presence (γ), in *current* step and *previous* step respectively; $\gamma \in \{0,1\}$; ϵ_{DGP} , ϵ_{E_h} and $\epsilon_{presence}$ are the event detection thresholds for DGP , E_h and presence respectively.

This event-based control will reduce the required calculation resources. For this specific case study, the thresholds for determining an event are $\epsilon_{DGP} = 3\%$, $\epsilon_{E_h} = 30 \text{ lux}$ and $\epsilon_{presence} = 1 \text{ or } -1$.

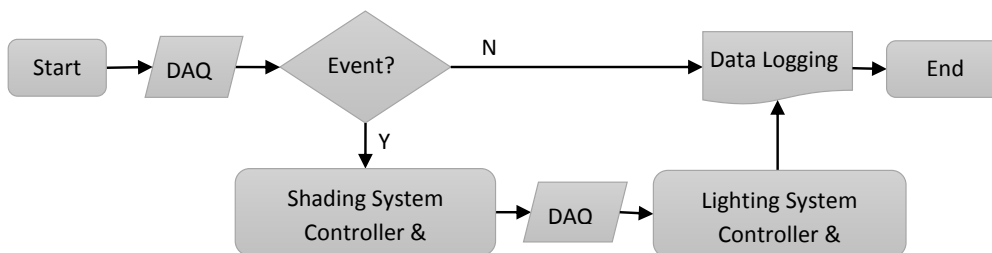


Figure 6.2 – Flow chart of event-based control, the “controller” block is detailed in Figure 6.3.

In order to overcome the disadvantages of the controllers stated in the Section 6.1, the following solution is proposed: The controller tunes automatically ten internal “memory” parameters based on the experiences it acquires during the first phase of operation (*learning* phase). The learning phase may last for several days. Having passed this phase and tuned these parameters, the shading system enters the *operational* phase. Further low-frequent learning processes may take place intermittently during the operational phase. The reason for the triggering of such learning processes may be seasonal changes of the outdoor settings such as trees or specular reflections from neighboring buildings.

On the commissioning day, open-loop geometry-based rules named Work Plan Protection (WPP) and a combination of cut-off angle and Anti-Reflection Slat Angle (ARSA) are proposed. The rules are detailed in Section 6.2.2 and are similar

to the rules used by the FLC listed in Appendix A. Basically, these rules are designed based on the best of our initial knowledge on the facade and workstation orientation, distance of the workstation to the window and window to wall ratio (WWR), acquired using building plans and/or a site visit. Thus, each time an event is detected, the shading system is adjusted (if the event successfully passes the filtering process) to the position/angle that is optimal for the sun profile and sky condition observed at that particular moment (Figure 6.3). However, there is a certain probability that this controller does not eliminate glare (i.e. *underact situation*) or that it reduces the indoor horizontal illuminance to below $E_{h_{ref}}$ (i.e. *overact situation*). This probability is considerable owing to the complex nature of venetian blinds and to simplified assumptions based on which the geometry-based rules are derived. For example, the reflections from the slat surfaces are not considered in the cut-off angle strategy and the slats are assumed to be flat while in most of the cases they are curved up. For these reasons, the first control action may require some improvements.

The BMS is expected to enforce the commands defined by the controller, if the latter successfully passed the criteria of the *time-dependent* and *minimum step* filters. These filters, inspired by [20], [156], are detailed in Section 5.3.3.5 for more information, the reader may also refer to Motamed et. al [79].

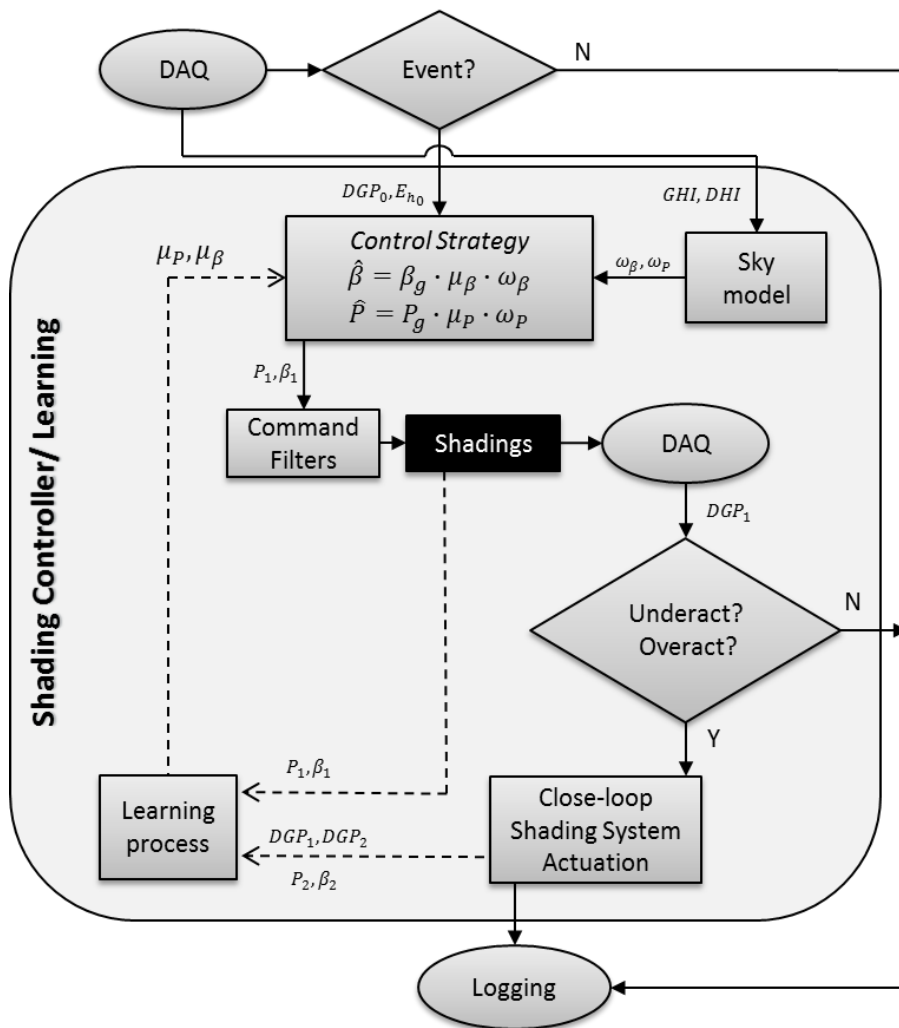


Figure 6.3 – Novel shading control system based on geometry-based rules enhanced with a reinforcement learning module. To simplify the Figure, the learning parameters μ_{β_i} and μ_{P_i} are shown as μ_{β} and μ_P ; the geometry-based rules are explained in Section 6.2.2; the command filter block is detailed in Section 5.3.3.5; the learning process is elaborated in Section 6.2.4.

In the next step, a DAQ is performed to verify the success of the open-loop controller in preparing an acceptable environment. If the DGP is still higher than DGP_{ref} , then the geometry-based controller is labeled as “*underaction*” or

“insufficient action”. On the other hand, if the horizontal illuminance is smaller than $E_{h_{ref}}$, provided that the horizontal illuminance was higher than $E_{h_{ref}}$ before the shading action, then this action is labeled as “overaction” or “excessive action”. Otherwise, the geometry-based rules performed a successful action and no further amendment is needed. This procedure is depicted by the lozenge block “Underact?/Overact?” in Figure 6.3 and is shown in Eq. (6-3).

$$DQ = \begin{cases} \text{Underact} & DGP_1 - DGP_{ref} > 0 \\ \text{Overact} & E_{h_1} - E_{h_{ref}} < 0 \ \& \ E_{h_0} > E_{h_{ref}} \\ \text{Just fine!} & \text{otherwise} \end{cases} \quad (6-3)$$

Where DQ is the decision quality, DGP_1 is the DGP index monitored after open-loop geometry-based rules, and E_{h_0} and E_{h_1} are the horizontal illuminance recorded before and after the open-loop rule’s decision respectively.

In the case of unsuccessful action, a sequence of closed-loop shading actuation is applied to modify the position and slat angle of the shading so as to drive the interior lighting condition to the comfort zone.

Having reached the comfort zone, the controller needs to *memorize* what has happened during this modification process to avoid the same unsuccessful actions in the future. To this end, some *memory* parameters must accordingly be updated. These parameters are initially equal to one and are multipliers of the result of *geometry-based* rules.

$$\begin{aligned} \hat{\beta} &= \mu_\beta \cdot \beta_g(\alpha_{sun}, h_{sun}, g) \cdot \omega_\beta(GHI, DHI) \\ \hat{P} &= \mu_P \cdot P_g(\alpha_{sun}, h_{sun}, g) \cdot \omega_P(GHI, DHI) \end{aligned} \quad (6-4)$$

where $\hat{\beta}$ [°] and \hat{P} [–] are the final decisions of the open-loop rules enhanced with learning and weather parameters; β_g [°] and P_g [–] are the slat angle and shading height by open-loop rules, which are functions of geometrical parameters such as α_{sun} sun azimuth [°], h_{sun} sun height [°] and g the remaining relevant dimensions in the office room; μ_β and μ_P are the memory parameters for slat angle and shading position respectively [–]; ω_β and ω_P take into account the effect of weather conditions [–]. The learning process is elaborated in detail in Section 6.2.4.

6.2.2. Geometry-Based Rules

As stated in Eq. (6-4), the geometry-based rules take into account the sun profile and room geometry.

For determining the position of the blinds, the Work Plane Protection (WPP) method, inspired from Konstantzos et al. [109] is applied. This method prevents the direct sun light from reaching the workstations. For the shading slat angle, occasionally the cut-off angle method is applied (Figure 6.4 (a)). A full description of this method is presented by Guillemin [156]. However, during the testbed preparation phase, the author observed that on several occasions, in the presence of direct sun rays, the double reflection from the surface of the slats would engender discomfort glare. In other words, large values for the DGP index were observed. The same issue was also reported by other researchers such as Chan et al. [49] and Chiayapinunt et al. [214]. Moreover, the basic assumption of the cut-off angle method is violated when in reality the slat profile deviates considerably from the flat surface profile. The slat profile of the shading system in the daylight testbed is shown schematically in Figure 6.4 (b). The slat angle profile for the current testbed is shown in Figure 3.29. All in all, a more conservative critical slat angle is needed to fully block excessive sun rays from reaching the occupant’s point of view.

Anti-Reflection Slat Angle (ARSA)

A novel method named *Anti-Reflection Slat Angle* (ARSA) is developed and implemented. The cut-off angle method is not fully abandoned and the final decision about the slat angle is the most conservative decision of both:

$$\beta_{c_{final}} = \max(\beta_{c_{cut-off}}, \beta_{c_{ARSA}}) \quad (6-5)$$

The ARSA method is based on the fact that the sun ray reflected from the surface of the lowest slat should not reach the occupant’s eye and may pass above his point of view. This principle is shown in Figure 6.4 (c).

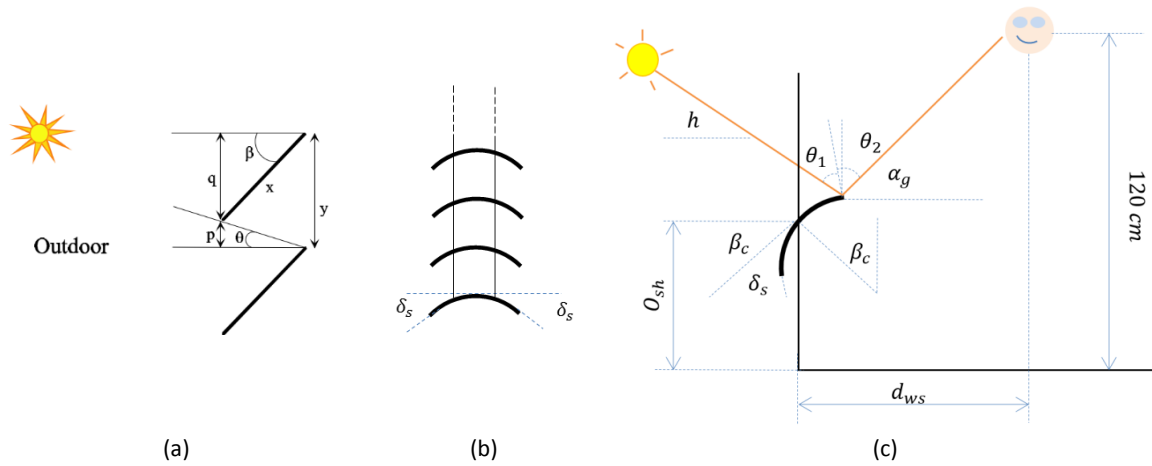


Figure 6.4 – (a) Lateral view of two slats of a venetian blind model for the cut-off angle method, the venetian blinds are assumed to be flat surfaces [156]; (b) Slat profile of the venetian shading system installed in the daylight testbed; (c) Demonstration of *Anti-Reflect Slat Angle* (ARSA) critical angle.

The idea is to find the critical slat angle (β_c) by knowing i) the sun height (h [°]), ii) the distance of the subject from the facade (d_{ws} [m]), and iii) the position of the lowest shading slat (O_{sh} [m]). The angular deviation between the middle and the edge of a shading slat is labeled by angle δ_s [°] (Figure 6.4 (b)). This problem is simplified to a 2D problem for practical reasons and the sun's azimuth is ignored. If during the experiment the evidence of insufficiency of this model is observed, then the 3D model will be developed and implemented. Another assumption is that slat surfaces reflect the sun rays as a perfect mirror does; thus, in Figure 6.4, $\theta_1 = \theta_2$. The height of the office occupant while sitting at his workstation is assumed to be 120 cm. By 2D geometry of angles, the series of equations (6-6) is derived.

$$\alpha_g = \tan^{-1} \left(\frac{120 - O_{sh}}{d_{ws}} \right)$$

$$\theta_1 + (h + \beta_c - \delta_s) = 90^\circ \quad (6-6)$$

$$\theta_2 + \alpha_g - (\beta_c - \delta_s) = 90^\circ$$

Combining these equations, Eq. (6-7) is derived, which returns the critical slat angle.

$$\beta_c = \frac{\alpha_g - h + 2 \cdot \delta_s}{2} \quad (6-7)$$

where α_g is found by Eq. (6-6) and depicted in Figure 6.4; h is the sun height and δ_s is the angular deviation between the middle and the edge of a shading slat. For example, for a case that happened during the testbed preparation phase (not documented in this text), at 12:06 on August 19th 2017 where $h = 50^\circ$, $O_{sh} = 40\% \cdot 250 \text{ cm} = 100 \text{ cm}$, $\delta_s = 40^\circ$, $d_{ws} = 80 \text{ cm}$, β_c is equal to 22° . In the same situation, the cut-off angle method would have returned $\beta_c = 0^\circ$ which lead to unwanted *perceptible* discomfort glare (DGP).

The geometry-based rules are designed by assuming that the sky is clear and the facade is exposed to the sunrays. This assumption may lead to too conservative actions when the sun is covered by clouds. In order to consider this knowledge in the controller, two weather parameters ω_p and ω_β are introduced. The main idea behind introducing weather condition parameters is to take less conservative actions when the sky is partially cloudy or overcast. To this end, the sky condition must be determined at each time step.

The sky condition is determined based on a model suggested by Fakra et al. [182], by Eq. (6-8).

$$SR = \frac{DHI}{GHI} \quad (6-8)$$

where SR is the Sky Ratio and DHI and GHI are global and diffuse horizontal irradiance [$W \cdot m^{-2}$]. In the next step, the sky condition category is defined by means of Eq. (6-9).

$$\chi = \begin{cases} 1. \text{Clear} & SR < 0.3 \\ 2. \text{Partially cloudy} & 0.3 \leq SR < 0.8 \\ 3. \text{Overcast} & 0.8 \leq SR \end{cases} \quad (6-9)$$

where χ is the sky condition. Once the sky condition is defined, the weather parameters ω_p and ω_β can accordingly be defined. By intuition, one knows that, for example for overcast sky, the blinds shall be lowered less than when the sky is clear, and the slat angles shall be also kept closer to the horizontal state (open) than the vertical one (closed). These intuitions are translated into the weather parameters as shown in Eq. (6-10).

$$(\omega_p, \omega_\beta) = \begin{cases} (1,1) & \chi = 1 \\ (1.1, 0.9) & \chi = 2 \\ (1.2, 0.8) & \chi = 3 \end{cases} \quad (6-10)$$

During a pre-study phase, the weather flags defined in Eq. (6-10) are found by a try and error approach through a close study of the shading actuations.

The geometry-based rules (GR_i) are elaborated as follows:

- **Rule GR_1 :** Glary situation when the occupant is present in the office. In this case, the WPP and ARSA principles are applied. This command is applied only if it reduces the opening fraction of the shading system or if it opts for higher slat angle degrees.
- **Rule GR_2 :** A dark condition in the indoor environment and no glare risk while the occupant is present and the sun rays potentially fall on the facade. In this case, WPP and ARSA are applied. However, this command is applied only if it opts for a larger opening fraction and smaller slat angle degrees.
- **Rule GR_3 :** Dark situation when the occupant is present and there is no potential sun ray falling on the facade. In this case, the shading system can be safely retracted in full.
- In the case where none of the previous situations is relevant and basically the indoor illumination condition is currently in the comfortable zone, the current shading position is taken as the decision.

$$\begin{cases} GR_1: WPP + ARSA & \text{if glary situation} \\ GR_2: WPP + ARSA & \text{if dark \& direct sunray on facade} \\ GR_3: Retract & \text{if dark \& no direct sunray on facade} \\ \text{No action} & \text{otherwise} \end{cases} \quad (6-11)$$

6.2.3. Closed-loop Shading Actuation

This module is activated when the geometry-based rules, enhanced with memory parameters, are not capable of preparing a visually comfortable environment (Figure 6.5). It is called closed loop since a sequence of actuation/sensing is performed until the comfortable situation is reached. This approach is contrary to the geometry-based rules, which are by principle based on open loop approach and once the actuation is performed, there is no feedback to the system to correct its decision.

There is however a subtlety in determining if an “Underaction” or “Overaction” has occurred: a situation is considered undergoing an “under” or an “over” action, only if the command filtering module does not exclude a geometry-based controller command due to the “Time filter” (see Section 5.3.3.5), a filter whose task it is to avoid too frequent shading movements. In other words, the geometry-based controller is responsible for an uncomfortable situation, if and only if its decision has had the opportunity to pass the “Time filter” test. Otherwise, even if the situation is glary, but the last shading movement was executed less than 15 minutes ago, the shading positions are not modified at all; the reason is to avoid unnecessary disturbances to the occupant.

In the absence of a room model describing the main geometrical and photometrical features of the office room, several closed-loop strategies can be applied to reach the comfort zone:

- i) Amending the slat angle by a predefined value followed by a predefined adjustment of the shading position

- ii) Modifying simultaneously both degrees of freedom using predefined values
- iii) Proportional change of the slat angle followed by a proportional adjustment of shading positions
- iv) Simultaneous proportional adjustments of the slat angle and the shading position.

It is favorable to reach the comfort zone with few movements (least disturbance to the occupant); therefore, the second closed-loop strategy is chosen. The predefined values are tuned by a trial-and-error process. In the case of “overaction”, the predefined variables are $(\Delta P, \Delta\beta) = (+20\%, -30^\circ)$ and in the case of “underaction” they are equal to $(\Delta P, \Delta\beta) = (-20\%, +30^\circ)$. These commands are applied consecutively until the comfortable situation is reached.

6.2.4. Learning Process

The main hypothesis behind having the memory parameters multiplied by the outcomes (decisions) of the geometry-based rules is that the latter do not always take sufficient actions and need further polishing. By learning from previous “mistakes” and adjusting the outcome of the geometry-based decision by means of memory parameters, the controller reaches the *efficient* performance: eliminating the glary/dark situation by one and only one action.

In order to facilitate the explanation of the learning process and to facilitate the control system commissioning procedure for another office room with a different facade and workstation orientation, the new parameters are introduced in Eq. (6-12):

$$\begin{aligned}\hat{\alpha}_f &= \alpha_{sun} - \alpha_{facade} \\ \hat{\alpha}_{ws} &= \alpha_{sun} - \alpha_{work\ station}\end{aligned}\tag{6-12}$$

where $\hat{\alpha}_f$ is the relative sun azimuth of the sun with respect to the facade orientation [°]; α_{sun} is the sun azimuth [°]; α_{facade} is the orientation of the facade [°]; $\hat{\alpha}_{ws}$ is the relative sun azimuth with respect to the workstation orientation and $\alpha_{work\ station}$ is the orientation of the workstation.

At this stage, the author suggests the learning parameters. In the absence of a room lighting model, our initial information about the phenomena which lead to glary situations is limited. The only pieces of information are based on an observation that suggests:

- the physics of discomfort glare through the venetian blinds *may* be different when i) the sun is in the field of view ($\hat{\alpha}_{ws} < 90^\circ$) and ii) when the sun is out of the field of view ($\hat{\alpha}_{ws} > 90^\circ$);
- when the sun ray does not fall on the facade ($\hat{\alpha}_f > 90^\circ$), the shading system can be safely retracted without any risk of glare.

These pieces of information are modeled and suggested as shown in Figure 6.5. Based on this flowchart, Control Strategy S_x is selected where $x \in \{a, b, c, d, e\}$. S_{NA} signifies “No Action”. As shown in Figure 6.3 and Eq. (6-4), the control strategy considers the geometry-based rules, sky model and memory parameters (past experiences). To each control strategy, two learning parameters are assigned:

- μ_{P_x} the learning parameter for the shading position;
- μ_{β_x} the learning parameter for slat angle.

By introducing these parameters, one can tune, i.e. amplify or attenuate, the output of each control strategy.

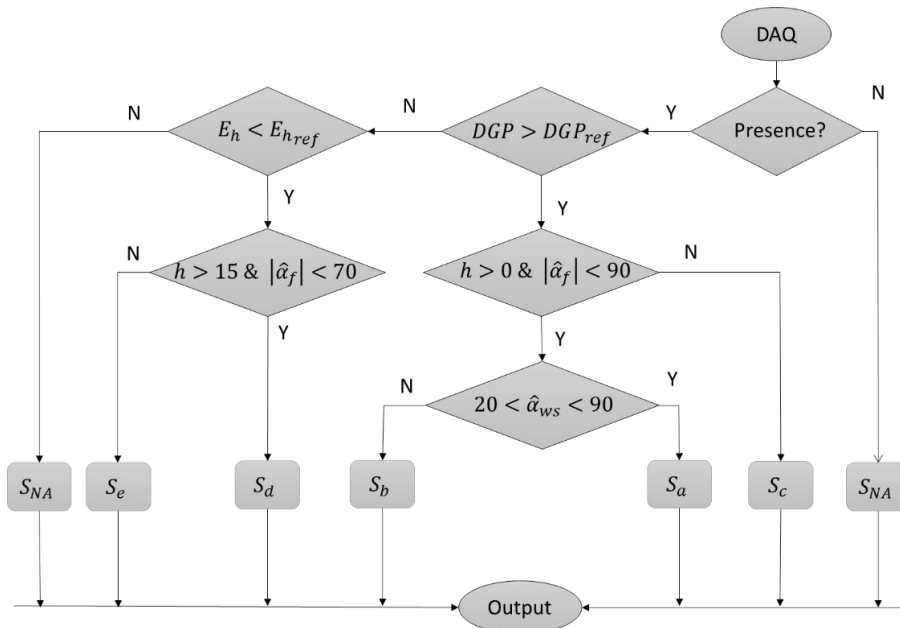


Figure 6.5 – Flowchart of control strategies for learning system.

As shown in Table 6.1, to each control strategy, one geometry-based rule is assigned. By assigning one geometry-based rule (GR) to several control strategies, the author introduced more learning parameters (redundancy) to the system and therefore a higher chance for convergence of the learning parameters. Based on the Vapnik-Chervonenkis (VC) dimension [215], adding redundancy can improve fault tolerance and generalization. Generalization in this context means the applicability of the control system for a building facade with a different orientation.

Control Strategies (S_x)	Geometry-based rules (GR_i)
S_a	GR_1
S_b	GR_1
S_c	GR_2
S_d	GR_1
S_e	GR_3
S_{NA}	No action

Table 6.1 – List of control strategies (S_x) and their corresponding geometry-based rules (GR_i).

If after the learning phase, the parameters converge to different values, one can conclude that the choice of introducing redundant learning parameters was correct.

A mechanism needs to be designed so as to update the learning parameters when a *faulty* action takes place. Faulty action in this context takes place when, following an open-loop actuation of the shading system, the indoor condition is still glary (Underaction) or dark (Overaction). The memory parameters for the Control Strategy S_x are updated based on a updating mechanism shown in Table 6.2. By this mechanism, each time the learning process is launched, the memory parameters of Strategy S_x for the next iteration ($k + 1$) are updated by adding or removing 10% to the current value (k) of the memory parameter.

Underaction	Overaction
$\mu_{P_{x,k+1}} = \mu_{P_{x,k}} - 10\%$	$\mu_{P_{x,k+1}} = \mu_{P_{x,k}} + 10\%$
$\mu_{\beta_{x,k+1}} = \mu_{\beta_{x,k}} + 10\%$	$\mu_{\beta_{x,k+1}} = \mu_{\beta_{x,k}} - 10\%$

Table 6.2 – Mechanism for updating memory parameters for *underaction* and *overaction*.

As an example, if the underaction situation occurs after applying control Strategy S_b , it means that the DGP index is still higher than DGP_{ref} (Eq. (6-1)) if the shading has a 50% opening fraction and a slat angle of 20° . In this case, next time in a similar situation, the opening fraction should be smaller and the slat angle should be larger so as to prevent the

glary situation. Thus, $\mu_{p_{b,k+1}}$, the memory parameter of the shading position, assigned to control strategy S_b for the next step $k + 1$, should be logically smaller than its current value ($\mu_{p_{b,k}}$). Accordingly, the value of the memory parameter assigned to control strategy S_b in next step $k + 1$ $\mu_{\beta_{b,k+1}}$ should be larger than its current value.

6.3. Testbed Preparation

In this section, the performance of the control strategy is evaluated through a case study in a daylight testbed at Fraunhofer ISE. A detailed description of the testbed is presented in Section 3.3.

As the daylight testbed is not occupied by a real human subject during the experiment, a predefined occupancy profile is put in place. This profile is extracted from previous work of Daum [191]. This occupancy profile is provided for a working day. The presence probability is calculated for the upcoming hours by taking a weighted sum of sampled probabilities with 3 increments (every 20 minutes). This is represented by red dashed lines in Figure 6.6. If the probability of presence at each time is higher than 25%, then the presence (black dash-dot line) is equal to 1. Finally, if the absence duration is higher than a certain threshold (here is 30 minutes), then this period of absence is considered as “long absence” (solid blue line).

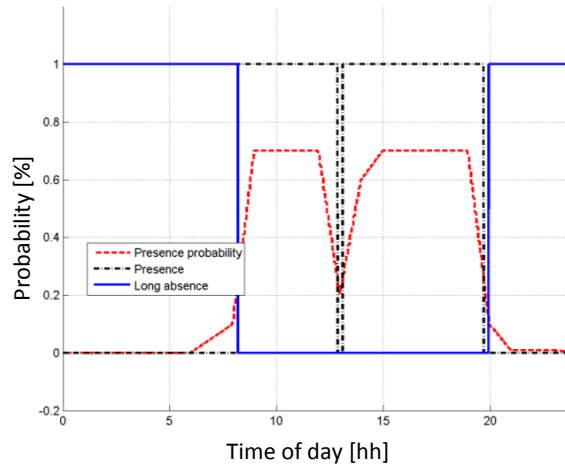


Figure 6.6 – Occupant presence probability, presence, and long absence flag. As the testbed is unoccupied, this profile is used.

The technical details of the data structure and control implementation in MATLAB can be found in Appendix B.2.

6.4. Experimental Results

The experiments took place for 22 days, from 7th September to 11th October 2017. The learning system converged after 11 days and during the rest of the days the enhanced open-loop control system could successfully respect the visual comfort zone while actuating the shading system on average 2.54 times per day.

Figure 6.7 shows the number of shading movements per day. The shading movements are presented according to the nature of the movement: open loop control in dark blue and closed-loop control in yellow. Closed-loop controls are meant to improve the decisions made by the geometry-based rules. Thus, as soon as no closed-loop control was required anymore (e.g. after 23rd September 2017), one can conclude that the learning module has converged: it took 11 days for the learning module to converge to its final status. This period is accordingly designated by *Commissioning or Learning phase*; the remaining experimental run is named *Operation phase*.

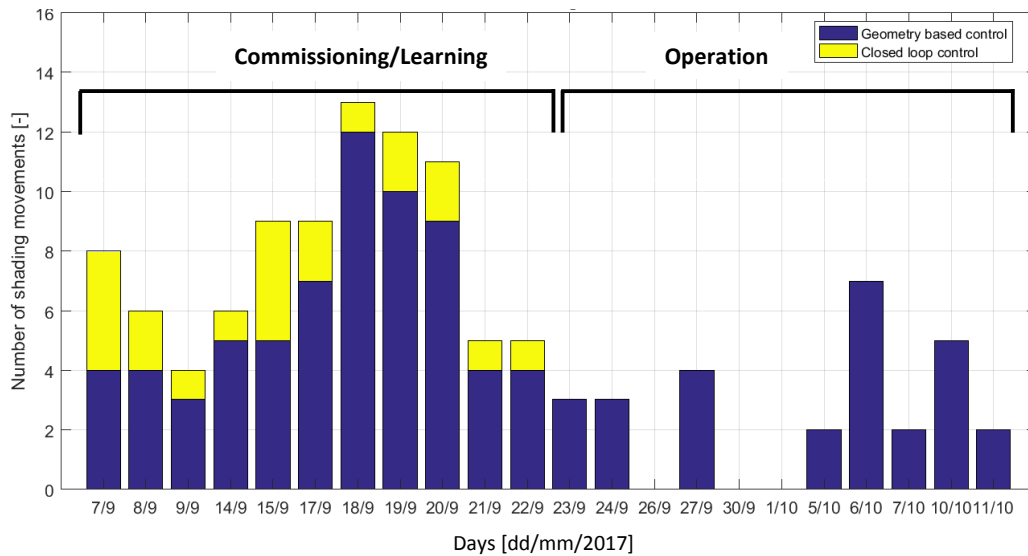


Figure 6.7 – Number of the shading movements per day separated by the actuation driver, either open-loop or closed-loop control.

Three examples of shading movements during the commissioning phase and the operation phase are detailed in Sections 6.4.1 to 6.4.3. In Section 6.4.4, an overall analysis of the case study is presented.

6.4.1. Underactions during Learning Phase

In this section, an example of two underaction occasions (during learning phase) is studied closely. As shown previously in Figure 6.7, on 8 September 2017, the shading system is activated 6 times: 4 times by geometry-based control and 2 times by closed-loop control.

New visualization techniques can help to better understand the daily behavior of the controller. Each line of Figure 6.8 (a) corresponds to a shading movement. The extremities of two green lines are numbered with “1” corresponding to the shading position (window opening fraction) before actuation and “2” corresponding to the shading position after actuation. Next to the number “1” the actuation time and a letter corresponding to the strategy of the geometry-based controller (Table 6.1) are indicated. At 10:46 AM, for instance, according to Strategy S_b , the shadings are lowered from $(P_1, \beta_1) = (1, 0^\circ)$ to $(P_2, \beta_2) = (0.47, 10^\circ)$ for the first time in the day, where P is the blinds position [–] and β is the slat angle [°].

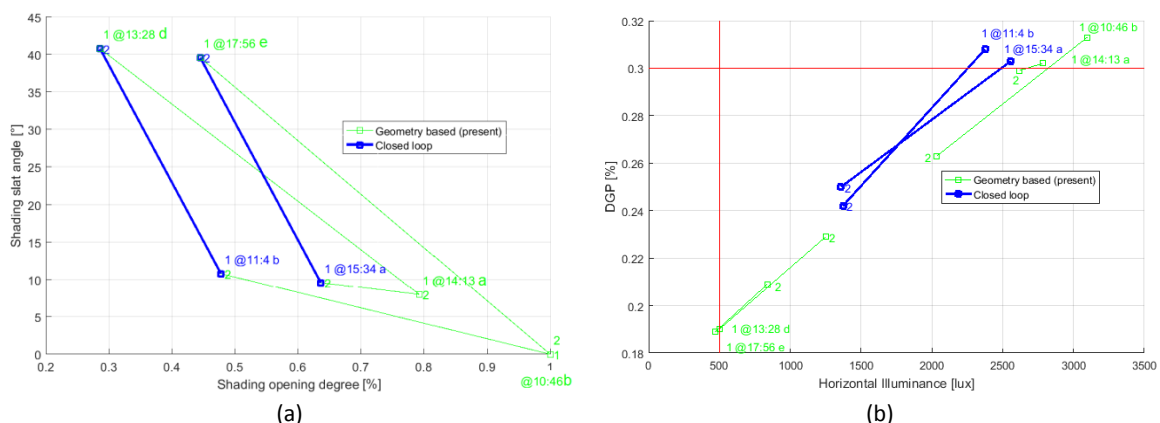


Figure 6.8 – Shading status and indoor illumination condition before and after each shading actuation during 8 September. DGP is accurate to 10% and illuminance to 5%.

The influence of this actuation on the indoor lighting conditions (i.e. DGP and E_h) is illustrated in Figure 6.8 (b). The figure is subdivided into comfort and discomfort zones by the red lines: a work plane illuminance lower than 500 lx is

considered as discomfort (it reduces the users visual performance) and a DGP larger than 30% reflects a glary situation. Thus, the comfort zone is located at the bottom right of the figure. One can observe that the influence of the shading actuation at 10:46 AM (top right corner) contributed to leading the indoor lighting condition toward the comfort zone, e.g. from $(E_{h_1}, DGP_1) = (3115 [lx], 31\%)$ to $(E_{h_2}, DGP_2) = (2051 [lx], 26\%)$.

As an another example one observes that at 5:56 PM, the shading system is retracted from $(P_1, \beta_1) = (0.45, 40^\circ)$ to $(P_2, \beta_2) = (1, 0^\circ)$; bringing the indoor condition from $(E_{h_1}, DGP_1) = (490 [lx], 19\%)$ to $(E_{h_2}, DGP_2) = (1261 [lx], 23\%)$

Not all geometry-based control decisions are successful though. In order to demonstrate the behavior of the learning module, Figure 6.9 is presented. It shows the shading positions and the indoor illumination conditions variation during the learning phase of the closed-loop control process. Three conditions corresponding to the numbering are enumerated in this figure: (1) Condition before a geometry-based decision, (2) Condition after a geometry-based decision (and a possible actuation) and (3) Condition after intervention of the closed-loop control and learning module. For example, as shown in Figure 6.9 (a), the Control Strategy S_b decided at 11:14 AM not to move the shadings, even in a glary situation was sensed.

Points 1 and 2 of the system actuation at 11:14 AM are both situated in the discomfort zone, signifying that the geometry-based controller is unable to lead the testbed toward the comfort zone. This is designated by “Underaction”, thus the closed-loop controller module being launched. In Figure 6.9 (b), one can observed that the shading position at 11:14 AM during the learning phase is modified from $(P_2, \beta_2) = (0.47, 10^\circ)$ to $(P_3, \beta_3) = (0.28, 40^\circ)$. This action leads the control system to the comfort zone, as $(E_{h_3}, DGP_3) = (1470 [lx], 25.5\%)$; the same thing happens for the Control Strategy S_a at 3:43 PM.

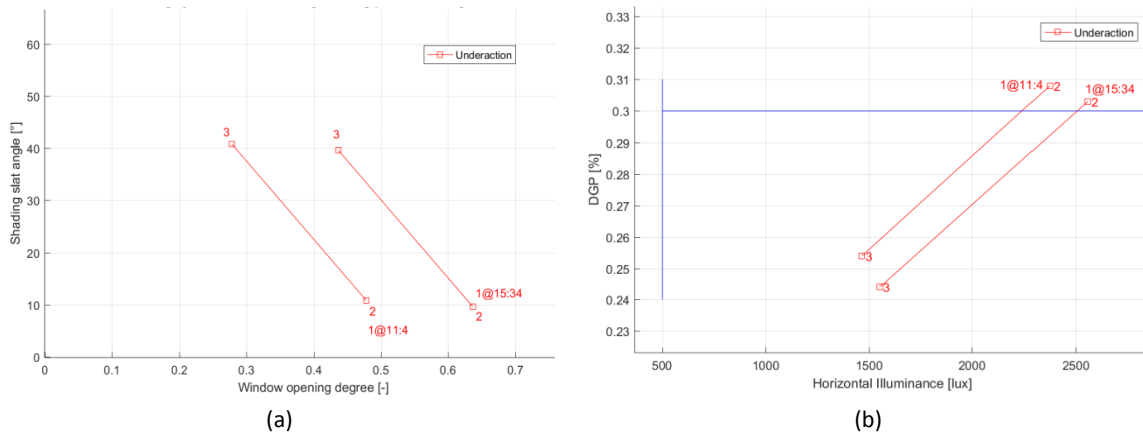


Figure 6.9 – Shading position and lighting conditions during the learning phase on the 8th September 2017.

6.4.2. Example of Overaction

The behavior of the controller and the learning module close to the end of the learning phase, is analyzed in this section. One can observe a single learning process during 22th September 2017 in Figure 6.10: the geometry-based actuation at 9:14 AM based on Strategy S_b can be classified as “Overaction”. Figure 6.11 (a) shows that the lighting condition after a geometry-based action swings from the “Glary” region to the “Dark” region of the discomfort zone, e.g. from $(E_{h_1}, DGP_1) = (1750 [lx], 30.3\%)$ to $(E_{h_2}, DGP_2) = (400 [lx], 20.2\%)$. Consequently, as shown in Figure 6.11 (b), the closed-loop controller is launched, which modifies the shading position from $(P_2, \beta_2) = (0.33, 85^\circ)$ to $(P_3, \beta_3) = (0.53, 53^\circ)$. Following this action, the indoor lighting condition is brought back to the comfort zone, i. e. $(E_{h_3}, DGP_3) = (910 [lx], 24.3\%)$.

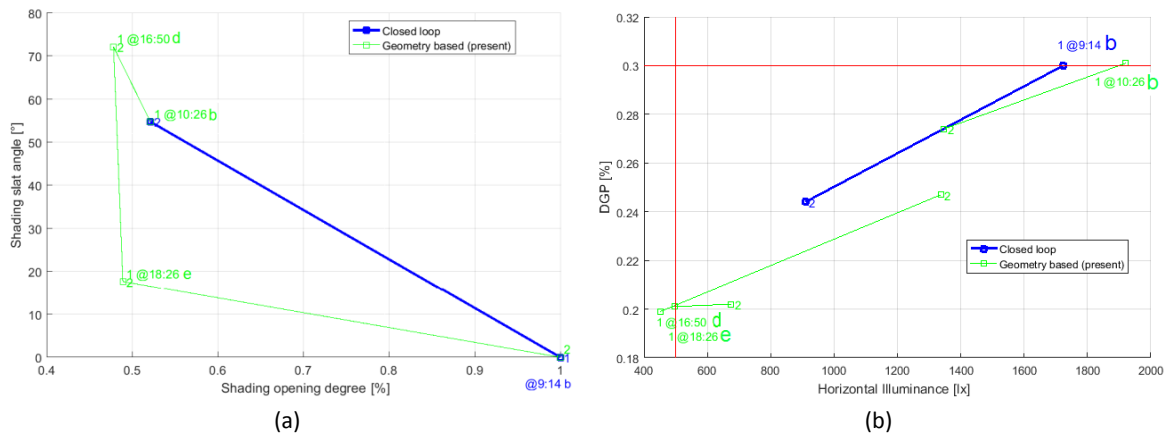


Figure 6.10 – Shading position and lighting condition before and after a shading actuation on 22nd Sept. 2017.

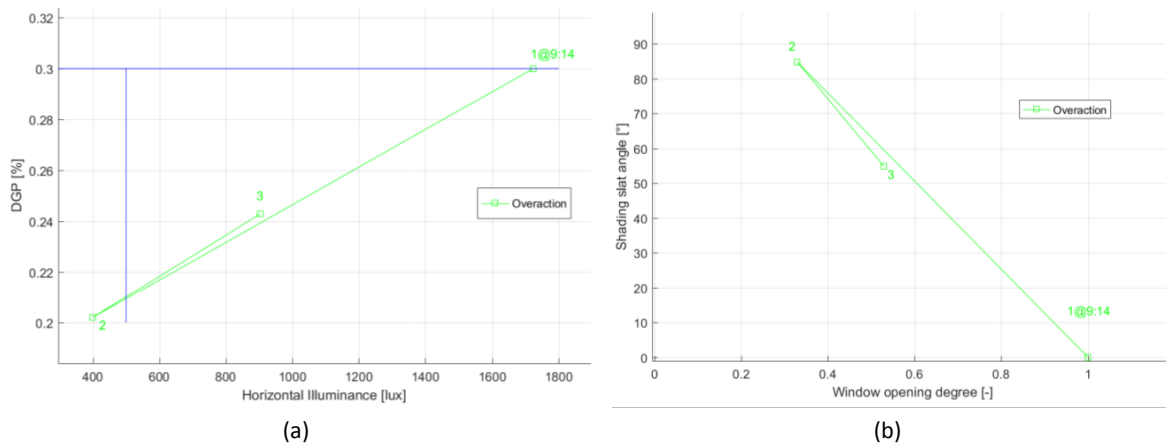


Figure 6.11 – Blinds' position and indoor lighting condition during the learning process on 22nd Sept. 2017.

6.4.3. Successful Action during Operation Phase

An example of a shading action following a convergence of the learning process is presented in this section. Figure 6.12 shows that only 3 actuations were made on the 24th September 2017: a first one at 9:35 AM based on Strategy S_b to prevent glare, a second one at 5:37 PM based on Strategy S_d as a reaction to an insufficient workplane illuminance and finally one at 6:21 PM based on Strategy S_e where the risk of glare is fully eliminated. The workplane illuminance and the DGP over time are illustrated in Figure 6.13; the electric lighting is used for a short moment after 7 PM.

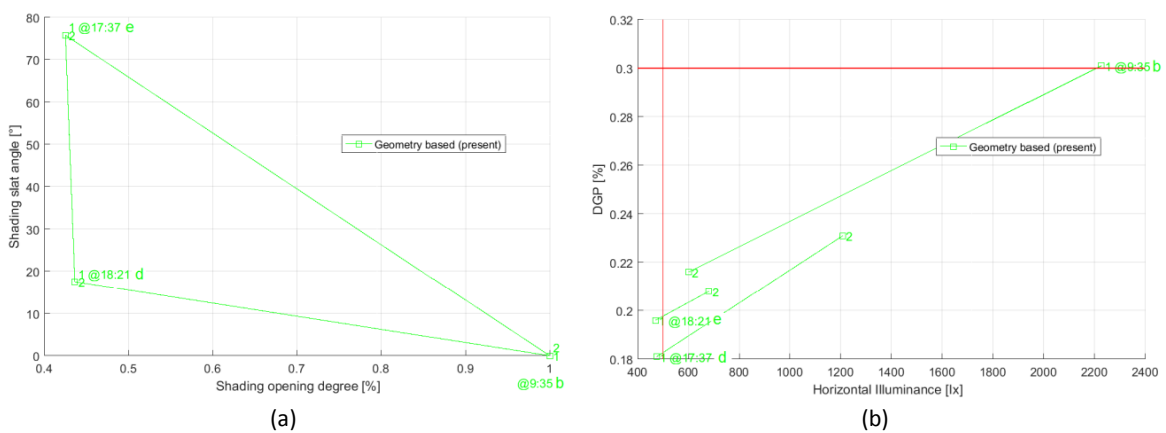


Figure 6.12 – Blinds' position and workplane illuminance before and after each shading system actuation on the 24th Sept. 2017.

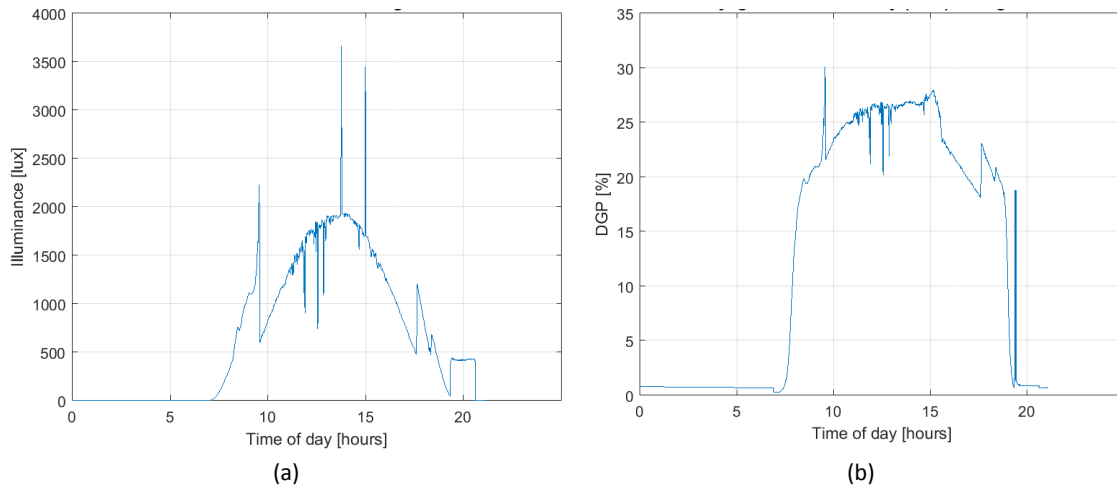


Figure 6.13 – Workplane illuminance E_h and DGP index over time on the 24th September 2017; the DGP accuracy is equal to 12% of the reading and 5% for the illuminance.

6.4.4. Overall Analysis of the Experiment

In order to be able to assess the sky condition variations, a new weather instability index was introduced. This index is equal to the daily number of sky type changes (according to Eq. (6-9)) divided by the total daily number of data samples. The higher this index, the more the sky type has varied among sunny, intermediate and overcast. One may observe that the instability of the sky condition is comparably high in the commissioning and learning phase.

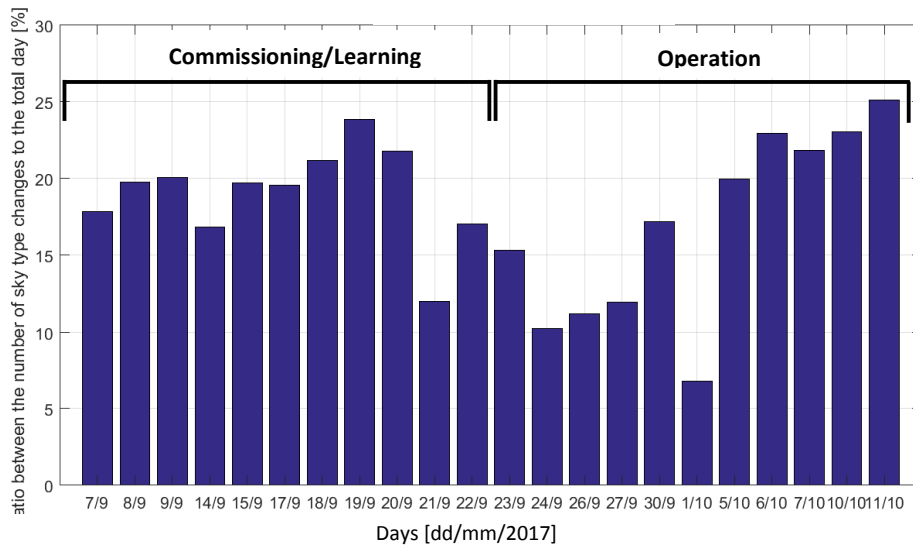


Figure 6.14 – Weather instability index between 8 AM and 6 PM for the whole duration of the experiment in Fraunhofer ISE.

The global and diffuse horizontal irradiance between 8 AM and 6 PM is given in Figure 6.15. The author observed that different sky types were experienced during the commissioning as well as the operation process.

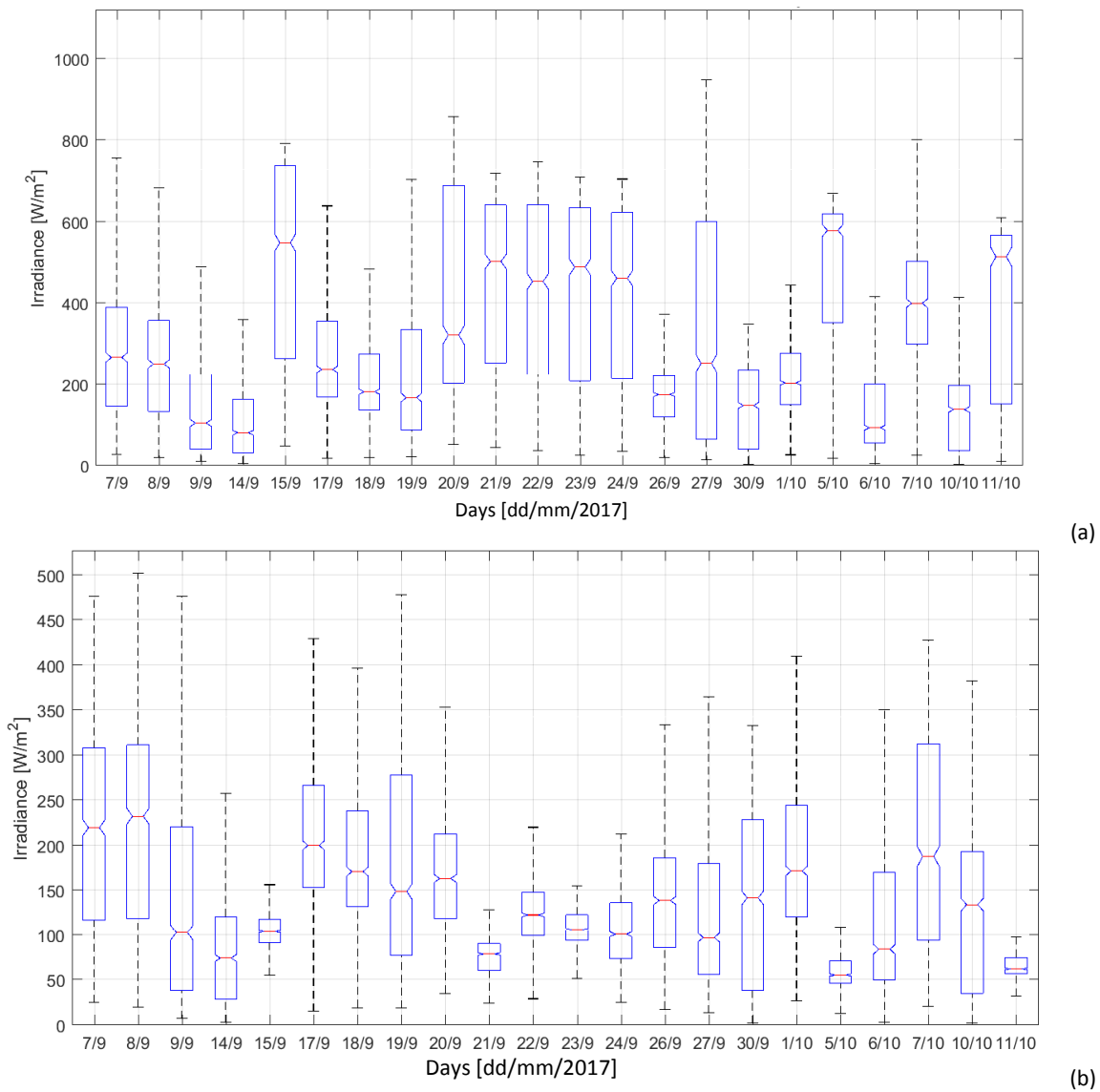


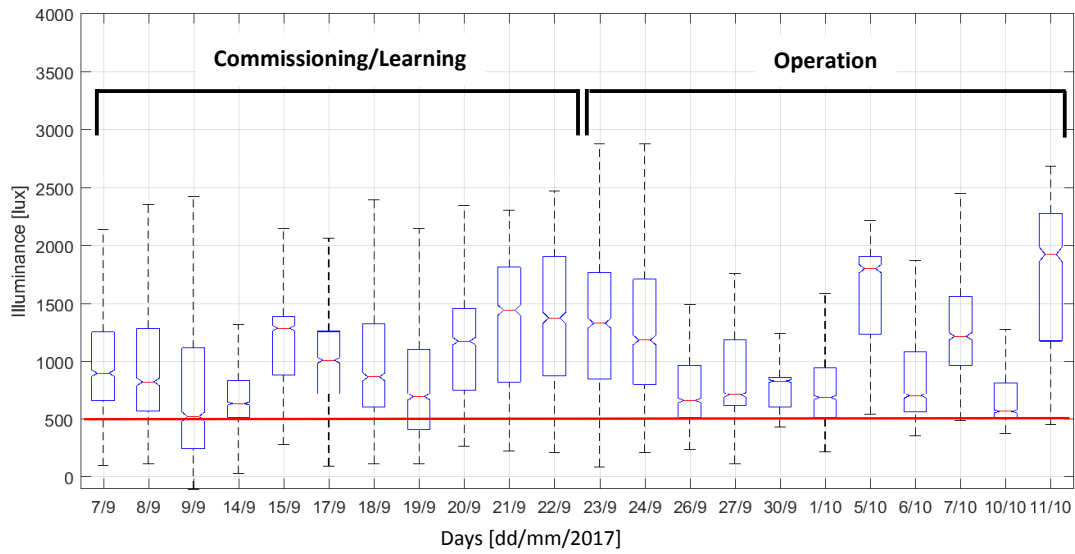
Figure 6.15 – Global and diffuse horizontal irradiance between 8 AM & 6 PM for the whole duration of the experiment in Fraunhofer ISE.

Detailed monitored data of the lighting conditions are presented in Figure 6.16. One can observe that the visual comfort constraints are respected owing to the fact that the most of the DGP readings fall underneath 30% and the workplane illuminance lay above 500 [lx]. The vertical illuminance E_v , measured by the HDR vision sensor and represented in Figure 6.16(c), is not driving the sun shading control system during these experimental runs; it is only presented here for the sake of completeness of the monitored data.

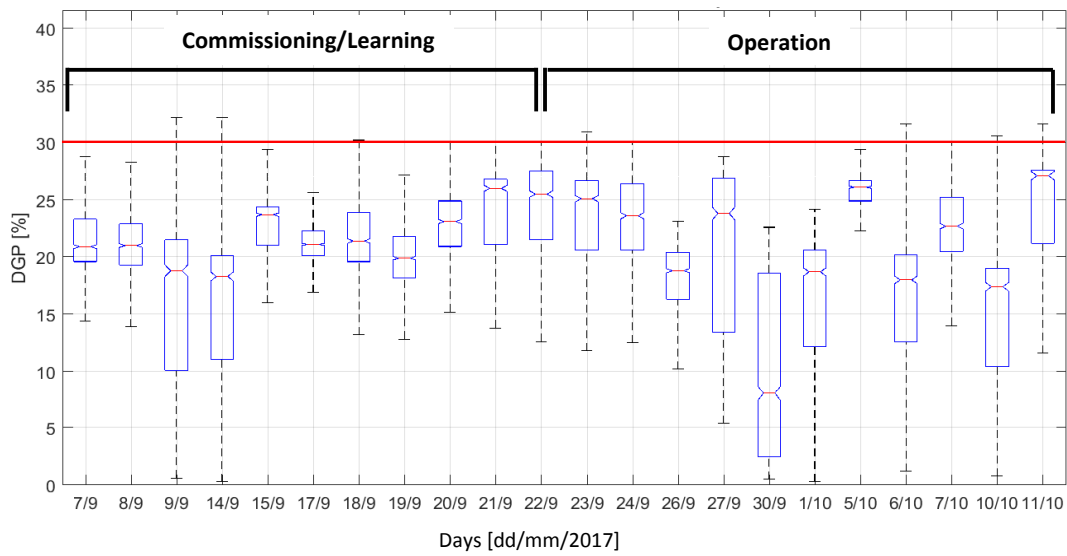
In a similar way as for the long-term in-situ monitoring carried out in the LESO solar experimental building (see Section 5.3), the relative time fraction for the work hours and in presence of the occupant, during which the lighting constraints are respected, is used to quantify the performance of the controller by Eq. (6-13).

$$\rho_{respect} = \frac{T_{(respect=1, Presence=1)}}{T_{total}} \cdot 100\% \quad (6-13)$$

where $T_{(respect=1, Presence=1)}$ is the time step during which both constraints are respected [s], e.g. $DGP < DGP_{ref}$ and $E_h > E_{h_{ref}}$, while the occupant is present ($Presence = 1$); T_{total} is the total duration of the experiment run during work hours (8 AM to 6 PM) [s].



(a)



(b)

Figure 6.16 – Boxplot of indoor lighting condition during working hours (8 AM- 6 PM); (a) DGP; (b) E_h ; The comfort thresholds are shown by horizontal solid red line.

Figure 6.17 shows that the controller succeeded during the last 11 days of the 23rd September to the 11th October 2017 in maintaining the visual comfort conditions for more than 96% of the time, corresponding to the operation phase between 8 AM and 6 PM when the office was considered occupied.

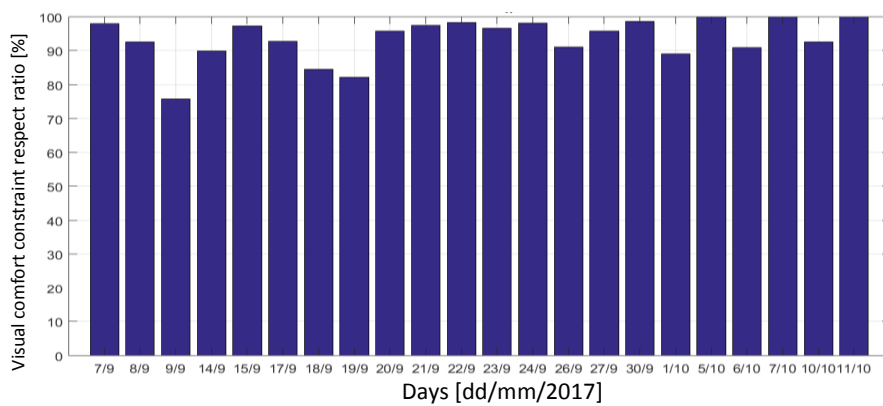


Figure 6.17 – Visual comfort constraint respect ratio by Eq. (6-13), evaluated between 8 AM and 6 PM.

Throughout the whole experimentation, including the commissioning phase, this ratio was on average equal to 93%.

If one considers only $DGP_{ref} = 35\%$ as threshold defining the visual comfort zone, complying with the EN standard draft [143], the respect ratio for the whole experimental run raises to 99%, indicating that the DGP exceeded 35% only during 1% of the time.

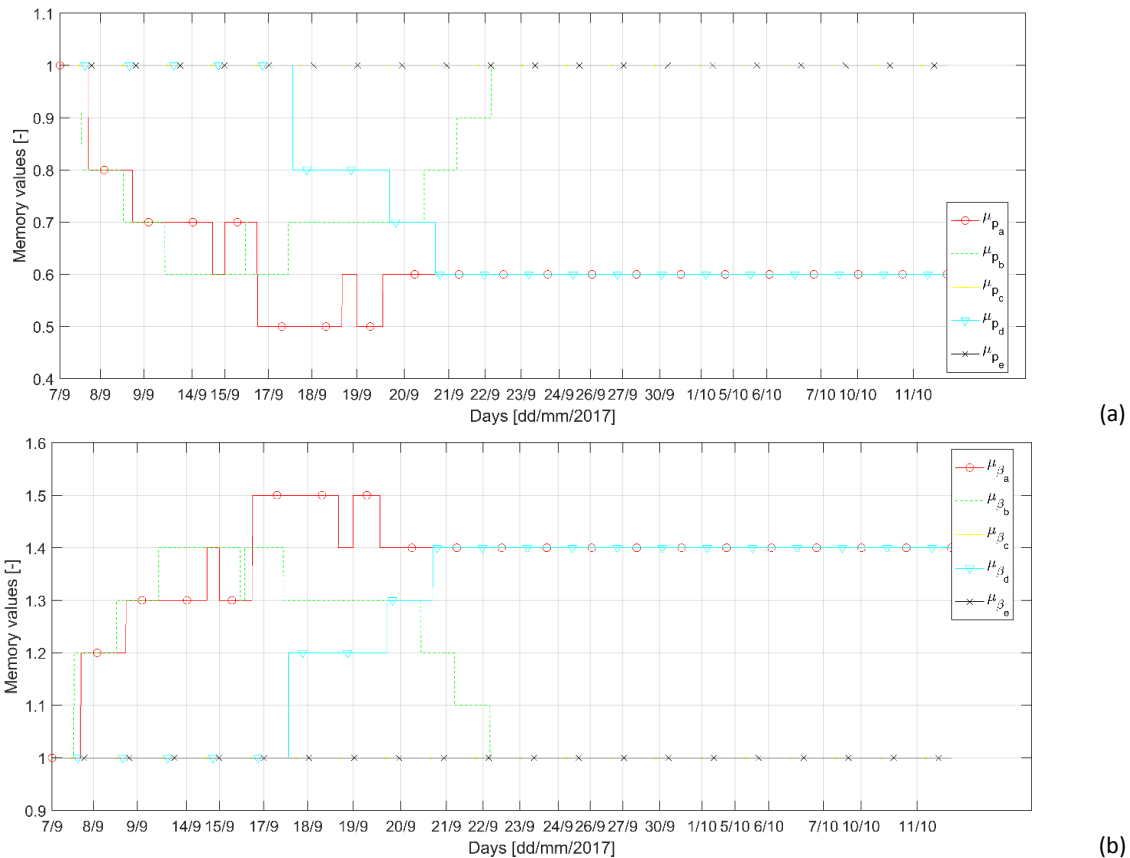


Figure 6.18 — Evolution of memory parameters along the experiment (a) shading position memory (μ_{P_x}); (b) shading slat angle memory (μ_{β_x}).

Figure 6.18 shows the evolution of the “memory parameters” over time. All ten parameters were initialized at the beginning of the experimentation to one and followed more or less a unidirectional convergence rate. They converged after 11 training days to two specific values, e.g. (1, 0.6) for the position and (1, 1.4) for the slat angle memory parameters.

6.5. Discussion

Seasonal variation may not disturb the suggested control system. The reason is that the geometry-based open-loop rules take into account the sun height and relative azimuth. This means that for another season, where the sun height varies, the controller should be able to adapt itself automatically. It is not excluded that the learning system continues to evolve slightly over the season due to alterations of the neighboring environment. These hypotheses need to be validated by yearly experimental or simulation studies.

Even though during the learning phase the comfort zone boundaries can be potentially contradictory and lead to dangling effects and instability of the system, the results show that the final stable system is capable of finding a feasible compromise between visual comfort and sufficient light provision.

Even though there is a closed-loop control in action right after a geometry-based control, one observes in Figure 6.16 (a, b) that during some days, the glare index and/or horizontal illuminance exceeds the comfort zone thresholds. The

phenomenon takes place basically because of the *minimum time filter*, i.e. for the sake of user acceptability, the maximum frequency for shading actuation is every 15 minutes. Consequently, even if, as an example, 5 minutes after an actuation the comfort constraints are violated because of sudden change in the sky condition, no action would be taken to cope with the situation.

The control strategy presented in this study showed that, upon performing an annual experiment, it may comply with the requirements of comfortable indoor lighting drafted in the recent European standard [143]. According to this standard, the factor $f_{DGP,exceed}$ should not go beyond 5% of the time between 8 AM and 6 PM from Monday to Friday through a year. Assuming the highest level of glare protection, the recommended threshold for DGP is 35% ($DGP_t = 35\%$). By this assumption, $f_{DGP,exceed}$ is 1.0% for these 11 days. Although it is not comparable with a *yearly cap*.

The time needed for the convergence in this experiment is 11 days. This is an acceptable and reasonable time span for installing a new control system in a new building, compared with Neurobat AG [216] who indicate that they need two weeks of data collection and model training for intelligent heating system control. However, for other scenarios and office and building configurations, this duration might be longer or shorter. Several new mechanisms are suggested in Table 6.3 for further scenarios.

The fact that ten memory parameters have converged to three final values (1, 0.4 and 0.6) suggests that the number of learning strategies can be reduced to 3 or 4. In this case, the convergence rate might be accelerated, leading to shorter commissioning procedures. On the other hand, one may bear in mind that there is a possibility of seasonal dependency of the learning system. In that case, the convergence situation might be different and all ten memory parameters may be amended at some point of the year. In any case, the present study is suggesting a framework that allows adding new strategies in the future if a need is identified.

Electric lighting energy demand reduction was not the main focus of this study, although by privileging daylight over electric light, the developed controller obviously lowers energy consumption. Since the experiments are mainly carried out in summer time with relatively long days, the influence of this system on the electric lighting energy consumption is not revealed.

Fortunately, the experimentation could enjoy from different sky conditions with different instability levels during the in-situ experiments. The results show that the number of shading actuations increases with the weather instability index. From an engineering point of view this behavior of the controller is justifiable:

- i) The controller makes the decisions regarding the shading position each time a new event is detected. Even if the geometry-based commands are filtered by time and magnitude filters [79], during a highly unstable day, the number of movements remain large.
- ii) The controller does not have any information about the weather conditions in the future. Thus, it cannot command the shading predictively.

Some suggestions to overcome this limitation are provided in Section 6.7.

6.6. Conclusion

In this chapter, a control approach is suggested to overcome the limitations of the open-loop fuzzy logic-based control systems presented in Chapter 5: i.e. i) necessity for a prior knowledge of the office room, ii) costly adaptation to new office room, and iii) no feedback to the control system in the case of failure. A novel *self-commissioning efficient* approach to overcome the stated issues is proposed: a set of open-loop geometry-based rules are enhanced with a supervised learning module and with information on weather conditions. This approach is validated through an in-situ experiment for 22 days from 7th September to 11th October 2017 in a daylight testbed at Fraunhofer Institute for Solar Energy (ISE), in Freiburg, Germany. This facility is equipped with a High Dynamic Range (HDR) vision sensor, model VIP, to evaluate Daylight Glare Probability (DGP), a horizontal luxmeter and a pyranometer. The goal is to command the shading and electric lighting system so as to keep the glare index and horizontal illuminance in a predefined range of visual comfort zone. For the first 11 days, the learning module fine-tunes some “memory parameters” so as to improve

the performance of the open-loop geometry-based rules. Having reached the convergence state by the end of 11th day, the controller is capable of successfully confining the indoor illumination conditions to the visual comfort zone while actuating the shading system efficiently, i.e. on average 2.54 times a day. The advantage of this model-free control algorithm is that it can be commissioned in another office room equipped with venetian blinds by updating some easy-to-obtain field parameters such as location and orientation of the facade and the workstation.

Having reached this conclusion, one can answer the forth research question raised in Section 1.3 by stating that “yes, it is possible; based on the outcome of an in-situ experiments, the self-commissioning efficient Venetian blind control proved to facilitate the system installation and guaranteed the visual comfort for 96% of working hours.”

6.7. Future Outlook

For updating the learning parameters, a constant magnitude of 10% shown in Table 6.2 is applied. This is a basic approach aiming to validate the presented concept. The constant value is found through a try-and-error approach and leads to successful convergence of the learning process in the case study. However, for other cases, if this basic approach does not lead to satisfactory results, some more intelligent approaches, which are proportional to the lighting situation and shading status during the learning process, can be applied. Some of these innovative approaches are listed in Table 6.3, ranking from the simplest to the most complicated. These methods are for the underaction case. The description of each method shows the advantages with respect to the basic scenario. Similarly, all memory parameters are initialized to 1 on day one of the commissioning. The variables are as follows: $\Delta P = P_2 - P_1$, $\Delta\beta = \beta_2 - \beta_1$, $\Delta DGP = DGP_2 - DGP_1$, μ_{P_k} is the memory parameter for the shading position in the current cycle (k), $\mu_{P_{k+1}}$ is the memory parameter for the shading position for the future control cycle (cycle $k + 1$).

Index	Updating Formula (Underact)	Description
1	$\mu_{P_{k+1}} = \mu_{P_k} - \frac{\Delta P}{P_1}$ $\mu_{\beta_{k+1}} = \mu_{\beta_k} + \frac{\Delta\beta}{\beta_1}$	The normalized amplitude of the shading position and the slat angle amendment is considered. Thus the larger the shading amendment is, the larger also the memory parameter difference.
2	$\mu_{P_{k+1}} = \mu_{P_k} - \frac{\Delta P}{P_1} \cdot \frac{\Delta DGP}{DGP_1}$ $\mu_{\beta_{k+1}} = \mu_{\beta_k} + \frac{\Delta\beta}{\beta_1} \cdot \frac{\Delta DGP}{DGP_1}$	The normalized amplitude of ΔDGP is considered to take into account the “seriousness” of the mistake. For example, if the ΔDGP is not large, it signifies that the decision was not originally too bad. Thus the amendment of memory parameters should not be logically too large.
3	$\mu_{P_{k+1}} = \mu_{P_k} - \frac{\Delta P}{P_1} \cdot \frac{\Delta DGP}{DGP_1} \cdot \frac{DGP_1}{DGP_{ref}}$ $\mu_{\beta_{k+1}} = \mu_{\beta_k} + \frac{\Delta\beta}{\beta_1} \cdot \frac{\Delta DGP}{DGP_1} \cdot \frac{DGP_1}{DGP_{ref}}$	The same as Scenario 3, but it considers the seriousness of the mistake it has committed in the first place by considering DGP_1 .
4	$\mu_{P_{k+1}} = \mu_{P_k} - \max\left(\frac{\Delta P}{P_1} \cdot \frac{\Delta DGP}{DGP_1} \cdot \frac{DGP_1}{DGP_{ref}}, 10\%\right)$ $\mu_{\beta_{k+1}} = \mu_{\beta_k} + \max\left(\frac{\Delta\beta}{\beta_1} \cdot \frac{\Delta DGP}{DGP_1} \cdot \frac{DGP_1}{DGP_{ref}}, 10\%\right)$	The same as Scenario 4 but limiting the changes in each iteration. A combination of Scenarios 4 and 1.

Table 6.3 – Proportional updating scenarios for memory parameters, suggestions for the other scenarios where control system does not converge at all or fast enough.

This approach does not work effectively when the sky condition does not remain stable during the day. It demonstrates too many movements and unnecessary memory updates. In those cases, several strategies can be adopted:

- One may choose a pre-defined maximum number of permitted movements per day, based on recommendations from an automatic shading manufacturer, for example 4 movements/day [217]. If the

majority of the movements (e.g. 3 movements) are made in a short period of the day, then the last movement shall be dedicated to setting the shadings in a position that may prevent glare and then turn the electric lights on to compensate for low horizontal illuminance.

- Develop a model based on the collected data over time and gradually replace the geometry based control with a model predictive control (MPC), by taking into account weather prediction. In this case, the controller may plan the movements ahead of time so as to deploy them in an optimum manner. Moreover, by considering the weather predictions at the beginning of each day, one is capable of categorizing the sky condition into “stable” and “unstable”. The objective function and constraints of the MPC model may be alerted by knowing the sky stability. For example, for “unstable” days, the visual comfort constraints may be relaxed since the occupant might appreciate illumination variation. Feedback from the occupant through his/her interaction with the building switches may be valuable clues for constraint updates.

In this study, the memory parameters for position and slat angle are updated together since the closed-loop control amends both position and slat angle in a single step in order to bring the office illumination to the visual comfort zone. The original idea behind this choice was to avoid too many movements during the learning process. However, the authors believe that if the mentioned amendments are made separately, by giving priority to slat angle and then to the shading position, the memory parameters may converge to more delicate and finer actions.

The initial tuning and commissioning procedure, i.e. orientation and location of the workstation and facade, can be even further simplified by integrating the information from the ceiling mounted HDR vision sensor equipped with a fisheye lens.

Although the learning system has converged in this experiment, before final technology transfer, one needs to perform extensive experiments for other situations and some other shading types such as roller blinds. Ergo, other configurations for the facade and workstation orientation can be tested to evaluate the convergence rate of the learning system as well as the overall performance of the control system. This idea could not be implemented due to the change of the season and dominantly overcast sky conditions.

A long-term experiment will confirm if the learning system will eventually evolve through the seasons or if current memory parameters apply for other seasons. Moreover, the experiments in winter may reveal the potential influence of this approach on electric lighting energy demand.

Chapter 7

Conclusion

The main objective of this doctoral thesis was to develop a novel control approach for sun shading and electric lighting systems in non-residential buildings based on High Dynamic Range vision sensors. The indoor lighting conditions, as well as the visual comfort perceived by a user from his/her viewpoint, are optimized by the controller while increasing simultaneously the energy performance of the building envelope and services. Discomfort glare indexes were monitored using this innovative HDR sensing technology and used to drive the integrated control system. Moreover, in the course of this work, a possible evolution of this integrated control system to a marketable product has been studied. An integrated control platform was developed and successfully implemented for this purpose in the LESO solar experimental building on the EPFL Campus in Lausanne (Switzerland), as well as in a building at the Fraunhofer Institute for Solar Energy (ISE), in Freiburg i.B. (Germany).

A summary of the achievements of this thesis is given in Section 8.1. The subsequent section indicates the limitations of the present approach; suggestions for a continuation and extension of this research work are finally presented in Section 7.4.

7.1. Achievements

The doctoral thesis has mainly addressed two research and development objectives: i) the empowerment and fine tuning of HDR vision sensors presented in Chapter 4; ii) the development of Fuzzy Logic based control systems presented in Chapters 5 and 6.

7.1.1. HDR Vision Sensor

A first generation of HDR vision sensors, named *IcyCAM*, has been customized by means of glass filters, calibrated with care and formerly used to develop an embedded 'on-the-fly' glare rating device. More specifically, a computationally efficient image processing program (Section 4.4) was written in C++ computer language and implemented in the embedded Digital Signal Processor of the sensor. The device was then able to create luminance maps of a built environment based on raw sensor readings, extract glaring pixels and group them to identify glare sources, which are characterized to be able to evaluate glare indices. The solid angles and position indexes matrices of each glare source are pre-calculated in order to reduce the computation time. Thus, the HDR vision sensor can assess the Discomfort Glare Probability (DGP) at a given viewpoint in about 12 seconds with a 2.5% RMSE with respect to the well-established glare rating computer program *Evalglare* (Section 4.5). The software is robust enough to operate uninterruptedly during an eight-month continuous in-situ monitoring campaign.

Meanwhile, a new generation of HDR vision sensors, named *Vision-In-Package (VIP)*, was prototyped by the Centre Suisse d'Electronique et de Microtechnique (CSEM): 4 VIP sensors, characterized by very tiny dimensions (e.g. $18\text{ mm} \times 18\text{ mm} \times 14\text{ mm}$) compared to *IcyCAM*, were acquired by the Solar Energy and Building Physics Laboratory of EPFL in

September 2016. The VIP sensor features the same CMOS imager technology as the IcyCAM; however, its embedded DSP is more than 3 times more powerful than the original one. This new device has been the subject of a comprehensive calibration procedure (Section 4.2), with consideration of technology transfer requirements: the glass filters, adapting the spectral response of the HDR sensor to the sensibility of human eyes and originally shaped for IcyCAM, were redesigned with gelatin-based filters for the sake of simplicity and cost savings. An innovative method was used for the filters' design and sizing, which does not significantly impair the sensor spectral response fitting the photopic response curve $V(\lambda)$: error function f'_1 [174] equal to 10.26% was observed for the VIP sensor (Section 4.2.3.2.3) with respect to 8.3% for the IcyCAM reported in a previous study by Borisuit [38]. Moreover it was shown that the luminance and illuminance readings for four indoor and one outdoor location around a building deviated by 19.6% and 10.1% respectively with respect to a LMK 98-4 highly accurate imager (Section 5.2). The VIP sensor was successfully employed as a luminance meter during a three-week exchange program in the Singapore-ETH Center (SEC) for characterizing and comparing the daylighting performance of innovative building facades in the Tropics (Section 4.7).

7.1.2. Advanced Control System

As a first step, a short-term in-situ monitoring campaign (15 days in the course of November and December 2015) was carried-out in the LESO solar experimental building in order to perform a subjective assessment of an advanced control approach for office buildings (Section 5.2). The main objective was to compare the performance of a fuzzy logic-based shading and lighting control system in an office room with the one of a 'best-practice' controller installed in a similar room (reference controller). Occupants related variables such as the control system acceptance, paper-based and VDT based visual performance and acuity, the electric lighting demand and the number of shading and lighting amendments were carefully monitored. Two HDR vision sensors were in operation in the advanced office room, one for glare rating from a workspace and another mounted on the ceiling to insure sufficient work plane illuminance. The reference room was equipped with a low-cost ceiling-mounted illuminance meter generally used for control purposes in practice.

30 human subjects, mainly EPFL students, occupied the two office rooms during 15 afternoons for this experimentation. The experimental results indicated that, while the subjects' visual performance remained comparable in the two offices, the electric lighting demand was reduced by 32% in the advanced room with respect to the reference one. On several occasions, especially when the sun disk was in the field of view of the subjects, the advanced control system was successful in preventing discomfort glare while the reference one was unable to detect unfavorable situations.

In a second step, a long-term in-situ monitoring campaign was carried out in the LESO building in order to quantify the impact of the novel control approach on the building energy performance (heat and electric lighting demand) and the indoor lighting conditions (Section 5.3). A robust control system involving IcyCAM, former version of HDR vision sensors was developed for that purpose and successfully operated during 8 months in the same office rooms. The office rooms were regularly occupied by research assistants during the work hours of the monitoring campaign. Prioritization of thermal and visual comfort was implemented in the advanced controller; the same principles of visual comfort and glare rating control were applied as during the short-term monitoring campaign. An image-based presence detection algorithm was used for this campaign and implemented in the ceiling-mounted HDR vision sensor. The experimental results show that the advanced control system maintained the indoor lighting conditions within the visual comfort zone for 88% of the users' presence time. Moreover, the sun shading control system allowed larger solar heat gains in the advanced office room during the heating season and lower cooling load gains during summertime. This optimal sun shading management during the heating season by the advanced controller led to a 19.2% mitigation of the energy performance gap with respect to the reference system, and by 71.9% with respect to a standard user management of solar blinds.

Finally, during a scientific exchange sojourn of 8 months from March to October 2017 at the Fraunhofer Institute for Solar Energy (ISE), a self-commissioning geometry-based controller empowered by a supervised learning algorithm was successfully tested during 22 days in September and October 2017 in an unoccupied daylighting testbed. This innovative controller incorporated the VIP vision sensors and considered the sun profile angle, the DGP glare index, the work plane horizontal illuminance and the solar blind positions for commanding the sun shading and lighting system. The learning module achieves a fine-tuning of ten "memory parameters", i.e. weighting parameters designating significance to geometry-based control rules, in order to improve the operation and performance of the geometry-based rules. The

supervised learning algorithm converged after 11 days: during the remaining time of experimentation the controller maintained the lighting conditions within the visual comfort zone by actuating the sun shading system on average 2.54 times per day. During the operation phase between 8 AM and 6 PM, the visual comfort constraints were respected during 96% of the time.

7.2. Solution Limitations

The novel integrated control approach of sun shadings and electric lighting equipped with HDR vision sensors has demonstrated its capacity of efficiency, flexibility and versatility within non-residential buildings and during office work hours. As is usually the case in the real world, the approach shows some limitations which can be listed as follows:

- The evaluation of work plane illuminance by a ceiling mounted HDR vision sensor cannot be easily generalizable without a sound commissioning procedure, handling the conversion function between the monitored work plane illuminance and its apparent monitored luminance (linked to its reflection factor).
- All the experimentations were performed in south-facing office rooms benefitting from substantial solar heat gain and daylighting provision; the generalization of the results to other orientations should be made with precaution.
- All the experimentations were carried out in single-occupied non-residential buildings; open plan office rooms as well as residential buildings may lead to different energy savings figures and users visual comfort results for the advanced controller.
- The HDR vision sensors produced by CSEM are using S2 CMOS imagers manufactured by Analogue Devices Instrument (ADI); this chip is currently not available as an ADI standard product jeopardizing the delivery capacity of VIP vision sensors in the future.

7.3. Technology Transfer

From the beginning of this project, a close relationship with several industrial partners was established. For this reason, calibration methodologies and control algorithms have been chosen by keeping an eye on the possibility of their transfer to one of the industrial partners. Several proposals were made in order to incorporate the HDR vision sensor approach and/or the developed algorithms to industry. One of the principal projects is the EPFL research unit in the NEST infrastructure at EMPA Dübendorf, called SolAce [218], designed, planned and constructed by LESO-PB with collaboration with LIPID [171] and Lutz Architects [219]. In this unit, illustrated in Figure 7.1, a collaboration with the shading manufacturer Griesser AG and the luminary manufacturer Regent Lighting AG is foreseen for the integration of shading and electric lighting control in an open-plan office. According to the construction planning, the unit will be operational from June 2018.



(a)

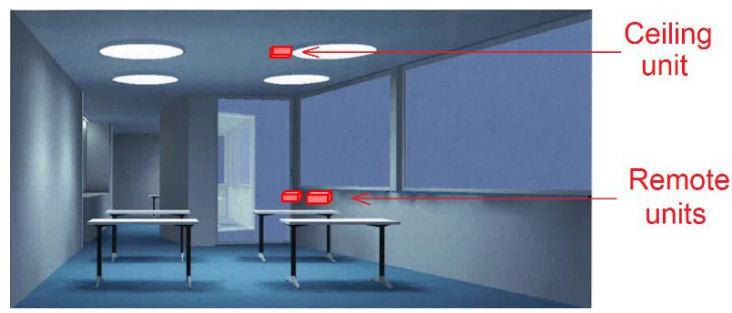


Figure 7.1 – Digitally rendered views of SolAce unit (a) outside; (b) open plan office area showing the intended location of HDR vision sensors.

In addition to this joint project with industrial partners, the HDR vision sensor technology has two potential markets, briefly described in the following sections.

7.3.1. Human Centric Lighting Control System

A joint study of Lighting Europe, the German Electrical and Electronic Manufacturers' Association (ZVEI) and A.T. Kearney, indicates that human centric lighting will become a multibillion-euro business sector covering around 7% of the European lighting market [220]. In the conservative growth scenario, human centric lighting is estimated to be a billion-euro business in Europe, reaching up to €1.4 billion in 2020 (Figure 16(a)). This revenue potential would cover around 20-25% of its high-end general lighting market segment in Europe. Biologically effective lighting will characterize the major part with 65% of the market share.

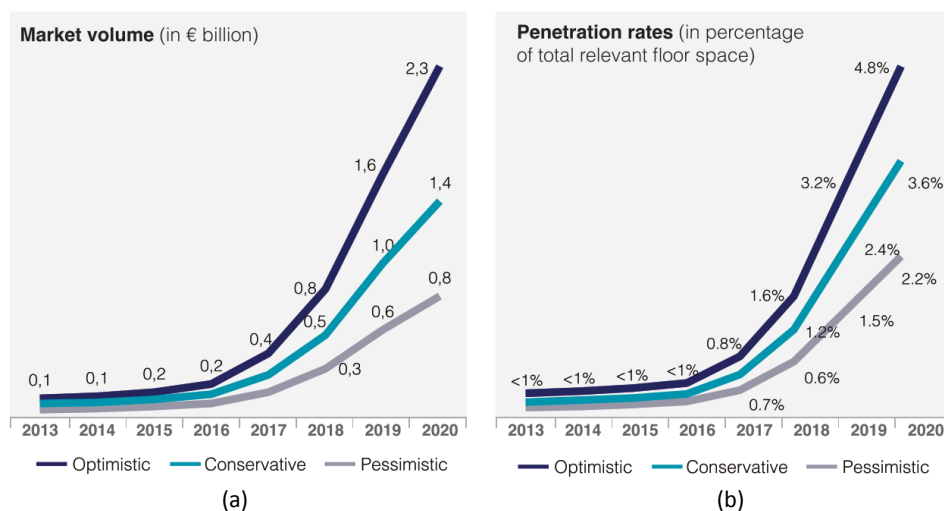


Figure 7.2 – European human centric lighting market growth by 2020; a market study by Lighting Europe, ZVEI and A.T. Kearney [220].

The whole building automation package developed in this thesis, namely, HDR vision sensors, data acquisition and smart control system shall play a major role in this market niche. However, the HDR vision sensor is currently not an interesting option for industrial partners, such as the shading and/or luminary manufacturers, since the current sensor price is too high. In other words, the sensor in its current status is a prototype manufactured by CSEM based on the commercial S2 imaging sensor from Analog Devices Instruments. The sensor price needs to be considerably lower than the current price. To reach this goal, the hardware of the HDR vision sensor must be adapted in a way that a balance between the cost, power consumption and computational power is achieved. Moreover, for industrial partners it is more convenient to integrate the sensor in their standard products if the vision sensor installed close to the user communicates with a central control platform through low-energy wireless communication protocols. In this case, the cabling costs would be cut and the commissioning would enjoy from a flexible position and orientation of the sensor. Finally, since the current

version of the HDR vision sensor does not differentiate the light spectrum, the biological effect of light on building occupants cannot be taken into account by the control system.

Bearing these points in mind, the LESO team from EPFL and CSEM formed a consortium that will pursue the investigations and further improvement of the HDR vision sensor control system in order to achieve an efficient and prompt technology transfer to the market.

A SWOT analysis was carried out to obtain a clearer picture of the current situation of the HDR sensor technology with respect to the market.

Moreover, a step-by-step transfer of the current HDR vision control system to a Swiss sun shading manufacturer has been initiated in Spring 2017. The first step consists in the identification of the shortcomings of the existing automated control technology. In the next step, a HDR vision sensor may be used for enhancing the current control system through on-site monitoring of the indoor lightings conditions during a commissioning procedure. Finally, the current technology may be implemented as a standard product.

Strength	Weakness
<ul style="list-style-type: none"> • Energy efficient solution • Comfortable indoor environment • Facilitated commissioning procedure 	<ul style="list-style-type: none"> • Large infrastructure adaptation • Compatibility with the existing BMS protocols • One sensor for each office occupant
Opportunities	Threats
<ul style="list-style-type: none"> • Rising market for intelligent dynamic building facade • More energy-conscious society • Energy prone legislation 	<ul style="list-style-type: none"> • Acceptability by the user (privacy) • Cyber Security • Similar approaches such as open-loop control

Table 7.1 – SWOT analysis for a human centric shading and lighting control system.

7.3.2. Enhanced Sensor Commercialization

The HDR vision sensing technology, at its current state, can be characterized by a Technology Readiness Level (TRL) of 6, since the system has been demonstrated in a relevant environment. The sensor hardware development is not the core competency acquired during this doctoral thesis. Nonetheless, the sensor calibration, knowledge about daylighting systems, embedded software development and adaptation to lighting industry are the capabilities that are the main skills gained during this period.

A consulting company, such as ESTIA SA, may use this vision sensing system in order to provide the lighting and shading manufacturers with insights into visual comfort issues of existing or new solar blinds. This may help manufacturers to reduce the occupants' complaints regarding the performance of their products. In other words, the sensors may be used as monitoring tools to provide more fundamental recommendations on product improvements.

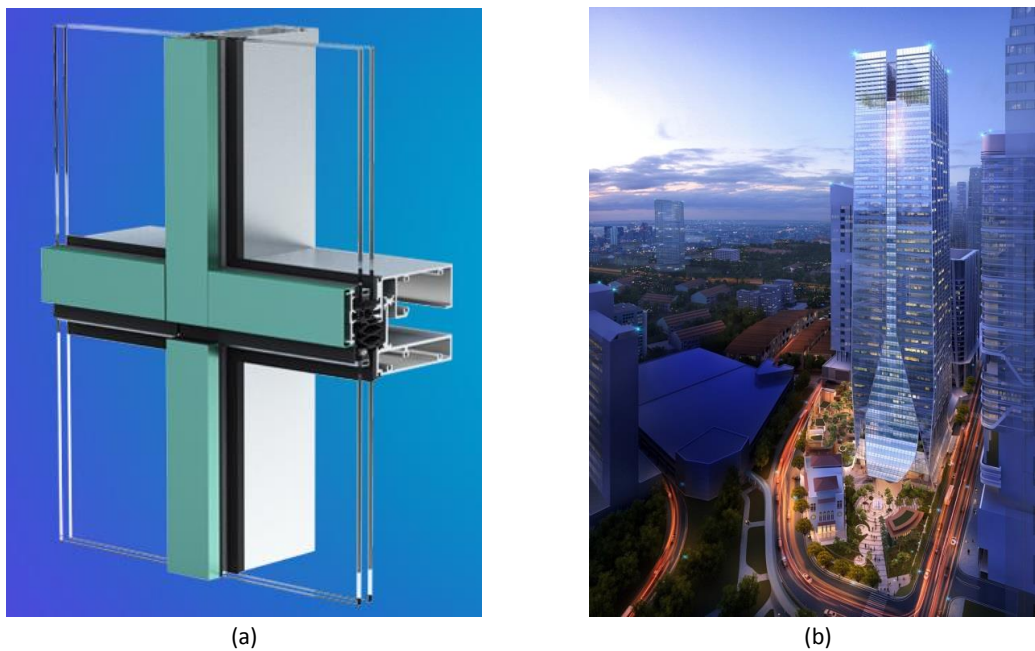


Figure 7.3 – (a) Unitized Curtain Wall, a technique to allow for cladding a building envelope with glass and aluminum, if needed span from floor to floor or even multiple floors; (b) Frasers Tower, double glazed system with active shading devices, in Singapore.

The consulting company may also perform an in-situ evaluation of the visual comfort perceived indoors or in the vicinity of a building for novel facade design during certain periods of year. YKK AP facade is a leading Japanese company in providing techniques, e.g. a unitized curtain wall shown in Figure 7.3 (a), to enable modern architecture to embrace green building design; a control strategy for shading is one of their ongoing projects. Frasers Tower in Singapore illustrated in Figure 7.3 (b), is only using indoor thermal comfort constraints while for such a high window to wall ratio, visual comfort constraints are critical during a considerable fraction of the day.

In this case, the control strategy for the shading and lighting systems can be improved by means of the HDR vision sensor. Control strategies can be adapted to each indoor environment through a pilot monitoring campaign during a commissioning phase.

In the more limited market niche, the device may be applied as an accurate but affordable luminance meter for research purposes. Thanks to its miniaturized design, several sensors can be placed in multi-story buildings for validation of existing glare indices and for visual comfort studies in real situations. For this purpose, a Graphical User Interface (GUI) was prototyped by the LESO IT support team.

The competitor for this use case of the technology is the commercially available digital Single-Lens Reflex (dSLR) cameras. Main players in this field have developed the know-how to evaluate the performance of new lighting systems by means of digital cameras. The competitive advantage of the HDR vision sensor technology developed in this thesis are:

- Lower operational costs due to on-the-fly image processing
- Lower material costs due to microelectronic manufacturing

A SWOT analysis was also carried-out and listed in Table 7.2.

Strength	Weakness
<ul style="list-style-type: none"> • Single platform for several applications • High accuracy • Small and convenient packaging and size • Competitive cost (if mass produced) 	<ul style="list-style-type: none"> • At the current state, it is expensive • Limited computation power • Not currently Integrated into luminaires
Opportunities	Threats
<ul style="list-style-type: none"> • Emerging demand for on-site monitoring 	<ul style="list-style-type: none"> • Dependency on ADI for the hardware

Table 7.2 – SWOT analysis for the sensor commercialization.

7.4. Future Outlook

Despite the results and achievements in developing a novel sun shading and electric lighting control system realized during this thesis, there is still a margin for future investigations and development toward a marketable product. A non-exhaustive list of suggestions for improvements is given in the following lines:

- The potentials of the enhanced BMS in the open-plan offices are not studied during this thesis. As these type of offices are getting prevalent in the modern non-residential buildings, the performance assessment of the system shall be of interest for evaluating the break-even-point of the initial investment for building constructors as well as BMS developers.
- Considering user wishes and personalization of the control strategy to individual occupant is a topic that was studied in the context of an EPFL master project in micro-engineering involving machine learning methods to parameterize glare rating [221]. Implementation of the results in the existing control platform may allow improving even further the control system acceptability by the users.
- The integration of the HDR vision sensors within BAS in day-to-day life would be facilitated by developing a plug-and-play connecting module for the vision sensors to a KNX- or OPC-UA-based network (the use of laptop computers as intermediates would be avoided, commissioning would be speed up).
- A Graphical User Interface (GUI) would facilitate the use of an HDR vision sensor as luminance monitoring device and should be developed to facilitate its utilization by non-specialists and laymen/laywomen.
- Embedded laptop cameras and/or VDT screens as well as digital cameras available on smart phones should also be considered as possible candidates after the necessary modifications and testing for building control.
- The control routine, the room model training and refinement can be embedded in the sensor itself. During the night, the embedded processor is in idle mode since there is no glare risk to evaluate. Thus, the computation resources can be allocated to room model enhancement by considering the collected data over the previous day. Moreover, the geometry-based controller as well as its supervised learning module are computationally efficient and can be implemented in the VIP sensor embedded DSP in order to facilitate the commissioning procedure.
- An algorithm for person recognition (e.g. facial, movement and gesture) is currently being developed and integrated in the VIP platform by CSEM, Section of Vision Embedded Systems [222]. The integration of the recognition features and the presence detection algorithm developed during this thesis could be a point for further development towards a fully “human centric” system.
- Reducing the energy consumption of the integrated control platform so as to power it with energy harvesting techniques and to use the VIP sensors in a stand-alone mode is an essential slope of development. The vision sensors may transmit information to the platform using lean wireless communication protocols, a development that may be pursued in collaboration with CSEM.
- The “melanopic” filters integrated into the HDR vision sensor platform may be utilized for taking into account Non-Image Forming (NIF) effects of light on occupants, leading to a more comprehensive user centric lighting system.
- The vision-based indoor presence detection algorithm may be used for novel approaches for Perception-based Human Building Interaction detection, such as the one developed in the iHomeLab research facility of the Lucerne University of Applied Sciences and Arts.

- User privacy is a critical issue for video imaging systems in non-residential buildings; numerous social and technical factors have a significant influence on this issue, such as the sensor location, the sensor size and visibility, the sensor brand as well as the type of the indoor environment (i.e. individual or open-plan office, conference room, etc.) and should be investigated further.

Thanks to the accurate and 'on-the-fly' glare rating provided by the HDR vision sensor, as well as the self-commissioning and integrated sun shading and electric lighting control system, more energy-efficient buildings and more comfortable indoor lighting environments can be envisaged. In addition, several potential market applications for this approach as well as the corresponding possible industrial partners have been identified.

This doctoral thesis demonstrated the large application field and potential of a novel discomfort glare rating and vision sensing technology, which is expected to foster human centric building technologies in favour of sustainable development, offering a wide range of encouraging interdisciplinary research and development opportunities.

Bibliography

- [1] P. H. Shaikh, N. B. M. Nor, P. Nallagownden, I. Elamvazuthi, and T. Ibrahim, "A review on optimized control systems for building energy and comfort management of smart sustainable buildings," *Renew. Sustain. Energy Rev.*, vol. 34, pp. 409–429, Jun. 2014.
- [2] M. R. Allen *et al.*, "Climate change 2014 synthesis report," 2014.
- [3] S. K. Wittkopf, E. Yuniarti, and L. K. Soon, "Prediction of energy savings with anidolic integrated ceiling across different daylight climates," *Energy Build.*, vol. 38, no. 9, pp. 1120–1129, 2006.
- [4] D. H. W. Li, T. N. T. Lam, and S. L. Wong, "Lighting and energy performance for an office using high frequency dimming controls," *Energy Convers. Manag.*, vol. 47, no. 9–10, pp. 1133–1145, Jun. 2006.
- [5] International Energy Agency (IEA), "Task 50 advanced lighting solutions for retrofitting buildings," 2013. [Online]. Available: <http://task50.ieajshc.org/>.
- [6] J. Khoury, Z. Alameddine, and P. Hollmuller, "Understanding and bridging the energy performance gap in building retrofit," *Energy Procedia*, vol. 122, no. September, pp. 217–222, 2017.
- [7] P. Hoes, J. L. M. Hensen, L. M.G.L.C., B. de Vries, and D. Bourgeois, "User behavior in whole building simulation," *Energy Build.*, vol. 41, no. 3, pp. 295–302, Mar. 2009.
- [8] C. Reinhart and K. Voss, "Monitoring manual control of electric lighting and blinds," *Light. Res. Technol.*, vol. 35, no. 3, pp. 243–258, Sep. 2003.
- [9] J. L. Scartezzini, A. Faist, and J. B. Gay, "Experimental comparison of a sunspace and a water hybrid solar device using the LESO test facility," *Sol. Energy*, vol. 38, no. 5, pp. 355–366, 1987.
- [10] J. Kim, R. de Dear, C. Cândido, H. Zhang, and E. Arens, "Gender differences in office occupant perception of indoor environmental quality (IEQ)," *Build. Environ.*, vol. 70, pp. 245–256, 2013.
- [11] P. R. Boyce, "Age, illuminance, visual performance and preference," *Light. Res. Technol.*, vol. 5, no. 3, pp. 125–144, Aug. 1973.
- [12] H. P. Huang, L. C. Ou, and Y. Yuan, "Effects of age and ambient illuminance on visual comfort for reading on a mobile device," *Color Res. Appl.*, vol. 42, no. 3, pp. 352–361, 2017.
- [13] R. A. Mangkuto, K. A. Kurnia, D. N. Azizah, R. T. Atmodipoero, and F. X. N. Soelami, "Determination of discomfort glare criteria for daylit space in Indonesia," *Sol. Energy*, vol. 149, pp. 151–163, 2017.
- [14] T. H. Karyono, "Report on thermal comfort and building energy studies in Jakarta-Indonesia," *Build. Environ.*, vol. 35, pp. 77–90, 2000.
- [15] P. O. FANGER, *Thermal comfort. Analysis and applications in environmental engineering*. Copenhagen: Danish Technical Press., 1970.
- [16] R. F. Rupp, N. G. Vásquez, and R. Lamberts, "A review of human thermal comfort in the built environment," *Energy Build.*, vol. 105, pp. 178–205, 2015.
- [17] J. Wienold and J. Christoffersen, "Evaluation methods and development of a new glare prediction model for daylight environments with the use of CCD cameras," *Energy Build.*, vol. 38, no. 7, pp. 743–757, Jul. 2006.
- [18] J. van Hoof, "Forty years of Fanger's model of thermal comfort: comfort for all?," *Indoor Air*, vol. 18, no. 3, pp. 182–201, Jun. 2008.

- [19] J. van Hoof, "Building emissions: female thermal demand," *Nat. Clim. Chang.*, vol. 5, no. 12, pp. 1029–1030, Dec. 2015.
- [20] D. Lindelöf, "Bayesian optimization of visual comfort," École polytechnique fédérale de Lausanne, 2007.
- [21] W. O'Brien and H. B. Gunay, "The contextual factors contributing to occupants' adaptive comfort behaviors in offices - A review and proposed modeling framework," *Build. Environ.*, vol. 77, pp. 77–88, 2014.
- [22] M. Foster and T. Oreszczyn, "Occupant control of passive systems: the use of Venetian blinds," *Build. Environ.*, vol. 36, no. 2, pp. 149–155, 2001.
- [23] A. G. Kostro, "Microstructured glazing for daylighting , glare protection , seasonal thermal control and clear view," 2015.
- [24] B. Paule, J. Boutillier, and S. Pantet, "Global lighting performance," Lausanne, 2014.
- [25] Y. Sutter, D. Dumortier, and M. Fontroynt, "The use of shading systems in VDU task offices: a pilot study," *Energy Build.*, vol. 38, pp. 780–789, 2006.
- [26] S. A. Sadeghi, P. Karava, I. Konstantzos, and A. Tzempelikos, "Occupant interactions with shading and lighting systems using different control interfaces: A pilot field study," *Build. Environ.*, vol. 97, pp. 177–195, 2016.
- [27] Y. Wu, J. H. Kömpf, and J.-L. Scartezzini, "Characterization of a quasi-real-time lighting computing system based on HDR imaging," *Energy Procedia*, vol. 122, pp. 649–654, 2017.
- [28] Pinterest, "Paul Riddle photographer Swiss re tower 'The Gherkin' London," 2017. [Online]. Available: <https://www.pinterest.ch/pin/550776229405924001/>. [Accessed: 16-Sep-2017].
- [29] G. Courret, J.-L. Scartezzini, D. Francioli, and J.-J. Meyer, "Design and assessment of an anidolic light-duct," *Energy Build.*, vol. 28, no. 1, pp. 79–99, 1998.
- [30] R. Altherr and J. B. Gay, "A low environmental impact anidolic facade," *Build. Environ.*, vol. 37, no. 12, pp. 1409–1419, 2002.
- [31] J. Gong, A. Kostro, A. Motamed, and A. Schueler, "Potential advantages of a multifunctional complex fenestration system with embedded micro-mirrors in daylighting," *Sol. Energy*, vol. 139, 2016.
- [32] B. Meerbeek, M. te Kulve, T. Gritti, M. Aarts, E. van Loenen, and E. Aarts, "Building automation and perceived control: A field study on motorized exterior blinds in Dutch offices," *Build. Environ.*, vol. 79, pp. 66–77, 2014.
- [33] F. Linhart, "Energetic , visual and non-visual aspects of office lighting," Swiss Federal Institute of Technology (EPFL), 2010.
- [34] London Hazards Centre Handbook, *Sick Building Syndrome, causes, effects and control*. 1990.
- [35] E. D. McIntyre and E. M. Sterling, "Building environment modificatio: An experimental study," in *Proceedings of the Indoor Air Conference*, 1982, pp. 1067–1072.
- [36] M. Rüger, M. C. M. Gordijn, D. G. M. Beersma, B. de Vries, and S. Daan, "Time-of-day-dependent effects of bright light exposure on human psychophysiology: comparison of daytime and nighttime exposure.," *Am. J. Physiol. Regul. Integr. Comp. Physiol.*, vol. 290, no. 5, pp. R1413-20, May 2006.
- [37] M. Münch, F. Linhart, A. Borisuit, S. M. Jaeggi, and J.-L. Scartezzini, "Effects of prior light exposure on early evening performance, subjective sleepiness, and hormonal secretion.," *Behav. Neurosci.*, vol. 126, no. 1, pp. 196–203, 2012.
- [38] A. Borisuit, "The impact of light including non-image forming effects on visual comfort," École polytechnique fédérale de Lausanne, 2013.
- [39] a. Borisuit, F. Linhart, J.-L. Scartezzini, and M. Munch, "Effects of realistic office daylighting and electric lighting conditions on visual comfort, alertness and mood," *Light. Res. Technol.*, Apr. 2014.
- [40] J. Langevin, J. Wen, and P. L. Gurian, "Simulating the human-building interaction: Development and validation

- of an agent-based model of office occupant behaviors," *Build. Environ.*, vol. 88, pp. 27–45, Jun. 2015.
- [41] S. D'Oca and T. Hong, "A data-mining approach to discover patterns of window opening and closing behavior in offices," *Build. Environ.*, vol. 82, pp. 726–739, 2014.
- [42] X. Zhou, D. Yan, T. Hong, and X. Ren, "Data Analysis and Stochastic Modeling of Lighting Energy Use in Large Office Buildings in China," *Energy Build. j*, vol. 86, pp. 275–287, 2015.
- [43] H. B. Gunay, W. O'Brien, S. D'Oca, and S. P. Corgnati, "On modelling and simulation of occupant models," *Build. Simul. Conf. Hyderabad, India*, no. December, 2015.
- [44] T. Hong, S. C. Taylor-Lange, S. D'Oca, D. Yan, and S. P. Corgnati, "Advances in research and applications of energy-related occupant behavior in buildings," *Energy Build.*, vol. 116, pp. 694–702, 2016.
- [45] D. Yan *et al.*, "Occupant behavior modeling for building performance simulation: Current state and future challenges," *Energy Build.*, vol. 107, pp. 264–278, 2015.
- [46] J. Xiong, Y. Chan, and A. Tzempelikos, "Model-based shading and lighting controls considering visual comfort and energy use," in *Proc. of CISBAT*, 2015, pp. 253–258.
- [47] A. Tzempelikos and H. Shen, "Comparative control strategies for roller shades with respect to daylighting and energy performance," *Build. Environ.*, vol. 67, pp. 179–192, Sep. 2013.
- [48] Y.-C. Chan, A. Tzempelikos, and I. Konstantzos, "A systematic method for selecting roller shade properties for glare protection," *Energy Build.*, vol. 92, pp. 81–94, 2015.
- [49] Y.-C. Chan and A. Tzempelikos, "Efficient venetian blind control strategies considering daylight utilization and glare protection," *Sol. Energy*, vol. 98, pp. 241–254, Dec. 2013.
- [50] J. Xiong and A. Tzempelikos, "Model-based shading and lighting controls considering visual comfort and energy use," *Sol. Energy*, vol. 134, pp. 416–428, 2016.
- [51] H. Shen and A. Tzempelikos, "Daylighting and energy analysis of private offices with automated interior roller shades," *Sol. Energy*, vol. 86, no. 2, pp. 681–704, Feb. 2012.
- [52] H. Shen and A. Tzempelikos, "Daylight-linked synchronized shading operation using simplified model-based control," *Energy Build.*, vol. 145, pp. 200–212, 2017.
- [53] L. L. Simon *et al.*, "Assessment of recent process analytical technology (PAT) trends: A multiauthor review," *Org. Process Res. Dev.*, vol. 19, no. 1, pp. 3–62, 2015.
- [54] H. Alavi, E. Churchill, D. Kirk, J. Nembrini, and D. Lalanne, "Deconstructing human-building interaction," *Interactions*, pp. 60–62, 2016.
- [55] A. Brambilla, H. Alavi, H. Verma, D. Lalanne, T. Jusselme, and M. Andersen, "'Our inherent desire for control': a case study of automation's impact on the perception of comfort," *Energy Procedia*, vol. 122, pp. 925–930, 2017.
- [56] M. Andersen, "Unweaving the human response in daylighting design," *Build. Environ.*, vol. 91, pp. 101–117, Sep. 2015.
- [57] M. L. Amundadottir, S. Hilaire, S. W. Lockley, and M. Andersen, "Modelling Non-visual Responses to Light: Unifying Spectral and Temporal Characteristics in a Single Model Structure," in *In Proc. of CIE Centenary Conference "Towards a New Century of Light"*, 2013, pp. 101–110.
- [58] M. Amundadottir, S. Lockley, and M. Andersen, "Unified framework to evaluate non-visual spectral effectiveness of light for human health," *Light. Res. Technol.*, vol. 49, no. 6, pp. 673–696, Oct. 2017.
- [59] P. Correia da Silva, V. Leal, and M. Andersen, "Occupants' behaviour in energy simulation tools: lessons from a field monitoring campaign regarding lighting and shading control," *J. Build. Perform. Simul.*, vol. 8, no. 5, pp. 338–358, 2015.
- [60] P. Correia da Silva, V. Leal, and M. Andersen, "Occupants interaction with electric lighting and shading systems

- in real single-occupied offices: Results from a monitoring campaign," *Build. Environ.*, vol. 64, no. Rsece 2006, pp. 152–168, 2013.
- [61] R. Jia and C. Spanos, "Occupancy modelling in shared spaces of buildings: a queueing approach," *J. Build. Perform. Simul.*, vol. 10, no. 4, pp. 406–421, 2017.
- [62] R. Jia, R. Dong, S. S. Sastry, and C. J. Spanos, "Privacy-enhanced architecture for occupancy-based HVAC Control," *Proc. 8th Int. Conf. Cyber-Physical Syst. - ICCPS '17*, vol. 1, pp. 177–186, 2017.
- [63] H. Zou, Y. Zhou, H. Jiang, S.-C. Chien, L. Xie, and C. Spanos, "WinLight: A WiFi-based occupancy-driven lighting control system for smart building," *Energy Build.*, 2017.
- [64] L. Nguyen, G. Hu, and C. J. Spanos, "Efficient spatio-temporal sensor deployments: A smart building application," in *IEEE International Conference on Control & Automation (ICCA)*, 2017.
- [65] H. B. Gunay, J. Bursill, B. Huchuk, W. O'Brien, and I. Beausoleil-Morrison, "Shortest-prediction-horizon model-based predictive control for individual offices," *Build. Environ.*, vol. 82, pp. 408–419, 2014.
- [66] W. O'Brien and H. B. Gunay, "Mitigating office performance uncertainty of occupant use of window blinds and lighting using robust design," *Build. Simul.*, vol. 8, no. 6, pp. 621–636, 2015.
- [67] S. Khashe, G. Lucas, B. Becerik-Gerber, and J. Gratch, "Buildings with persona: Towards effective building-occupant communication," *Comput. Human Behav.*, vol. 75, pp. 607–618, 2017.
- [68] Z. Yang and B. Becerik-Gerber, "Assessing the impacts of real-time occupancy state transitions on building heating/cooling loads," *Energy Build.*, vol. 135, pp. 201–211, 2017.
- [69] F. Jazizadeh, A. Ghahramani, B. Becerik-Gerber, T. Kichkaylo, and M. Orosz, "User-led decentralized thermal comfort driven HVAC operations for improved efficiency in office buildings," *Energy Build.*, vol. 70, pp. 398–410, 2014.
- [70] S. Ahmadi-Karvigh, B. Becerik-Gerber, and L. Soibelman, "A framework for allocating personalized appliance-level disaggregated electricity consumption to daily activities," *Energy Build.*, vol. 111, pp. 337–350, 2016.
- [71] A. Ghahramani, C. Tang, and B. Becerik-Gerber, "An online learning approach for quantifying personalized thermal comfort via adaptive stochastic modeling," *Build. Environ.*, vol. 92, pp. 86–96, 2015.
- [72] S. Ahmadi-Karvigh, A. Ghahramani, B. Becerik-Gerber, and L. Soibelman, "One size does not fit all: Understanding user preferences for building automation systems," *Energy Build.*, vol. 145, pp. 163–173, 2017.
- [73] A. Heydarian, E. Pantazis, A. Wang, D. Gerber, and B. Becerik-Gerber, "Towards user centered building design: Identifying end-user lighting preferences via immersive virtual environments," *Autom. Constr.*, vol. 81, no. June 2016, pp. 56–66, 2017.
- [74] A. Katsifaraki, B. Bueno, and T. E. Kuhn, "A daylight optimized simulation-based shading controller for venetian blinds," *Build. Environ.*, vol. 126, no. August, pp. 207–220, 2017.
- [75] F. Oldewurtel *et al.*, "Energy efficient building climate control using Stochastic Model Predictive Control and weather predictions," *Proc. 2010 Am. Control Conf.*, pp. 5100–5105, Jun. 2010.
- [76] M. Benedetti, "Impact of lighting control systems based on 'Non-Image-Forming' effects of light on electric lighting energy demand and user's comfort and performance," 2016.
- [77] M. Benedetti, A. Motamed, and L. Deschamps, "On the integration of Non-Image-Forming effects of light on venetian blinds and electric lighting control," *Energy Procedia*, vol. 122, pp. 1039–1044, 2017.
- [78] A. Motamed, M. Benedetti, and J. Scartezzini, "On the impact of integration of Non-Image Forming (NIF) effect of light on electrical lighting control in non-residential buildings," in *9th International Conference on Indoor Air Quality Ventilation & Energy Conservation In Buildings*, 2016.
- [79] A. Motamed, L. Deschamps, and J.-L. Scartezzini, "On-site monitoring and subjective comfort assessment of a sun shadings and electric lighting controller based on novel High Dynamic Range vision sensors," *Energy Build.*,

- vol. 149, 2017.
- [80] A. Motamed, L. Deschamps, and J.-L. Scartezzini, "Validation and Preliminary Experiments of Embedded Discomfort Glare Assessment through a Novel HDR Vision Sensor," in *CISBAT*, 2015.
 - [81] M. Luckiesh and F. K. Moss, *The science of seeing*. New York: D. Van Nostrand Company, Inc., 1937.
 - [82] P. Petherbridge and R. G. Hopkinson, "Discomfort glare and the lighting of buildings," *Light. Res. Technol.*, vol. 15, no. 2 IEStrans, pp. 39–79, Feb. 1950.
 - [83] P. Chauvel, J. B. Collins, R. Dogniaux, and J. Longmore, "Glare from windows: current views of the problem," *Light. Res. Technol.*, vol. 14, no. 1, pp. 31–46, Mar. 1982.
 - [84] M. Boubekri and L. L. Boyer, "Effect of window size and sunlight presence on glare," *Light. Res. Technol.*, vol. 24, no. 2, pp. 69–74, Jun. 1992.
 - [85] H. D. Einhorn, "Discomfort glare: a formula to bridge differences," *Light. Res. Technol.*, vol. 11, no. 2, pp. 90–94, Jun. 1979.
 - [86] H. D. Einhorn, "A new method for the assessment of discomfort glare," *Light. Res. Technol.*, vol. 1, no. 4, pp. 235–247, Dec. 1969.
 - [87] J. A. Jakubiec, "The use of visual comfort metrics in the design of daylight spaces," Massachusetts Institute of Technology, 2014.
 - [88] M. B. Hirning, G. L. Isoardi, S. Coyne, V. R. Garcia Hansen, and I. Cowling, "Post occupancy evaluations relating to discomfort glare: A study of green buildings in Brisbane," *Build. Environ.*, vol. 59, pp. 349–357, Jan. 2013.
 - [89] I. Konstantzos and A. Tzempelikos, "Daylight glare evaluation with the sun in the field of view through window shades," *Build. Environ.*, pp. 1–13, 2016.
 - [90] M. B. Hirning, G. L. Isoardi, and I. Cowling, "Discomfort glare in open plan green buildings," *Energy Build.*, vol. 70, pp. 427–440, Feb. 2014.
 - [91] M. Hirning, "The application of luminance mapping to discomfort glare : a modified glare index for green buildings student," Queensland University of Technology, 2014.
 - [92] G. Yun, K. C. Yoon, and K. S. Kim, "The influence of shading control strategies on the visual comfort and energy demand of office buildings," *Energy Build.*, vol. 84, pp. 70–85, Dec. 2014.
 - [93] K. Konis, "Predicting visual comfort in side-lit open-plan core zones: Results of a field study pairing high dynamic range images with subjective responses," *Energy Build.*, vol. 77, pp. 67–79, Jul. 2014.
 - [94] F. Haldi and D. Robinson, "Adaptive actions on shading devices in response to local visual stimuli," *J. Build. Perform. Simul.*, vol. 3, no. 2, pp. 135–153, 2010.
 - [95] X. Guo, D. Tiller, G. Henze, and C. Waters, "The performance of occupancy-based lighting control systems: A review," *Light. Res. Technol.*, vol. 42, no. 4, pp. 415–431, Aug. 2010.
 - [96] Y. Agarwal, B. Balaji, R. Gupta, J. Lyles, M. Wei, and T. Weng, "Occupancy-driven energy management for smart building automation," *Proc. 2nd ACM Work. Embed. Sens. Syst. Energy-Efficiency Build. - BuildSys '10*, p. 1, 2010.
 - [97] Y. Bai and Y. Ku, "Automatic room light intensity detection and control using a microprocessor and light sensors," *2008 IEEE Int. Symp. Consum. Electron.*, pp. 1–4, Apr. 2008.
 - [98] D. Han and J. Lim, "Smart Home Energy Management System using IEEE," pp. 1403–1410, 2010.
 - [99] H. J. Keller, "Advanced passive infrared presence detectors as key elements in integrated security and building automation systems," in *Proceedings of IEEE International Carnahan Conference on Security Technology CCST-94*, 1993, pp. 75–77.
 - [100] B. Song, H. Choi, and H. S. Lee, "Surveillance tracking system using passive infrared motion sensors in wireless sensor network," in *2008 International Conference on Information Networking*, 2008.

- [101] Y. Wen, U. C. Berkeley, J. Granderson, and A. M. Agogino, "Towards embedded wireless-networked intelligent daylighting systems for commercial buildings," in *Proc. of the IEEE Int. Conf. on Sensor Networks, Ubiquitous and Trustworthy Computing (SUTTC'06)*, 2006.
- [102] F. J. Bellido-outeirino, J. M. Flores-arias, F. Domingo-perez, A. Gil-de-castro, A. Moreno-munoz, and S. Member, "Building lighting automation through the integration of DALI with wireless sensor networks," *IEEE Trans. Consum. Electron.*, vol. 58, no. 1, pp. 47–52, 2012.
- [103] M. Inanici and J. Galvin, "Evaluation of high dynamic range photography as a luminance mapping technique," Berkeley, 2004.
- [104] A. Thanachareonkit, E. S. Lee, and A. McNeil, "Empirical assessment of a prismatic daylight-redirecting window film in a full-scale office testbed," *Leukos, J. IESNA*, vol. 10, no. August, pp. 19–45, 2013.
- [105] T. Ivergård, B. Hunt, and T. Ivergård, *Handbook of control room design and ergonomics : a perspective for the future*. CRC Press, 2009.
- [106] S. Doyle and C. F. Reinhart, "High dynamic range imaging & glare analysis (II)," 2010.
- [107] G. Ward, *Real pixels. In Graphics Gems II*. Boston, MA: Academic Press Inc., 1991.
- [108] L. Bellia, A. Cesarano, G. F. Iuliano, G. Spada, and N. Federico, "HDR luminance mapping analysis system for visual comfort evaluation," in *Instrumentation and Measurement Technology Conference, 2009. I2MTC'09. IEEE, 2009*, pp. 957–961.
- [109] I. Konstantzos, A. Tzempelikos, and Y.-C. Chan, "Experimental and simulation analysis of daylight glare probability in offices with dynamic window shades," *Build. Environ.*, vol. 87, pp. 244–254, 2015.
- [110] D. Fan, B. Painter, and J. Mardaljevic, "A data collection method for long-term field studies of visual comfort in real-world daylit office environments," in *Proceedings of PLEA, 2009*, pp. 251–256.
- [111] B. Painter, D. Fan, and J. Mardaljevic, "Minimally intrusive evaluation of visual comfort in the normal workplace," in *7th International Radiance Workshop*, 2008.
- [112] E. Lee, "Advanced windows testbed," Berkeley, 2013.
- [113] K. Van Den Wymelenberg and M. Inanici, "A critical investigation of common lighting design metrics for predicting human visual comfort in offices with daylight," *J. Illum. Eng. Soc. North Am.*, vol. 10, no. 3, pp. 145–164, Feb. 2014.
- [114] J. Suk and M. Schiler, "Investigation of evalglare software, daylight glare probability and high dynamic range imaging for daylight glare analysis," *Light. Res. Technol.*, vol. 45, pp. 450–463, 2013.
- [115] Y.-S. Chiou and P.-C. Huang, "An HDRi-based data acquisition system for the exterior luminous environment in the daylight simulation model," *Sol. Energy*, vol. 111, pp. 104–117, 2015.
- [116] C. Goovaerts, F. Descamps, and V. A. Jacobs, "Shading control strategy to avoid visual discomfort by using a low-cost camera: A field study of two cases," *Build. Environ.*, vol. 125, pp. 26–38, 2017.
- [117] T. Iwata, T. Taniguchi, and R. Sakuma, "Automated blind control based on glare prevention with dimmable light in open-plan offices," *Build. Environ.*, vol. 113, pp. 232–246, 2017.
- [118] J. Wienold, "EvalGlare- a radiance based tool for glare evaluation," 2012.
- [119] a. I. Dounis and C. Caraiscos, "Advanced control systems engineering for energy and comfort management in a building environment—A review," *Renew. Sustain. Energy Rev.*, vol. 13, no. 6–7, pp. 1246–1261, Aug. 2009.
- [120] F. Rubinstein, G. Ward, and R. Verderber, "Improving the performance of photo-electrically controlled lighting systems," *Journal of the Illuminating Engineering Society*, vol. 18, no. 1. p. 39, 1989.
- [121] L. Bellia, F. Fragiasso, and E. Stefanizzi, "Why are daylight-linked controls (DLCs) not so spread? A literature review," *Build. Environ.*, vol. 106, pp. 301–312, 2016.

- [122] L. Doulos, A. Tsangrassoulis, and F. V. Topalis, "Multi-criteria decision analysis to select the optimum position and proper field of view of a photosensor," *Energy Convers. Manag.*, vol. 86, pp. 1069–1077, 2014.
- [123] M. S. Rea, Ed., *The IESNA Lighting Handbook*. Illuminating Engineering Society of North America, 2000.
- [124] a. Guillemin and N. Morel, "An innovative lighting controller integrated in a self-adaptive building control system," *Energy Build.*, vol. 33, no. 5, pp. 477–487, May 2001.
- [125] a. J. . van Breemen and T. J. . de Vries, "Design and implementation of a room thermostat using an agent-based approach," *Control Eng. Pract.*, vol. 9, no. 3, pp. 233–248, Mar. 2001.
- [126] A. M. Nygard Ferguson, "Predictive thermal control of building systems," 1990.
- [127] E. S. Lee and S. E. Selkowitz, "The design and evaluation of integrated envelope and lighting control strategies for commercial buildings," in *ASHRAE*, 1995.
- [128] F. Oldewurtel *et al.*, "Energy efficient building climate control using stochastic model predictive control and weather predictions," *Proc. 2010 Am. Control Conf.*, pp. 5100–5105, Jun. 2010.
- [129] F. Oldewurtel *et al.*, "Use of model predictive control and weather forecasts for energy efficient building climate control," *Energy Build.*, vol. 45, pp. 15–27, Feb. 2012.
- [130] D. Sturzenegger, D. Gyalistras, and M. Gwerder, "Model Predictive Control of a Swiss Office Building," in *11th REHVA World Congress Clima*, 2013.
- [131] B. Lehmann, D. Gyalistras, M. Gwerder, K. Wirth, and S. Carl, "Intermediate complexity model for Model Predictive Control of Integrated Room Automation," *Energy Build.*, vol. 58, pp. 250–262, Mar. 2013.
- [132] K. Le, R. Bourdais, and H. Gueguen, "Optimal control of shading system using Hybrid Model Predictive control," in *2014 European Control Conference (ECC)*, 2014, pp. 134–139.
- [133] A. Parisio, D. Varagnolo, M. Molinari, G. Pattarello, L. Fabietti, and K. H. Johansson, "Implementation of a scenario-based MPC for HVAC systems: an experimental case study," in *The International Federation of Automatic Control*, 2014, pp. 599–605.
- [134] D. Kolokotsa, A. Pouliezios, G. Stavrakakis, and C. Lazos, "Predictive control techniques for energy and indoor environmental quality management in buildings," *Build. Environ.*, vol. 44, no. 9, pp. 1850–1863, Sep. 2009.
- [135] L. A. Zadeh, "Fuzzy sets," *Inf. Control*, vol. 8, no. 3, pp. 338–353, Jun. 1965.
- [136] A. I. Dounis, M. J. Santamouris, and C. C. Lefas, "Building visual comfort control with fuzzy reasoning," *Energy Convers. Manag.*, vol. 34, no. 1, pp. 17–28, Jan. 1993.
- [137] C. Kurian, R. Aithal, J. Bhat, and V. George, "Robust control and optimisation of energy consumption in daylight-artificial light integrated schemes," *Light. Res. Technol.*, vol. 40, no. 1, pp. 7–24, Mar. 2008.
- [138] P. H. Shaikh, N. Bin, M. Nor, P. Nallagownden, and I. Elamvazuthi, "Indoor building fuzzy control of energy and comfort management," *Res. J. Appl. Sci. Eng. Technol.*, vol. 6, no. 23, pp. 4445–4450, 2013.
- [139] Ž. Kristl, M. Košir, M. Trobec Lah, and A. Krainer, "Fuzzy control system for thermal and visual comfort in building," *Renew. Energy*, vol. 33, no. 4, pp. 694–702, Apr. 2008.
- [140] Commission Internationale de l'Eclairage (CIE), "Guide on interior lighting," 1986.
- [141] ISO/CIE, "Lighting of Indoor Work Places, ISO 8995-1:2002(E)/CIE S 008/E:2001," 2001.
- [142] European Committee for Standardization, "EN 12464-1:2011: E," Brussels, 2011.
- [143] Technical Committee CEN/TC 169 "Light and Lighting," "European standard prEN17037:2016 E (draft)," Brussels, 2016.
- [144] "DIN SPEC 67600. Biologically effective illumination - Design guidelines.," no. April. pp. 1–68, 2013.

- [145] International WELL building institute, "The WELL building standard, V 1.0," New York, 2015.
- [146] Green Building Council, "LEED USGBC v4," 2017. [Online]. Available: <https://new.usgbc.org/leed>. [Accessed: 07-Oct-2017].
- [147] Federal Office for the Environment FOEN, "Swiss climate policy," 2017. [Online]. Available: <https://www.bafu.admin.ch/bafu/en/home/topics/climate/info-specialists/climate-policy.html>. [Accessed: 20-Sep-2017].
- [148] Federal Office for the Environment (FOEN), "The federal and cantonal buildings programme," 2017. [Online]. Available: <https://www.bafu.admin.ch/bafu/en/home/topics/climate/info-specialists/climate-policy/buildings/buildings-programme.html>. [Accessed: 20-Sep-2017].
- [149] K. Hassan-Shafique, N. Hearing, S. Biswas, and A. J. Lipton, "Video-based sensing for lighting controls," WO2008085815A1, 2008.
- [150] A. Bernd, "Controlling a shading devices by means of image recognition," WO2010116274 A1, 2010.
- [151] W. Yao-Jung and B. Dagnachew, "A unified controller for integrated lighting, shading and thermostat control," WO2013153480 A2, 2013.
- [152] N. David, "System for controlling active windows with glare sensor," US 2013/0258484 A1, 2013.
- [153] C. Hubschneider and J. De Boer, "Device and method for controlling the incidence of light," WO 2016/207208 A1, 2016.
- [154] L. Delu *et al.*, "Light control system based on visual comfort," CN204465979U U, 2015.
- [155] S. Lundy and B. Protzman, "Motorized window treatment monitoring and control," 2016.
- [156] A. Guillemin, "Using genetic algorithms to take into account user wishes in an advanced building control system," École polytechnique fédérale de Lausanne, 2003.
- [157] N. Zarkadis, A. Ridi, and N. Morel, "A multi-sensor office-building database for experimental validation and advanced control algorithm development," *Procedia Comput. Sci.*, vol. 32, pp. 1003–1009, 2014.
- [158] N. Zarkadis, "Novel Models towards Predictive Control of Advanced Building Systems and Occupant Comfort in Buildings," vol. 6440, 2015.
- [159] F. Linhart and J.-L. Scartezzini, "Occupant satisfaction in office rooms equipped with anidolic daylighting systems," in *EUROSUN*, 2008.
- [160] F. Linhart and J.-L. Scartezzini, "Evening office lighting – visual comfort vs. energy efficiency vs. performance?," *Build. Environ.*, vol. 46, no. 5, pp. 981–989, May 2011.
- [161] Y. Benezeth, P. M. Jodoin, B. Emile, H. Laurent, and C. Rosenberger, "Review and evaluation of commonly-implemented background subtraction algorithms," *2008 19th Int. Conf. Pattern Recognit.*, pp. 2–5, 2008.
- [162] C. R. Wren, a. Azarbayejani, T. Darrell, and a. P. Pentland, "Pfinder: real-time tracking of the human body," *IEEE Trans. Pattern Anal. Mach. Intell.*, vol. 19, no. 7, pp. 780–785, 1997.
- [163] D. Duque, H. Santos, and P. Cortez, "Moving object detection unaffected by cast shadows, highlights and ghosts," *Proc. - Int. Conf. Image Process. ICIP*, vol. 3, pp. 413–416, 2005.
- [164] E. Sàrl, "Solutions adapted to your building," 2017. [Online]. Available: <http://ergo3.ch/?lang=en>. [Accessed: 11-Oct-2017].
- [165] A. Rysanek *et al.*, "The design of a decentralized ventilation system for and office in Singapore: Key findings for future research," *Proc. CISBAT 2015*, no. May 2016, pp. 77–82, 2015.
- [166] International Commission on Illumination CIE, "Characterization of the Performance of Illuminance meters and luminance meters," S 023/E:2013, 2013.

- [167] "SinBerBEST, Building Efficiency and Sustainability in the Tropics," 2017. [Online]. Available: <http://sinberbest.berkeley.edu/>. [Accessed: 10-Sep-2017].
- [168] A. Schlueter *et al.*, "3for2 : Realizing Spatial , Material , and Energy Savings through Integrated Design," *Counc. Tall Build. Urban Habitat J.*, no. 11, pp. 40–45, 2016.
- [169] A. Schlueter and C. K. Wee, "Leveraging low exergy building systems for symbiotic building design in the tropics," in *Proc. of the SB 13 Singapore- Realising Sustainability in the Tropics*, 2013, vol. 4, pp. 978–981.
- [170] P. J. Waldram, *A standard of daylight illumination of interiors*, vol. 3. The Estates Gazette, 1909.
- [171] "EPFL LIPID," 2017. [Online]. Available: <http://lipid.epfl.ch/>. [Accessed: 15-Sep-2017].
- [172] P. Rüedi, P. Heim, S. Gyger, and F. Kaess, "An SoC Combining a 132dB QVGA Pixel Array and a 32b DSP / MCU Processor for Vision Applications," in *IEEE International Solid-State Circuits Conference*, 2009, pp. 46–48.
- [173] M. Andersen, "Innovative bidirectional video-goniophotometer for advanced fenestration systems," 2004.
- [174] Commission Internationale de l'Éclairage (CIE), "Methods of characterizing Illuminance meters and luminance meters - Performance, characteristics and specifications 19476:2014 (E)." CIE, 1987.
- [175] A. Borisuit, J.-L. Scartezzini, and A. Thanachareonkit, "Visual discomfort and glare rating assessment of integrated daylighting and electric lighting systems using HDR imaging techniques," *Archit. Sci. Rev.*, vol. 53, no. 4, pp. 359–373, Nov. 2010.
- [176] E. (Etienne) Grandjean, *Ergonomics in computerized offices*. Taylor & Francis, 1987.
- [177] M. Vieira, A. Motamed, P. Sergio, and J. L. Scartezzini, "Toward proper evaluation of light dose in indoor office environment by frontal lux meter," in *Proc. of CISBAT*, 2017.
- [178] A. Aarts, MPJ; van Duijnhoven, J; Aries, MBC; Rosemann, "Performance of personally worn dosimeters to study non-image-forming effects of light: Assessment methods," *Build. Environ. J.*, vol. 117, pp. 60–72, 2017.
- [179] K. Bhagavathula, A. H. Titus, and C. S. Mullin, "An extremely low-power CMOS glare sensor," *IEEE Sens. J.*, vol. 7, no. 8, pp. 1145–1151, 2007.
- [180] A. Bierman, T. R. Klein, and M. S. Rea, "The Daysimeter: a device for measuring optical radiation as a stimulus for the human circadian system," *Meas. Sci. Technol.*, vol. 16, pp. 2292–2299, 2005.
- [181] M. G. Figueiro, R. Hamner, A. Bierman, and M. S. Rea, "Comparisons of three practical field devices used to measure personal light exposures and activity levels," *Light Res Technol*, vol. 45, no. 4, pp. 421–434, 2013.
- [182] A. H. Fakra, H. Boyer, F. Miranville, and D. Bigot, "A simple evaluation of global and diffuse luminous efficacy for all sky conditions in tropical and humid climate," *Renew. Energy*, vol. 36, no. 1, pp. 298–306, 2011.
- [183] The MathWorks Inc., "Goodness of fit between test and reference data - Math works Switzerland," *Product Documentation*, 2017. [Online]. Available: <https://ch.mathworks.com/help/ident/ref/goodnessoffit.html>. [Accessed: 18-Aug-2017].
- [184] A. Motamed, L. Deschamps, and J.-L. Scartezzini, "Lighting control system," 2016.
- [185] C. C. Lee, "Fuzzy logic in control systems: fuzzy logic controller, Part II," *IEEE Trans. Syst. Man. Cybern.*, vol. 20, no. 2, pp. 404–418, 1990.
- [186] K. Tanaka, *An Introduction to Fuzzy Logic for Practical Applications*. 1997.
- [187] G. Chen and T. T. Pham, *Introduction to fuzzy sets, fuzzy logic and fuzzy control systems*. New York: CRC Press, 2000.
- [188] E. Jang, J.S.R., Sun, C.T. and Mizutani, *Neuro-fuzzy and soft computing; a computational approach to learning and machine intelligence*. 1997.
- [189] E. H. Mamdani and S. Assilian, "An experiment in linguistic synthesis with a fuzzy logic controller," *Int. J. Man.*

- Mach. Stud.*, vol. 7, no. 1, pp. 1–13, Jan. 1975.
- [190] M. Sugeno and G. T. Kang, "Structure identification of fuzzy model," *Fuzzy Sets Syst.*, vol. 28, no. 1, pp. 15–33, 1988.
- [191] D. Daum, "On the adaptation of building controls to the envelope and the occupants," 2011.
- [192] F. Linhart and J.-L. Scartezzini, "Minimizing lighting power density in office rooms equipped with Anidolic Daylighting Systems," *Sol. Energy*, vol. 84, no. 4, pp. 587–595, Apr. 2010.
- [193] G. Courret, "Systèmes anidoliques d'éclairage naturel." 1999.
- [194] Universitätsklinikum Freiburg, "Klinik für Augenheilkunde, Back," 2015. [Online]. Available: <https://www.uniklinik-freiburg.de/augenklinik/mit/bach.html>. [Accessed: 15-Nov-2015].
- [195] M. Bach, "The freiburg visual acuity test--automatic measurement of visual acuity.," *Optom. Vis. Sci.*, vol. 73, no. 1, pp. 49–53, Jan. 1996.
- [196] D. M. Levi, S. A. Klein, and A. P. Aitsebaomo, "Vernier acuity, crowding and cortical magnification," *Vision Res.*, vol. 25, no. 7, pp. 963–977, 1985.
- [197] Y. Akashi and P. R. Boyce, "A field study of illuminance reduction," *Energy Build.*, vol. 38, no. 6, pp. 588–599, 2006.
- [198] M. G. Leary, "Reasonable expectations of privacy for youth in a digital age," *Miss. Law J.*, vol. 80, no. 3, pp. 1033–1092, 2011.
- [199] L. G. Bakker, E. C. M. Hoes-van Oeffelen, R. C. G. M. Loonen, and J. L. M. Hensen, "User satisfaction and interaction with automated dynamic facades: A pilot study," *Build. Environ.*, vol. 78, pp. 44–52, 2014.
- [200] J. Page, D. Robinson, N. Morel, and J. L. Scartezzini, "A generalised stochastic model for the simulation of occupant presence," *Energy Build.*, vol. 40, no. 2, pp. 83–98, 2008.
- [201] C.-A. Roulet, *Santé et qualité de l'environnement intérieur dans les bâtiments*. Lausanne: Presses Polytechniques et Universitaires Romandes, 2004.
- [202] E. of the physical environment International Organization for Standardization; Technical Committee ISO/TC 159, Ergonomics, Subcommittee SC 5, "ISO 7730:2005(en), Ergonomics of the thermal environment — Analytical determination and interpretation of thermal comfort using calculation of the PMV and PPD indices and local thermal comfort criteria." 2005.
- [203] C. van Dronkelaar, M. Dowson, C. Spataru, and D. Mumovic, "A review of the regulatory energy performance gap and its underlying causes in non-domestic buildings," *Front. Mech. Eng.*, vol. 1, no. January, pp. 1–14, 2016.
- [204] C. Demanuele, T. Tweddell, and M. Davies, "Bridging the gap between predicted and actual energy performance in schools," in *World Renewable Energy Congress XI*, 2010.
- [205] B. Li and D. Lim, "Occupant behavior and building performance," in *Design and Management of Sustainable Built Environments*, 2013, pp. 1–432.
- [206] L. Karlsen, P. Heiselberg, and I. Bryn, "Occupant satisfaction with two blind control strategies: Slats closed and slats in cut-off position," *Sol. Energy*, vol. 115, pp. 166–179, 2015.
- [207] J. Wienold, F. Frontini, S. Herkel, and S. Mende, "Climate based simulation of different shading device systems for comfort and energy demand," in *12th Conference of International Building Performance Simulation Association*, 2011, pp. 2680–2687.
- [208] H. Ben and K. Steemers, "Tailoring domestic retrofit by incorporating occupant behaviour," *Energy Procedia*, vol. 122, pp. 427–432, 2017.
- [209] E4tech, "LESOSAI 2016: certification and thermal balance calculation for buildings." [Online]. Available: <http://www.lesosai.com/en/>. [Accessed: 11-Jul-2016].

- [210] T. E. Kuhn, "Solar control: A general evaluation method for facades with venetian blinds or other solar control systems," *Energy Build.*, vol. 38, no. 6, pp. 648–660, 2006.
- [211] T. E. Kuhn, "Solar control: Comparison of two new systems with the state of the art on the basis of a new general evaluation method for facades with venetian blinds or other solar control systems," *Energy Build.*, vol. 38, no. 6, pp. 661–672, 2006.
- [212] A. Faist, *Le Soleil - Chaleur et lumière dans le bâtiment*. Lausanne: Société suisse des ingénieurs et des architectes (SIA), 1990.
- [213] R. Dones, T. Heck, and S. Hirschberg, "Greenhouse gas emissions from energy systems: comparison and overview," Villigen, 2004.
- [214] S. Chaiyapinunt and N. Khamporn, "Heat transmission through a glass window with a curved venetian blind installed," *Sol. Energy*, vol. 110, pp. 71–82, 2014.
- [215] D. S. Phatak, "Relationship between fault tolerance, generalization and the Vapnik-Chervonenkis (VC) dimension of feedforward ANNs," *Neural Networks, 1999. IJCNN '99. Int. Jt. Conf.*, vol. 1, no. Vc, p. 705–709vol.1, 1999.
- [216] "Neurobat AG - Interior climate technology," 2017. [Online]. Available: <http://www.neurobat.net/en/home/>. [Accessed: 20-Nov-2017].
- [217] Y. Rittener, "Private communication with Griesser SA." Lausanne, 2016.
- [218] E. Marchesi, "EMPA-399-NEST-SolAce," 2017. [Online]. Available: <https://www.empa.ch/web/nest/solace>. [Accessed: 15-Sep-2017].
- [219] "Architecture Fribourg: Lutz associé sàrl," 2017. [Online]. Available: <https://www.lutz-architectes.ch/>. [Accessed: 15-Sep-2017].
- [220] LightingEurope, German Electrical and Electronic Manufacturers' Association (ZVEI), and A.T. Kearney, "Market study on human centric lighting : going beyond energy efficiency," 2013.
- [221] C. Lehot, "Smart adaptive control of blinds, electric lighting and heating system integrating novel high dynamic range vision sensor," Ecole Polytechnique fédérale de Lausanne, Lausanne, 2017.
- [222] E. Türetken, E. Franzi, and P.-A. Beuchat, "Real-time face detection and recognition on the Vision-In-Package system," 2016.
- [223] A. Motamed, L. Deschamps, and J. L. Scartezini, "Toward an integrated platform for energy efficient lighting control of non-residential buildings," in *Sustainable Built Environment (SBE)*, 2016.
- [224] Nikon Corporation, "Nikkon Imaging products," 2014. [Online]. Available: http://imaging.nikon.com/products/images/technology/nikkor/n06_e.htm. [Accessed: 15-Sep-2014].

Appendix A

Fuzzy Logic Controller (FLC) Principles

A.1. Overview of the FLC

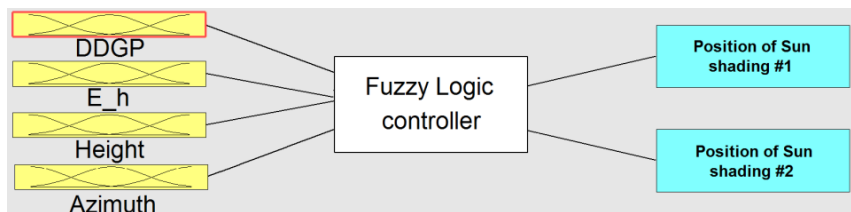
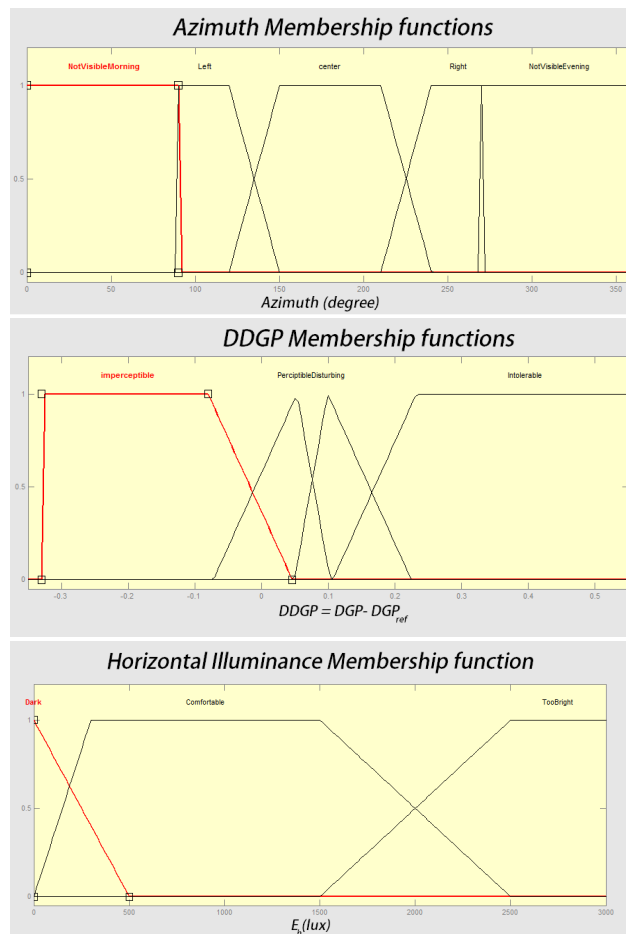


Figure A.1 – Overview of the inputs and outputs of the FLC for short-term and long-term experiments.

A.2. FLC Membership Functions



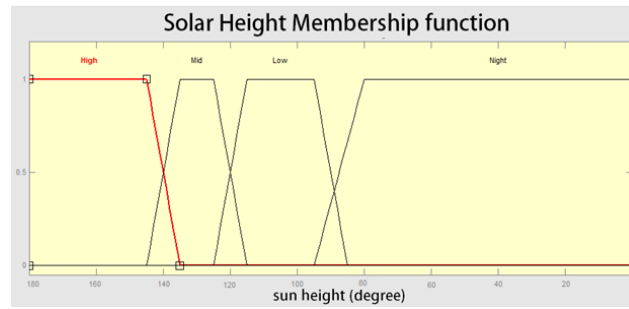


Figure A.2 – Fuzzy logic membership shape functions for short-term and long-term experiments.

Output values of the FLC are the top and bottom shading position (P_{top} & P_{down}) and are crisp value of the following values: $P_{top} \in \{0, 0.5, 0.7, 1\}$, $P_{down} \in \{0, 0.65, 0.83, 1\}$ for fuzzy variables $\in \{\text{Closed, AlmostClosed, AlmostOpen and Open}\}$ respectively. When the shading is fully deployed, it is in “Closed” state.

The FLC rule base

E_h is the horizontal illuminance; h is the sun height; α is the sun azimuth; $DDGP$ is difference between the evaluated daylight glare probability and the perceptible glare threshold; P_{down} is the position of the shading of the normal window and P_{top} is the position of the shading of the anidolic window.

1. If (E_h is dark) or (h is Night) then (P_{down} is Open) & (P_{top} is Open)
2. If (α is NotVisibleEvening) then (P_{down} is Open) & (P_{top} is Open)
3. If ($DDGP$ is not imperceptible) & (h is Low) & (α is center) then (P_{down} is AlmostOpen) & (P_{top} is Open)
4. If ($DDGP$ is not imperceptible) & (h is Low) & (α is Left) then (P_{down} is Open) & (P_{top} is Open)
5. If ($DDGP$ is not imperceptible) & (h is Low) & (α is Right) then (P_{down} is AlmostClosed) & (P_{top} is Open)
6. If ($DDGP$ is not imperceptible) (h is Mid) & (α is Center) then (P_{down} is AlmostOpen) & (P_{top} is AlmostClosed)
7. If ($DDGP$ is not imperceptible) (h is Mid) & (α is Left) then (P_{down} is Open) & (P_{top} is AlmostClosed)
8. If ($DDGP$ is not imperceptible) (h is Mid) & (α is Right) then (P_{down} is AlmostOpen) & (P_{top} is AlmostClosed)
9. If ($DDGP$ is not imperceptible) (h is High) & (α is Right) then (P_{down} is Open) & (P_{top} is AlmostClosed)
10. If ($DDGP$ is not imperceptible) (h is High) & (α is Center) then (P_{down} is Open) & (P_{top} is AlmostOpen)
11. If ($DDGP$ is not imperceptible) (h is High) & (α is Left) then (P_{down} is Open) & (P_{top} is AlmostOpen)
12. If ($DDGP$ is not imperceptible) (E_h is Dark) then (P_{down} is Open) & (P_{top} is Open)
13. If ($DDGP$ is Disturbing) then (P_{down} is AlmostClosed) & (P_{top} is Closed)
14. If ($DDGP$ is Intolerable) then (P_{down} is AlmostClosed) & (P_{top} is Closed)

Appendix B

Technical Details on Testbeds

B.1. The LESO Solar Experimental Building

This appendix is aimed to keep track of the technical aspects of the project. This section will be included in the thesis for facilitating further development in LESO-PB.

B.1.1. Shading Position

The actual positions of the shadings of both offices are, from now on, measured and reported in a text file ('aliValueBlind.txt') by the experimental building's EIB/KNX system. Laurent Deschamps engineered its implementation. As soon as a command, either through the present controller or by physical switches in each office, is sent to the shading or lighting installation, a new line is added to the text file and the new state is reported. This capability is needed in order to detect the occupant/building interaction since the controller that runs on the local laptop is blind to the user/building interactions.

B.1.2. Data Acquisition Fault Detection

A universal data monitoring and fault detection system is designed to reject the faulty data and turn on a flag for data rejection. As soon as the `data_corrupted` flag is turned on, the recorded data is rejected until the correct data is collected. The flag is turned on if input values are out of the physically possible range: positive indoor illuminance and solar radiation values, positive daylight glare probability, positive shading position.

B.1.3. Data Logging File Structure

The data of the measurement campaign is automatically registered on the ad-hoc system [223] where the main controller is running in MATLAB. There are three main files that register the acquired data of the experiment: `DAQ_LE001`, `DAQ_LE002`, `controllers`; where the first file contains the time stamped sensor readings of advanced office room (taking place physically in the office 001 of building LE of EPFL campus; the second file contains the sensor readings of the reference office room (in office LE002) and the third file contains the inputs and outputs of the controllers in the two offices in separate matrices. The file structures are elaborated in Table B.1.

DAQ_LE001		DAQ_LE002		Controller_LE001		Controller_LE002	
i	Quantity	i	Quantity	i	Quantity	i	Quantity
1	Year	1	Year	1	Year	1	Year
2	Month	2	Month	2	Month	2	Month
3	Day	3	Day	3	Day	3	Day
4	Hour	4	Hour	4	Hour	4	Hour
5	Minute	5	Minute	5	Minute	5	Minute
6	Second	6	Second	6	Second	6	Second
7	Sun Height	7	Sun Height	7	Controller type	7	E_h
8	Su Azimuth	8	Su Azimuth	8	DDGP	8	Occupancy
9	DGP	9	E_h	9	E_h	9	Sun height

10	E_h	10	Occupancy	10	Occupancy	10	Sun azimuth
11	Occupancy	11	Indoor temp	11	Sun height	11	Top Shad. Pos.
12	Indoor temp.	12	Roof Horiz. Illum	12	Sun azimuth	12	Bottom Shad. Pos.
13	Roof Horiz. Illum	13	GHI	13	Indoor temp.	13	Lighting Status
14	GHI	14	DHI	14	Top Shad. Pos.		
15	DHI	15	Outdoor temp	15	Bottom Shad. Pos.		
16	Outdoor temp	16	Energy heating	16	Lighting Status		
17	Energy heating	17	Energy lighting				
18	Energy lighting	18	Energy plugs				
19	Energy plugs	19	Top shad. Pos.				
20	Top shad. Pos.	20	Bottom shad. Pos.				
21	Bottom shad. Pos.						

Table B.1 – “DAQ”s and “controllers” file structure.

At mid-night, a new folder is created, the memory is erased from the data of the previous day and new registration files are initiated.

B.1.4. Location of the sensors

The indoor thermometers are integrated in the electric light switches found at the entrance of each office room, as shown in

Figure B.1. These light switches are also equipped with manual temperature setpoint control buttons

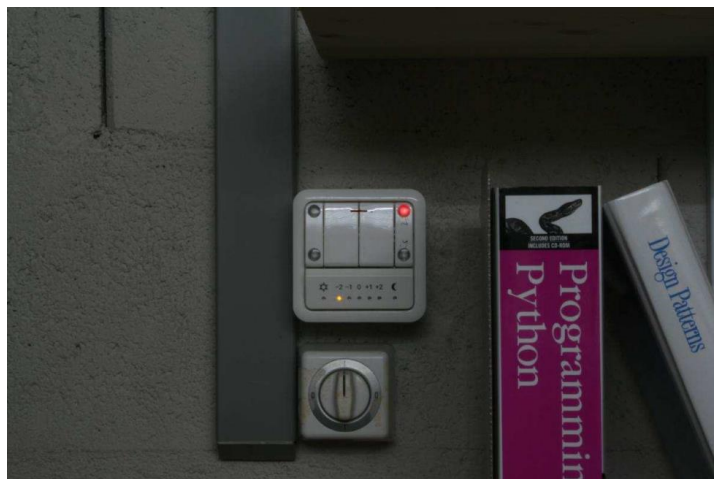


Figure B.1 – Electric light switches, integrating the thermometers and temperature setpoint control buttons. The leftmost rocker is used to adjust the temperature setpoint. The occupant could set the dimming level by means of these switches by pressing and holding the two middle rockers for a couple of seconds [20].

The outdoor air temperature and the pyranometer are both installed on the building's rooftop. The electric lighting energy meters are installed in the electric boxes found in the hallway of the ground floor. The locations of the HDR vision sensors and the ceiling-mounted luminance meters are depicted in Figure 3.2 and Figure 3.3.

B.2. Daylight Testbed at Fraunhofer Institute for Solar Energy (ISE)

B.2.1. Data Logging File Structure

Similar to the experiments in the LESO solar experimental building, for each day, a folder is created in which the following files are registered: `DAQ_ISE.mat`, `controller_ISE.mat`, `memory_history_ISE.mat`, `data_corrupted_time.mat`, `log_ISE`. The restructuring of the first 3 files is shown in Table B-2.

`data_corrupted_time` records the time stamp of the moments when the faulty data were reported by the DAQ system.

`log_ISE`, registers all the run-time notices and messages, facilitating the post analysis of the controller behavior. An example of the runtime messages is shown in Figure B.2.

DAQ_ISE		controller_ISE		memoery_history_ISE	
i	Quantity	i	Quantity	i	Quantity
1	Year	1	Year	1	Year
2	Month	2	Month	2	Month
3	Day	3	Day	3	Day
4	Hour	4	Hour	4	Hour
5	Minute	5	Minute	5	Minute
6	Second	6	Second	6	Second
7	Sun height	7	eDGP	7	Shad. Pos. before Geom. Ctrl
8	Sun azimuth	8	$E_{h_{raw}}$	8	Shad. Slat before Geom. Ctrl
9	DGP	9	Presence	9	DGP before Geom. Ctrl
10	E_v	10	Sun azimuth	10	E_v before Geom. Ctrl
11	E_h	11	Sun height	11	E_h before Geom. Ctrl
12	presence	12	Indoor Temp.	12	Shad. Pos. before Closed-loop Ctrl
13	Indoor Temp.	13	Weather flag	13	Shad. Slat before Closed-loop Ctrl
14	GHI	14	Weather pos.	14	DGP before Closed-loop Ctrl
15	DHI	15	Weather slat.	15	E_v before Closed-loop Ctrl
16	Outdoor temp	16	Output: shad. pos.	16	E_h before Closed-loop Ctrl
17	Shading position	17	Output: shad. slat	17	Shad. Pos. after Closed-loop Ctrl
18	Slat angle	18	Control strategy	18	Shad. Slat after Closed-loop Ctrl
19	Light status			19	DGP after Closed-loop Ctrl
20	Memo. pos. #1			20	E_v after Closed-loop Ctrl
21	Memo. pos. #2			21	E_h after Closed-loop Ctrl
22	Memo. pos. #3			22	Closed loop Act. (Underaction)
23	Memo. pos. #4			23	Closed loop Act. (Overaction)
24	Memo. pos. #5			24	Memo. pos. #1
25	Memo. slat #1			25	Memo. pos. #2
26	Memo. slat #2			26	Memo. pos. #3
27	Memo. slat #3			27	Memo. pos. #4
28	Memo. slat #4			28	Memo. pos. #5
29	Memo. slat #5			29	Memo. slat #1
30	Shad. pos. Intern.			30	Memo. slat #2
				31	Memo. slat #3
				32	Memo. slat #4
				33	Memo. slat #5

Table B-2 – Structure of the data registration files

For communication with the testbed, the in-house “mux” software should be running in the background. To execute this software, one should browse to `.. \mux` folder and type `./mux`.

The sensor readings from the testbed are stored in `.. \mux\data\current_data.txt` and are updated with high frequency.

For sending a command to the shadings, one should browse to `.. \mux` and apply the following commands:

Command	Typeset
---------	---------

Reading the shading position	<code>./get_shared.exe SMI_GET_POS1</code>
Setting the shading position	<code>./set_shared.exe SMI_POS1 target_position</code>
Changing the slat angle	<code>./set_shared.exe SMI_SET_STEP1 delta_angle</code>
Setting the lighting dimming level	<code>./set_shared.exe Dimmer_Licht target_digit</code>

Table B.3 – typesets for sending commands to the actuators

The state of the slate angle is not reported by the testbed DAQ system. For this reason, the shading slat angle memorized by a variable is updated each time it is changed and is initialized to zero as the experiment starts.

In the default system coordinates, the shading position is equal to zero when the shading system is fully retracted (open) and is 100 when it is fully deployed (closed). Moreover, negative values should be applied for closing the slat angles (horizontal to vertical) and to move from horizontal to vertical, “-50” points should be sent.

B.2.2. Controller Implementation

The controller is implemented in MATLAB with routines similar to the one implemented in the LESO solar experimental building (Section 3.1.3). The sensor readings from the testbed are stored in structured text files; these files are opened by a MATLAB routine and pertinent pieces of information are extracted.

The control system posts messages in the command window of the MATLAB (Figure B.2) at each step; these messages are registered at midnight so as to facilitate a further analysis and improvement of the control strategy.

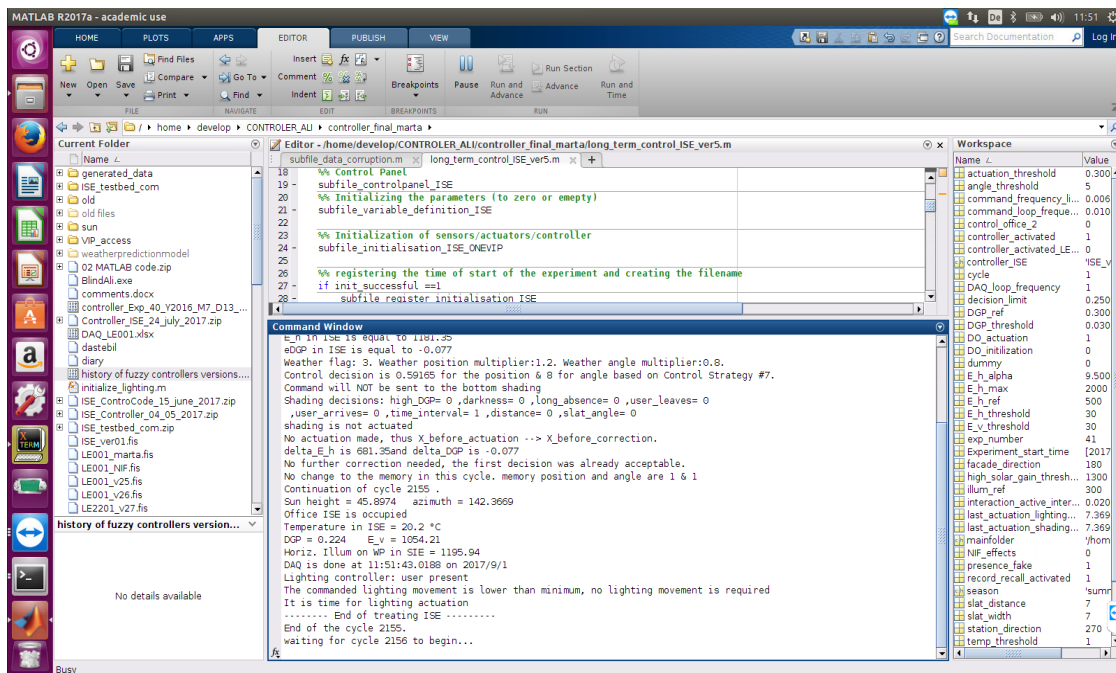


Figure B.2— Screen shot of the remotely accessed desktop of the laptop at daylight testbed in Fraunhofer ISE.

Appendix C

Questionnaire for Subjective Assessment

Survey on the visual and thermal comfort

1. I like the **lighting** in this room: 4 5 6 7 8 9 10

No 2 3 Yes

2. Generally, the **lighting** in this room is comfortable:

No Yes

3. There is **enough** light for proper working/reading:

No Yes

4. There is **too much** light for proper working/reading:

No Yes

5. The light is **poorly distributed** in this room:

No Yes

6. I have the **glare feeling** in this room:

Imperceptible Acceptable Perceptible Uncomfortable Intolerable

1 2 3 4 5

7. I feel:

Extremely nervous Extremely relaxed

8. I feel physically:

Uncomfortable Comfortable

9. I feel:

Extremely tired Extremely awake

10. I feel:

Starving Full/satiated

11. I feel:

In bad mood In good mood

12. I feel:

Extremely hot Extremely cold

[Version française](#)

Figure C.1 – Online questionnaire for subjective assessment during short-term experiments.

Appendix D

Dimming Feature of Electric Lighting

D.1. Foreword

This appendix summarizes the lighting commanding identification and development of a MATLAB function that performs the task of lighting dimming for offices LE001 and LE002. This feature is used for the long-term experiments elaborated in Section 5.3.

D.2. Background

The Luminaires provided by Regent for experimental tests in the LESO experimental building are equipped with a dimming functionality. This functionality allows enhancing energy saving capability of the control algorithm.

There are 16 possible commands (ranging from 0000 to 1111) for dimming with a Digital Addressable Lighting Interface (DALI) system. The dimming command is generated by a MATLAB based program addressing an executable file (.exe) created by the experimental building's IT manager, Laurent Deschamps. This file sends the command through the KNX network communication protocol (EN 50090, ISO/IEC 14543) and a KNX-DALI gateway passes this command to the DALI interface. The impact of each command on the dimming is unknown. An initial guess is that the dimming action happens as a function of the current status of the lighting system and the applied action. Thus, there should be a ratio between the initial and final status.

D.3. Experiment

This ratio should be logically constant for each command however it differs from one command to the other. In order to identify this ratio, an extensive study is performed and the initial and final relative power consumptions for each command are recorded. For each command, at least 6 measurements are captured for different initial relative powers. The precision of power consumption measurement is a tenth of watt. The maximum power consumption is 22W per luminaire. In addition to these measurements, the relative power consumption of the lighting in *off* mode is recorded. Having studied the recorded values, the author figure that there is a constant ratio per command which is calculable as follows:

$$\alpha_c = \frac{\gamma_f - b}{\gamma_i - b} \quad (\text{D-1})$$

where α_c is the ratio that corresponds to the command c ; γ_i is the relative power consumption before applying the command c ; γ_f is the final relative power consumption resulting from applying the command c ; and finally b is the relative power consumption of the lighting when the luminaires are in minimum lighting mode.

It is worth to mention that it is not possible to turn the lighting off completely by means of the dimming command. Instead, the turn on/off command must be applied. The least power consumption attainable by dimming commands is 1.8W, as shown in Figure D.1.

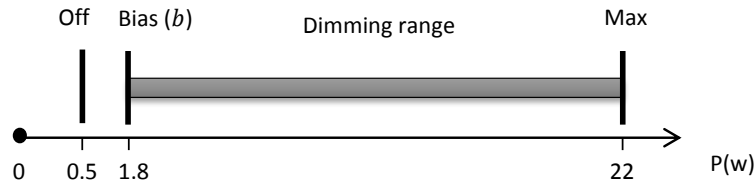


Figure D.1- The power consumption of one LED luminaire (Provided by Regent Lighting, article#: 78H14L1224JA).

$$\gamma_f = \alpha_c(\gamma_i - b) + b \tag{D-2}$$

Where b is the bias of power consumption when the lighting is in dimming mode and it is in its minimum status. For our lighting system $b = 8.2\%$ ($1.8W$).

The commands correspond to all the combinations that a 4-bit variable can obtain. The Most Significant Digit (MSD) correspond to the direction of the variation (increase or decrease). The rest of the digits define the ratio. It is worth mentioning that the values in the first row of Table D.1 are the inverse ($1/x$) of the values of the second row.

Command (c)		(m011)	(m100)	(m101)	(m110)	(m111)
α_c	Decrease ($m = 0$)	0.17	0.39	0.60	0.77	0.84
	Increase ($m = 1$)	6.07	2.53	1.65	1.30	1.23

Table D.1 –Multiplication ratio (α_c) corresponding to each command c . The Most Significant Digit (in this case m) determines the direction of dimming (increase or decrease).

The duration of application of each command is set to 16 seconds by system manager, M. Deschamps.

D.4. Adaptation to Control Platform

It is more favorable for our control platform to be able to pass a desirable power consumption percentage to our dimming function and this function takes care of reaching that percentage. In other words, the following function is favorable:

$$result = dimming (office, \gamma_{desired})$$

The inputs are $office \in \{LE001, LE002\}$ and $\gamma_{desired} \in \{x | 0 < x < 1\}$. However, since there is no feedback/sensor on the lighting system to return its current percentage, in the control platform, the author keep record of the current status (relative power consumption) of the lighting system. Thus, the dimming function is improved to the following equation:

$$[success, \gamma_{final}] = dimming (office, \gamma_{current}, \gamma_{desired}) \tag{D-3}$$

By applying the *dimming* command for *office*, the lighting situation will be changed from the user defined value $\gamma_{current}$ to the desired one $\gamma_{desired}$. As an output, the function returns the final relative power consumption that is attained (γ_{final}). In the next paragraphs, we will explain why $\gamma_{final} \neq \gamma_{desired}$

In an attempt to reach this goal, a new variable is calculated (α_{req}): the required power ratio.

$$\alpha_{req} = \frac{\gamma_{desired} - b}{\gamma_{current} - b} \tag{D-4}$$

Where b is the minimum power consumption reachable by the dimming functionally (Figure D.1). Then, a combination of commands is found whose multiplication leads to the required power ratio:

$$\prod \alpha_{c,i} \cong \alpha_{req} \quad (D-5)$$

$$\alpha_{req} = \frac{\gamma_1 - b}{\gamma_{current} - b} \times \frac{\gamma_2 - b}{\gamma_1 - b} \times \frac{\gamma_3 - b}{\gamma_2 - b} \times \dots \times \frac{\gamma_{desired} - b}{\gamma_n - b} = \alpha_{c,1} \times \alpha_{c,2} \times \alpha_{c,3} \times \dots \times \alpha_{c,n}$$

Obviously, it is not possible to construct *any* required α_{req} by means of commands with predefined ratios for each command. However, it is possible to reach a value close to what the user expressed through α_{req} . Thus, the final relative power consumption (output of the function) reachable by the given condition is evaluated as follows:

$$\gamma_{final} = \gamma_{current} \times \prod \alpha_{c,i} \quad (D-6)$$

This value is provided as the output of the function so as to be used as the $P_{current}$ for the next application of the *dimming*. A MATLAB function called *dimming.m* is debugged and delivered for performing dimming task. This function is ready to be integrated in the control platform.

Appendix E

Supplementary Information Regarding Embedded Glare Assessment by VIP

E.1. Equidistant vs Orthographic Projection

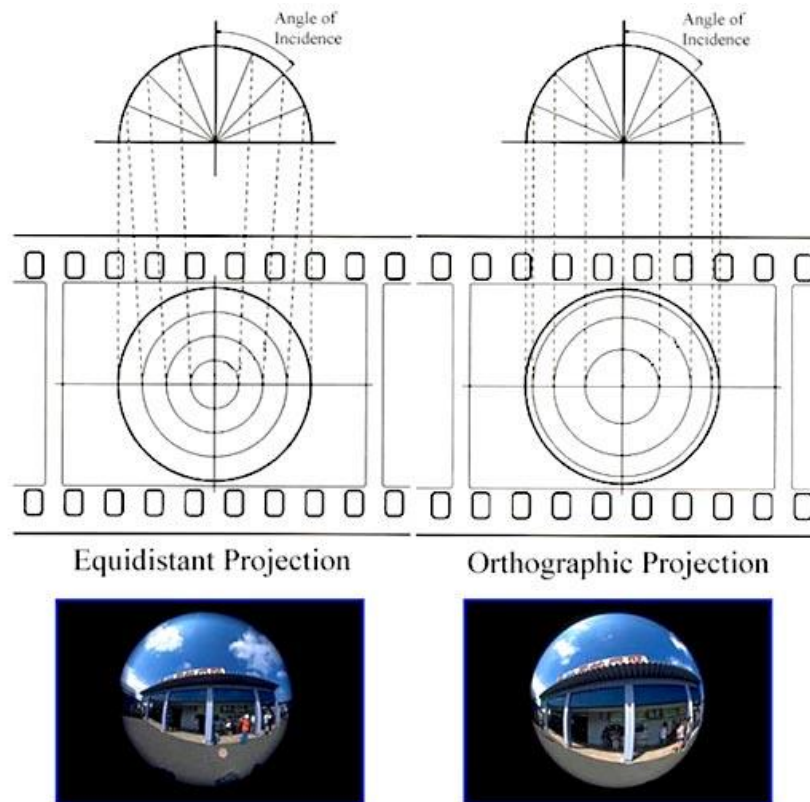


Figure E.1 – Comparison of equidistant and orthographic projection [224].

E.2. Curve Fitting to Simplify the Solid Angle Calculation Process

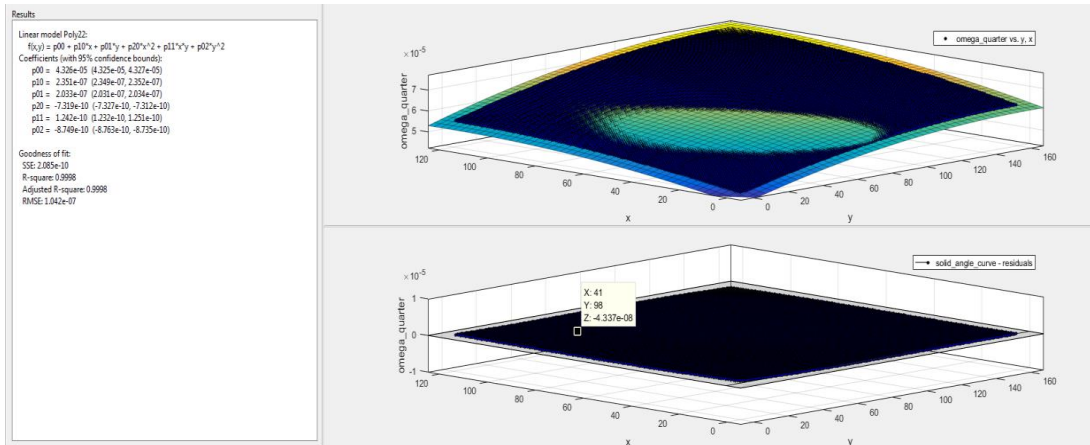


Figure E.2 – Coefficients of the fitted curve to the solid angle matrix.

E.3. Comparison of the Solid Angle Subtended by Pixel in IcyCAM and VIP

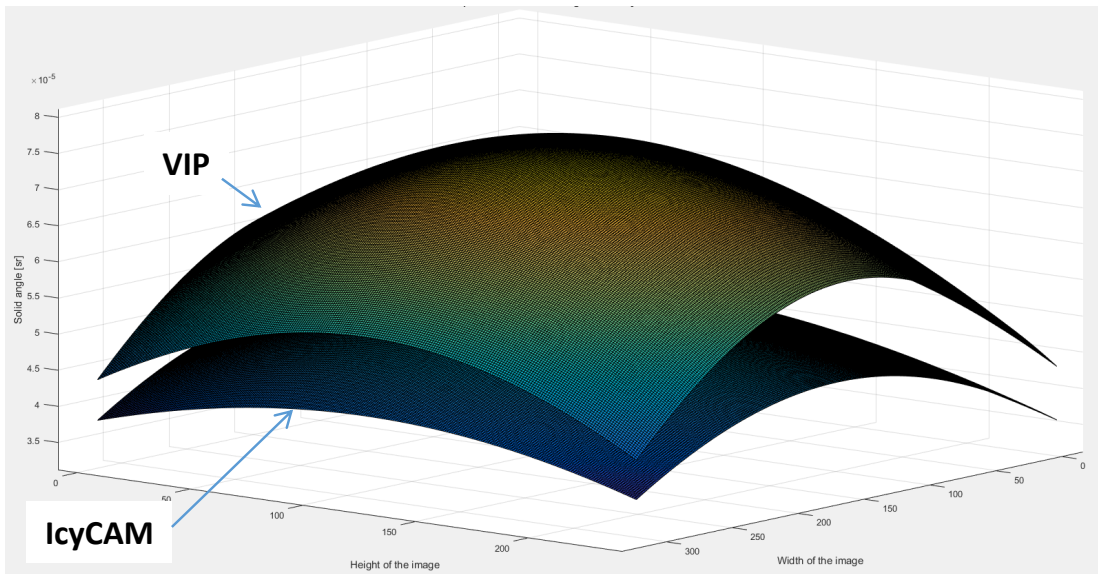


Figure E.3 – Comparison of the solid angle subtended by pixel in IcyCAM and VIP.

E.4. VIP Saturated as Exposed to Sun at Sun Set

The sun disk is visible in the middle of the picture. The captured luminance in the perimeter of the sun disk is larger (and equal to the saturated point) than the luminance of the rest of the sun disk.

The maximum luminance value measurable by VIP is $952'302 \frac{cd}{m^2}$. It is worth noticing that none of the reference luminance meters in the laboratory is capable of capturing the luminance of the sun disk.

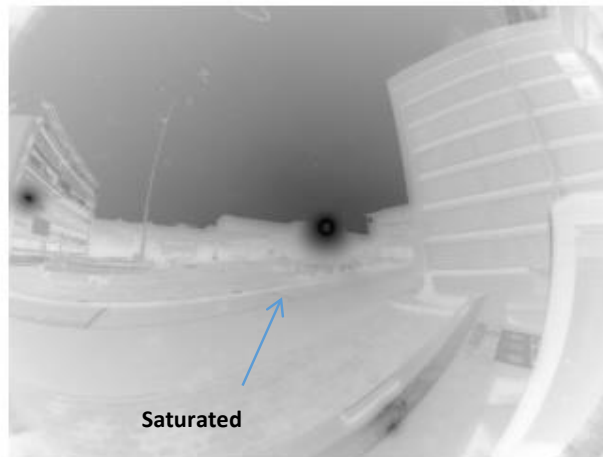


Figure E.4 — The VIP pixel values are saturated as exposed to the direct sun light.

E.5. Spectral Composition of the Light Sources Used for Spectral Calibration of VIP

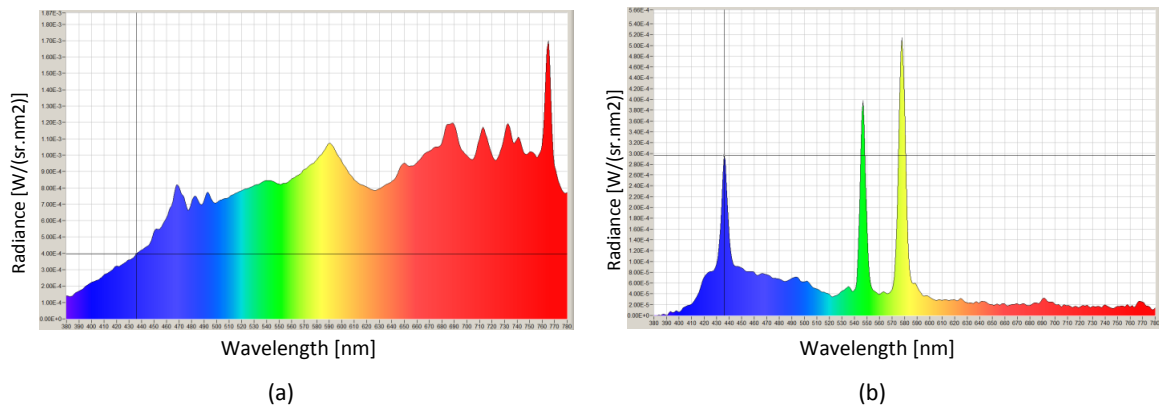


Figure E.5 — (a) Halogen quart-tungsten lamp; (b) Followspot KORRIGAN HMI 1200.

E.5.1. Transferring the Data over Telemetry Channel

The developed routines were recorded in the flash memory of the VIP and can be run by calling a specific identifier (e.g. DGP_calc) in the serial port output. In return, the embedded software sends the output data to a serial port. This port is monitored and read by MATLAB. The routine must be launched once and as long as it is not commanded to stop, it generates the output data in a continuous way. This process is schematically illustrated in Figure E.6.

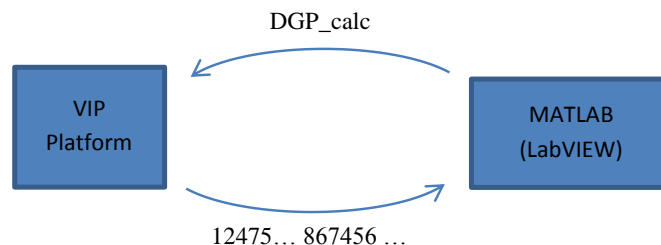


Figure E.6 — Schematic representation of MATLAB/VIP communication protocol.

The data format sent over telemetry channels was chosen by the CSEM developers as an integer format. They used a light version using an integer format so that it accelerates the data transfer. Thus, for maintaining the variables precision in a float format, they are firstly multiplied by 100 and then converted to integer. The integer format accepted by MATLAB is converted back into a float format and divided by 100 to retrieve the original value. The Graphical User Interface (GUI) of the telemetry channel is depicted in Figure E.7.

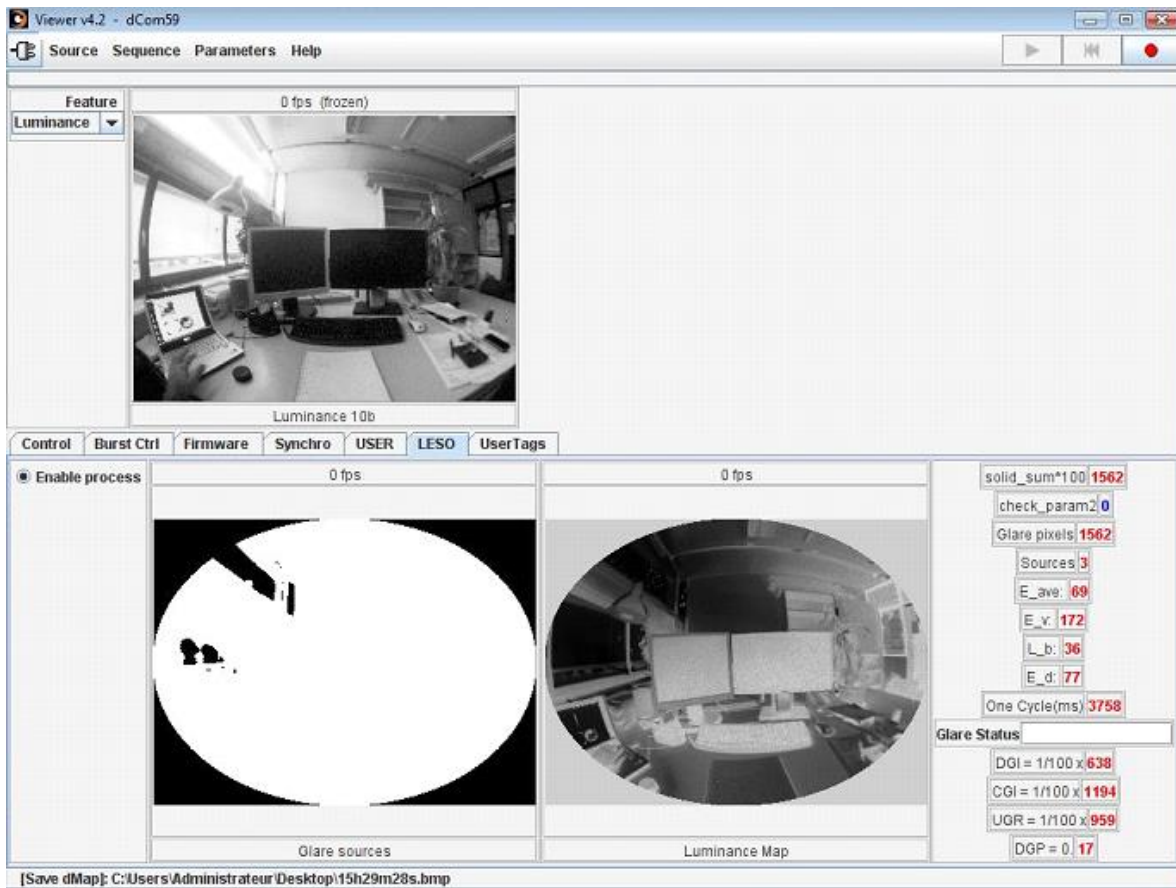
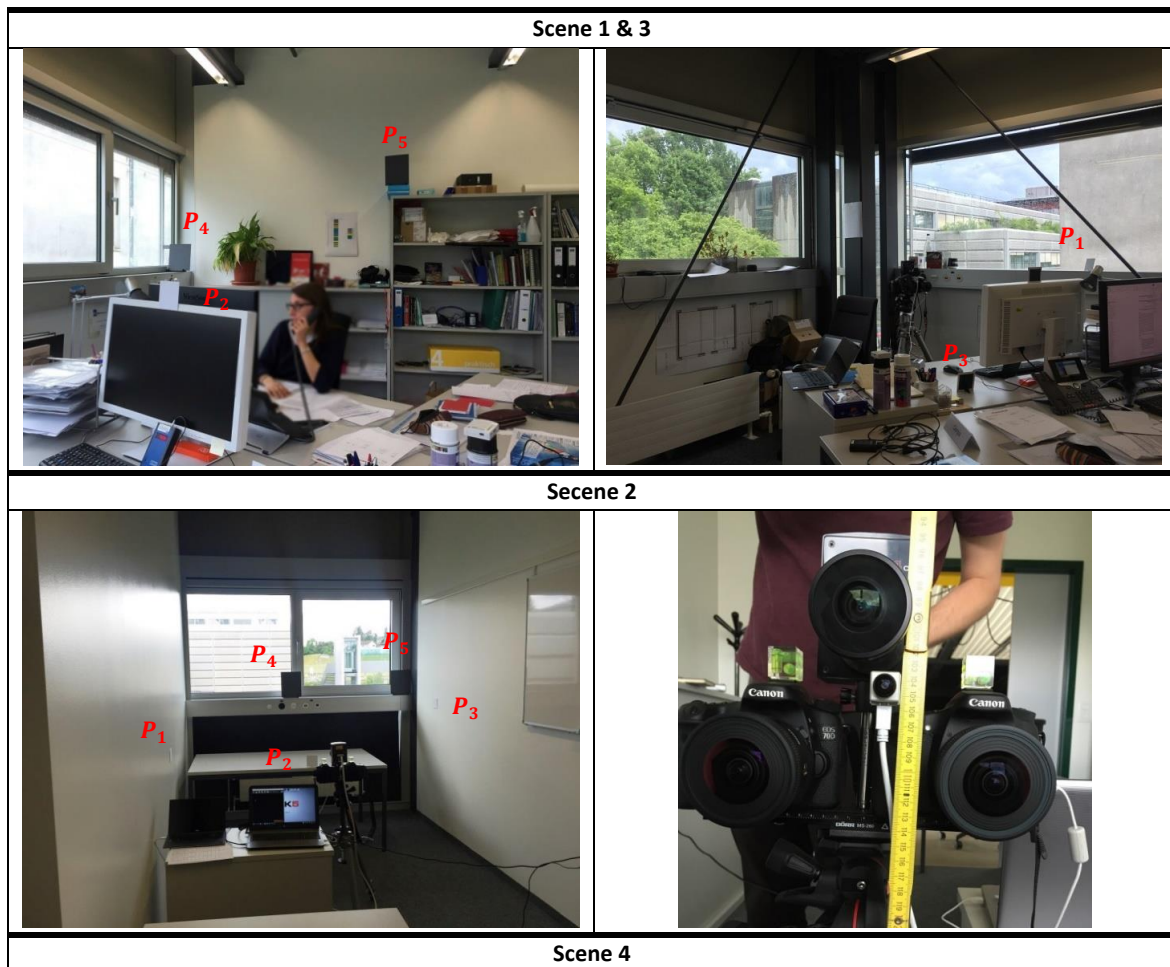


Figure E.7 – The Graphical User Interface (GUI) of the telemetry software connecting the HDR vision sensor to the PC, top left graph: raw data on gray scale; bottom left: glare sources; bottom right: luminance map.

Appendix F

Testbed for HDR Vision Sensor Calibration Checking

In this appendix, the images from the environment used for VIP calibration validation, as reported in Section 4.3, are presented. This study was carried out as a joint project with Laboratory of Integrated Performance in Design (LIPID) [171].





Scene 5



Scene 6



Appendix G

Workplane Illuminance Sensing

This section is partly based on a work presented and published in 2016 at the SBE Sustainable Built Environment Conference in Zürich (Switzerland) [223].

An HDR vision sensor, mounted on the ceiling and facing downward, was used for estimating the work plane illuminance (Figure G.1); this operation usually carried-out by a low cost photosensor fixed to the ceiling is intended to offer appropriate lighting conditions to the users by adjusting the work plane illuminance to the recommended values (e.g. 300 to 500 lux for office work for instance).

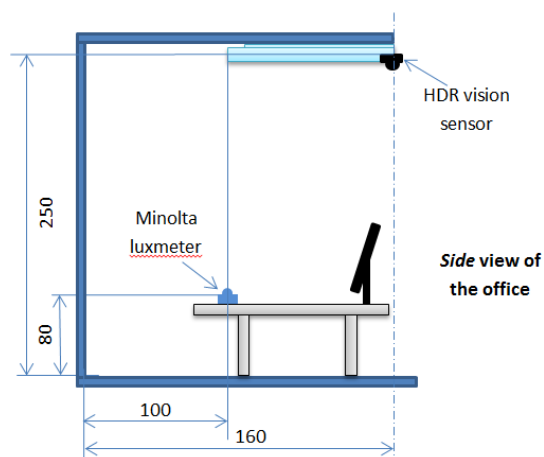


Figure G.1- HDR vision sensor mounted on the ceiling with a work plane illuminance meter calibration setup.

This technique is based on the assumption that all surfaces in the office room are Lambertian, meaning that their apparent brightness is constant whatever the observer's angle of view. This means that the surfaces luminance is isotropic and that the luminous intensity obeys to a cosine law. In other words, the surface illuminance is linearly proportional to the observed luminance according to the inverse of the Lambert law as shown in Eq. (G-1).

$$E = \frac{L \cdot \pi}{\rho} \quad (\text{G-1})$$

where the E is the illuminance of the perfect disusing surface [lx], L is its apparent luminance and ρ is the reflection factor [–] and L is the average apparent luminance of the workstation monitored from the ceiling $cd \cdot m^{-2}$. On the other hand, since it is equipped with a fisheye lens, the illuminance of one or several work spaces located anywhere in the office can be monitored at each image sampling (Figure G.2 (a)).

The ceiling mounted luminance meter has been calibrated using a conventional illuminance meter. A Minolta CL-200A illuminance meter was placed for that purpose directly underneath the ceiling mounted HDR vision sensor to measure the horizontal illuminance on that desk; 160 samples were recorded leading to the calibration curve illustrated on (Figure G.2 (b)).

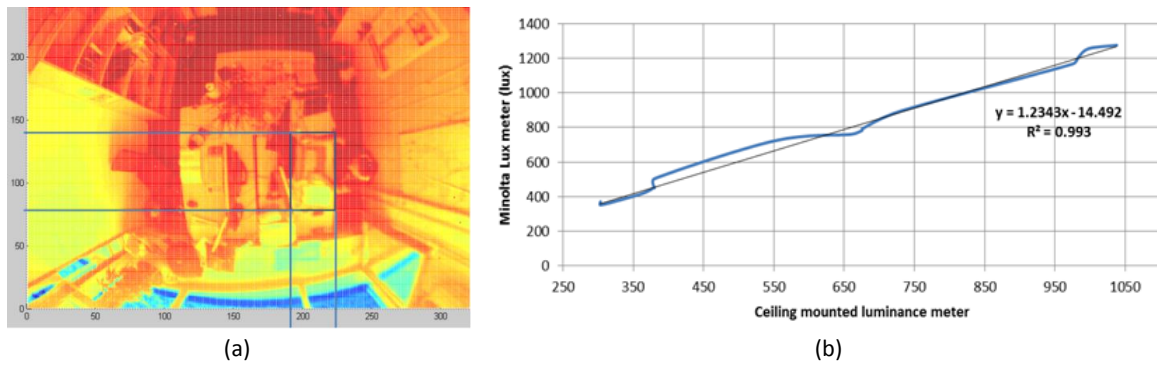


Figure G.2- (a) View from the ceiling mounted HDR vision sensor with a defined zone corresponding to the work plane
 (b) Calibration of the ceiling mounted luminance meter by means of Minolta CL-200A illuminance meter.

A linear correlation between the ceiling mounted luminance meter readings (L_{sensor}) and the workplane illuminance (E_{desk}) was obtained; the average mean square error is $\pm 27 [lx]$. Thus:

$$E_{desk} = 1.2343 \times L_{sensor} - 14.492 \pm 27 [lx] \quad (G-2)$$

Ali MOTAMED



Born on 21 Sept. 1987, Shiraz, Iran, Married
Av. du Tir-Fédéral 29, 1024, Ecublens, Switzerland
ali.motamed@gmail.com +41(0)76 693 24 46
[linkedin.com/in/ali-motamed-55214820](https://www.linkedin.com/in/ali-motamed-55214820)

- EPFL graduate in Mechanical Engineering & Management of Technology and Entrepreneurship
- Research assistant with 3 years of experience in industry and academia
- Entrepreneurial spirit and experienced team player in multicultural contexts
- Project manager at SolAce unit in EMPA NEST; researcher member of SCCER FEEB&D
- Strong analytical, communication and presentation skills; fluent in English, French and Persian

EDUCATION	Doctoral Assistant in Energy EDEY Laboratory of Solar Energy and Building Physics, EPFL, Switzerland Thesis Director: Prof. Jean-Louis Scartezzini	08/2014 – present
	Doctoral Assistant Manufacturing System and Robotics EDPR Laboratory of Applied Mechanics and Reliability Analysis, EPFL Thesis Director: Prof. Thomas Gmür	08/2013 – 8/2014
	Master in Mechanical Engineering, EPFL; Specialization in System Control; Minor in Management of Innovation & Technology GPA: 5.24/6.; Master Thesis: 5.5/6	09/2009 – 09/2012
	Bachelor in Mechanical Engineering Sharif University of Technology (SUT), Tehran, Iran. Cumulative GPA: 3.84/4, ranked 9 th in class	09/2005 – 09/2009
WORK EXPERIENCE	• Project Manager at EMPA NEST SolAce unit Building Automation Technologies, Dübendorf, Switzerland	10/2016 – present
	• Visiting Research Scholar Fraunhofer- Institute for Solar Energy (ISE), Freiburg, Germany	3/2017 – 11/2017
	• Visiting Research Scholar Future Cities Laboratory (FCL), ETH Center, Singapore	1/2017 – 2/2017
	• Responsible for TpC of the course “Techniques de Mesure” Lab. of Applied Mechanics and Reliability Analysis, EPFL	2/2014 – 8/2014
	• Research assistant at Mechanical Systems Design Laboratory EPFL, Switzerland	10/2012 – 7/2013
	• Internship at ABB Switzerland Mineral Local Business Unit, Baden-Dättwil, Switzerland	10/2010 – 9/2011
• Summer Internship at Automatic Control Laboratory Supervisor: Dr. Philippe Müllhaupt, EPFL, Switzerland	Summer 2010	

	<ul style="list-style-type: none"> • Teacher Assistant for Automatic Control Mechanical Engineering Department of Sharif Uni. of Tech., Iran 	09/2008 – 02/2009
	<ul style="list-style-type: none"> • Internship in Bio-mechanics Laboratory Mechanical Engineering Department of Sharif Uni. of Tech., Iran 	Summer 2008
HONORS & AWARDS	<ul style="list-style-type: none"> • IAQVEC2016 Best Paper Award 	10/2016
	<ul style="list-style-type: none"> • Doctoral Exchange Grant by Zeno Karl Schindler Foundation Hosting Institutes: Fraunhofer ISE & Singapore-ETH Center 	04/2016
	<ul style="list-style-type: none"> • Mallefer Prize for Master thesis, EPFL Rewarded for originality, novelty and feasibility of solution 	06/2012
	<ul style="list-style-type: none"> • ABB Scholarship Rewarded for originality, novelty and feasibility of solution 	02/2012
	<ul style="list-style-type: none"> • <i>University Entrance Exam (Nationwide Concours)</i> Ranked 44th among 500,000 competitors, 1st in Shiraz, Iran 	6/2005
SELECTED COURSES	<ul style="list-style-type: none"> • Bio-inspired artificial intelligence; Model predictive control; Modeling, optimization, design & analysis of integrated systems; Design methodology. • Entrepreneurship; Venture challenge; Negotiation techniques; Strategic marketing & technology commercialization 	
LANGUAGE PROFICIENCY	<ul style="list-style-type: none"> • English: excellent command, highly proficient in spoken and written (C1) • French: excellent command, highly proficient in spoken and written (C1) • German: good command, good working knowledge (B1) • Arabic: basic communication skills, working knowledge (A1) • Persian: Native 	
VOLUNTEER EXPERIENCE & MEMBERSHIPS	<ul style="list-style-type: none"> • Peer reviewer of Solar Energy Journal 	01/2015 – present
	<ul style="list-style-type: none"> • Vice-president of Iranian Student Association 	06/2015 – 06/2016
	<ul style="list-style-type: none"> • Board member of Association du Corps Intermédiaire (ACIDE) de l'EPFL 	06/2015 – 06/2016
	<ul style="list-style-type: none"> • Member of Illumination Engineering Society 	03/2014 – present
	<ul style="list-style-type: none"> • Vice-president of Sharif Student Tourism Association 	09/2006 – 09/2008
SOFTWARE SKILLS	<ul style="list-style-type: none"> • MATLAB & Simulink, LabView, C/C++, VB, Maple • Solid Works, ADAMS/view, ANSYS, CATIA, ABAQUS, COMSOL, AutoCAD • All common office and word processing applications 	
PUBLICATIONS & PATENTS	<ul style="list-style-type: none"> • A. Motamed, B. Brueno, A. Katsifaraki, T. Kuhn, J.-L. Scartezini, "Experimental study of self-commissioning glare-based venetian blind control system," (In preparation) • A. Motamed, A. Rysanek, A. Schlueter, J.-L. Scartezini, "Experimental evaluation of daylight performance of novel facade design in tropical climate by HDR vision sensor," (In preparation) • A. Motamed, L. Deschamps, J.-L. Scartezini, "Long-term influence of advanced glare-based 	

shading control on office's performance gap," (In preparation)

- A. Motamed, M. Vieira, P. Sergio, J.-L. Scartezzini, "Experimental study on optimum placement of HDR vision sensor for glare assessment," (In preparation)
- A. Motamed, L. Deschamps and J.-L. Scartezzini, "On-site monitoring and subjective comfort assessment of a sun shadings and electric lighting controller based on novel High Dynamic Range vision sensors," *Energy Build.*, vol. 149, 2017
- M. Vieira, A. Motamed, P. Sergio, and J. L. Scartezzini, "Toward proper evaluation of light dose in indoor office environment by frontal lux meter," in *Proc. of CISBAT*, 2017
- M. Benedetti, A. Motamed, and L. Deschamps, "On the integration of Non-Image-Forming effects of light on venetian blinds and electric lighting control," *Energy Procedia*, vol. 122, pp. 1039–1044, 2017
- A. Motamed, M. Benedetti, and J. Scartezzini, "On the Impact of Integration of Non-Image Forming (NIF) Effect of Light on Electrical Lighting Control in Non-Residential Buildings," in *9th International Conference on Indoor Air Quality Ventilation & Energy Conservation in Buildings*, 2016 (Best Paper)
- A. Motamed, L. Deschamps, and J. L. Scartezzini, "Toward an Integrated Platform for Energy Efficient Lighting Control of Non-residential Buildings," in *Sustainable Built Environment (SBE)*, 2016
- J. Gong, A. Kostro, A. Motamed, and A. Schueler, "Potential Advantages of a Multifunctional Complex Fenestration System with Embedded Micro-mirrors in Daylighting," *Sol. Energy*, vol. 139, 2016
- A. Motamed, L. Deschamps, and J.-L. Scartezzini, "Validation and Preliminary Experiments of Embedded Discomfort Glare Assessment through a Novel HDR Vision Sensor," in *CISBAT*, 2015

**HOBBIES &
INTERESTS**

- Mountain climbing, skiing, biking and traveling
- Psychoanalysis & social psychology

